Spring 1993

Modeling Nutrient and Plankton Processes in the California Coastal Transition Zone

John Roland Moisan
Old Dominion University

MODELING NUTRIENT AND PLANKTON PROCESSES IN THE CALIFORNIA COASTAL TRANSITION ZONE

by

John Roland Moisan
Bachelor of Science May 1983
University of New England, Biddeford, Maine, USA

A Dissertation submitted to the Faculty of
Old Dominion University in Partial Fulfillment of the
Requirement for the Degree of

DOCTOR OF PHILOSOPHY
OCEANOGRAPHY

OLD DOMINION UNIVERSITY
May, 1993

Approved by:

Eileen E. Hofmann (Director)

Larry P. Atkinson

Dale B. Haidvogel

John M. Klinck

Philip R. Wohl

Abstract

MODELING NUTRIENT AND PLANKTON PROCESSES
IN THE CALIFORNIA COASTAL TRANSITION ZONE

John Roland Moisan
Old Dominion University, 1993
Director: Dr. Eileen E. Hofmann

Two time- and space-dependent, physical-bio-optical models have been developed for the California Coastal Transition Zone (CTZ) region with the overall objective of understanding and quantifying the processes that contribute to the spatial and temporal development of nutrient and plankton distributions in the CTZ. The first of these models considers only time- and vertical processes at specific locations in the CTZ. The model food web components include: silicate, nitrate, ammonium, two phytoplankton size fractions, copepods, doliolids, euphausiids and a detritus pool. The wavelength dependent attenuation of the subsurface irradiance field, due to sea water, phytoplankton pigment concentrations and dissolved organic matter, is incorporated as a depth-dependent energy flux which balances the phytoplankton energy uptake and the kinetic energy flux (ΔT) into the water. The one-dimensional model adequately simulates the development and maintenance of a subsurface chlorophyll maximum at different regions within the CTZ. An analysis of the individual terms in the model governing equations reveals that phytoplankton *in situ* growth is primarily responsible for the creation and maintenance of the subsurface chlorophyll maximum. The depth to

which maximum *in situ* growth occurs is controlled by the combined effect of light and nutrient limitation. Also, the simulated bio-optical fields demonstrate the effect of nonlinear couplings between food web components and the subsurface irradiance field on vertical biological distributions. In particular, the depth of the 10% light (PAR) level is influenced by the level of zooplankton grazing.

The second model considers the three-dimensional time-dependent structure of plankton populations in the CTZ. A three-dimensional primitive equation model, developed to simulate the circulation features (filaments) observed in the CTZ, is used to advect the food web constituents of the bio-optical model. The simulated nutrient, plankton and submarine light fields agree well with those observed within the CTZ. Specifically, high nutrient and plankton biomass occur onshore and within the core of the simulated filament. The depth of the 1% light (PAR) level, which results from the simulated plankton distributions, shallows to < 30 m in regions of high phytoplankton biomass, and deepens to > 75 m in regions of low phytoplankton biomass. The onshore and offshore surface carbon flux patterns are similar in shape due to the meander-like flow patterns of the filament; however, the net cross-shelf area-integrated carbon flux is predominantly offshore. The total 20-day integrated carbon transport for the model domain varies with distance from shore and is highest, (35×10^9 g C), in the region where the filament circulation pattern develops into an anticyclonic and cyclonic pair of eddies. Integrated carbon transport by filaments along the California coast is estimated to be 1.89×10^{12} g C over one year.

To my wife

Tiffany Kay Moisan

Acknowledgements

There are many people to whom I owe much gratitude for their inspiration and support in this endeavor. Foremost, I am very grateful to my advisor, Dr. Eileen E. Hofmann, for giving me years of guidance and financial support; for giving me insight into the inner world of the scientific community; for bringing me into the world of numerical modeling; and, for always supporting my work and interests. I also thank my committee members, Drs. Larry Atkinson, John Klinck, Dale Haidvogel and Philip Wohl, for their help, comments and criticisms. I thank Drs. Robert Bidegare, Raleigh Hood, Sharon Smith, Dave Mackas, Libe Washburn, Burton Jones, Curtiss Davis, Francisco Chavez, Jane Huyer, Clayton Paulson and others within the CTZ group for providing me with the wealth of data used to complete this study. A special thanks go to Dr. Joe McCarthy for nurturing my early curiosities and love of nature; and, to Dr. Gilbert Samuels for his dedication to teaching. I am very grateful to both my father and mother for their unending support, patience and love. I am also very grateful to my siblings, Jeanine, Michael, Paul, Peter, Lucie, David, Danny, Marc, Lisa and Chris, for all the encouragement they have given me along the way, and for letting me eat all the food at the table. To my wife, Tiffany, there are no words to express my heartfelt gratitude for all the support, help and love she has given me during the hard times. I also thank Tiffany's parents, sister and grandparents for their support and interest. To my close friends along the way, Phil, Greg, Chuck, Cem and Joan, thanks for all the support and beer. I also thank Dr. Larry Atkinson for his support and for providing such a wonderful working environment (CCPO). Will it ever again be as

good? I thank Drs. Denny Kirwan and Chet Grosch for providing an environment where new ideas and lively discussions are allowed to flourish. A special thanks go to Dr. Kate Hedström for help in understanding and using the SPEM code. A special thanks also to my classmates, Joji Ishizaka, Jorge Capella, Don Eliason, Ana Martins, Cathy Lascara, Lisa Hommel, Peter Becker, G. V. R. K. Vital, Surya Dhakar and others, for all their helpful discussion and support. Finally, I thank the CCPO staff, Karal, Julie, Wayne, Beverly and Carole for all the help along the way.

This research was supported by the Office of Naval Research under grant number N00014-90-J-1930. Computer resources and facilities were provided by the Commonwealth Center for Coastal Physical Oceanography, Naval Research Laboratory and Stennis Space Center. This support is gratefully acknowledged.

Table of Contents

List of Tables

List of Figures

Chapter 1

Introduction

The coastal regions of the oceans encompass the surf zone, shelf, slope and continental rise. Although these regions account for only 10% of the total ocean, they support more than 25% of the total ocean primary productivity (Walsh, 1988); and, are estimated to provide 95% of the worldwide fisheries yield (Ryther, 1969; Walsh, 1988). Coastal regions are also important for commercial trade and recreational activities, are strategic areas for national defense and provide the linkage between estuarine and open ocean waters. The latter point of across-shelf exchange, which allows properties (e.g. chemical and biological) to move from the coastal region to the open ocean and vice versa, is the focus of this study. However, the complex, three-dimensional, time-dependent nature of oceanographic processes in coastal regions makes understanding and quantification of across-shelf exchanges difficult.

During the past decade increased awareness and concern for the coastal regions has resulted in a number of research programs [e.g. California Cooperative Oceanic Fisheries Investigations (CalCOFI; Chelton, 1984); Ocean Prediction Through Observations, Modeling, and Analysis (OPTOMA 21 and 22; Mooers and

Robinson, 1984); Organization of Persistent Upwelling Structures (OPUS; Atkinson et al., 1986); Coastal Ocean Dynamics Experiment (CODE I and II; Beardsley and Lentz, 1987); Central California Coastal Circulation Study (CCCCS; Chelton et al., 1988); Northern California Coastal Circulation Study (NCCCS; Magnell et al., 1990); Coastal Transition Zone (CTZ; Strub et al., 1991)] that had as their primary focus the understanding of oceanographic processes within the coastal ocean. One objective that was common to all these programs was the understanding of across-shelf transfer of mass and energy within coastal regions. One of these programs was the Coastal Transition Zone (CTZ) study (Brink and Cowles, 1991; Strub, et al., 1991) which took place from 1986 to 1988 and focused on a region off the coast of California (Fig. 1). This program had as a primary objective the understanding of the physical and biological nature, structure and cause of formation of cold filaments (Coastal Transition Zone Group, 1988), which were often observed in satellite sea surface temperature and pigment concentration images of the waters off the western coast of North America (Fig. 2). The CTZ program consisted of two field sampling seasons (1987 and 1988), the data from which have provided the basis for this study.

Previous studies of the region off California [e.g. CalCOFI, OPTOMA 21 and 22, OPUS; CODE I and II; CCCCS; NCCCS; CTZ] show that it is primarily a coastal upwelling ecosystem. During spring and summer months, upwelling favorable winds from the north cause a surface divergence at the coast which injects nutrient-rich waters from depth into the euphotic zone. This seasonal pulse of nutrients supports coastal phytoplankton blooms which are dominated

Figure 1. The Coastal Transition Zone study region. The region included in the CTZ physical-bio-optical model domain is indicated by the box. Within this domain, the standardized station grid, which was used during the 1988 CTZ surveys, is shown. The red points indicate the station locations.

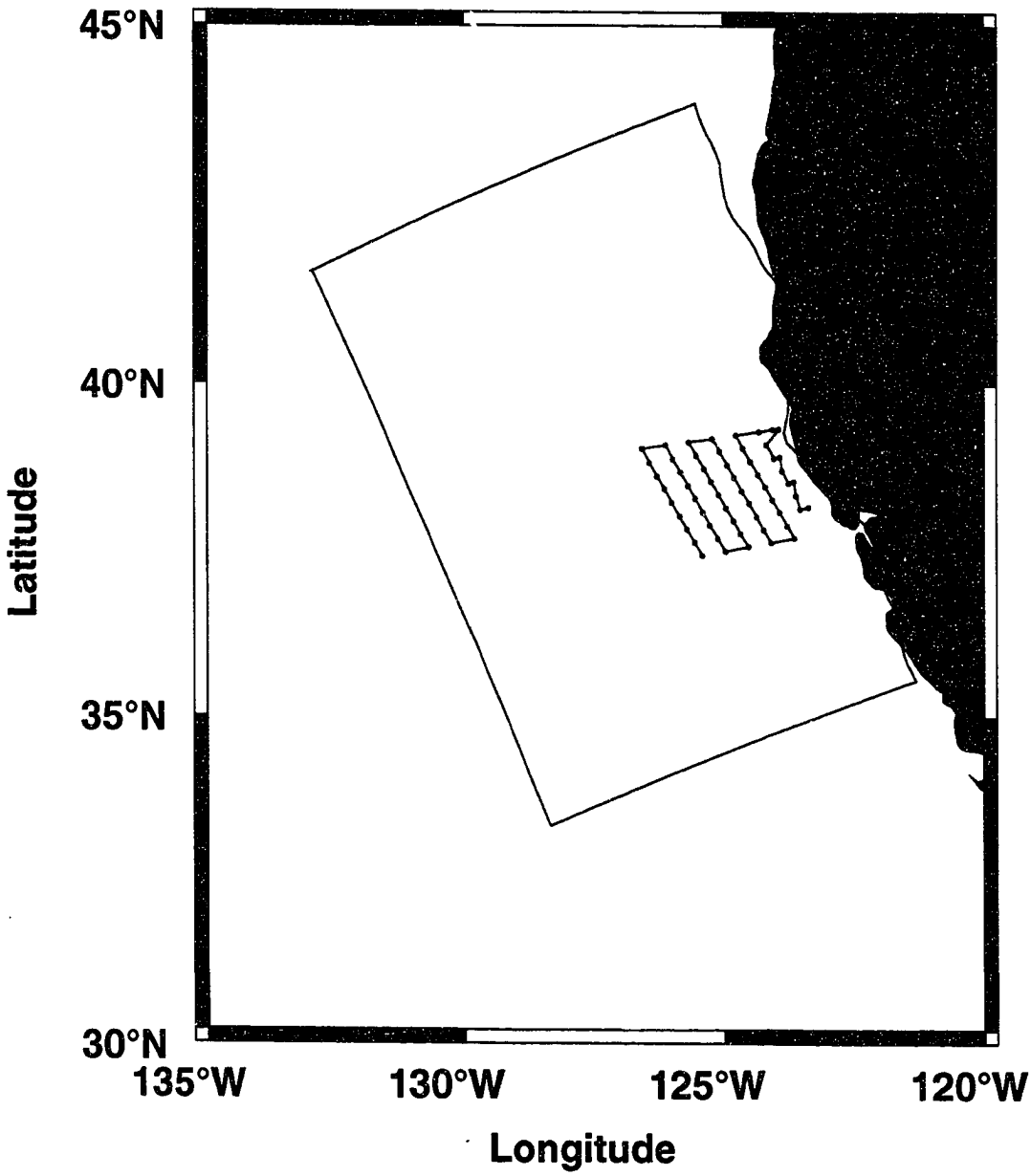

Figure 2. Satellite-derived pigment concentration (left) and sea surface temperature (right) distribution observed in 1981 during the upwelling season off the west coast of the United States. High pigment concentrations associated with colder temperatures indicate areas of upwelling. The upwelling filaments are the elongated features that extend offshore from the coast (Figure from Brink and Cowles, 1991).

by silicate-dependent diatoms and nitrate-dependent dinoflagellates. The phytoplankton bloom in turn supports a suite of secondary producers such as copepods, euphausiids and doliolids. In general, the productivity of coastal waters decreases offshore of the coastal upwelling region (Smith et al., 1988; Hood et al., 1990). Superimposed on the coastal upwelling circulation are the processes and dynamics associated with the California Current System (CCS).

Prior to the introduction of satellites as tools for gathering synoptic surface data on the oceans, the CCS was generally thought to be a broad, shallow, slow, eastern boundary current with a steady, southward drift (Hickey, 1979; Mooers and Robinson, 1984). However, Coastal Zone Color Scanner (CZCS) and Advanced Very High Resolution Radiometer (AVHRR) measurements (Breaker and Gilliland, 1981; Flament et al., 1985; Abbott and Zion, 1985, 1987; Pelaéz and McGowan, 1986; Reinecker and Mooers, 1989*a* and *b*; Dewey and Moum, 1990; Paduan and Niiler, 1990) show the CCS to be characterized by features such as tongues, plumes, filaments (Flament et al., 1985; Strub et al., 1991).

On the basis of satellite-derived measurements and recent field studies, it is now recognized the CTZ, a region of the CCS, is characterized by cold, nutrient- and pigment-rich filaments that originate near the coast and extend offshore as much as 300 km (Breaker and Gilliland, 1981; Abbott and Zion, 1985; CTZ Group, 1988; Strub et al., 1991). Transports and maximum velocities associated with these filaments are 2–6 Sv and 50 cm s^{-1}, respectively (Strub et al., 1991). These narrow (50 km wide) filaments may provide an important mechanism for the across-shelf transport of heat, nutrients, biota and pollutants (Mooers and Robinson, 1984). The circulation dynamics underlying these mesoscale features (Haidvogel et al.,

1991*a*; Allen et al., 1991; Pierce et al., 1991; Walstad et al., 1991) and their effects on plankton processes have only recently been investigated (Bucklin et al., 1989; Abbott and Barksdale, 1991; Mackas et al., 1991; Chavez et al., 1991; Bucklin, 1989; Hofmann et al., 1991; Smith and Lane, 1991). However, quantification of the effect of the physical and biological processes, associated with the filaments, on the distribution, development and fate of plankton in the CTZ is difficult to do on the basis of field studies alone because of the time-dependent nature of this region. Hence, this study presents two time- and space-dependent, physical-bio-optical models which have been developed for the CTZ region (cf. Fig. 1.) with the overall objective of understanding and quantifying the spatial and temporal development of nutrient and plankton distribution in the CTZ. The first of these models considers only time- and vertical processes at specific locations in the CTZ. The results from this model are compared with field observations made at specific locations within the CTZ. The second model considers the three-dimensional time-dependent structure of plankton populations in the CTZ. The results of this are compared to Lagrangian drifter measurements made in the CTZ and are used to obtain estimates of across-shelf fluxes.

Specifically, the results obtained from these models addressed the following questions:

(1) What is the contribution of the biological and/or physical processes to the development of the subsurface chlorophyll maximum at specific locations and throughout the CTZ?

(2) What percent of the total primary production in the CTZ was derived from upwelled nutrients? What percent of the total primary production was advected offshore?

(3) What was the relative contribution of physical and biological processes in producing the observed horizontal distributions in the CTZ? To what extent did these physical and biological interactions affect the plankton population dynamics in the CTZ?

(4) How do the plankton populations develop within the filaments? What is the ultimate fate of these plankton populations?

The ephemeral nature of the filaments that occur in the CTZ make modeling studies an important part of understanding the physical and biological interactions that are responsible for the plankton dynamics associated with the filaments. However, while this study was specific to the CTZ, the models and approaches used are appropriate for addressing similar questions in other coastal environments.

The following section presents background information on the physical circulation patterns and chemical and biological processes associated with the CTZ. Chapter 3 provides details of the models that were used to generate the results presented in Chapter 4. Chapter 5 is a discussion of the model results and Chapter 6 presents the conclusions from this study.

Chapter 2

Background

The following sections provide a review of the studies related to this research. The first section is a description of the physical oceanography of the CTZ. This is followed by an overview of the biological and chemical characteristics of this region.

2.1 Physical Oceanography and Models

2.1.1 The California Current System

The first detailed studies of the CCS were made by Sverdrup and Fleming (1941). Since that time, interest in the CCS has continued in response to the needs of coastal fisheries management and the desire to answer basic scientific questions about the dynamics of eastern boundary currents. The CCS (Fig. 3) is composed of the California Current, California Undercurrent, Davidson Current and the Southern California Countercurrent [also called the Southern California Eddy (Hickey, 1979)]. Simpson et al. (1984) also includes the Deep Poleward Flow in their definition of the CCS. The seasonal variability of the CCS and its associated component currents has been reviewed by Hickey (1979).

Figure 3. Schematic of the mean flow patterns of the four major currents that make up the California Current System (CCS): California Current (green); California Undercurrent (red); Southern California Countercurrent (blue); Davidson Current (purple).

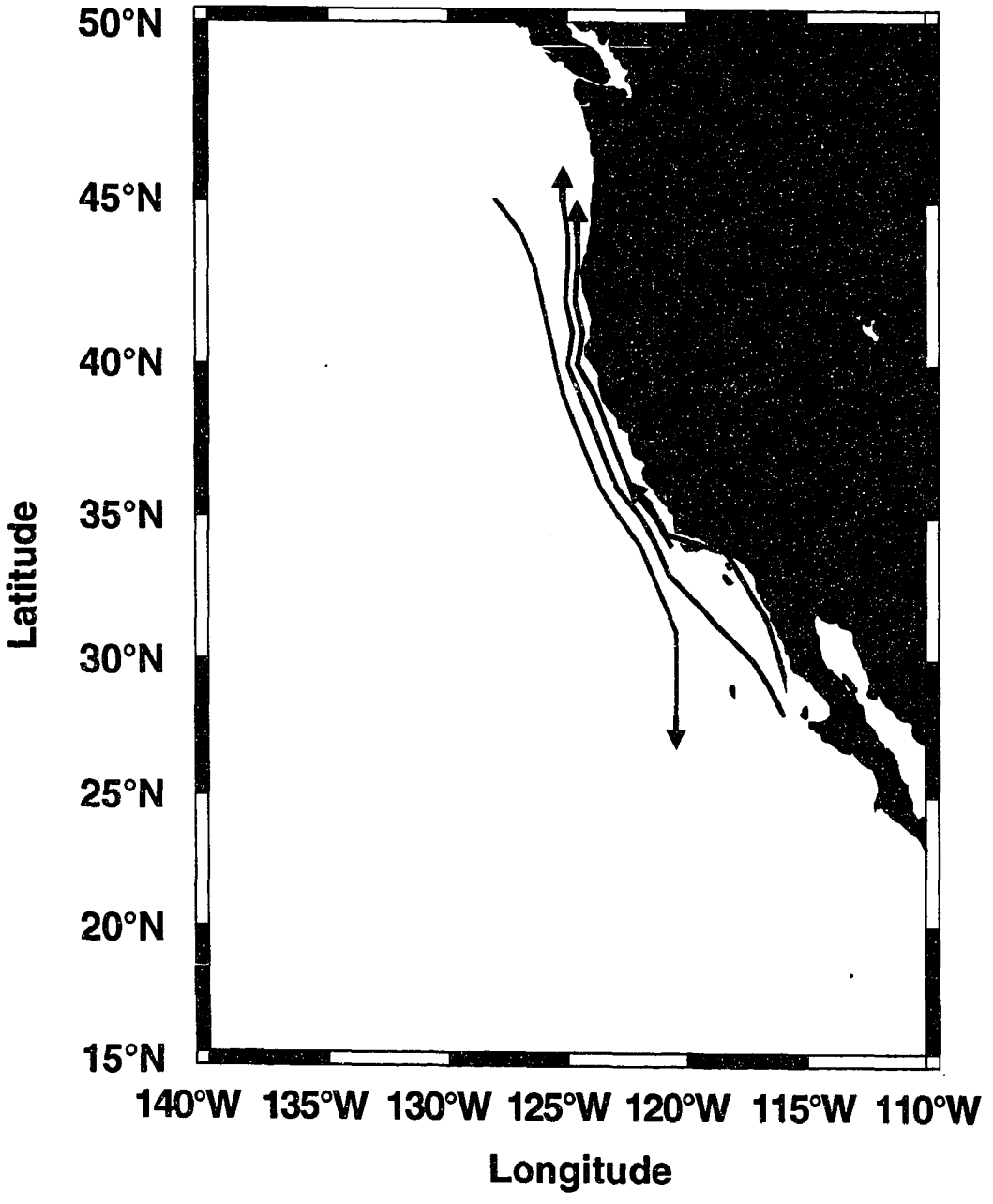

The main current in the CCS is the California Current. The California Current, the upper, equatorward, surface flow along the western coast of the United States, is the southward continuation of the North Pacific West Wind Drift and, as such, forms the eastern boundary current of the North Pacific gyre (Tchernia, 1978). The California Current is restricted to the upper 200–250 m of the water column and is characterized by slow [O(0.01–0.10 m s^{-1})] equatorward surface flow. However, velocities in the range of 0.25 m s^{-1} with a maximum of 1 m s^{-1} have been reported (Simpson et al., 1984). The mean annual location of the core of the current varies with latitude, having its maximum offshore extent ($\approx$450 km) off Cape Mendocino. North of this region, off Oregon and Washington, the California Current is about 250–350 km offshore. Southward, off Point Conception, the current is about 270 km offshore (Hickey, 1979). Two offshore seasonal maxima in flow strength occur in the core of the flow, one during February–March and the other in July–August. Two other seasonal maxima in flow strength occur nearshore during March–April and June–September (Chelton, 1984). These offshore and nearshore velocity maxima are also shown in the seasonally averaged along-shore components of the geostrophic flow (Hickey, 1979)

The California Undercurrent flows poleward in the California Bight between the Channel Islands and the mainland (cf. Fig. 3) and continues north to Point Conception, and perhaps as far north as Oregon (Huyer and Smith, 1975). This current is generally observed over the continental slope at depths of about 200 m. Geostrophic velocities, computed relative to 200 db, indicate that, for the most part, the flow associated with the undercurrent is slow (< 0.10 m s^{-1}) and diffuse. However, direct measurements within the current have indicated jet-like velocity

maxima of 0.40 m s^{-1} off Baja and 0.16 m s^{-1} off Oregon (Hickey, 1979). The transports associated with the undercurrent decreased from 2 Sv off Baja to 0.5 Sv off Oregon (Hickey, 1979). Water property relationships suggest that this current may be a continuation of subsurface flow of equatorial origin (Tsuchiya, 1975; Hickey, 1979; Lynn and Simpson, 1990). The width and depth of the undercurrent was estimated to be about 20 km and 300 m, respectively (Hickey, 1979) off both the northern Baja coast and Oregon. However, the continuity of the current throughout this coastal domain has not yet been determined. The depth of the velocity maximum associated with the California Undercurrent varies with latitude and season (Hickey, 1979). North of Point Conception, the region of interest to this study, the velocity maximum is observed at a depth of 200–300 m during the spring and summer months. It has been suggested (Pavlova, 1966; Hickey, 1979) that during the late fall and winter the high-speed core rises to the surface and becomes the Davidson Current which is a poleward, nearshore (within 100 km from the coast) surface current that is found in the region north of Point Conception. Typical poleward velocities associated with the Davidson Current can approach 0.25 m s^{-1}. The absence of a subsurface velocity maximum for this current led Hickey (1979) to suggest that the current, "may be a surface expression of the California Undercurrent, rather than superimposed on it."

In the fall and winter an atmospheric low pressure system, centered near the Aleutian Islands, develops along with an atmospheric high pressure system centered midway between the Hawaiian Islands and the California Bight (Fig. 4). A second high pressure system located over California serves to create a continuity in the high pressure zone from the continent to the high pressure located offshore

of the California Bight area. At this time the Davidson Current appears along the coast, the California Current flows equatorward along the coast between 40°N to 20°N, and the Southern California Countercurrent is observed to flow north inshore of the California Bight from 30°N to 35°N where it connects with the Davidson Current (Hickey, 1979).

During the summer months, the high pressure system, which in the winter is located west of the California Bight at about 30°N, becomes more intense and moves north to its summer position at 40°N (Fig. 5). The low pressure system, which is located above the Aleutian Islands in the winter, becomes slightly diminished and moves north into the Bering Sea region (Tchernia, 1978). Finally, a low pressure system develops in the Sea of Cortez (Gulf of Mexico) and serves to intensify the pressure gradient along Baja California. These changes in the atmospheric pressure field completely eliminate the Davidson Current, the California Current intensifies offshore and extends further inshore, and upwelling occurs along the coast (Chelton, 1984; Lynn and Simpson, 1987; Strub et al., 1987*a*; 1987*b*; Strub et al., 1990). Also during this season, the Southern California Countercurrent becomes separated from the Davidson Current, which is seldom observed during this time except during wind relaxation events (Chelton et al., 1988), and establishes itself as an eddy system. It is from this circulation pattern that it derives its alternate name, the Southern California Eddy.

The effect caused by the change in the strength of the California Current and coastal upwelling between these two seasons can be observed by comparing the along-shore surface temperature distribution for the winter and summer periods. The surface isotherms are zonal in the winter when the California Current is

Figure 4. The long-term mean atmospheric pressure at sea level for January over the North Pacific Ocean (Anon., 1961). Contours are in millibars with a contour interval of 2.5 mb Hg. High and low pressure centers are denoted by H and L, respectively.

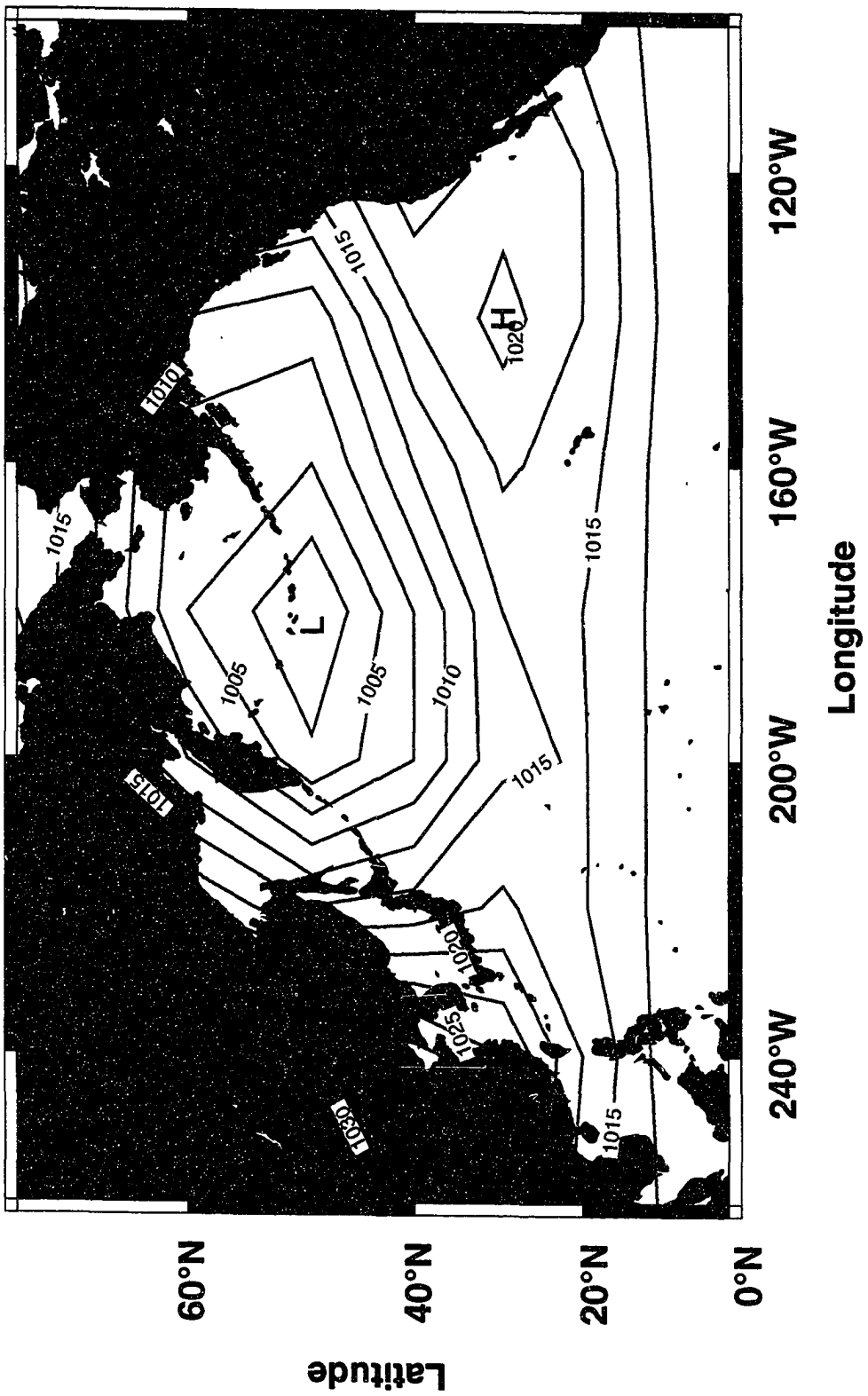

Figure 5. The long-term mean atmospheric pressure at sea level for July over the North Pacific Ocean (Anon., 1961). Contours are in millibars with a contour interval of 2.5 mb Hg. High and low pressure centers are denoted by H and L, respectively.

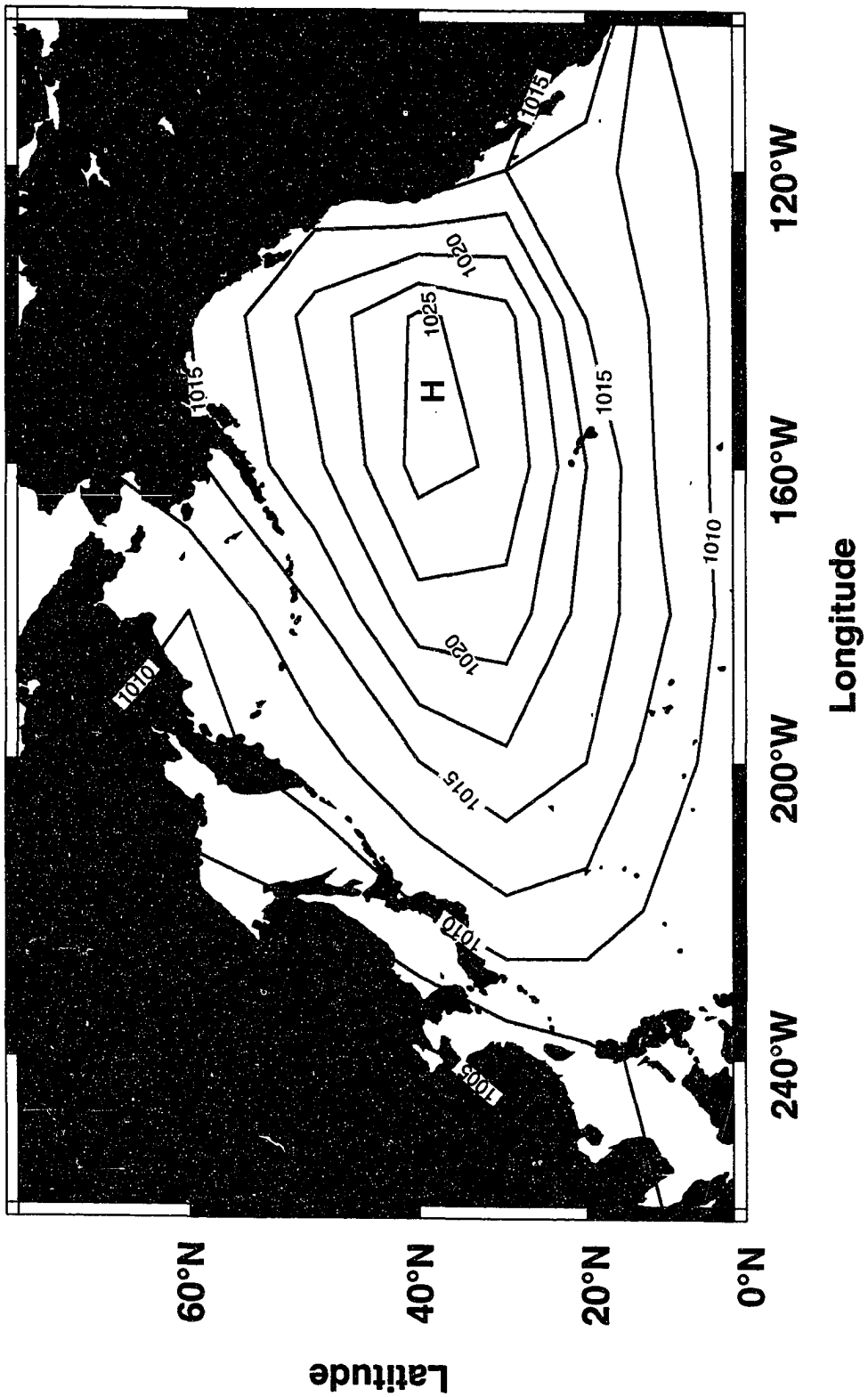

weakest and the coastal winds are upwelling unfavorable (Tchernia, 1978: Plates 15–18; Huyer, 1983: Fig. 8). In the summer, when the California Current is strongest and the coastal winds are upwelling favorable, the coastal isotherms closely parallel the California coast.

The basic coastal upwelling circulation that develops along the coast of California in the summer months can be attributed to offshore surface Ekman transport (Huyer, 1983). For coastal upwelling off California, the depth of influence of the offshore surface Ekman transport is about 30 m (Huyer, 1983). However, Ekman suction, which brings the deeper water to the surface, must also be coupled with the near-surface mixing process if the upwelled water is to be entrained in the surface flow pattern (Brink, 1983).

Along-shore variations in the strength of upwelling along the coast of California are directly linked to latitudinal variations in wind stress (Huyer, 1983). Computed offshore Ekman transport along the west coast of the United States during different times of the year (Huyer, 1983) demonstrates the existence of large variations in the offshore Ekman flux between San Francisco and Point Arena (a site commonly associated with filaments). Although upwelling plume formation can be correlated with wind stress curl, the plume direction can vary considerably with constant, or similar, wind conditions (Atkinson et al., 1986; Lutjeharms and Stockton, 1987).

2.1.2 California Coastal Transition Zone

Most satellite-derived observations (Fig. 2.; Bernstein et al., 1977; Traganza et al., 1980 and 1981; Breaker and Gilliland, 1981; Abbott and Zion, 1985, 1987; Stramma et al., 1986; Thomson and Papadakis, 1987; Brink and Cowles, 1991) of

the surface thermal (AVHRR) or pigment (CZCS) distributions in the CCS show the presence of filament-like structures propagating offshore during periods of intense coastal upwelling (most active in the spring and summer months). These features, while a permanent part of the CCS, are also observed in other coastal upwelling environments, such as the west coast of South Africa (Shannon, et al., 1984; Lutjeharms and Stockton, 1987) and the coasts of Portugal and Spain (Barton, 1986; Haynes and Barton, 1990 and 1991). The Peru Current System, by contrast, does not show filament structures (Brink, 1983; Brink et al., 1983) and upwelling plumes associated with this system rarely extend beyond the shelf break.

There have been many oceanographic research programs along the California coast during the last four decades (Table 1). The longest running of these, the California Cooperative Fisheries Investigation (CalCOFI), uses a coarse resolution sampling grid, that is 195 km along-shelf and 65 km across-shelf. However, these surveys are adequate to describe the large-scale features of the CCS. In fact, the latitudinal distributions of climatological mean temperature and salinity calculated from the CalCOFI measurements show the existence of a broad meandering southward flow (Chelton, 1984; Strub et al., 1991). Other field programs focused on smaller regions of the CCS and as a result provided detailed analysis of more localized features. For example, the OPUS (Organization of Persistent Upwelling Structures) study which occurred in 1983 provided detailed sampling of an intense coastal upwelling plume centered around Point Conception, California (Atkinson et al., 1986).

Although the existance of eddies in the CCS was noted three decades ago (Wooster and Reid, 1963), the combined use of satellite and *in situ* measurements

to study the CCS provided a basis for Mooers and Robinson (1984) to describe the CCS as a system of "filamented jets meandering between synoptic-mesoscale cyclonic and anticyclonic eddies." The filamented jets have also been referred to as squirts. The velocity and density fields of these filaments (Flament et al., 1985; Kosro and Huyer, 1986) were first measured (Beardsley and Lentz, 1987) during CODE I and II (Coastal Ocean Dynamics Experiment I and II).

On the basis of recent programs, it is now known that filaments in the CTZ develop and decay over a period of a few weeks (Flament et al., 1985) and occur most frequently during the spring and summer (Pelaéz and McGowan, 1986). Most of the filaments extend offshore for over 300 km (Flament et al., 1985; Pelaéz and McGowan, 1986; Kosro and Huyer, 1986). The filaments are about 50 km wide at peak development, and show considerable curvature and meandering (Flament et al., 1985). In the vertical, the filaments are restricted to the upper 50 m, yet vertical displacement of the isopycnal surfaces occurs to greater depths as would be expected from a classical cyclonic eddy disturbance (Flament et al., 1985). These features are of considerable interest because they may be an important aspect of across-shelf carbon and nutrient transport.

Many recent studies have focused on describing the physical structure of these filament features (Huyer, 1984; Flament et al., 1985; Reinecker et al., 1985; Huyer and Kosro, 1987; Kosro, 1987; Barth and Brink, 1987; Reinecker and Mooers, 1989*a*, 1989*b*; Brink and Cowles, 1991; Brink et al., 1991; Dewey et al., 1991; Huyer et al., 1989, 1991; Kosro et al., 1986, 1991; Ramp et al., 1991; Strub et al., 1991; Hayward and Mantyla, 1990). Flament et al. (1985) mapped the thermohaline structure of a developing filament off Point Arena, California during

Table 1. Oceanographic Programs Along the California Coast.

Program	Sampling Dates	Region	Reference
CalCOFI	1949–Present	24°–38°N	Chelton (1984)
CODE I & II	1981–1982	38°–39°N	Beardsley and Lentz (1987)
OPTIMA 21 & 22	1982	37°–40°N	Mooers and Robinson (1984)
OPUS	1983	34°–35°N	Atkinson et al. (1986)
CCCCS	1984–1985	34°–38°N	Chelton et al. (1988)
CTZ	1987–1988	37°–42°N	Brink and Cowles (1991)
NCCCS	1987–1989	38°–42°N	Magnell et al. (1990)

a two week period in July 1982. The corresponding surface wind regime was upwelling favorable with velocities of about 10 m s^{-1} from the northwest. The observed boundaries of the filament were not symmetric; the southern boundary existed as a sharp frontal zone with steep temperature gradients, the northern boundary was more diffuse. However, the across-filament density distributions showed that the southern filament boundary had no density front associated with it due to salinity and temperature compensation; whereas, a sharp density front did occur along the diffuse northern boundary as a result of the northward temperature increase across the filament (Flament et al., 1985).

On the basis of temperature and salinity distributions, Flament et al. (1985) described three types of water present at the surface across the filament: two water masses bordered the filament to the north and south, and a cold low salinity coastal water existed in the filament core. The waters to the south of the filament had relatively high salinity ($\approx$ 33.2 psu) and temperature (13°– 14°C). Conversely, the northern boundary of the filament had a diffuse 10 km wide boundary which showed constant relatively low salinity ($\approx$ 32.7 psu), and high temperature ($\approx$ 14.5°C).

The overriding of the filament core at its northern edge by the lighter surface waters to the north suggested that convergence along the frontal zone may have been occurring (Flament et al., 1985). The presence of a deeper chlorophyll maximum downstream of the filament (CTZ Newsletter, 3(1), 1988) also indicated that a subduction process may have been occurring.

Flament et al. (1985) described flow in a filament that is consistent with that characteristic of a meander. Maximum offshore velocities at the northern side of

the filament were 0.5 m s^{-1}; the southern branch of the filament had onshore velocities near 0.35 m s^{-1}. Mass balance calculations showed that the offshore transport was 1 Sv larger than the calculated offshore Ekman transport (Flament et al., 1985). A similar study by Kosro and Huyer (1986) measured offshore jets with velocities as high as 0.8 m s^{-1} and offshore transports, largely geostrophic, greater than 1.5 Sv. Mooers and Robinson (1984) found mass transport in another filament as high as 2 Sv.

Strub et al. (1991) advanced three conceptual models (Fig. 6) to explain the mesoscale current structure observed in the CTZ. The first model suggests that the filaments in the CTZ are the result of offshore-flowing jets (squirts) which advect cold, upwelled coastal water offshore. At the offshore extent of this feature are two counterrotating eddies. This model is supported by the observation of mesoscale eddy dipoles in the offshore California current (Simpson and Lynn, 1990). The second conceptual model envisions the CTZ as a mesoscale eddy field embedded within the slow southward flowing CCS. This conceptual model is supported by the observation of eddies within the CCS, which give rise to squirt-like features as they draw recently upwelled waters offshore (Mooers and Robinson, 1984; Reinecker et al., 1987), and by the observation of an offshore mesoscale eddy field in the California Current region (White et al. 1990). The third conceptual model, the meandering jet theory, is strongly supported by observations obtained during the CTZ field and modeling experiments (Strub et al., 1991). This model suggests that most of the offshore transport in the CCS occurs as a meandering jet which transports nutrient-poor waters into the CTZ from the north. In conjunction with this meandering jet, strong cutoff eddies and squirts are observed to form. Cold,

upwelled, nutrient-rich water lying between this meandering jet and the coast is then advected offshore.

A number of numerical and laboratory modeling studies have investigated the three-dimensional structure, dynamics and variability of the filaments, squirts and eddies within the CTZ (McCreary et al., 1991; Strub et al., 1991). Several laboratory modeling studies examined the behavior of upwelling frontal instabilities using a rotating annulus filled with water of two different densities (Griffiths and Linden, 1982; Chia et al., 1982). Results from their modeling studies showed that small-scale instabilities along the density front, which the authors attributed to Kelvin-Helmholtz instability, are able to develop into cyclonic and anticyclonic eddy pairs. The effect of bathymetric features such as, ridges and capes, wind stress and wind stress curl on coastal currents and fronts was investigated in a series of laboratory experiments using a rotating conical bottom tank filled with water of two different densities (Narimousa and Maxworthy, 1985; 1986; 1987; and, 1989). Their results showed that: both capes and ridges could reproduce meanders in the current downstream of the feature; a positive wind stress curl offshore was able to produce offshore eddies which in turn interacted with the coastal waters; and, only bathymetric ridges were able to form the offshore-onshore meander-like feature observed in the CTZ (Strub et al., 1991). Several numerical models examined the effect of wind forcing with and without wind stress curl (Batteen et al., 1989 and 1990; McCreary et al., 1991*a*; 1991*b*) and demonstrated that the steady wind forcing was a possible generation mechanism for eddies within the CCS. Other studies investigated the interaction of an evolving, along-shore, baroclinic jet with coastal topographic features, such as capes (Ikeda and Emery, 1984;

Figure 6. Schematic of the three conceptual models that have been suggested to explain the mesoscale structure observed to be associated with the California Current System (CCS) in the CTZ. **A**) offshore-flowing jet (squirt); **B**) mesoscale eddy field embedded in the CCS; and, **C**) meandering jet. See text for a description of each conceptual model. Figure from Strub et al., 1991.

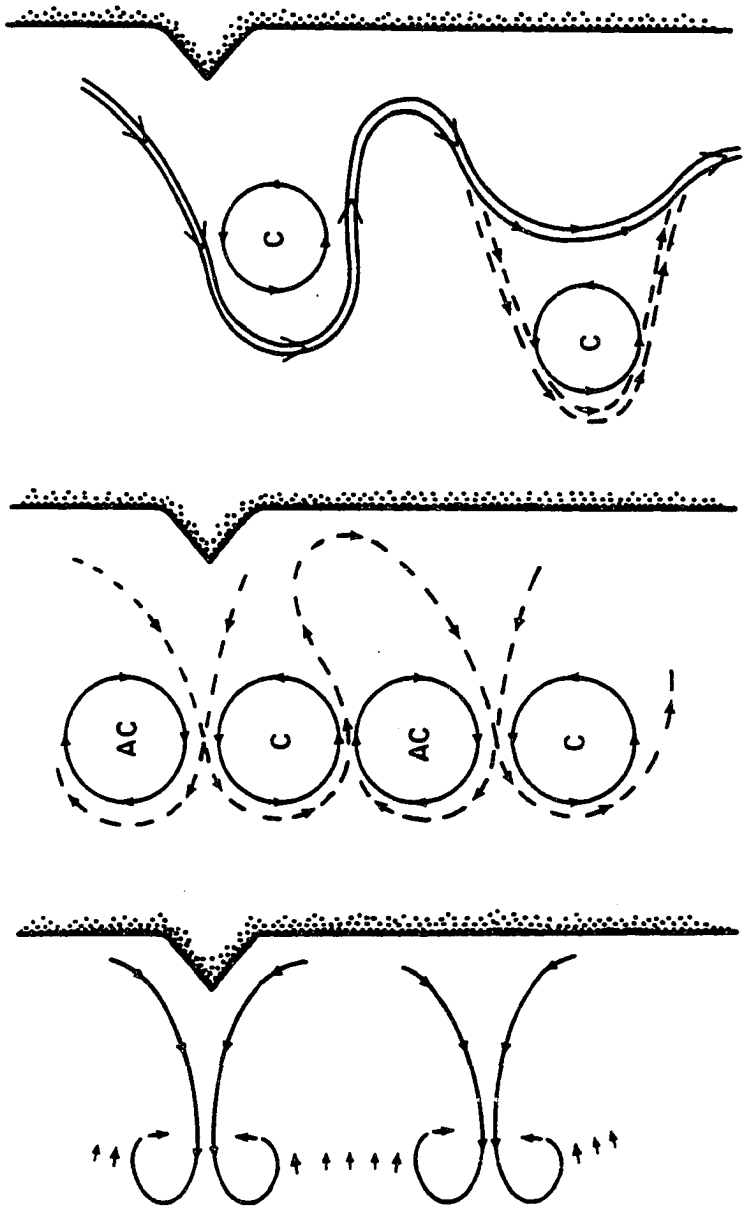

Haidvogel et al., 1991a). Results from these studies demonstrated that filament-like features could develop without the need for wind stress, wind stress curl or topographic ridges, but relied on internal effects caused by the interaction between a southward-flowing, along-shore, baroclinic current and a cape.

2.2 Biological and Chemical Features

Many studies have investigated the time and space variability of the plankton and nutrient fields associated with the CCS and CTZ. The biological and chemical distributions within the CTZ are greatly influenced by the strong seasonal variation in the coastal wind field. In the spring, the coastal wind field changes to upwelling favorable in a short period of time (Lentz, 1987). The effect of the seasonal change in wind field pattern on the phytoplankton populations has been the subject of numerous studies (Abbott and Zion, 1987; Michaelsen et al., 1988; Abbott and Barksdale, 1991; Thomas and Strub, 1989 and 1990). During the spring transition, pigment concentrations along the coast increase from 0.5 mg-chl a m^{-3} to $>$ 3 mg-chl a m^{-3} (Thomas and Strub, 1989). The spatial and temporal variability of the phytoplankton populations in this region has been attributed to large and small scale variations in the wind stress and wind stress curl (Abbott and Zion, 1987; Abbott and Barksdale; 1991). In general, the coastal upwelling zone consists of an inshore region which contains high phytoplankton populations in conjunction with high nutrient concentrations. Offshore, the phytoplankton and nutrient concentrations decrease and become increasingly variable (Abbott and Zion; 1987).

Using CZCS-derived fields, Pelaéz and McGowan (1986) showed that the CCS could be characterized by six different pigment distributions. A high pigment band

was observed to extend along the coast from San Francisco to its southern extent near Point Conception, where it was advected offshore and developed into one of several "high" pigment rings. These rings were observed to occur during the fall and winter seasons, when the Davidson Current is directly coupled with the Southern California Countercurrent. A low pigment intrusion was observed in the Southern California Bight during the summer, winter and fall. This low pigment water may have resulted from an onshore flow of nutrient poor water into the bight as a recirculation process of the Southern California Eddy. A low pigment region was observed just south of the offshore "high" pigment rings. Again, this may have been associated with the onshore recirculation of water onto the California Bight. Other features included coastal attached eddies near San Quentin, and low pigment eddies between the high pigment filaments, which propagated "high" pigment rings offshore. These filament-like structures may be responsible for the across-shore advection of heat, salt, nutrients and carbon. These features occur with a time-scale of 30 days and appear to be anchored, or rooted, to specific sites along the coast (Brink, 1983; Flament et al., 1985).

Observations from the 1988 CTZ field surveys provided a basis to describe the plankton dynamics associated with these filaments (Hood, 1990; Chavez et al., 1991; Hood et al., 1990 and 1991). In general, the inshore (neritic) plankton populations appear to be separated from the offshore (pelagic) plankton populations by the presence of a strong equatorward-flowing baroclinic coastal jet–density front (Hood et al., 1990; 1991). Meanders in this along-shore jet–front cause the entrained neritic plankton populations to become advected rapidly offshore. Downwelling within the core of the meandering jet subducts the phytoplankton

populations to depths greater than 70 m. Evidence for this subduction process was observed in ^{222}Rn, nutrients, oxygen, temperature and salinity distributions (Kadko et al., 1991).

The phytoplankton species composition and their associated primary production rates vary depending on their location relative to the density front (Hood, 1990; Chavez et al., 1991; Hood et al., 1990, 1991). Onshore of the density front, higher nutrients supported a large phytoplankton population, between 1-10 mg-chl *a* m^{-3}, which was dominated by large, productive (5-20 mg C mg Chla^{-1} hr^{-1}) silicate-dependent diatoms, e.g. *Chaetoceras* spp., *Sleletonema costatum*, *Rhizosolenia alata* and *Thalassiosira* spp., (Hood, 1990; Hood et al., 1990 and 1991; Chavez et al., 1991). In the waters offshore of the density front, smaller, less productive, non-silicate-dependent phytoplankton cells ($< 5\mu m$) were dominant in the low nutrient, low phytoplankton biomass waters.

The distribution of the zooplankton communities within the CTZ showed a trend in their distribution relative to the position of the filaments (Mackas et al., 1991). High concentrations of the doliolid, *Dolioletta gegenbauri*, were observed south and east of filaments. Along the warm side of the jet and extending into nonfilament waters to the west and north, the zooplankton community was composed primarily of high concentrations of *Dolioletta* sp. along with a mixture of smaller copepods, pteropod larvae and chaetognaths. The euphausiid, *Euphausia pacifica*, was found throughout the filament, but was primarily concentrated along the southern margin of the filament. High concentrations of the copepod, *Eucalanus californicus*, were found within the cold core of the filament and along the northern and western margins (Mackas et al., 1991). Finally, Bucklin et al. (1989)

and Bucklin (1991) found intra-specific variations in the genetic makeup of the calanoid copepod, *Metridia pacifica*, could be related to physical features in the circulation fields within the CTZ. Their studies showed that eddies and density fronts were able to isolate plankton assemblages and prevent homogenization of their genetic stock.

Increased copepod concentrations have been observed in other upwelling frontal zones. Smith et al. (1986a) found high concentrations of the copepod, *Calanus pacificus*, within an upwelling plume centered off Point Conception, California. The concentrations of copepodid stage V, the deep-living, diapausing stage of this copepod, increased and concentrations of adults decreased with increasing upwelling intensity, which indicated that the upwelling zone brought nutrient-rich waters containing seed zooplankton to the surface. Furthermore, Smith and Lane (1991) found that the increased phytoplankton biomass and primary production rates within the filament were capable of supporting high secondary production and egg production rates for the copepod, *Eucalanus californicus.*

The offshore advection of nutrient-rich, high phytoplankton and zooplankton biomass may help to explain the high zooplankton biomass located to the north and offshore about 100-150 km in the 30 year average of the CalCOFI data (Chelton et al., 1982).

Chapter 3

Methods

3.1 One-Dimensional Physical-Bio-Optical Model

3.1.1 Model Equations

The first model developed was a one-dimensional (vertical) time-dependent physical-bio-optical model. The physical portion includes the effects of vertical velocity (biological and advective) and vertical diffusion. The biological portion of the model consists of a nine-component food web (Fig. 7) that includes silicate, nitrate, ammonium, two phytoplankton size fractions, three zooplankton categories and a detrital pool. Transfers within the food web occur through nutrient uptake by phytoplankton, differential grazing by zooplankton and nutrient recycling. Coupled to the food web model is a modified version of the subsurface spectral irradiance model of Sathyendranath and Platt (1988).

The model, therefore, is a system of nine coupled partial differential equations that govern the vertical and time distribution of a non-conservative quantity, and is of the form;

$$\frac{\partial B}{\partial t} + (w + w_{biology})\frac{\partial B}{\partial z} - K_z \frac{\partial^2 B}{\partial z^2} = S, \qquad (1)$$

Figure 7. Schematic of the biological components included in the time- and depth-dependent physical-bio-optical model.

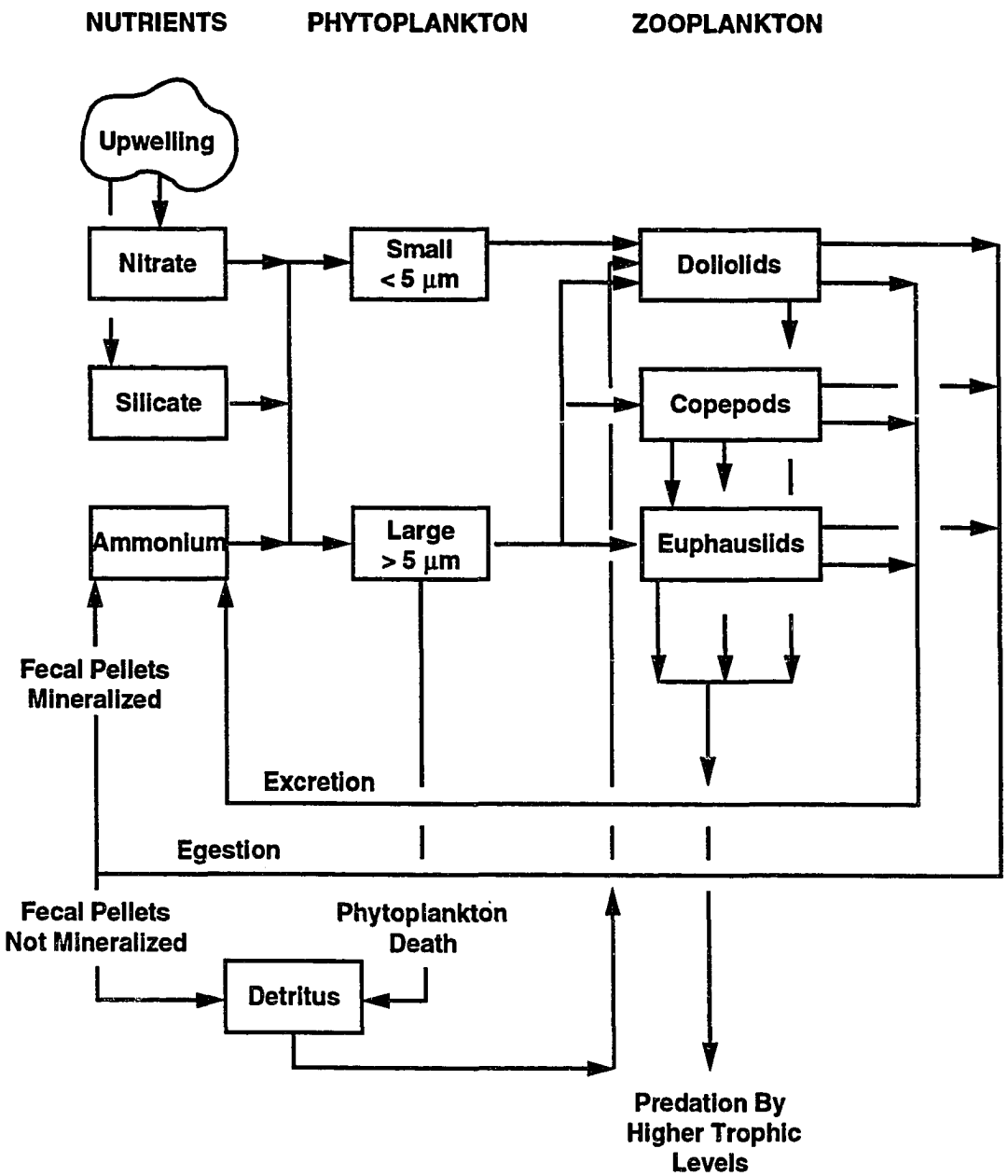

where B is a non-conservative quantity (one of the nine components in the biological model), w is the vertical advective velocity, $w_{biology}$ is the vertical sinking rate of the biological component and S is the source or sink term for B. The vertical sinking rates, $w_{biology}$, for the large (1 m day^{-1}) and small (0.1 m day^{-1}) phytoplankton size fractions were based on laboratory measurements given in Smayda (1970), Bienfang and Szyper (1982), Bienfang et al. (1982) and Smetacek (1985). The source and sink terms, S, for the biological processes of the model are adapted from the time-dependent biological model of Hofmann and Ambler (1988) for the CTZ. Detailed descriptions of these are presented in later sections.

The model described by equation (1) was implemented in a domain that was 100 m deep. Simulations were extended for 20 days to coincide with the generation time of a filament (Kosro and Huyer, 1986).

3.1.2 Vertical Velocity and Diffusion

The vertical advective velocities were obtained from simulated velocity fields generated by a regional primitive equation circulation model that was configured to simulate circulation conditions in the CTZ (Haidvogel et al. 1991a and b). The vertical velocity at the sea surface, the top of the model domain, was set to zero,

$$w(z = 0\ m, t) = 0.$$

The vertical velocity at 100 m, the bottom of the domain, was defined as:

$$w(z = 100\ m, t) = f(t),$$

where $f(t)$ represents a time-varying vertical velocity. The time-varying vertical velocity was obtained at 100 m from days 140 to 160 of the simulated circulation distributions described by Haidvogel et al. (1991a). These values were extracted from simulated fields at intervals of 4.8 hours and then interpolated to the 5 minute time step used in this calculation. The interior vertical velocities were obtained by assuming a linear dependence in the vertical between 0 and 100 m,

$$\frac{\partial w(z,t)}{\partial z} = \frac{w(z = 100\ m, t) - w(z = 0\ m, t)}{100\ m}.$$

The interior vertical velocities are then obtained from:

$$w(z,t) = \frac{w(z = 100\ m, t)}{100} z,$$

where z is the depth. This method assumes a constant horizontal divergence throughout the upper 100 m.

The vertical diffusion parameter K_z was set at a constant value of 1 cm^2 s^{-1}. This value was lower than the range of values used in the three-dimensional model, 5 to 25 cm^2 s^{-1} (Haidvogel et al., 1991a), however it was within the range of observed values for upwelling regions such as off the coast of Oregon (Wroblewski, 1983).

3.1.3 Biological Processes

3.1.3.1 Phytoplankton

The large ($> 5\ \mu m$) phytoplankton size fraction included in the model is a typical silicate- and nitrate-dependent neritic-type diatom that grows best under high

nutrient and light conditions. In contrast, the small ($< 5\ \mu m$) phytoplankton size fraction represents a typical, non-silicate-, nitrate-dependent, oceanic-type flagellate that grows best under low nutrient and light conditions. These phytoplankton size fractions are representative of the dominant taxa observed in the CTZ (Hood, 1990; Hood et al., 1990; 1991; Chavez et al., 1991). The concentration and relative abundance of these two size fractions change in response to differences in growth and loss processes:

$$S = Growth - Respiration - Death - Grazing, \tag{2}$$

where the first two processes represent net production. Phytoplankton net production was obtained from estimated carbon uptake rates (mg C mg Chl a^{-1} s^{-1}) which was then used to estimate a nitrogen uptake rate by assuming a constant $C :: N$ Redfield ratio of 6.

Net primary production rates for the large $PP_{lpp}(z,t)$ and small $PP_{spp}(z,t)$ phytoplankton size fractions are calculated using a relationship modified from Platt et al. (1980), which allows for nutrient limitation, diurnal variation and photoinhibition. This relationship is of the form:

$$PP_{lpp}(z,t) = L_{lpp}(z,t)N_{lpp}(z,t)Ps^{B}_{lpp}(t)\left[1 - e^{-\frac{\alpha_{lpp}(t)PAR(t,z)}{Ps^{B}_{lpp}(t)}}\right] e^{-\frac{\beta_{lpp}(t)PAR(t,z)}{Ps^{B}_{lpp}(t)}} \tag{3}$$

$$PP_{spp}(z,t) = L_{spp}(z,t)N_{spp}(z,t)Ps^{B}_{spp}(t)\left[1 - e^{-\frac{\alpha_{spp}(t)PAR(t,z)}{Ps^{B}_{spp}(t)}}\right] e^{-\frac{\beta_{spp}(t)PAR(t,z)}{Ps^{B}_{spp}(t)}}. \tag{4}$$

The terms on the right side of equations 3 and 4 represent nutrient limitation (L_{lpp}, L_{spp}), the time- and depth-dependent phytoplankton concentrations (N_{lpp}, N_{spp}) and the biomass normalized nitrogen fixation rate which is further defined as:

$$Ps^{B}_{lpp}(t) = \frac{Pmax_{lpp}(t)}{\left(\frac{\alpha_{lpp}(t)}{\alpha_{lpp}(t)+\beta_{lpp}(t)}\right)\left(\frac{\beta_{lpp}(t)}{\alpha_{lpp}(t)+\beta_{lpp}(t)}\right)^{\frac{\beta_{lpp}(t)}{\alpha_{lpp}(t)}}} \tag{5}$$

$$Ps^{B}_{spp}(t) = \frac{Pmax_{spp}(t)}{\left(\frac{\alpha_{spp}(t)}{\alpha_{spp}(t)+\beta_{spp}(t)}\right)\left(\frac{\beta_{spp}(t)}{\alpha_{spp}(t)+\beta_{spp}(t)}\right)^{\frac{\beta_{spp}(t)}{\alpha_{spp}(t)}}}. \tag{6}$$

The final term in equations 3 and 4 modifies the available underwater irradiance ($PAR(z,t)$). Definitions and values of the parameters used in the terms in equations 3–6 are given in Table 2.

The above formulations used for estimating primary production are based on standard photosynthesis versus irradiance models which give a hyperbolic relationship between the rate of photosynthesis and irradiance. This relationship can be described if the initial slope and asymptotic values of the hyperbolic function are known. For this study, photosynthesis versus light measurements obtained for the CTZ (Hood, 1990; Hood et al., 1990 and 1991; Fig. 8) were used to specify these values. The CTZ photosynthesis versus light data were sufficient to also allow parameterization of diel periodicity of photosynthesis (MacCaull and Platt, 1977; Harding et al., 1981, 1982a and b; Harding and Heinbokel, 1984; Prézelin et al., 1986; Putt and Prézelin, 1988; Putt et al., 1988) by using the empirical equation given in MacCaull and Platt (1977) of the form:

Table 2. Definition and Units of the Parameters Used For the Large and Small Phytoplankton Photosynthetic Relationships.

Parameter	Definition	Units
$Pmax_{lpp}$	Maximum Realized Photosynthetic Rate Normalized to Biomass for the Large Phytoplankton	(mg N) [mg N]$^{-1}$ s^{-1}
$Pmax_{spp}$	Maximum Realized Photosynthetic Rate Normalized to Biomass for the Small Phytoplankton	(mg N) [mg N]$^{-1}$ s^{-1}
α_{lpp}	Initial Slope of the P/I Curve for the Large Phytoplankton	(mg N) [mg N]$^{-1}$ [Einstein m^{-1} s^{-1}]$^{-1}$
α_{spp}	Initial Slope of the P/I Curve for the Small Phytoplankton	(mg N) [mg N]$^{-1}$ [Einstein m^{-1} s^{-1}] $^{-1}$
β_{lpp}	Photoinhibition Term for the Large Phytoplankton	(mg N) [mg N]$^{-1}$ [Einstein m^{-1} s^{-1}]$^{-1}$
β_{spp}	Photoinhibition Term for the Small Phytoplankton	(mg N) [mg N]$^{-1}$ [Einstein m^{-1} s^{-1}]$^{-1}$

$$v(t) = b_m + b_a 2^{-n}\left[1 + cos\left(\frac{2\pi}{24}(t - b_p)\right)\right]^n, \quad (7)$$

where $v(t)$ gives the diurnal variation for the six time-dependent photosynthetic parameters. The magnitude of the diurnal variation, $b_a 2^{-n}$, about the mean value, b_m, is offset by some time, t, from local noon, b_p. The curvature of this diurnal variation is modified by the parameter n. Values for these parameters are shown in Table 3 and were obtained by fitting the data from the CTZ to the above equation.

The primary production rate calculated from equation 3 has a hyperbolic dependence on light (Fig. 9) at all intensities over twenty-four hours, the primary production rate increases from an initial low value to a maximum at local apparent noon, after which it decreases. The maximum values at mid-day coincide with maximum solar irradiance. Thus, the time and light characteristics of the primary production rates are consistent with expected patterns. Similarly, the time and depth varying dependence of the primary production rate (Fig. 10) is as expected. Photoinhibition occurs at the surface, the maximal photosynthetic rate occurs below this after which it decreases exponentially to zero.

Phytoplankton nutrient dependence was assumed to follow Michaelis-Menten kinetics for both size fractions (Davis et al., 1978; Dugdale et al., 1981; Dugdale and Wilkerson, 1989). Because the model contains three nutrients (nitrate, silicate and ammonia), a multiple nutrient limitation model with a "threshold" (i.e. Leibig's "Law of the Minimum") relation (DeGroot, 1983) was used. Thus, the nutrient limitation terms in equations 3 and 4 were obtained from:

Table 3. Values of the Parameters Used For the Large and Small Phytoplankton Photosynthetic Relationships.

Parameter	Maximum Values	b_m	b_a	b_p^*	n
$Pmax_{lpp}$	1.042 x 10^{-4}	0.25	0.75	1200 h	1
$Pmax_{spp}$	2.430 x 10^{-4}	0.90	0.10	1200 h	1
α_{lpp}	.6944	0.90	0.10	1200 h	2
α_{spp}	.1736	0.90	0.10	1200 h	2
β_{lpp}^{**}	5.555 x 10^{-3}	1.00	0.00	1200 h	1
β_{spp}^{**}	8.333 x 10^{-3}	1.00	0.00	1200 h	1

* b_p = Local Apparent Time

** β_{lpp} and β_{spp} did not show time variability

Figure 8. Primary production versus light intensity (PAR) data from the CTZ field surveys. Data provided courtesy of Dr. Raleigh Hood.

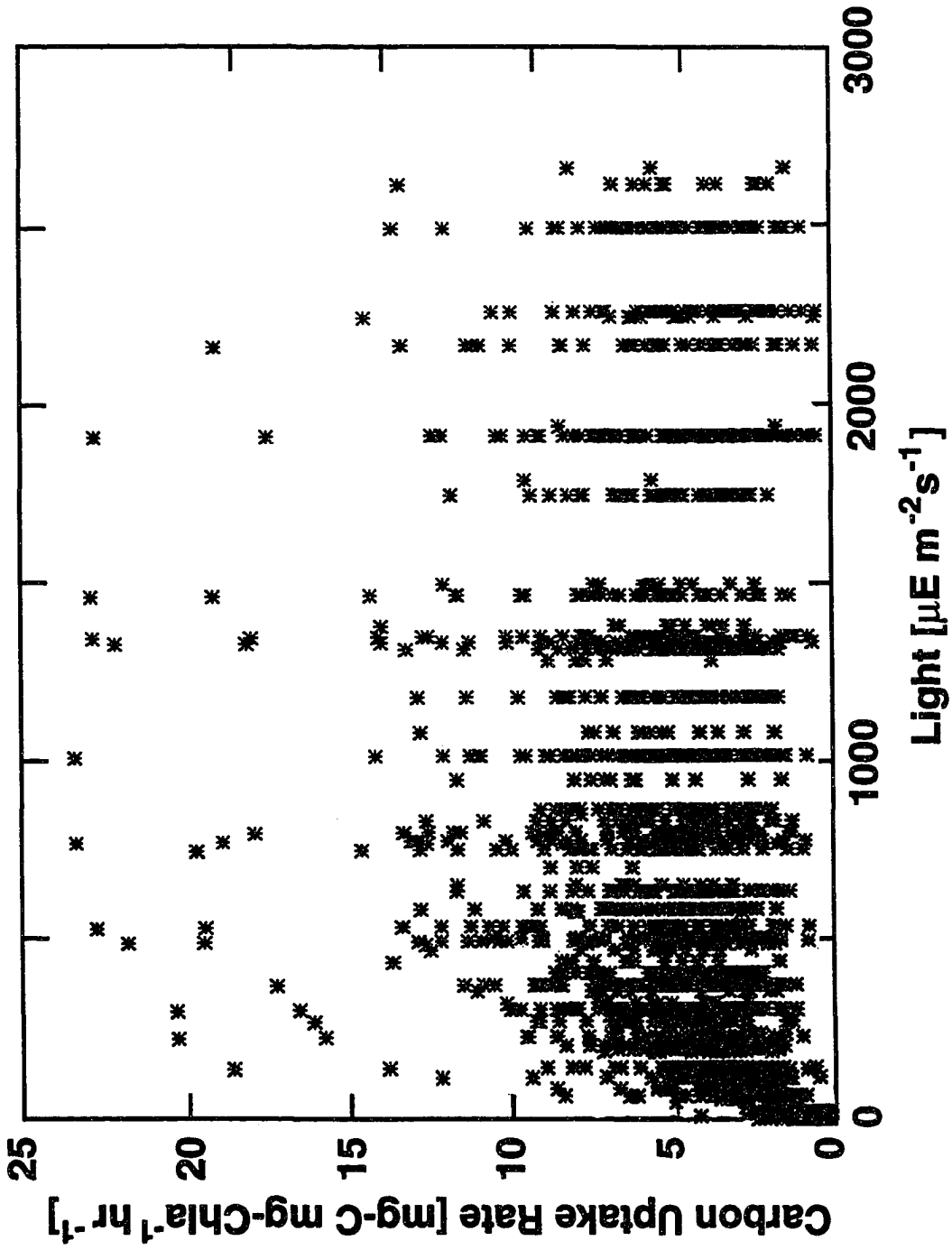

Figure 9. Time variation of relative primary production as a function of relative light intensity calculated from equation 3.

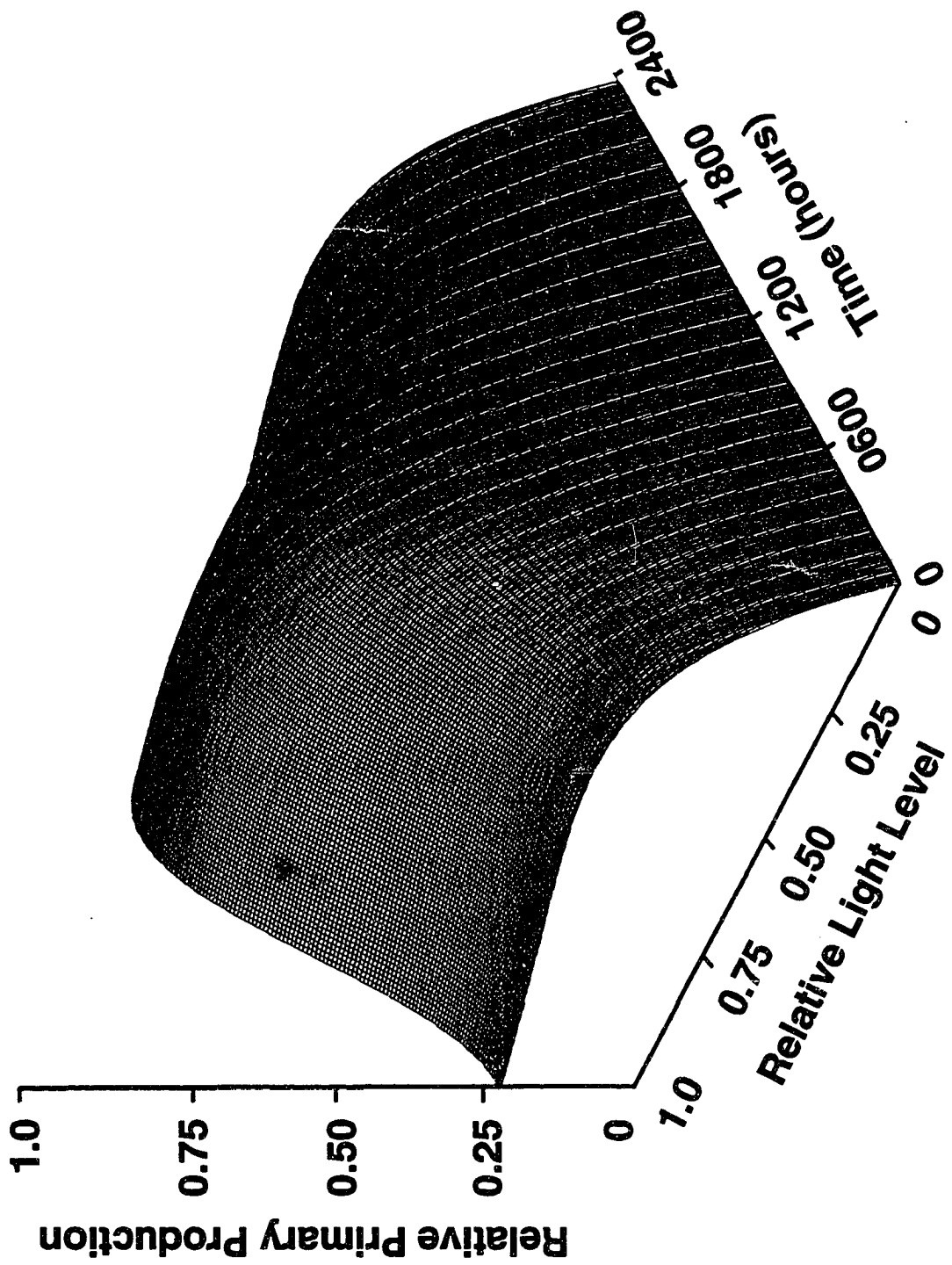

Figure 10. Time and depth variation of relative primary production calculated from equation 3. The decrease in primary production rate near the surface at local noon is the result of photoinhibition.

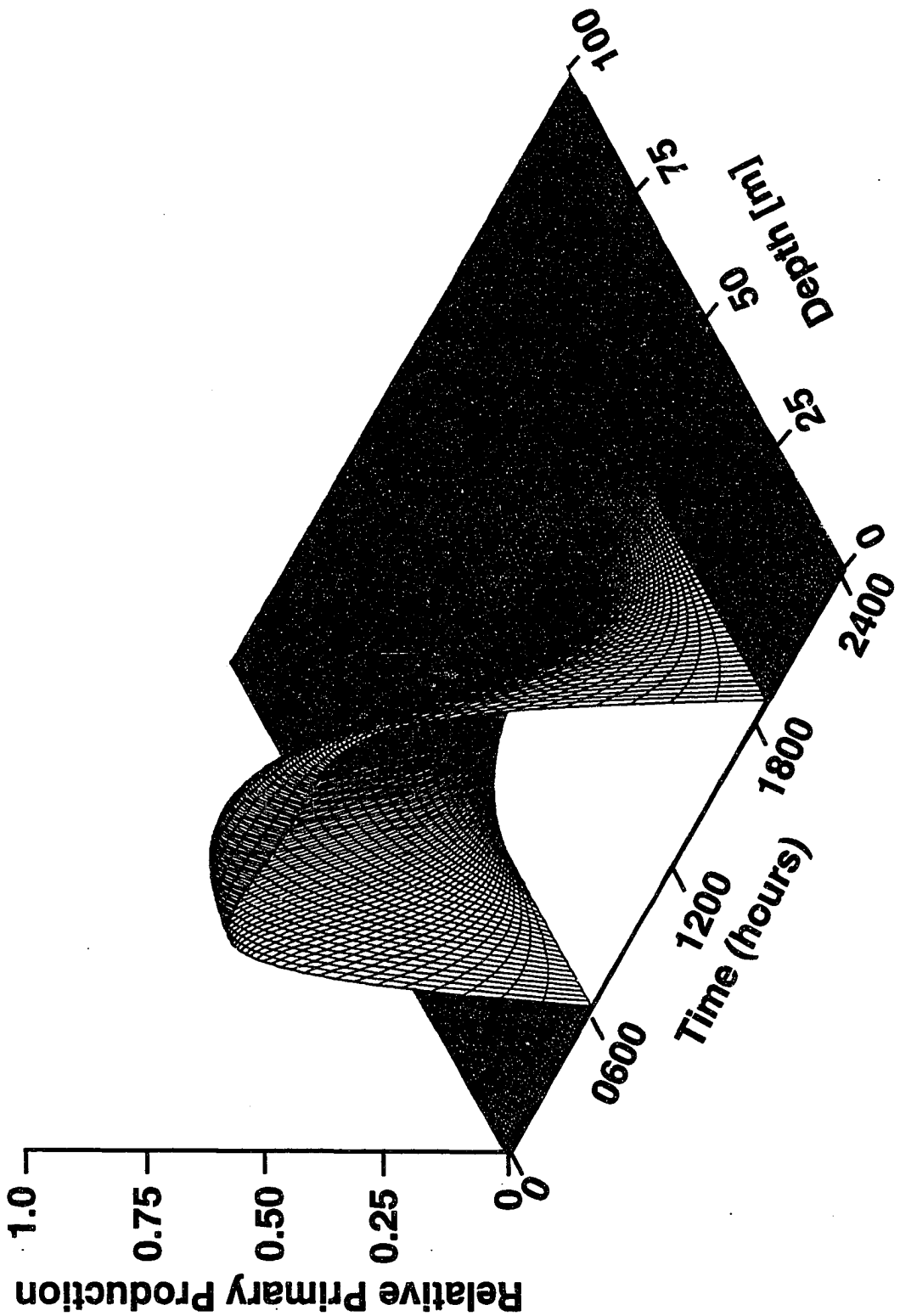

$$L_{lpp}(z,t) = MIN\left[\frac{([SiO_4] - SC_{lpp})}{KS_{lpp} + [SiO_4] - 2SC_{lpp}},\right.$$

$$f_{lpp}(z)\frac{[NO_3^-]\sigma_{lpp}(z,t)}{[NO_3^-] + KN_{lpp})} +$$

$$\left.(1 - f_{lpp}(z))\frac{[NH4^+]}{[NH_4^+] + KA_{lpp}}\right] \quad (8)$$

$$L_{spp}(z,t) = MIN\left[\frac{[SiO_4] - SC_{spp}}{KS_{spp} + [SiO_4] - 2SC_{spp}},\right.$$

$$f_{spp}(z)\frac{[NO_3^-]\sigma_{spp}(z,t)}{[NO_3^-] + KN_{spp}} +$$

$$\left.(1 - f_{spp}(z))\frac{[NH4^+]}{[NH_4^+] + KA_{spp}}\right], \quad (9)$$

where $[SiO_4]$, $[NO_3^-]$ and $[NH_4^+]$ are the concentrations of silicate, nitrate and ammonia at a given depth and time, and SC_{lpp} and SC_{spp} are the critical concentrations of silicate for the large and small phytoplankton size fractions, respectively, below which no growth will occur. The existence of a critical silicate concentration for phytoplankton growth in the CTZ was suggested by the lack of silicate values below $\approx$1 μM SiO_4^- (Fig. 11). The lack of a critical silicate concentration for phytoplankton growth allows the phytoplankton to use silicate at low concentrations and, therefore, the silicate values in the CTZ would be lower than that observed. The remaining coefficients in the Michaelis-Menten expressions in equations 8 and 9 are defined in Table 4.

The coefficients, $\sigma_{lpp}(z,t)$ and $\sigma_{spp}(z,t)$, in equations 8 and 9 give the fraction of the total nitrogen used by the large and small phytoplankton size class relative to

the concentration of ammonia and are specified using the "flip-switch" relationship of McCarthy et al. (1981), as:

$$\sigma_{lpp}(z,t) = \sigma_{spp}(z,t) = \begin{cases} 1 - 0.06071[NH_4^+] & [NH_4^+] \leq 15.12 \\ 0.82e^{-0.00976([NH_4^+]-15.12)} & [NH_4^+] > 15.12, \end{cases} \quad (10)$$

where the coefficients in equation 10 were determined by fitting the equation 10 to the McCarthy relationship (McCarthy et al., 1981). As ammonium increases, more of the required nitrogen needed to support phytoplankton growth comes from this part of the available nitrogen.

The final parts of the nutrient limitation term are the depth-dependent f-ratios (Harrison et al., 1987), $f_{lpp}(z,t)$ and $(f_{spp}(z,t))$, for the two phytoplankton size fractions. These ratios indicate the relative effect of nitrate- versus ammonia-based primary production and are given by:

$$f_{lpp}(z,t) = \frac{\frac{[NO_3^-]\sigma_{lpp}(z,t)}{[NO_3^-]+KN_{lpp}}}{\frac{[NO_3^-]\sigma_{lpp}(z,t)}{[NO_3^-]+KN_{lpp}} + \frac{[NH_4^+]}{[NH_4^+]+KA_{lpp}}} \quad (11)$$

$$f_{spp}(z,t) = \frac{\frac{[NO_3^-]\sigma_{spp}(z,t)}{[NO_3^-]+KN_{spp}}}{\frac{[NO_3^-]\sigma_{spp}(z,t)}{[NO_3^-]+KN_{spp}} + \frac{[NH_4^+]}{[NH_4^+]+KA_{spp}}}, \quad (12)$$

where the terms and coefficients in equations 11 and 12 have been defined previously. The two f-ratio terms are used to partition the primary production rates into old, for regenerated production derived from ammonium, and new, for production derived from nitrate, production (Dugdale and Goering, 1967).

Overall the nutrient limitation terms show a hyperbolic dependence on the concentration of silicate and nitrate at a zero (Fig. 12A) and constant (Fig. 12B)

Figure 11. Silicate versus nitrate relationship constructed from values obtained from the CTZ. Data were provided courtesy of Dr. Burt Jones.

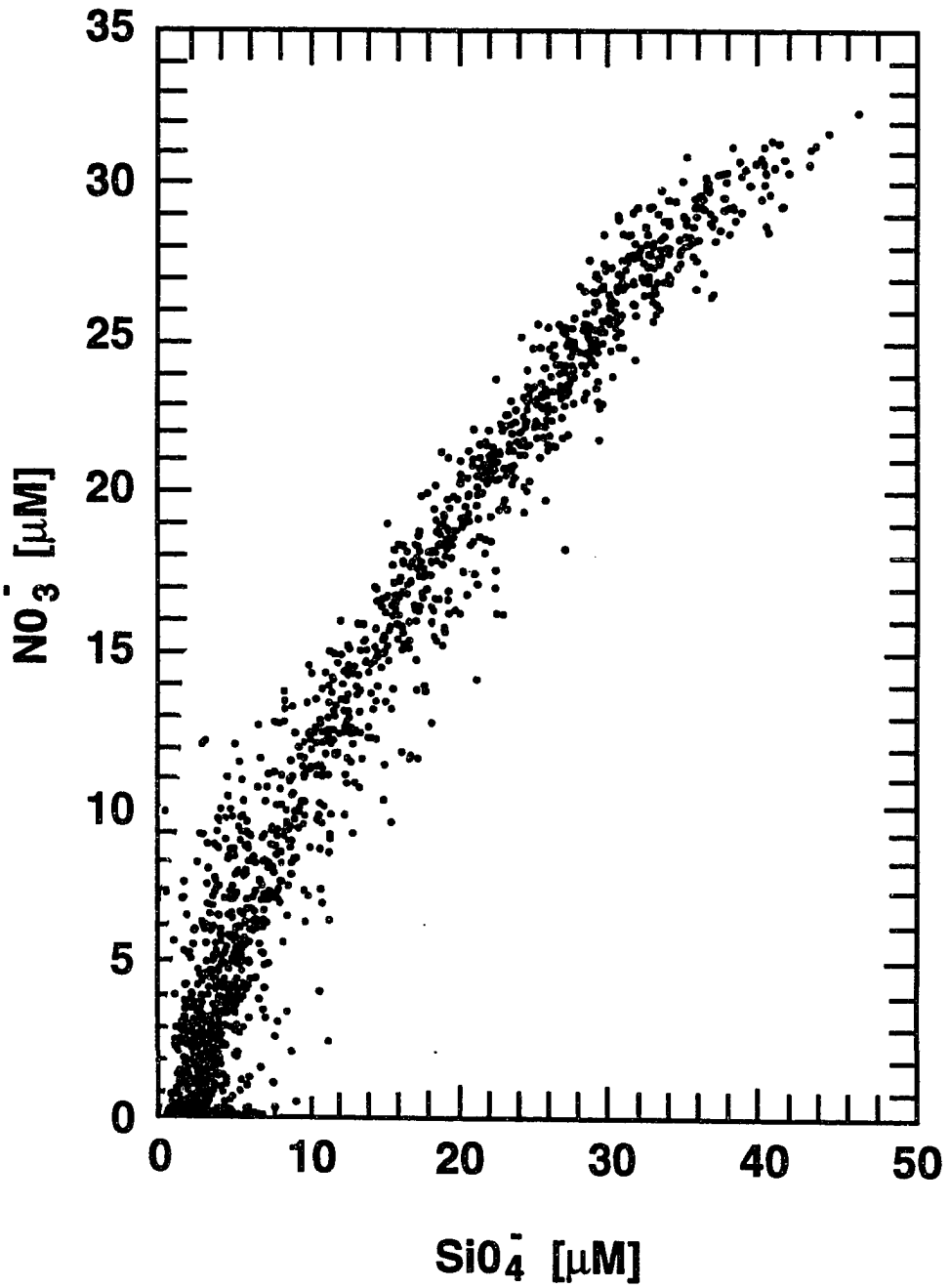

Table 4. Definition, Value, Units and Source For the Coefficients in Michaelis-Menten Relationships Used in the Phytoplankton Nutrient Limitation Terms.

Large Phytoplankton Nutrient Uptake Coefficients				
Name	Definition	Value	Units	Reference
SC_{lpp}	Critical Silicate Concentration	18.62	mg SiO_4^- m^{-3}	Paasche, 1973a and 1973b
KS_{lpp}	Half-Saturation Constant for Silicate	47.18	mg SiO_4^- m^{-3}	Paasche, 1973a and 1973b
KN_{lpp}	Half-Saturation Constant for Nitrate	42.00	mg NO_3^- m^{-3}	MacIsaac and Dugdale, 1969 and 1972
KA_{lpp}	Half-Saturation Constant for Ammonium	32.62	mg NH_4^+ m^{-3}	Eppley et al., 1969, 1979a and b
Small Phytoplankton Nutrient Uptake Coefficients				
Name	Definition	Value	Units	Reference
SC_{spp}	Critical Silicate Concentration	0.00*	mg SiO_4^- m^{-3}	
KS_{spp}	Half-Saturation Constant for Silicate	0.00*	mg SiO_4^- m^{-3}	
KN_{spp}	Half-Saturation Constant for Nitrate	26.60	mg NO_3^- m^{-3}	MacIsaac and Dugdale, 1969 and 1972
KA_{spp}	Half-Saturation Constant for Ammonium	8.12	mg NH_4^+ m^{-3}	Eppley et al., 1969 1979a and b

* No silicate limitation for the small phytoplankton.

ammonium concentration. The nitrate concentrations at which the nutrient uptake is zero correspond to critical silicate concentrations at which nutrient uptake is inhibited. As the ammonium concentration increases (Fig. 12B) the effect of silicate limitation on phytoplankton growth is more apparent. The rnage of concentrations of nutrients for which the phytoplankton are either silicate- or nitrate-limited is indicated in Figs. 12A and B. Silicate and nitrate limitation occurs to the right and left, respectively, of the demarkation line on Figs. 12A and A. Changes in ammonium concentration cause the region of nitrate-limitation to decrease and increases the region of silicate-limitation.

An alternative method for the calculation of the primary production rates that is based on the photosynthetically absorbed radiation by each phytoplankton size fraction and the maximum quantum yield for nitrogen fixation, ϕ_{max} (mol N Einstein^{-1}), is built into the phytoplankton portion of the model. This formulation is based on the approach taken for the bio-optical models described by Smith et al (1989). However, this formulation does not allow for a photoinhibition term; thus, it was not used for the CTZ simulations.

The final processes controlling the phytoplankton (eq. 2) represent losses due to cell death and zooplankton grazing. Cell death consists of processes such as cell autolysis, sloppy feeding, disease (e.g. viral infections), as well as others. Measurements from the CTZ that can be used to parameterize these processes are not available. Thus, phytoplankton loss was assumed to have a linear dependence on phytoplankton concentration. The rate of cell death was further assumed to be 10% per day for both phytoplankton size fractions. This rate is consistent with

Figure 12. Relationship between the nutrient uptake coefficient (eq. 8) for a range of nitrate and silicate concentrations at **A**) zero ammonium concentration and **B**) 1 μM NH_4^+. The effect of the critical silicate value on the nutrient uptake coefficient shows up as the flat portion of the surface at low silicate concentrations. Regions of silicate and nitrate limitation are on the right and left, respectively, side of the solid curved lines.

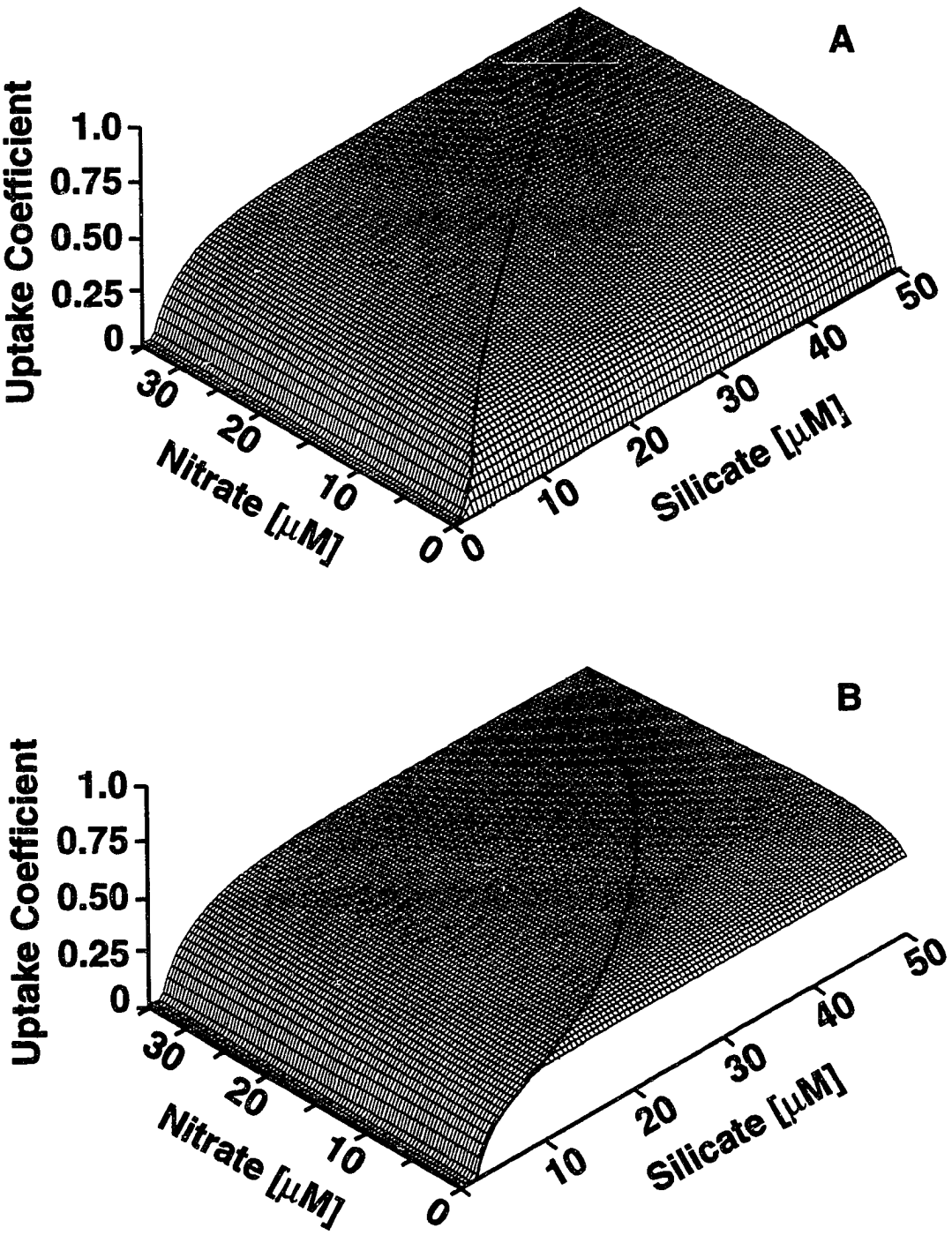

that used in other biological models (e. g. Hofmann and Ambler, 1988). Losses due to zooplankton grazing were obtained as described in the following section.

3.1.3.2 Zooplankton

The zooplankton distributions obtained during the CTZ field studies (Mackas et al., 1991; Smith and Lane, 1991) indicated that three taxa accounted for a large portion (≈75%) of the zooplankton biomass. The herbivorous copepod, *Eucalanus californicus*, was found throughout the CTZ. The omnivorous euphausiid, *Euphausia pacifica*, was associated primarily with the offshore-flowing filaments. The gelatinous doliolid, *Dolioletta gegenbauri*, was found primarily in the nearshore region and in the offshore-flowing filaments, with concentrations that approached 30 mg C m^{-3}. These three species provided the basis for the three zooplankton grazers that are included in the biological model. The abundance of these species was assumed to be regulated as:

$$S(z,t) = Growth - Predation\ Mortality - Natural\ Mortality, \qquad (13)$$

where $S(t,z)$ is the change in species concentration at a given time and depth. Zooplankton growth results from the sum of the assimilated ingestion and metabolic losses and may be negative. Predation represents losses from the three zooplankton species through transfers to higher trophic levels. Natural mortality includes processes such as disease. The formulations that were used to describe the processes on the right side of equation 13 for each of the three species are described in the following sections.

3.1.3.2.1 Copepod, *Eucalanus californicus*

Eucalanus californicus is a large copepod, 0.004—0.6 mg C individual^{-1}, whose genus can selectively graze prey that is greater than 5 μm (Mackas, 1991; Price and Paffenhöfer, 1983 and 1984). Therefore, in this model, *E. californicus* ingests only the largest phytoplankton size fraction. Ingestion rates as a function of prey concentration measured specifically for *E. californicus* are not available. Therefore, ingestion rates for this animal were obtained using values measured for *Calanus pacificus*, a copepod of similar size and trophic state. The grazing rates for *C. pacificus* (Frost, 1972, 1975, 1980, 1985 and 1988; Smith and Lane, 1988; Vidal et al., 1985; Downing and Rigler, 1984) were used with an Ivlev-type model to obtain the time- and depth-dependent ingestion rate, $I_{cop}(z,t)$ as:

$$I_{cop}(z,t) = \frac{N_{cop}(z,t)}{M_{cop}} I_{cop}^{max}(1 - e^{-\delta_{cop}(N_{lpp}(z,t) - Th_{cop}^{I})}). \qquad (14)$$

The values used for the parameters that define the Ivlev grazing curve, the maximum ingestion rate (I_{cop}^{max}), the e-folding scale (δ_{cop}) and the grazing threshold (Th_{cop}^{I}), are given in Table 5. The effect of the large phytoplankton on the grazing rate is included through $N_{lpp}(z,t)$ which represents the ambient concentration of large phytoplankton at a given depth and time. For values of $N_{lpp}(z,t)$ less than the grazing threshold, the copepod ingestion rate is zero. The ingestion rate is weighted by the ratio of the ambient copepod concentration ($N_{cop}(z,t)$) to the equivalent nitrogen mass of the animal (M_{cop}). The value used for M_{cop} is given in Table 5. This weighting factor scales the ingestion rate to the zooplankton population. The ingestion rate given by equation 14 is constrained with a mass

balance requirement, such that the amount of food ingested in a time step does not exceed the available food.

The efficiency with which the copepod assimilates food was assumed to vary with ingestion rate and hence food concentration. The formulation suggested by Landry et al. (1984) assumes that the assimilation efficiency, $AE_{cop}(z,t)$, varies between a minimum and maximum value as:

$$AE_{cop}(z,t) = AE_{cop}^{min} + \left[(AE_{cop}^{max} - AE_{cop}^{min})e^{-\tau_{cop} I_{cop}(z,t)}\right]. \qquad (15)$$

where AE_{cop}^{max} and AE_{cop}^{min} are the upper and lower bounds on the assimilation efficiency. The assimilation efficiency decreases or increases exponentially between these bounds with an e-folding scale given by τ_{cop} that is modified by the ingestion rate, $I_{cop}(z,t)$. As the ingestion rate increases in response to higher food concentrations, the assimilation efficiency approaches its lower bound. The values for the parameters in equation 15 are given in Table 5 and the relationship between assimilation efficiency and food concentration is shown in Fig. 13A. Once the assimilation efficiency and ingestion rates are known, then the assimilated ingestion, $A_{cop}(z,t)$, is calculated as:

$$A_{cop}(z,t) = AE_{cop}(z,t) I_{cop}(z,t). \qquad (16)$$

The fraction of ingested food that is not assimilated represents egestion, i. e. fecal pellet formation. The relationship between ingestion, assimilated ingestion and egestion over a range of food concentrations is shown in Fig. 13B.

In order for the copepod population to increase, the growth term in equation 13 must be positive which requires that the assimilated ingestion be larger than

Table 5. Values, Units and Source For the Parameters Used In the Equations to Calculate Growth, Ingestion, Egestion, Predation, Death, Molting and Reproduction Rates For the Copepod *Eucalanus californicus*.

Parameter	Value	Units	Reference
M_{cop}	0.11167	mg N (copepod)$^{-1}$	calculated
I_{cop}^{max}	2.701 x 10^{-7}	mg N (copepod)$^{-1}$ s^{-1}	Frost, 1980 and 1975
δ_{cop}	0.1050	(mg N)$^{-1}$ m^3	estimated, this study
Th_{cop}^{I}	1.229 x 10^{1}	mg N m^{-3}	Frost, 1980 and 1975
AE_{cop}^{max}	9.250 x 10^{1}	Dimensionless	Landry et al., 1983
AE_{cop}^{min}	7.390 x 10^{1}	Dimensionless	Landry et al., 1983
τ_{cop}	7.330 x 10^{6}	(mg N)$^{-1}$ (copepod) s	estimated, this study
DW_{cop}	1.061	mg dry weight (copepod)$^{-1}$	Omori & Ikeda, 1984
RQ_{cop}	0.97	Dimensionless	Omori & Ikeda, 1984
CN_{cop}	3.900	mM C (mM N)$^{-1}$	Omori & Ikeda, 1984
G_{cop}^{max}	6.753 x 10^{-8}	mg N (copepod)$^{-1}$ s^{-1}	Vidal, 1980a & 1980b
ζ_{cop}	0.105	mg N^{-1} m^3	estimated, this study
$Dmax_{cop}^{pred}$	6.753 x 10^{-9}	mg N (copepod)$^{-1}$ s^{-1}	estimated, this study
ϵ_{cop}	0.1188	(mg N)$^{-1}$ m^3	estimated, this study
Th_{cop}^{P}	1.944 x 10^{-2}	mg N m^{-3}	estimated, this study
D_{cop}^{nat}	6.753 x 10^{-9}	mg N (copepod)$^{-1}$ s^{-1}	estimated, this study

Figure 13. Relationship between the processes included in the copepod portion of the model at 10°C for a range of food concentrations: **A**) assimilation efficiency and **B**) ingestion, assimilated ingestion, growth, reproduction, egestion, respiration and molting.

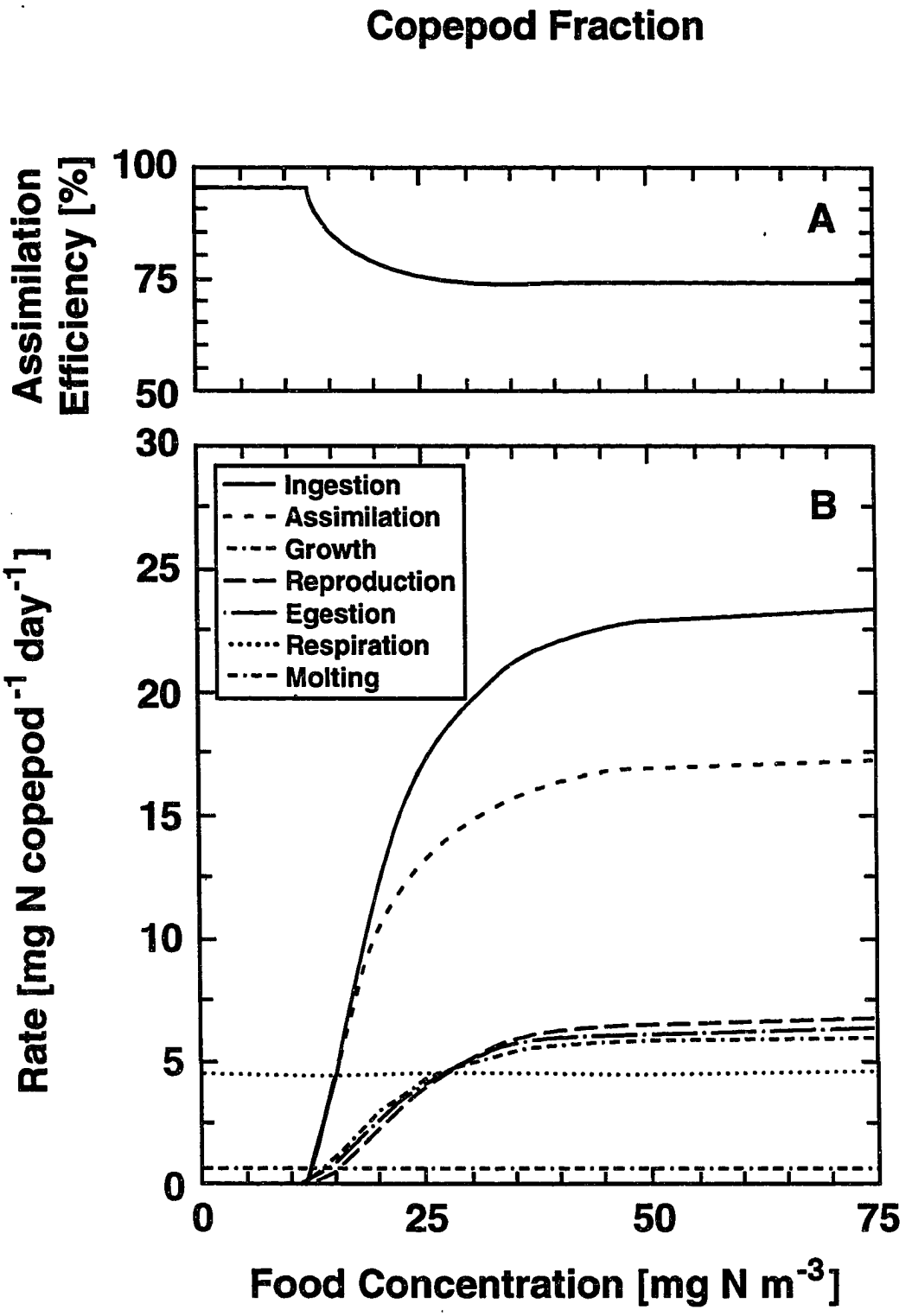

the metabolic losses. For *E. californicus*, metabolic losses were assumed to be the result of excretion, molting and reproduction. The excretion rate of nitrogenous waste by respiration for *E. californicus* was obtained using a general relationship suggested by Omori and Ikeda (1984) that relates respiration rate, animal body weight and temperature as:

$$Ex_{cop}(z,t) = \left(\frac{N_{cop}(z,t)}{M_{cop}}\right)\left(\frac{DW_{cop}a(DW_{cop})^b RQ_{cop}14}{22.4CN_{cop}}\right), \qquad (17)$$

where $Ex_{cop}(z,t)$ is the respiration rate at a given depth and time, DW_{cop} is the mean dry weight of a copepod, RQ_{cop} is the respiratory quotient and CN_{cop} is the general copepod carbon to nitrogen ratio. The values 22.4 (l O_2 M^{-1}) and 14 (mg N M^{-1}) are used to convert the respiration rate into the necessary units. The values of the parameters used in equation 17 are given in Table 5. As with the ingestion rate, the excretion rate is scaled by the population size. The effect of the ambient temperature on the respiration rate is included through the coefficients that modify the effect of the animal dry weight, DW_{cop}, as:

$$a = 10^{0.02438\ TEM(z,t) - 0.1838}$$

$$b = -\ 0.01090\ TEM(z,t) - .1082.$$

where $TEM(z,t)$ is the ambient temperature at a given depth and time. The formulations for a and b were obtained from general relationship suggested by Omori and Ikeda (1984) and the values obtained from this equation for *Eucalanus californicus* compare well with other derived general respiration curves specific to copepods (Dagg et al., 1982; Vidal and Whitledge, 1982; Vidal, 1980a).

The loss of nitrogen due to molting was estimated from a growth- and temperature-dependent relationship that was obtained for *Calanus pacificus* (Vidal, 1980b) and is of the form:

$$MT_{cop}(z,t) = \begin{cases} \frac{N_{cop}(z,t)}{M_{cop}}(a + b\ G_{cop}(z,t))M_{cop} & G_{cop}(z,t)\ 0. \\ \frac{N_{cop}(z,t)}{M_{cop}}a\ M_{cop} & G_{cop}(z,t) \leq 0., \end{cases} \quad (18)$$

where the effect of temperature is introduced through the empirical coefficients

$$a = -0.371 + 0.586\ log(TEM(z,t))$$

$$b = 0.02192 + 0.001278\ TEM(z,t).$$

The above relationship depends on animal growth, $G_{cop}(z,t)$, which is the assimilated nitrogen remaining after respiration losses. For times when the respiration rate exceeds the assimilation rate, the term is negative, i.e. starvation occurs. As a consistency check, the optimal growth rate at a given food concentration is obtained from an Ivlev-type growth relationship which was empirically derived from the growth relationship given in Vidal (1980a, b, c and d) as:

$$G_{cop}^{opt} = \frac{N_{cop}(z,t)}{M_{cop}} G_{cop}^{max}\left(1 - e^{-\zeta_{cop}(N_{lpp} - Th_{cop}^{I})}\right). \quad (19)$$

The values for the parameters in equation 19, the maximum growth rate (G_{cop}^{max}) and the e-folding scale (ζ_{cop}), are given in Table 5. The actual growth rate used to determine the molting rate is specified using the the minimum of the optimal and calculated growth rate. This ensures mass conservation. The dependence of the growth rate and the molting rate on food concentrations at a given temperature (10°C) is shown in Fig. 13.

The nitrogen loss due to reproductive processes was assumed to be the fraction of assimilated ingestion remaining after the demands of respiration, molting and growth had been met (Runge, 1985). Reproduction was only allowed during periods of positive growth. This dependence of reproductive rate on food concentration is shown in Fig. 13.

The mortality due to predation by higher trophic levels and other natural causes was assumed to be dependent on the concentration of the zooplankton *E. californicus* and to increase to a maximal predation rate at some prey concentration. As discussed in the next section, *E. californicus* was grazed by *Euphausia pacifica* as well, because *Euphausia pacifica* feed preferentially on copepod (Price et al., 1988). Thus, predation losses were assumed to be given by:

$$D_{cop}^{pred}(z,t) = I_{eup}^{cop}(z,t) + \frac{N_{cop}(z,t)}{M_{cop}} Dmax_{cop}^{pred}(1 - e^{-\epsilon_{cop}(N_{cop}(z,t) - Th_{cop}^{P})}), \quad (20)$$

where the first term represents ingestion by *E. pacifica* and the second represents ingestion by other predators. As with the ingestion rate, predation by other predators is assumed to cease below some threshold concentration Th_{cop}^{P} of *E. californicus*, $N_{cop}(z,t)$. The values used for the coefficients in the predation equation are given in Table 5.

The final loss term of *E. californicus* is natural mortality, $D_{cop}^{nat}(z,t)$, which is assumed to be a linear function of population concentration such that:

$$D_{cop}^{nat}(z,t) = \frac{N_{cop}(z,t)}{M_{cop}} D_{cop}^{nat}. \quad (21)$$

E. californicus has an average life span of 60–120 days. Therefore, the natural mortality rate, $D_{cop}^{nat}(z,t)$, was chosen such that in the absence of starvation and predation, the turnover time of the population was within the average lifespan. The value thus estimated for $D_{cop}^{nat}(z,t)$ is given in Table. 5.

3.1.3.2.2 Euphausiid, *Euphausia pacifica*

Euphausia pacifica, is the most abundant euphausiid off the California coast (Lasker, 1966; Mackas et al., 1991; Smith and Lane, 1991). Euphausiids are large (0.3–4 mg C per individual) omnivorous zooplankton that feed over a wide range of particle sizes that includes small net phytoplankton up to large copopods and fish larvae (Price et al., 1988). Therefore, total ingestion for this animal included the herbivorous copepod and the large phytoplankton fraction:

$$I_{eup}(z,t) = I_{eup}^{lpp}(z,t) + I_{eup}^{cop}(z,t), \tag{22}$$

where the terms on the right represent the grazing rates on large phytoplankton and *E. pacifica*, respectively. The ingestion rates for *E. pacifica* reported in Lasker (1966) and Ross (1982a and b) were used with an Ivlev-type model to obtain ingestion rates for a range of concentrations of large phytoplankton,

$$I_{eup}^{lpp}(z,t) = \frac{N_{eup}(z,t)}{M_{eup}} Imax_{eup}^{lpp} HC(z,t)(1 - e^{-\delta_{eup}^{lpp}(N_{lpp}(z,t) - Th_{eup}^{I_{lpp}})}) \tag{23}$$

and for *E. californicus*

$$I_{eup}^{cop}(z,t) = \frac{N_{eup}(z,t)}{M_{eup}} Imax_{eup}^{cop}(1 - HC(z,t))(1 - e^{-\delta_{eup}^{cop}(N_{cop}(z,t) - Th_{eup}^{I_{cop}})}). \tag{24}$$

The parameters in equations 23 and 24 are defined as those in the *E. californicus* ingestion equation (eq. 14) and the values are given in Table 6. Both ingestion equations contain threshold concentrations, $Th_{eup}^{I_{lpp}}$ and $Th_{eup}^{I_{cop}}$, below which ingestion ceases. The primary difference between the euphausiid ingestion equation and that used for *E. californicus* is the inclusion of a weighting factor, $HC(z,t)$, that allows for the relative preference of *E. pacifica* for the phytoplankton or copepod prey. This factor is based upon measurements given in Ohman (1985) and Price et al. (1988). and is defined as:

$$HC(z,t) = \frac{N_{lpp}(z,t)}{3N_{cop}(z,t) + N_{lpp}(z,t)}. \tag{25}$$

As the relative abundance of the *E. californicus* increases, *E. pacifica* will feed more preferentially on the copepod fraction than the large phytoplankton fraction.

The relationship between ingestion rate and assimilation efficiency for *E. pacifica* (Lasker, 1966) is similar to that used for *E. californicus*. The values for the parameters in the assimilation efficiency relationship were modified using the values for *E. pacifica* given in Lasker (1966). The resultant values are given in Table 6. The assimilated ingestion is then calculated from the assimilation efficiency and ingestion rate. That portion of ingestion not assimilated is egested. The relationship amoung these three quantities for a range of food concentrations for *E. pacifica* is shown in Fig. 14.

The partitioning of assimilated ingestion into growth and metabolic losses for *E. pacifica* was assumed to be governed by relationships similar to those used for *E. californicus*. Excretion rates for nitrogenous waste by respiration for *E. pacifica*, obtained from equation 17, compared well with field and laboratory measurements

Table 6. Values, Units and Source For the Parameters Used In the Equations to Calculate Growth, Ingestion, Egestion, Predation, Death, Molting and Reproduction Rates For the Euphausiid *Euphausia pacifica*.

Parameter	Value	Units	Reference
M_{eup}	0.375	mg N (euphausiid)$^{-1}$	calculated
$Imax_{eup}^{lpp}$	4.891 x 10^{-7}	mg N (euphausiid)$^{-1}$ s^{-1}	Ross, 1982a & 1982b
$Imax_{eup}^{cop}$	4.891 x 10^{-7}	mg N (euphausiid)$^{-1}$ s^{-1}	Ross, 1982a & 1982b
δ_{eup}^{lpp}	6.3 x 10^{-2}	(mg N)$^{-1}$ m^3	estimated, this study
δ_{eup}^{cop}	0.105	(mg N)$^{-1}$ m^3	estimated, this study
$Th_{eup}^{I_{lpp}}$	1.229 x 10^1	mg N m^{-3}	estimated, this study
$Th_{eup}^{I_{cop}}$	1.229 x 10^1	mg N m^{-3}	estimated, this study
AE_{eup}^{max}	9.500 x 10^1	Dimensionless	Ross, 1982a & 1982b
AE_{eup}^{min}	7.000 x 10^1	Dimensionless	Ross, 1982a & 1982b
τ_{eup}	8.554 x 10^5	(mg N)$^{-1}$ s	estimated, this study
DW_{eup}	1.061	mg dry weight (euphausiid)$^{-1}$	Mackas et al., 1991
RQ_{eup}	0.97	Dimensionless	Omori and Ikeda, 1984
CN_{eup}	3.5	mM C (mM N)$^{-1}$	Omori and Ikeda, 1984
G_{eup}^{max}	3.739 x 10^{-8}	mg N euphausiid^{-1} s^{-1}	Ross, 1982a & 1982b
ζ_{eup}	0.105	mg N^{-1} m^3	estimated, this study
Q_{10}^{molt}	1.86	Dimensionless	Ross, 1982a & 1982b
MT_0	1.326	mg N (euphausiid)$^{-1}$ s^{-1}	Ross, 1982a & 1982b
$Dmax_{eup}^{nat}$	6.753 x 10^{-9}	mg N (euphausiid)$^{-1}$ s^{-1}	estimated, this study
$Dmax_{eup}^{pred}$	6.753 x 10^{-9}	mg N (euphausiid)$^{-1}$ s^{-1}	estimated, this study
ϵ_{eup}	0.1188	(mg N)$^{-1}$ m^3	estimated, this study
Th_{eup}^{P}	1.944 x 10^{-2}	mg N m^{-3}	estimated, this study

Figure 14. Relationship between the processes included in the euphausiid portion of the model at 10°C for a range of food concentrations: **A**) assimilation efficiency and **B**) ingestion, assimilated ingestion, growth, reproduction, egestion, respiration and molting.

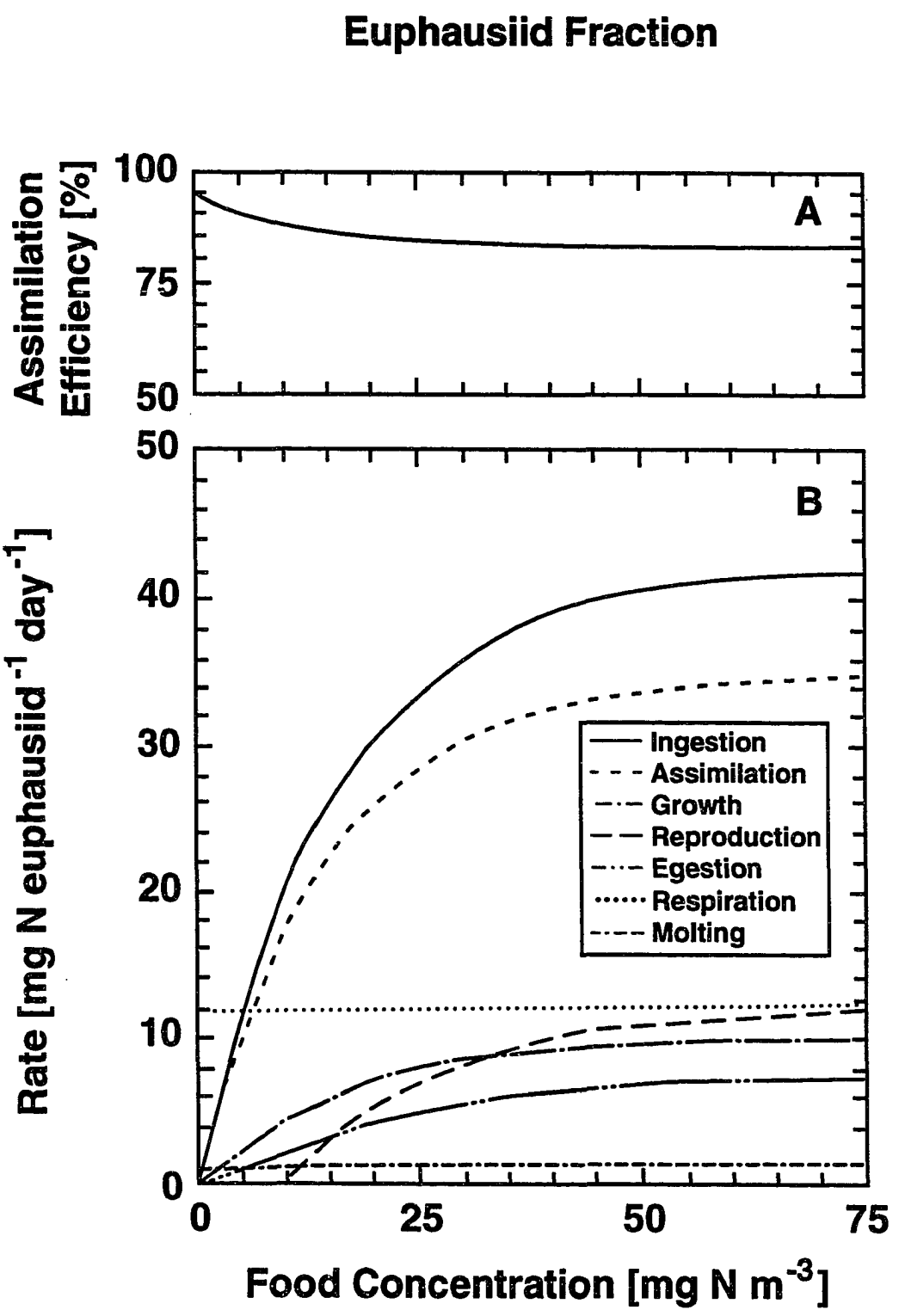

given in Lasker (1966), Jawed (1969), Ross (1981; 1982a and b) and Ross et al. (1982), for *E. pacifica*. The parameters in the excretion equation are defined as for those in the *E. californicus* excretion equation and the values are given in Table 6.

The loss of nitrogen due to molting was estimated from a temperature-dependent molting relationship that was obtained for *E. pacificus* (Ross, 1982a and b) and is of the form:

$$MT_{eup}(z,t) = \frac{N_{eup}(z,t)}{M_{eup}} MT_0 \, (Q_{10}^{molt})^{\frac{TEM(z,t)}{10}}, \tag{26}$$

where MT_0 is the extrapolated molting rate at 0°C; and, Q_{10}^{molt} is the calculated Q_{10} value for the molting process. The values used for the parameters in equation 26 are given in Table 6. Unlike the molting equation used for *E. californicus*, the above relationship does not depend on animal growth, $G_{eup}(z,t)$, because molting is a continuous process in *E. pacifica*, even during periods of starvation (Ross, 1981).

The growth rate, $G_{eup}(z,t)$, is the assimilated nitrogen remaining after respiration losses. For times when the respiration rate exceeded the assimilation rate, the term is negative, i.e. starvation occurs. As a consistency check, the optimal growth rate at a given food concentration was obtained from an Ivlev-type growth relationship which was empirically derived from the growth relationship from the field and laboratory measurements given in Ross (1981; 1982a; 1982b) and Ross et al. (1982) and is written as:

$$G_{eup}^{opt} = \frac{N_{eup}(z,t)}{M_{eup}} G_{eup}^{max} \left(1 - e^{-\zeta_{eup} Th_{eup}^{I}}\right). \tag{27}$$

The parameters in equation 27 are defined similar to those used in the *E. californicus* optimal growth relationship (eq. 19) and the values are given in Table 6. The dependence of the molting rate and the growth rate on food concentrations at a given temperature is illustrated in Fig. 14.

The nitrogen loss due to reproductive processes was assumed to be the remaining fraction of assimilated ingestion after respiration, molting and growth has been removed. Reproduction was only allowed during periods of positive growth. This dependence of reproductive rate on food concentration is shown in Fig. 14.

Mortality due to predation by higher trophic levels and other natural causes was assumed to be dependent on the concentration of *E. pacifica* and to increase to a maximal predation rate at some prey concentration. Thus, predation losses were assumed to be given by:

$$D_{eup}^{pred}(z,t) = \frac{N_{eup}(z,t)}{M_{eup}} Dmax_{eup}^{pred}(1 - e^{-\epsilon_{eup}(N_{eup}(z,t) - Th_{eup}^{P})}). \qquad (28)$$

As with the ingestion rate, predation by other predators is assumed to cease below some threshold concentration, Th_{eup}^{P}, of *E. pacifica*. The values used for the coefficients in the predation equation are given in Table 6.

The final loss term of *E. pacifica* is natural mortality, $D_{eup}^{nat}(z,t)$, which is assumed to be a linear function of population concentration such that:

$$D_{eup}^{nat}(z,t) = \frac{N_{eup}(z,t)}{M_{eup}} D_{eup}^{nat}. \qquad (29)$$

E. pacifica has an average life span of 210–236 days (Ross, 1982b). Therefore, the natural mortality rate, $D_{cop}^{nat}(z,t)$, was chosen such that in the absence of starvation

and predation, the turnover time of the population was within the average lifespan. The value thus estimated for $D_{eup}^{nat}(z,t)$ is given in Table. 6.

3.1.3.2.3 Gelatinous Zooplankton, *Dolioletta gegenbauri*

The gelatinous zooplankton in the model is representative of the doliolid, *Dolioletta gegenbauri.* This animal is a nonselective filter feeder and is capable of ingesting both large, being constrained only by the diameter of its aperture (Deibel, 1982*b*), and small phytoplankton ($<$ 50 μm, Deible, 1985) fractions as well as detritus. Unlike the copepod and euphausiid animals, the ingestion rate of the doliolid is dependent upon the animal's filtration rate which is limited by the flux of water through the animal's aperture. Thus, the filtration rate of water, $F_{dol}(z,t)$, for a doliolid of average size, M_{dol}, is expressed as:

$$F_{dol}(z,t) = F_{dol}^{max} e^{-0.01 N_{lpp}(z,t)}, \tag{30}$$

where F_{dol}^{max} is the maximum volume flux through the aperture. The exponential term represents the decrease in flux due to the clogging of the animals filtration mechanism by the large phytoplankton fraction (Madin, 1974; Deibel, 1982b).

The ingestion of food by *D. gegenbauri* is obtained as:

$$I_{dol}(z,t) = I_{dol}^{lpp}(z,t) + I_{dol}^{spp}(z,t) + I_{dol}^{det}(z,t), \tag{31}$$

where the terms on the right represent the time and depth dependent grazing rates on the large, $I_{dol}^{lpp}(z,t)$, and small, $I_{dol}^{spp}(z,t)$, phytoplankton fraction and detritus, $I_{dol}^{det}(z,t)$. The ingestion rates for *D. gegenbauri* are calculated using the filtration rates, $F_{dol}(z,t)$, as:

$$I_{dol}^{lpp}(z,t) = \frac{N_{dol}(z,t)}{M_{dol}} Filt_{dol}(z,t) N_{lpp}(z,t) \quad (32)$$

$$I_{dol}^{spp}(z,t) = \frac{N_{dol}(z,t)}{M_{dol}} Filt_{dol}(z,t) N_{spp}(z,t) \quad (33)$$

$$I_{dol}^{det}(z,t) = \frac{N_{dol}(z,t)}{M_{dol}} Filt_{dol}(z,t) N_{det}(z,t), \quad (34)$$

where $N_{lpp}(z,t)$, $N_{spp}(z,t)$ and $N_{det}(z,t)$ are the depth- and time-dependent concentrations (mg N m^{-3}) of the large and small zooplankton size fractions and the detrital pool, respectively. The ingestion rates are weighted by the ratio of the ambient doliolid concentration ($N_{dol}(z,t)$) to the equivalent nitrogen mass of the animal (M_{dol}). The value used for M_{dol} is given in Table 7. This weighting factor scales the ingestion rate to the zooplankton population. The ingestion rates given by equations 32–34 are constrained with a mass balance requirement, such that the amount of food ingested in a time step does not exceed the available food. The values of the parameters in the ingestion equations are given in Table 7.

The assimilation efficiency for *D. gegenbauri* was assumed to follow the same relationship used for *E. californicus*. However, the parameter values were modified for *D. gegenbauri* and these are given in Table 7. The assimilated ingestion is then calculated from the assimilation efficiency and ingestion rate. That portion of ingestion not assimilated is egested. The relationships amoung these three quantities for a range of food concentrations for *D. gegenbauri* are shown in Fig. 15.

The partitioning of assimilated ingestion into growth and metabolic losses for *D. gegenbauri* was assumed to be governed by relationships similar to those used for *E. californicus*. Excretion of nitrogenous waste by respiration for *D. gegenbauri* was obtained using a general relationship suggested by Omori and Ikeda (1984)

Table 7. Values, Units and Source For the Parameters Used In the Equations to Calculate Growth, Ingestion, Egestion, Predation, Death and Reproduction Rates For the Doliolid *Dolioletta gegenbauri*.

Parameter	Value	Units	Reference
F_{dol}^{max}	1.029 x 10^{-9}	$m^3\ s^{-1}$	Deibel, 1982a & 1982b
M_{dol}	1.953 x 10^{-2}	mg N doliolid^{-1}	Mackas et al., 1991
AE_{dol}^{max}	9.5 x 10^1	Dimensionless	Omori and Ikeda, 1984
AE_{dol}^{min}	7.0 x 10^1	Dimensionless	Omori and Ikeda, 1984
τ_{dol}	1.466	$(mg\ N)^{-1}\ m^3$	estimated, this study
DW_{dol}	0.1953	mg dry weight $(doliolid)^{-1}$	Mackas et al., 1991
RQ_{dol}	0.97	Dimensionless	Omori and Ikeda, 1984
CN_{dol}	4.200	mM C $(mM\ N)^{-1}$	Omori and Ikeda, 1984
G_{dol}^{max}	3.729 x 10^{-8}	mg N $(doliolid)^{-1}\ s^{-1}$	Deibel, 1982a
ζ_{dol}	5.250 x 10^{-2}	$mg\ N^{-1}\ m^3$	estimated, this study
$Dmax_{dol}^{nat}$	7.535 x 10^{-9}	mg N $(doliolid)^{-1}\ s^{-1}$	estimated, this study
$Dmax_{dol}^{pred}$	7.535 x 10^{-9}	mg N $(doliolid)^{-1}\ s^{-1}$	estimated, this study
ϵ_{dol}	6.935 x 10^{-2}	$(mg\ N)^{-1}\ m^3$	estimated, this study
Th_{dol}^{P}	1.0	mg N m^{-3}	estimated, this study

Figure 15. Relationship between the processes included in the doliolid portion of the model at 10°C for a range of food concentrations: **A**) assimilation efficiency and **B**) ingestion, assimilated ingestion, growth, reproduction, egestion and respiration.

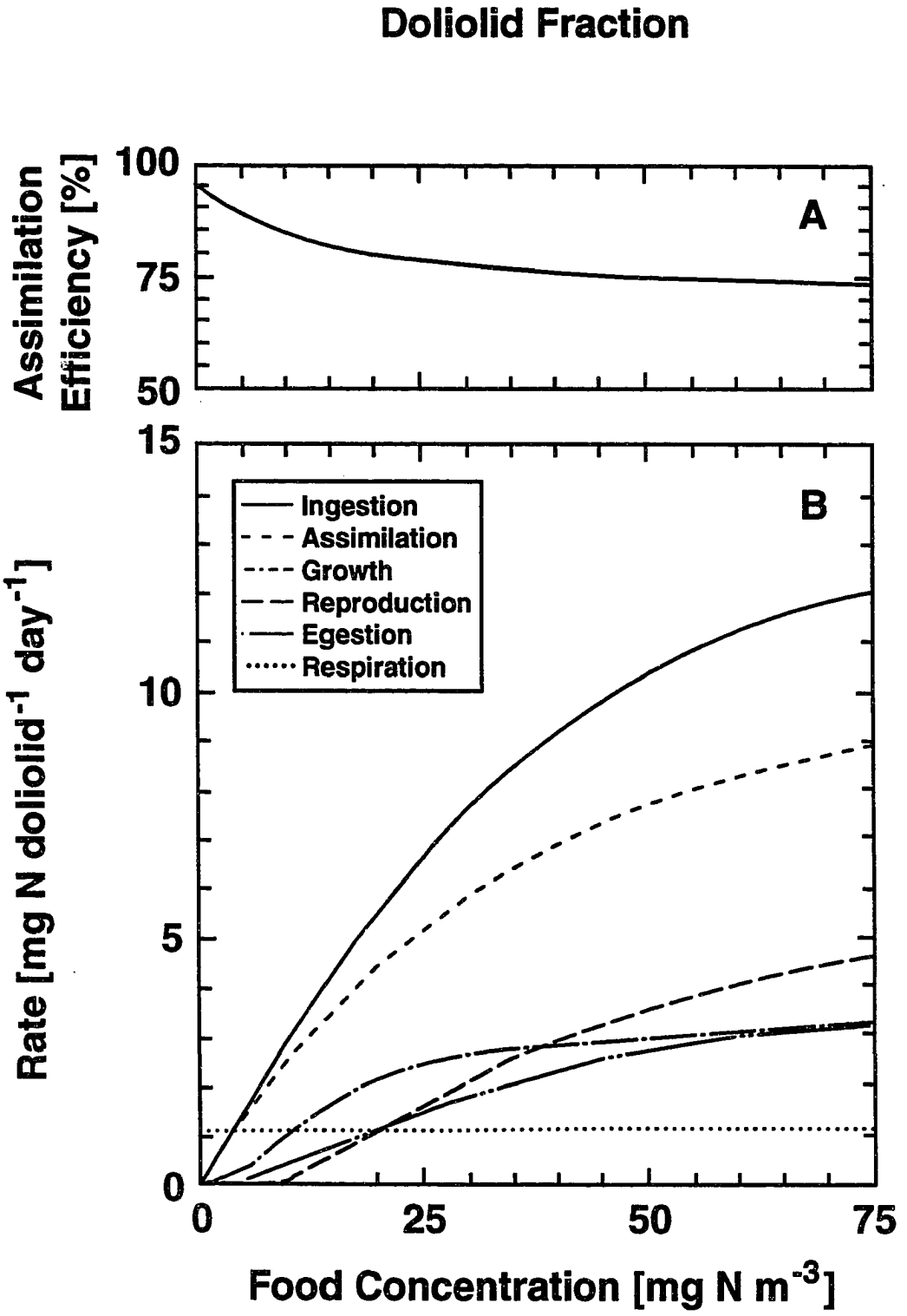

that relates respiration rate, animal body weight and temperature. The parameters in the excretion equation are defined as those in the *E. californicus* excretion equation and the values are given in Table 7. *D. gegenbauri* does not molt; therefore, nitrogen loss due to molting was not included as a metabolic process for this animal.

The growth rate, $G_{dol}(z,t)$, is the assimilated nitrogen remaining after respiration losses. For times when the respiration rate exceeded the assimilation rate, the term is negative, i.e. starvation occurs. As a consistency check, the optimal growth rate at a given food concentration was obtained from an Ivlev-type growth relationship which was empirically derived from the growth relationship from the field and laboratory measurements given in Heron (1972 a and b), Deibel (1982a; 1982b) and Deibel (1985) and is written as:

$$G_{dol}(z,t) = \frac{N_{dol}(z,t)}{M_{dol}} G_{dol}^{max}\left(1 - e^{-\zeta_{dol} N_{lpp}}\right). \tag{35}$$

The parameters in equation 35 are defined similar to those used in the *E. californicus* optimal growth relationship (eq. 19) and the values are given in Table 7. The dependence of the growth rate on food concentrations at a given temperature is illustrated in Fig. 15.

The nitrogen loss due to reproductive processes was assumed to be the remaining fraction of assimilated ingestion after respiration and growth has been removed. Reproduction was only allowed during periods of positive growth. The dependence of reproductive rate on food concentration is shown in Fig. 15.

The mortality due to predation by higher trophic levels and other natural causes was assumed to be dependent on the concentration of the zooplankton

D. gegenbauri and to increase to a maximal predation rate at some prey concentration. Thus, predation losses were assumed to be given by:

$$D_{dol}^{pred}(z,t) = N_{dol}(z,t) Dmax_{dol}^{pred}(1 - e^{-\epsilon_{dol}(N_{dol}(z,t) - Th_{dol}^{P})}). \quad (36)$$

As with the ingestion rate, predation by other predators is assumed to cease below some threshold concentration Th_{dol}^{P} of *D. gegenbauri*, $N_{dol}(z,t)$. The values used for the coefficients in the predation equation are given in Table 7.

The final loss term of *D. gegenbauri* is natural mortality, $D_{dol}^{nat}(z,t)$, which is assumed to be a linear function of population concentration such that:

$$D_{dol}^{nat}(z,t) = \frac{N_{dol}(z,t)}{M_{dol}} Dmax_{dol}^{nat}. \quad (37)$$

D. gegenbauri has an average life span of 21–42 days (Ross, 1982b). Therefore, the natural mortality rate, $D_{dol}^{nat}(z,t)$, was chosen such that in the absence of starvation and predation, the turnover time of the population was within the average lifespan. The value thus estimated for $D_{dol}^{nat}(z,t)$ is given in Table. 7.

3.1.3.3 Detritus

Detritus is included in the model both as a closure term for the nitrate pool and as a food supply for the doliolids. The biological processes affecting the concentration of detritus are given as:

$$S = Phytoplankton\ Mortality + Zooplankton\ Mortality -$$

$$Grazing - Detrital\ Remineralization. \quad (38)$$

Sources of detritus are provided by phytoplankton and zooplankton mortality. The phytoplankton mortality term is the sum of the large and small natural mortality terms. The zooplankton mortality term is the sum of the *E. californicus*, *E. pacifica* and *D. gegenbauri* natural mortality terms, equations 21, 29 and 37, respectively. Detritus is removed by ingestion by *D. gegenbauri* and remineralization into nitrate. This latter process is assumed to be a linear function of the concentration of detritus such that the mean turnover time of the detrital pool was 10 days.

3.1.3.4 Nutrients

The biological processes affecting the concentration of nitrate are given as:

$$S = Phytoplankton\ Nitrate\ Uptake, \tag{39}$$

where removal of nitrate by phytoplankton uptake is governed by the amount of primary production and the f-ratio of the two phytoplankton size fractions as:

$$Phytoplankton\ Uptake = PP_{lpp}(z,t)f_{lpp}(z,t) + PP_{spp}(z,t)f_{spp}(z,t), \tag{40}$$

where the terms $PP_{lpp}(z,t)$, $PP_{spp}(z,t)$, $f_{lpp}(z,t)$ and $f_{spp}\ (z,t)$ were defined in section 3.1.3.1 and are given in equations 3, 4, 11 and 12, respectively. As the f-ratio increases more of the nitrogen required to support phytoplankton growth comes from the available nitrate.

The biological processes affecting the concentration of ammonium are given as:

$$S = Zooplankton\ Excretion + Detrital\ Remineralization$$
$$- Phytoplankton\ Ammonia\ Uptake. \quad (41)$$

Inputs to ammonium pool come from the sum of all the respiratory waste from the three zooplankton in the model (section 3.1.3.2) and remineralization of detritus (section 3.1.3.3). Removal of ammonium by phytoplankton uptake is governed by the amount of primary production and the f-ratio of the two phytoplankton size fractions as:

$$Phytoplankton\ Uptake = PP_{lpp}(z,t)(1 - f_{lpp}(z,t))$$
$$+ PP_{spp}(z,t)(1 - f_{spp}(z,t)). \quad (42)$$

Finally, the concentration of silicate is changed by biological processes through removal by phytoplankton:

$$S = Phytoplankton\ Silicate\ Uptake. \quad (43)$$

This removal rate is calculated from the nitrate uptake and the slope of the silicate to nitrate relationship in the CTZ region (Fig. 11). The change in the slope of this relationship results from changes in species composition within the different water masses. Silicate-dependent diatoms, e.g. *Chaetoceras* sp., were dominant in the nutrient-rich waters along the coast, while nonsilicate-dependent phytoplankton, e.g. *Synechococcus* sp., were dominant in the nutrient-poor waters; therefore, the uptake of silicate was higher in the nutrient-rich waters. Dissolution of silicate from

the detrital fraction was assumed to be unimportant given the short generation time of a filament relative to the time scale associated with the dissolution process.

3.1.4 Optical Model

The purpose of the optical portion of the model is to determine the magnitude of the subsurface, depth-, wavelength- and time-dependent irradiance field. The energy flux from this field is then used to determine the large and small phytoplankton energy uptake rate ($PHAR_{lpp}(z,t)$ and $PHAR_{spp}(z,t)$) and the kinetic energy flux (ΔT) into the water. However, the one-dimensional model contains no heat dissipation mechanism, thus the kinetic energy uptake term is not used and the temperature field in the model contains no source/sink term.

The wavelength-dependent attenuation of the subsurface irradiance field, due to sea water, phytoplankton and dissolved organic matter is incorporated as a depth-dependent energy flux which balances the phytoplankton energy uptake and the kinetic energy flux (ΔT) into the water. Both the direct and diffuse components of spectral irradiance at the sea surface are calculated using a simple, wavelength-dependent, solar model for direct-normal and diffuse horizontal irradiance (Bird, 1984). The direct-normal spectral irradiance at the surface of the ocean, $I_d(\lambda,t)$ (Einsteins h^{-1} m^{-2} nm^{-1}), for a given wavelength, λ (nm), and at some time, t (hours), can be obtained from:

$$I_d(\lambda,t) = H_0(\lambda,t)T_r(\lambda)T_a(\lambda)T_o(\lambda)T_w(\lambda)T_u(\lambda)cos(\theta_z(t)), \qquad (44)$$

where the parameters on the right side of equation (44) are defined in Table 8. Specific values for each expression are given in Bird (1984). The diffuse horizontal

spectral irradiance at the surface of the ocean, $I_s(\lambda,t)$ (Einsteins h^{-1} m^{-2} nm^{-1}), for a given wavelength, λ (nm), and at some time, t (hours), is:

$$I_s(\lambda,t) = [I_r(\lambda,t) + I_a(\lambda,t)]C_{\lambda\theta_z(t)} + I_g(\lambda,t), \tag{45}$$

where $I_r(\lambda,t)$, $I_a(\lambda,t)$ and $I_g(\lambda,t)$ are the Rayleigh scattered, aerosol scattered and sea/air reflected irradiance on a horizontal surface at wavelength λ, respectively, and $C_{\lambda\theta_z(t)}$ is a correction factor that is wavelength- and zenith angle-dependent (therefore, also time-dependent). These irradiance terms can be calculated from the following equations:

$$I_r(\lambda,t) = H_0(\lambda)cos(\theta_z(t))T_o(\lambda)T_u(\lambda)T_w(\lambda)T_a(\lambda)[1 - T_r(\lambda)]0.5 \tag{46}$$

$$I_a(\lambda,t) = H_0(\lambda)cos(\theta_z(t))T_o(\lambda)T_u(\lambda)T_w(\lambda)T_r(\lambda)[1 - T_a(\lambda)]W_0F_a \tag{47}$$

$$I_g(\lambda,t) = \frac{[I_d(\lambda,t)cos(\theta_z(t)) + [I_r(\lambda,t) + I_a(\lambda)]C_{\lambda\theta_z(t)}]\rho_s\rho_a}{1 - \rho_s\rho_a}. \tag{48}$$

Definitions for the parameters in equations 46–48 are given in Table 8 and specific values for each are found in Bricaud et al. (1981), Bird (1984 and 1986), Carder et al. (1989), Peacock et al. (1988) and Sathyendranath and Platt (1988, 1989 and 1991).

The subsurface total downwelling spectral irradiance field at some depth, $E(z,\lambda,t)$ (Einsteins h^{-1} m^{-2} nm^{-1}), is divided into component parts as:

$$E(z,\lambda,t) = E_d(z,\lambda,t) + E_s(z,\lambda,t), \tag{49}$$

Table 8. Definition and Units of Parameters Used in the Relationship to Calculate Direct-Normal and Diffuse Horizontal Spectral Irradiance at the Surface of the Ocean.

Parameter	Definition	Units
$H_0(\lambda,t)^*$	Extraterrestrial Spectral Irradiance	Einsteins h^{-1} m^{-2} nm^{-1}
$T_r(\lambda)^*$	Transmission Function for Rayleigh Scattering	Dimensionless
$T_a(\lambda)^*$	Transmission Function for Aerosol Extinction	Dimensionless
$T_o(\lambda)^*$	Transmission Function for Ozone Absorption	Dimensionless
$T_w(\lambda)^*$	Transmission Function for Water Vapor Absorption	Dimensionless
$T_u(\lambda)^*$	Transmission Function for Absorption by Uniformly Mixed Gases	Dimensionless
$\theta_z(t)$	Solar Zenith Angle Coefficient	Dimensionless
W_0	Single Scattering Albedo for the Aerosol	Dimensionless
F_a	Forward Total Scattering Ratio for the Aerosol	Dimensionless
ρ_s	Sea Surface Albedo	Dimensionless
ρ_a	Air Albedo	Dimensionless

* Spectral Coefficients Between 400 nm and 700 nm with 5 nm resolution

where $E_d(z,\lambda,t)$ is the direct downwelling irradiance on a horizontal surface (Einsteins h^{-1} m^{-2} nm^{-1}) and $E_s(z,\lambda,t)$ is the diffuse irradiance (Einsteins h^{-1} m^{-2} nm^{-1}). Values of $E_d(z,\lambda,t)$ and $E_s(z,\lambda,t)$ at the sea surface are given by:

$$E_d(z = 0\ m,\lambda,t) = I_d(\lambda,t)$$

$$E_s(z = 0\ m,\lambda,t) = I_s(\lambda,t).$$

Values for $E_d(z,\lambda,t)$ and $E_s(z,\lambda,t)$ at depths consistent with the grid points in the model are obtained by numerical integration:

$$E_d(z,\lambda,t) = E_d(z - \Delta z,\lambda,t)e^{-K_d(z,\lambda,t)\Delta z} \tag{50}$$

$$E_s(z,\lambda,t) = E_s(z - \Delta z,\lambda,t)e^{-K_s(z,\lambda,t)\Delta z}, \tag{51}$$

where Δz is the depth increment between grid points. The equations use wavelength-dependent attenuation coefficients for direct, $K_d(z,\lambda,t)$, and diffuse, $K_s(z,\lambda,t)$, submarine irradiance. These attenuation coefficients are calculated as:

$$K_d(z,\lambda,t) = \frac{a(z,\lambda,t) + b_b(z,\lambda,t)}{cos(\theta_z(t))} \tag{52}$$

$$K_s(z,\lambda,t) = \frac{a(z,\lambda,t) + b_b(z,\lambda,t)}{\overline{\mu}}, \tag{53}$$

where the parameters affecting the values of $K_d(z,\lambda,t)$ and $K_s(z,\lambda,t)$ are defined in Table 9. The backscattering coefficient, $b_b(z,\lambda,t)$, is calculated following the approach given in Sathyendranath and Platt (1988).

As indicated by equations 52 and 53, both irradiance attenuation coefficients are affected by the volume absorption coefficient, $a(z,\lambda,t)$. This coefficient represents the three major groups of light absorbing substances: pure sea water, nonchlorophyllous particles and chlorophyllous particles. Thus, the wavelength-dependent absorption of light is given by:

$$a(z,\lambda,t) = a_w(\lambda) + P(z)a_p(\lambda) + Y(z)a_y(\lambda) + C_{lpp}(z,t)a_{lpp}(\lambda) + C_{spp}(z,t)a_{spp}(\lambda), \quad (54)$$

where the terms in equation 54 are defined in Table 10. The form of equation 54 is a modified version of the absorption coefficient given in Prieur and Sathyendranath (1981). For the CTZ, the absorption due to Gelbstoff and nonchlorophyllous particles was neglected due to low freshwater runoff from the coast in the CTZ. Hence, $P(z)$ and $Y(Z)$ in equation 54 are zero.

The absorption spectra for the large and small phytoplankton were obtained using the *in vivo* weight-specific absorption coefficients, $a_i'(\lambda)$, characteristic of the major pigment types associated with the two phytoplankton size class. The wavelength dependence of these weight-specific absorption spectra are shown in Figure 16A. Thus, attenuation coefficients for each phytoplankton size class can be obtained by summing the appropriate number of absorption spectra as:

Table 9. Definitions of the Parameters in the Relationships for Calculating Diffuse and Direct Attenuation Coefficients.

Coefficient	Definition
$a(z, \lambda, t)$	Total Volume Absorption Coefficient
$b_b(z, \lambda, t)$	Backscattering Coefficient
θ	Sun Zenith Angle in Water
$\overline{\mu}$	Mean Cosine for Perfectly Diffuse Skylight After Refraction at a Flat Sea Surface

Table 10. Definition and Units of Coefficients Used in the Relationship for the Total Volume Absorption Coefficient.

Coefficient	Definition	Units
$a_w(\lambda)$	Specific Absorption Coefficient for Pure Sea Water	m^{-1}
$a_p(\lambda)$	Weight-Specific Absorption Coefficient for Nonchlorophyllous Particles	$mg^{-1}\ m^2$
$a_y(\lambda)$	Weight-Specific Absorption Coefficient for Dissolved Organic Matter (Gelbstoff)	$mg^{-1}\ m^2$
$a_{lpp}(\lambda)$	*in vivo* Weight-Specific Absorption for the Large Phytoplankton	mg Chl $a^{-1}\ m^2$
$a_{spp}(\lambda)$	*in vivo* Weight-Specific Absorption for the Small Phytoplankton	mg Chl $a^{-1}\ m^2$
$P(z)$	Concentration of Nonchlorophyllous Particles	$mg\ m^{-3}$
$Y(z)$	Concentration of Dissolved Organic Matter (Gelbstoff)	$mg\ m^{-3}$
$C_{lpp}(z,t)$	Chlorophyll Concentration for the Large Phytoplankton	mg Chl $a\ m^{-3}$
$C_{spp}(z,t)$	Chlorophyll Concentration for the Small Phytoplankton	mg Chl $a\ m^{-3}$

$$a_{lpp}(\lambda) = \sum_{i=1}^{n_{lpp}} \Gamma_i^{lpp} a_i^l(\lambda) \tag{55}$$

$$a_{spp}(\lambda) = \sum_{i=1}^{n_{spp}} \Gamma_i^{spp} a_i^l(\lambda), \tag{56}$$

where, Γ_i^{lpp} and Γ_i^{spp} are the pigment to chlorophyll a ratios for the large phytoplankton and small phytoplankton size fractions, respectively. The pigment to chlorophyll a ratios for each pigment and for each phytoplankton size fraction are given in Table 11. These values are based upon data sets presented in Jeffrey (1980), Stauber and Jeffrey (1988), Smith et al. (1989) and Bidigare et al. (1987). The resulting reconstructed *in vivo* weight-specific absorption spectra for both the large and small phytoplankton size fractions are shown in Fig. 16B.

Once values for the wavelength-dependent direct and diffuse light are known, the photosynthetically available radiance (PAR) (Einsteins m^{-2} s^{-1}) can be calculated by summing over the photosynthetically important wavelengths as:

$$PAR(z,t) = \int_{400nm}^{700nm} [E_d(z,\lambda,t) + E_s(z,\lambda,t)]d\lambda \tag{57}$$

.

The distribution of PAR with depth and wavelength calculated from equation 57 using values appropriate for the CTZ is shown in Figure 17. Increased attenuation occurs at wavelengths where the attenuation coefficients are maximum due to the combined effects of attenuation by sea water and chlorophyll. Strong attenuation is observed at about 450 nm, which coincides with a peak in the chlorophyll absorption spectra. Finally, the photosynthetically absorbed radiance for the large

Figure 16. Wavelength-dependent **A**) specific absorption coefficients, $a_i^*(\lambda)$ (m^2 mg^{-1}), which were used to construct the phytoplankton absorption spectra for the two phytoplankton size fractions and **B**) reconstructed *in vivo* weight-specific absorption spectra for both the large and small phytoplankton size fractions. Data obtained from Bidigare, et al. (1990)

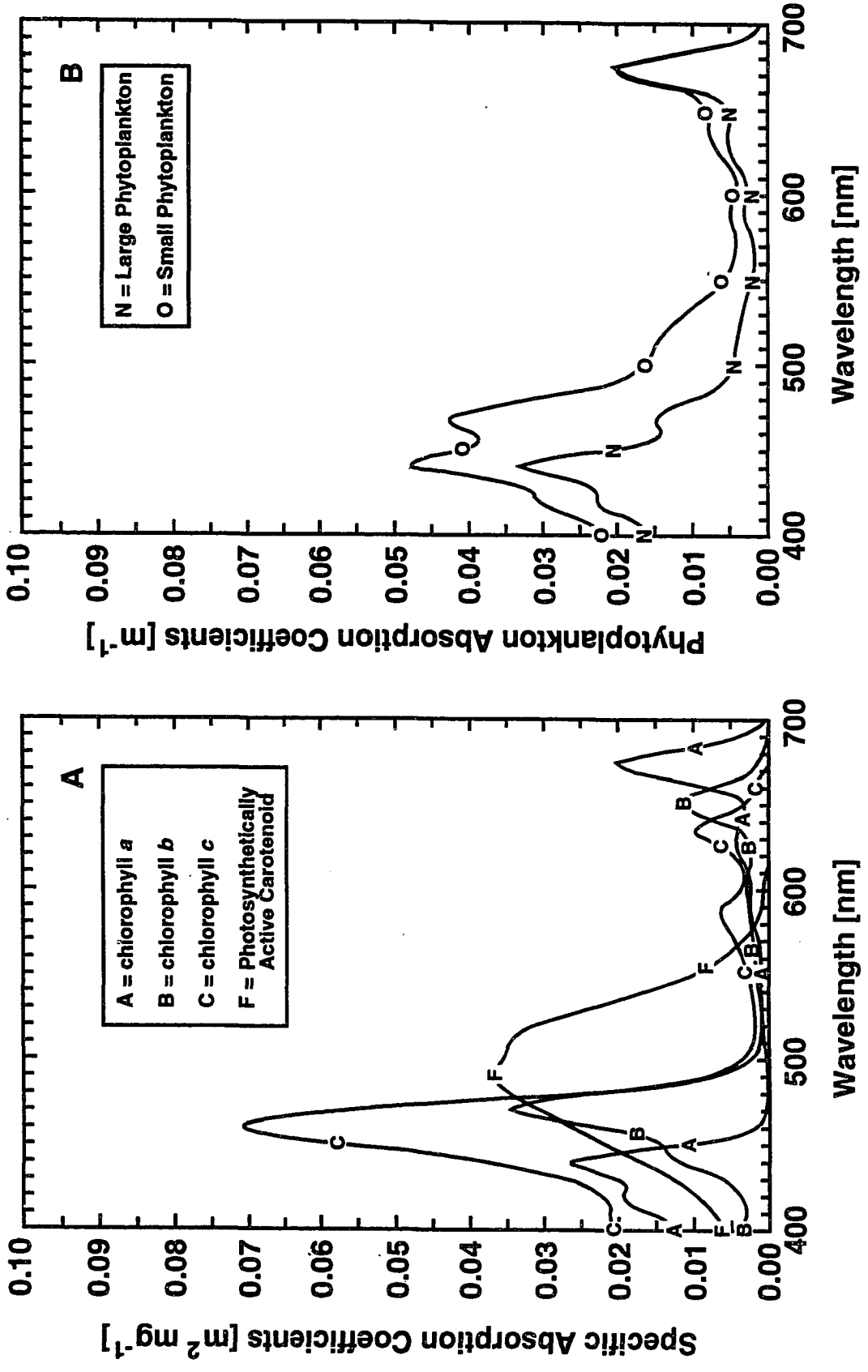

Table 11. Pigments and Pigment to Chlorophyll *a* Ratios Used for Reconstructing the *in vivo* Absorption Spectra for the Large and Small Phytoplankton.

Large Phytoplankton		Small Phytoplankton	
Pigment	Ratio	Pigment	Ratio
Chlorophyll *a*	1.00	Chlorophyll *a*	1.00
Chlorophyll *b*	0.18	Chlorophyll *b*	0.41
Chlorophyll *c*	0.09	Chlorophyll *c*	0.27
PSC*	0.10	PSC*	0.40

* PSC = Photosynthetically Active Carotenoids

($PHAR_{lpp}(z,t)$) and small ($PHAR_{spp}(z,t)$) phytoplankton size fractions (Einsteins m^{-3} s^{-1}) are calculated, using the Smith et al. (1989) formulation which has been slightly modified to include the effects of changing solar zenith angles ($\theta_z(t)$) and the mean cosine for the diffuse subsurface light ($\overline{\mu}$), as:

$$PHAR_{lpp}(z,t) = \int_{400nm}^{700nm} [[E_d(z,\lambda,t)\frac{C_{lpp}(z,t)a_{lpp}(\lambda)}{cos(\theta_z(t))}] + E_s(z,\lambda,t)\frac{C_{lpp}(z,t)a_{lpp}(\lambda)}{\overline{\mu}}]d\lambda \quad (58)$$

$$PHAR_{spp}(z,t) = \int_{400nm}^{700nm} [E_d(z,\lambda,t)\frac{C_{spp}(z,t)(z)a_{spp}(\lambda)}{cos(\theta_z(t))} + E_s(z,\lambda,t)\frac{C_{spp}(z,t)a_{spp}(\lambda)}{\overline{\mu}}]d\lambda. \quad (59)$$

This quantity is used in the model only as a diagnostic tool to estimate the quantum yield with depth. It may also be used in conjunction with measured quantum yields, ϕ, to estimate primary production (Smith et al., 1989). However, because this method does not allow for photoinhibition it was not used in the model.

3.1.5 Model Implementation

3.1.5.1 Numerical Integration

A spectral collocation, method was used to solve the system of equations that define the physical-bio-optical model. This provides consistency with the approach used to obtain solutions to the circulation model (Haidvogel et al., 1991a) that provided input to this model. A sigma coordinate transformation of the form

Figure 17. The downwelling irradiance spectra at several depths calculated from equation 49 using parameter values characteristic of the CTZ and a constant chlorophyll *a* concentration of 7 mg Chl *a* m^{-3}. The spectra correspond to local apparent noon. Depth values correspond to vertical node locations in the model.

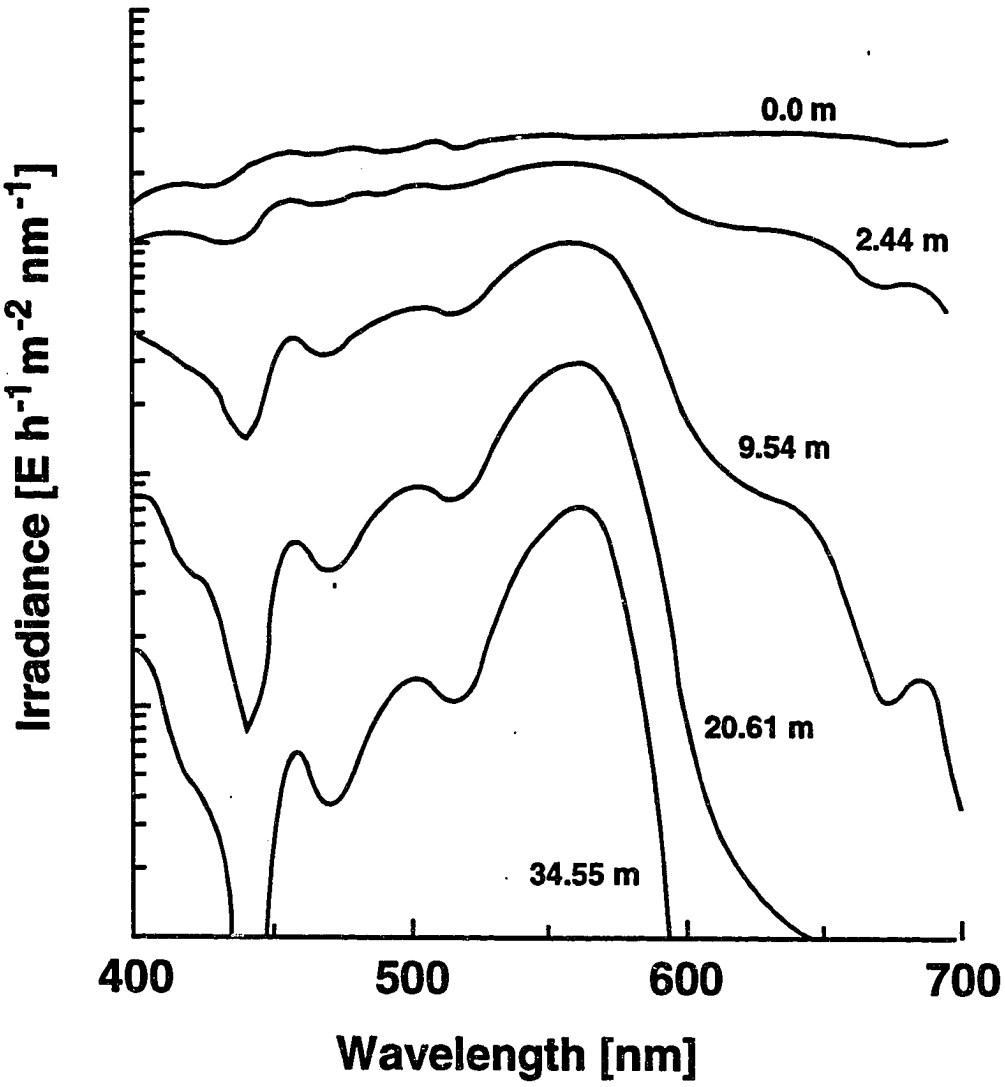

$$\sigma = 1 + 2\left(\frac{z}{h}\right), \tag{60}$$

was made for the vertical coordinate. This allows the vertical (σ) dependence of the model components to be represented as an expansion of a modified, finite Chebyshev polynomial basis set, $P_k(\sigma)$,:

$$B(\sigma) = \sum_{k=0}^{N} P_k(\sigma)\hat{b}_k, \tag{61}$$

where the modified Chebyshev polynomials are defined as:

$$P_k(\sigma) = \begin{cases} T_0(\sigma) & k = 0 \\ T_k(\sigma) & k \geq 1, k \text{ odd} \\ T_k(\sigma) + \frac{1}{k^2-1} & k \geq 2, k \text{ even}, \end{cases} \tag{62}$$

where

$$T_k(\sigma) = cos[k\ cos^{-1}(\sigma)] \tag{63}$$

are the Chebyshev polynomials. The collocation method explicitly solves for the variables at actual collocation points, σ_n. The collocation points are chosen to correspond to the location of the extrema of the highest order polynomial. The values of the model variables at the collocation points, B_n, can be defined as,

$$B_n = B(\sigma_n) = \sum_{k=0}^{N} P_k(\sigma_n)\hat{b}_k, \quad 0 \leq n \leq N. \tag{64}$$

A more complete description of this spectral technique can be found in Haidvogel et al. (1991). The time integration of the model is started with an initial forward time step using an Euler approximation:

$$\frac{B(t+\Delta t)-B(t)}{\Delta t} = F(t), \tag{65}$$

which is accurate to $O(\Delta t)$. After this, the model is integrated forward through time using a leapfrog technique:

$$\frac{B(t+\Delta t)-B(t-\Delta t)}{2\Delta t} = F(t), \tag{66}$$

which is accurate to $O(\Delta t^2)$. A trapezoidal correction step:

$$\frac{B(t+\Delta t)-B(t)}{\Delta t} = \frac{1}{2}[F(t)+F^*(t+\Delta t)], \tag{67}$$

was taken every n^{th} timestep to avoid mode splitting, where $F^*(t+\Delta t)$ represents the terms on the right side of equation 1 calculated from an initial guess using a leapfrog approximation. Hedström (1990) presents a complete description of this time stepping technique.

3.1.5.2 Initial Conditions — One-Dimensional Model Simulations

The initial nutrient and biological distributions were obtained from measured distributions of phytoplankton and nutrients from various regions (coastal, oceanic and filament) in the CTZ (Fig. 18). The regions were chosen based upon the water mass source definitions (Table 12) given by Strub et al. (1991). For simplicity, the vertical velocities of both the fluid and the biological constituents were assumed to be zero in these simulations. The effect of the vertical velocities on the model results will be shown in the results from the sensitivity analysis.

The vertical and time-dependent model was used to investigate the physical-bio-optical interactions that occur at specific locations (coastal, filament and

oceanic) within the CTZ. Comparison of the results obtained from these simulations provided insight into the mechanisms controlling the temporal and spatial development of the plankton populations within the CTZ. The model is also used as a validation of the parameterization of the biological source and sink terms in the CTZ. With this in mind, the model has served as a testing stage in the development of the three-dimensional, time-dependent model, which is described below.

The initial conditions for the temperature, silicate and nitrate fields were obtained by linearly interpolating the vertical profiles collected during the 1988 CTZ field surveys (Huyer et al., 1991; Chavez, et al., 1991; Kosro, et al., 1991) onto the vertical grid used in the model. Ammonia and detritus initial concentrations were set to zero. Vertical distributions of the large and small phytoplankton size fractions were initialized by interpolating chlorophyll *a* vertical profiles collected during the 1988 CTZ field surveys onto the model grid. The chlorophyll *a* concentrations were apportioned into large and small phytoplankton size fractions by using the size fractionation data from Chavez et al. (1991). The copepod, doliolid and euphausiid initial conditions were obtained from zooplankton biomass data from the 1988 CTZ field surveys (Mackas et al., 1991).

3.1.5.3 Lagrangian Drifter Experiment

A simulated Lagrangian drifter experiment was carried out in order to determine the time-dependent development and fate of the biological constituents entrained in filaments generated in the CTZ. The model was initialized with data collected from stations sampled while following a Lagrangian drifter in the CTZ study area in 1988. The vertical advective velocities at the bottom of the model

Figure 18. Location of the coastal (A1, medium spot), filament (A10, dark spot) and oceanic (E2, light spot) stations from which data were obtained to initialize the one-dimensional physical-bio-optical model. The lines indicate the standardized grid that was sued for the 1988 CTZ field studies. The filled squares indicate station locations. Figure adapted from Huyer et al. (1991).

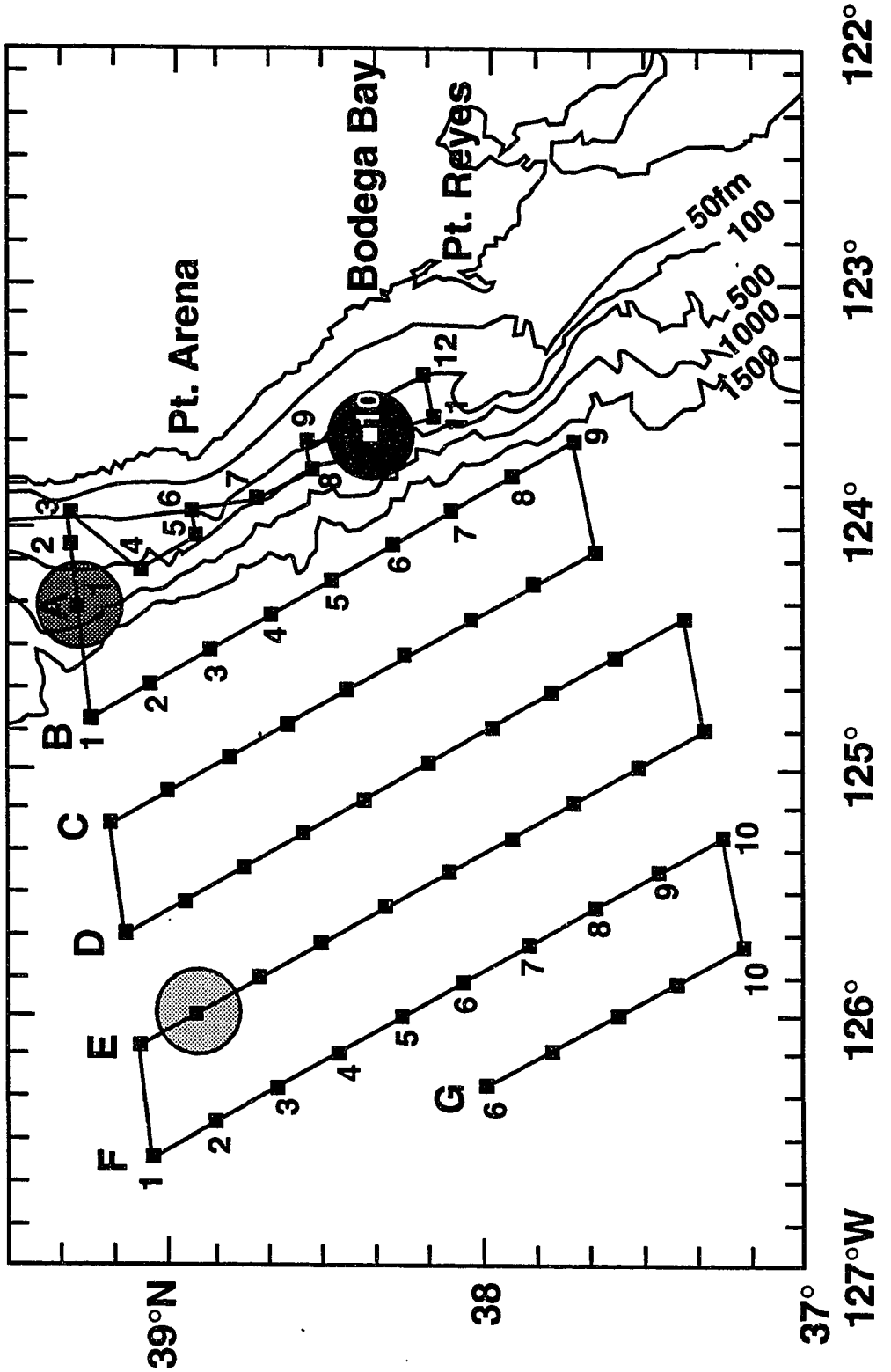

Table 12. Water Mass Source Definitions*

	Station Sources					
	Station	T, °C	S, psu	NO_3 μM	PO_4 μM	SiO_4 μM
Inshore	117	10.3	33.3	12.00	1.40	8.93
Jet	115	12.5	32.6	0.01	0.50	2.15
Offshore	143	16.1	32.9	0.11	0.44	2.57

* Table obtained from Strub et al. 1991

were obtained from a simulated Lagrangian drifter. The chosen drifter was one of 880 simulated Lagrangian drifters which were generated by a regional primitive equation circulation model that has been configured to simulate circulation conditions in the CTZ (Fig. 19; Hofmann et al., 1991; Haidvogel et al. 1991*a*). The drifter was initially released in a region where an offshore-flowing filament was observed to form in the model. The path of the simulated Lagrangian drifter, after remapping to the actual drifter path, is shown in Figure 20A. The vertical velocities experienced by the simulated Lagrangian drifter was negative (downwelling) throughout the simulation (Fig. 20B) and therefore, the drifter was displaced vertically from its initial depth of 90 m to a final depth of $\approx$170 m (Fig. 20C). This deepening along the filament density front was observed to occur in the offshore-flowing portion of the filament during the 1988 CTZ field surveys (Washburn et al., 1991).

The model was integrated for 20 days. The resulting simulated chemical and biological distributions are compared to the data collected from stations sampled while following a Lagrangian drifter in the CTZ study area in 1988. As a comparison, a second simulation was performed with the same initial conditions; however, for this case the vertical advection was set to zero throughout the 20-day integration.

Figure 19. The CTZ study region. The region included in the CTZ circulation domain is indicated by the box. Within this domain, the release points for the Lagrangian drifter experiments are indicated by crosses. The dots indicate the stations at which nutrient, phytoplankton and zooplankton measurements were made during the 1988 CTZ field sampling period. These stations follow along the track of a drifter that was deployed in an offshore-flowing filament. The dashed line represents the actual coastal topography; the solid line represents the idealized coastal topography used in the circulation model.

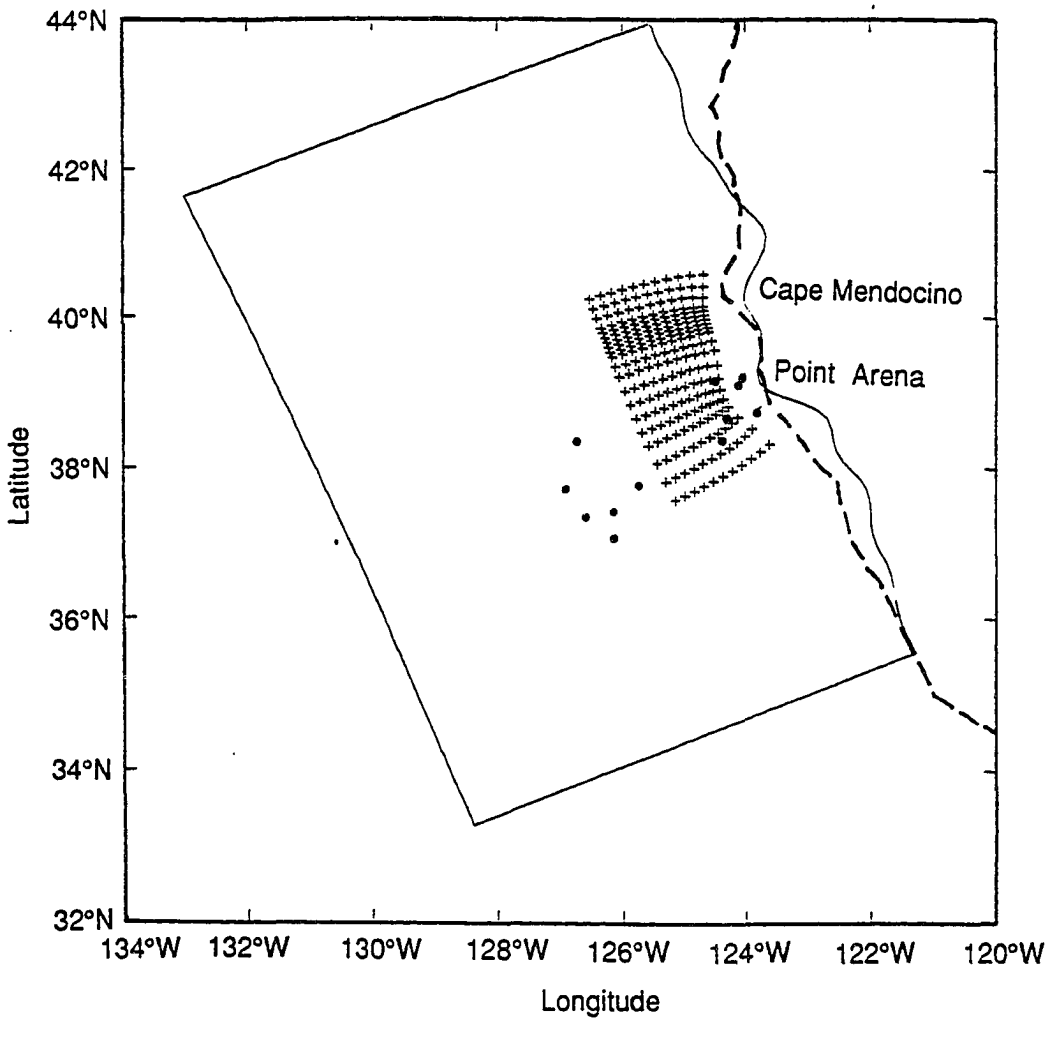

Figure 20. (**A**) The trajectory followed by the simulated Lagrangian drifter released near the region of the start of the actual drifter track. The dots indicate the stations at which nutrient, phytoplankton and zooplankton measurements were made during the 1988 CTZ field sampling period. (**B**) The vertical displacement of the simulated Lagrangian drifter over time. (**C**) The vertical velocity (m s^{-1}) experienced by the simulated Lagrangian drifter as it was advected offshore of the model domain.

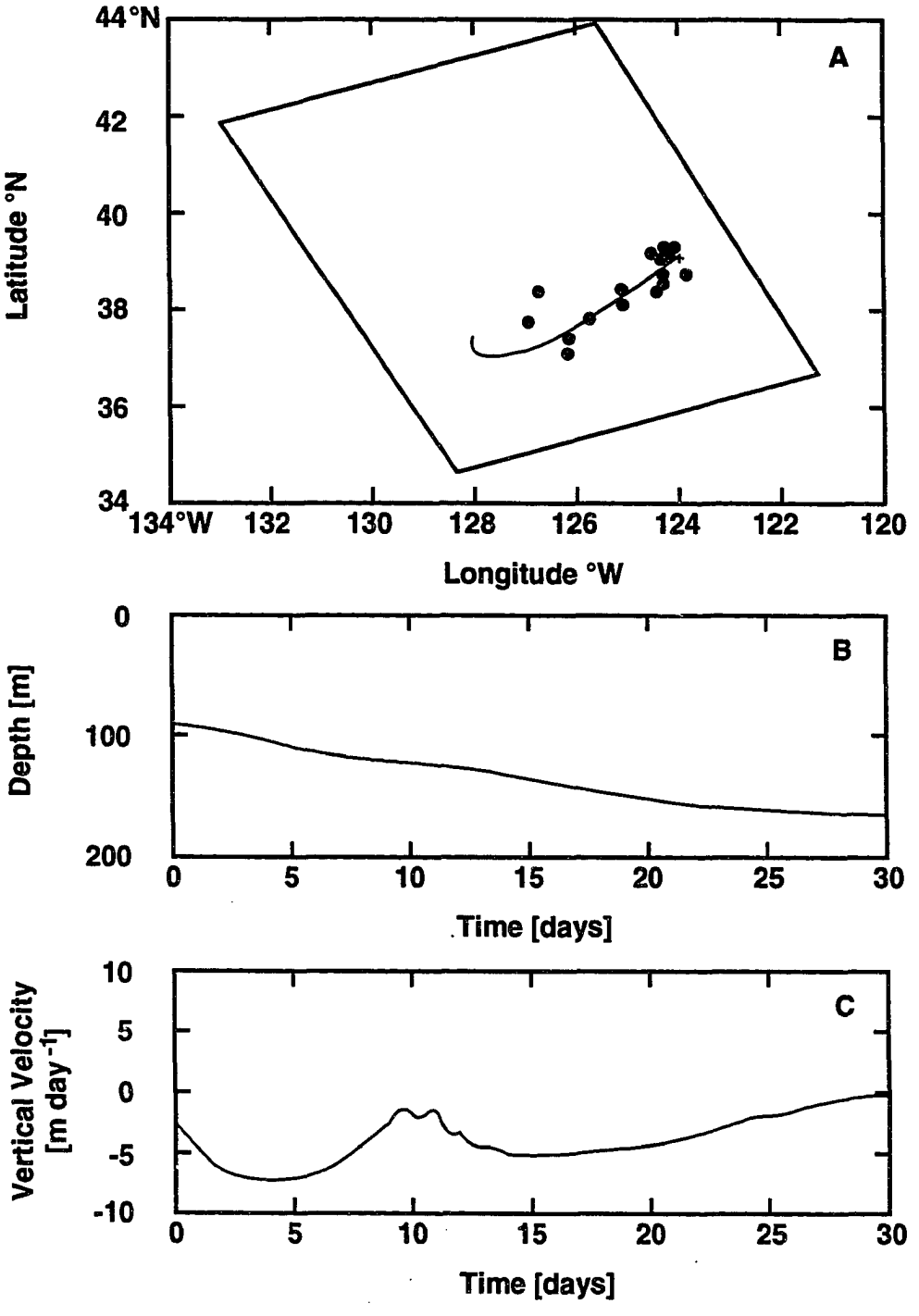

3.2 Three-Dimensional Physical-Bio-Optical Model

3.2.1 Model Equations

The second model developed was a three-dimensional, time-dependent, physical-bio-optical model. The physical portion includes the effects of vertical (biological and physical) and horizontal velocity and vertical and horizontal diffusion. The biological portion of the model consists of the nine-component food web (cf. Fig. 7) presented in section 3.1. The model, therefore, is a system of nine coupled partial differential equations that govern the vertical and time distribution of a non-conservative quantity, which is of the form;

$$\frac{\partial B}{\partial t} + (\vec{v} + \vec{v}_{biology}) \cdot \nabla B - K\nabla^2 B = S, \tag{68}$$

where B is a non-conservative quantity (one of the nine components in the biological model), $\vec{v}$ is the velocity of the fluid, $\vec{v}_{biology}$ is the vertical sinking rate of the biological components. The vertical sinking rates for the large (1 m day^{-1}) and small (0.1 m day^{-1}) phytoplankton size fractions were estimated from Beinfang and Szyper (1982) and Smayda (1970). The velocity, $\vec{v}$, and the kinematic eddy diffusivity, K, were obtained as described below.

3.2.2 Velocity and Diffusion

The velocities, $\vec{v}$, and kinematic eddy diffusivities, K, which were used to advect and diffuse the biological distributions, were provided by the simulated circulation distributions obtained from the regional primitive equation model that was developed for to the CTZ region (Haidvogel et al., 1991). Because of this, the physical-bio-optical model uses a domain (cf. Fig. 1.) and grid (Fig. 21) that is

identical to that used for the regional circulation model. The physical dynamics that are included in the circulation model and the numerical solution techniques are presented by Haidvogel et al. (1991a and 1991b) and Hedström (1990). The governing equations which are used in this model are the hydrostatic primitive equations:

$$\frac{\partial u}{\partial t} + \vec{v} \cdot \nabla u - fv = -\frac{\partial \phi}{\partial x} + \mathcal{F}_u + \mathcal{D}_u \tag{69}$$

$$\frac{\partial v}{\partial t} + \vec{v} \cdot \nabla v + fu = -\frac{\partial \phi}{\partial y} + \mathcal{F}_v + \mathcal{D}_v \tag{70}$$

$$\frac{\partial T}{\partial t} + \vec{v} \cdot \nabla T = \mathcal{F}_T + \mathcal{D}_T \tag{71}$$

$$\frac{\partial S}{\partial t} + \vec{v} \cdot \nabla S = \mathcal{F}_S + \mathcal{D}_S \tag{72}$$

$$\frac{\partial \phi}{\partial z} = -\frac{\rho g}{\rho_o} \tag{73}$$

and

$$\frac{\partial u}{\partial x} + \frac{\partial v}{\partial y} + \frac{\partial w}{\partial z} = 0, \tag{74}$$

where the terms and parameters in equations 69-74 are defined in Table 13.

Equations 69 and 70 express the u, v momentum balances, respectively. The time evolution of the perturbation temperature, $T(x, y, z, t)$, and salinity, $S(x, y, z, t)$, fields, which govern the perturbation density, $\rho(x, y, z, t)$, are given by equations 71 and 72, respectively. The vertical momentum balance, equation 73, is obtained by using the Boussinesq approximation, where density variations are neglected in the momentum equations except for their contribution to the buoyancy forcing. Finally, equation 74 is the continuity equation for an incompressible fluid.

Table 13. Definition of Terms in the Hydrostatic Primitive Equations For the Three-Dimensional Model

Terms	Definition
(u, v, w)	(x, y, z) components of the velocity vector, $\vec{v}$
$\rho_o + \rho(x, y, z, t)$	total density
$T(x, y, z, t)$	total temperature
$S(x, y, z, t)$	total salinity
$\phi(x, y, z, t)$	dynamic pressure, (ρ/ρ_o)
$f(x, y)$	Coriolis parameter
g	acceleration of gravity
$(\mathcal{F}_u, \mathcal{F}_v, \mathcal{F}_T, \mathcal{F}_S)$	forcing terms
$(\mathcal{D}_u, \mathcal{D}_v, \mathcal{D}_T, \mathcal{D}_S)$	diffusive terms

Further description of these equations and their terms are presented in Hedström (1990).

3.2.3 Biological Components and Optics

The subsurface irradiance field and the phytoplankton, zooplankton and nutrient source/sink terms in the three-dimensional model were calculated using the same formulations developed for the one-dimensional model. However, these formulations were extended to three dimensions by allowing them to occur at all locations in the spatial fields.

3.2.4 Model Implementation

The three-dimensional time-dependent physical-bio-optical model was initialized using the resulting circulation and density field from day 140 of the SPEM simulation (Haidvogel et al. 1991*a*) and integrated foward in time for 20 days. During this time period, a filament was observed to form at the coastal bump and propagate offshore.

The three-dimensional time-dependent physical-bio-optical model was used to investigate the temporal and spatial development of nutrient and plankton distributions within the CTZ. Specifically, the model attempts to simulate the spatial and temporal evolution of the subsurface chlorophyll maximum. Model simulations are compared to the data gathered during the 1988 CTZ surveys. These results are used to provide estimates of the time and space scales, and the magnitude and variability of the across-shore transport of nutrients and carbon within the CTZ.

Figure 21. The orthogonal curvilinear grid (129 x 81 points) used for the three-dimensional numerical model. The domain is 1000 km wide (along shelf) and 700 km wide (across-shore). The three solid wide lines indicate along-shelf sections that are extracted from the model to display selected vertical distributions.

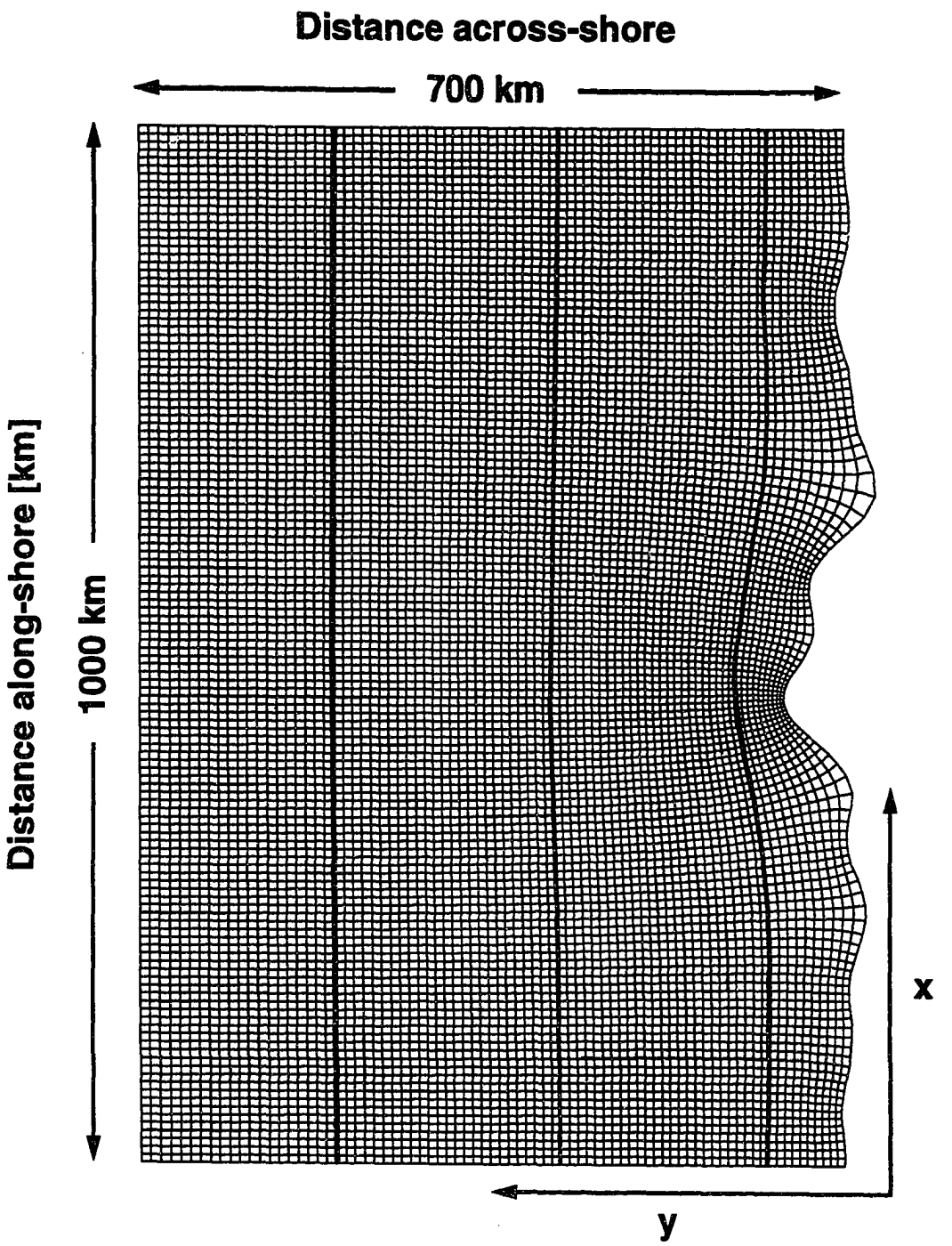

3.2.4.1 Numerical Integration

As in the one-dimensional model, a spectral collocation method was used to solve the time- and space-dependent system of equations. This provides consistency with the circulation model. The time stepping techniques are presented in Hedström (1990). The momentum, temperature and salinity fields were initialized with the velocity and density fields obtained from the regional circulation model of Haidvogel et al. (1991a) at a time when a filament was beginning to form. The model was integrated forward in time for 20 days to coincide with the generation time of a filament (Kosro and Huyer, 1986).

3.2.4.2 Initial Conditions — Three-Dimensional Model Simulations

The initial conditions for the three-dimensional model were determined from relationships derived from the CTZ field observations (Strub et al., 1991). Initial velocity, salinity, temperature and density fields were obtained from the circulation simulations presented in Haidvogel et al. (1991*a*). The salinity and temperature fields were derived using the standard equation of state relationship. In order to decrease the number of calculations, the salinity field within the physical model was replaced with the actual density values. An example simulated vertical velocity and density distribution at 100 m from day 140 obtained from the circulation model is shown in Fig. 22. The full three-dimensional fields from day 140 were used as initial conditions. The initial temperature field at 100 m obtained from the simulated density fields and the temperature to density relationship for the CTZ is shown in Fig. 23.

Initial distribution for the large and small phytoplankton fractions (Fig. 24 and Fig. 25, respectively) were obtained using the chlorophyll *a* to percent size

Figure 22. Horizontal distribution of the initial vertical velocity (color, m day^{-1}) and density (line contours; σ_t) at 100 m derived from simulated circulation fields obtained for the CTZ by Haidvogel et al. (1991*a*). Line contours for density range from 23.6 to 25.4 by intervals of 0.25. Upwelling and downwelling velocities with magnitudes greater than 9.5 m day^{-1} are shown in dark red and dark blue, respectively.

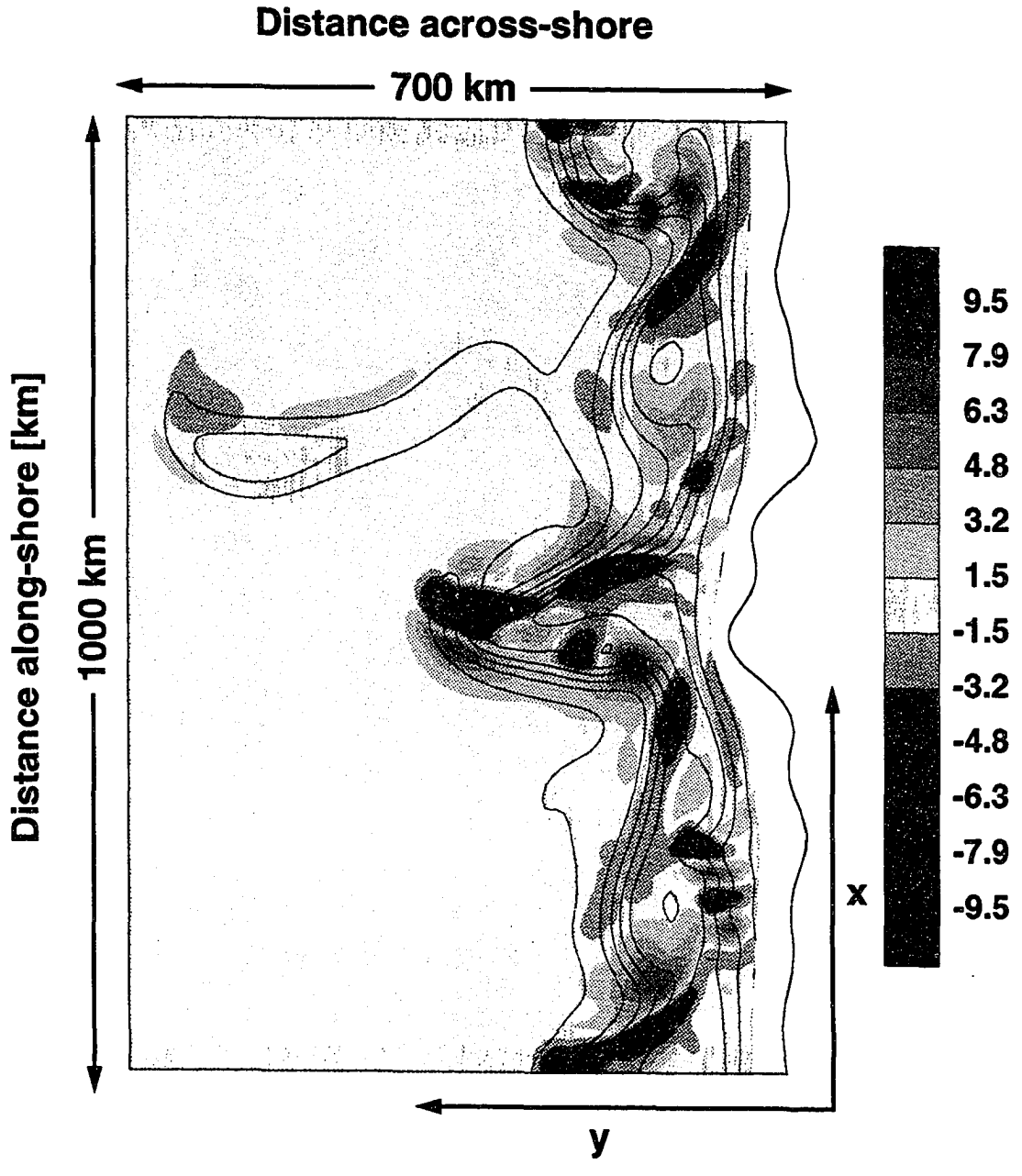

Figure 23. Horizontal distribution of the initial temperature (color, °C) and density (line contours; σ_t) at the surface derived from simulated circulation fields obtained for the CTZ by Haidvogel et al. (1991*a*). Line contours for density range from 22.75 to 25 by intervals of 0.25. Regions with temperatures greater than 21°C or lower than 10°C are shown in dark red and dark blue, respectively.

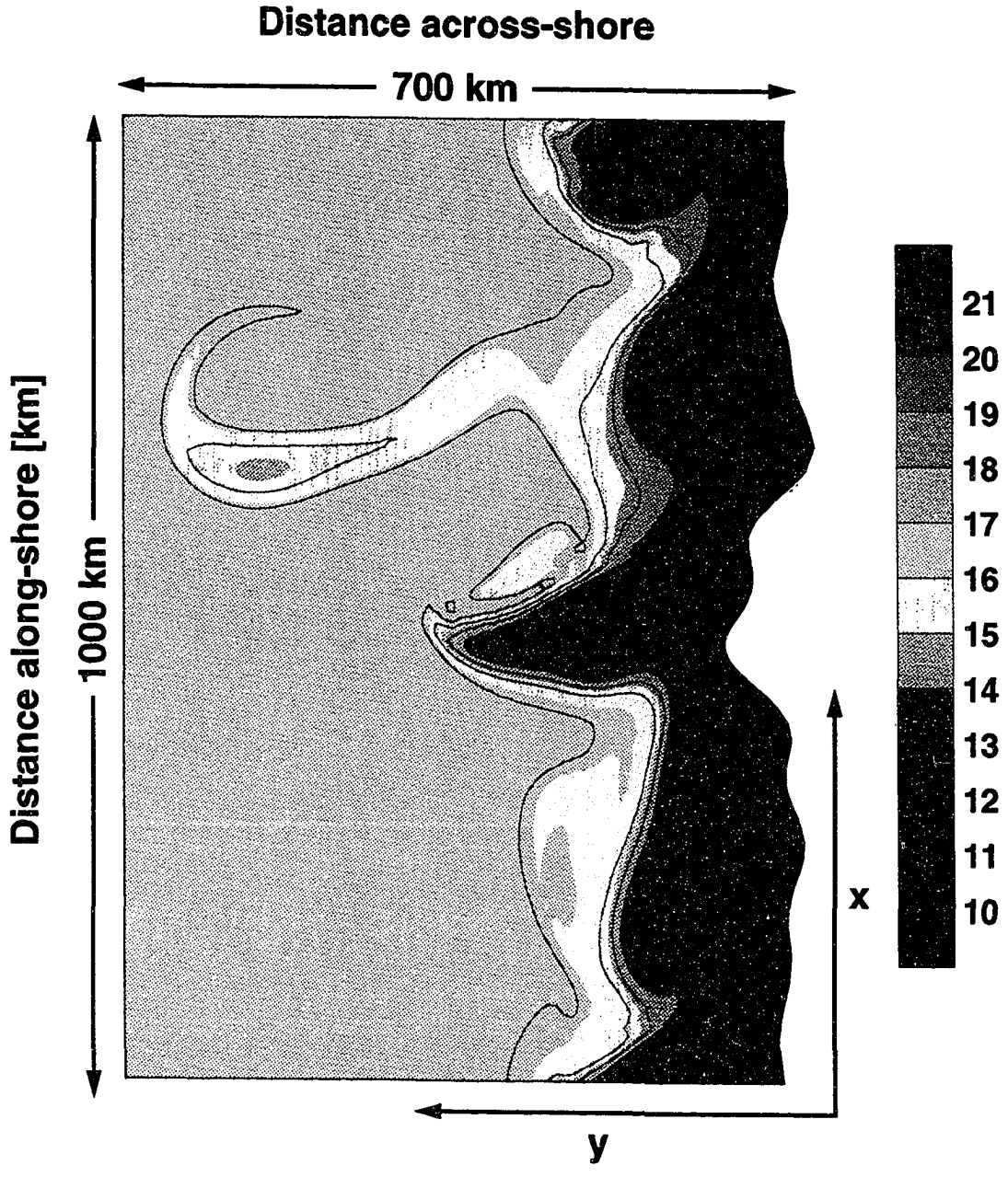

fractionation relationship and the chlorophyll *a* to dynamic height ($\phi_{0/500}$ m^2 s^{-2}) relationship, both from Chavez et al. (1991). Initial distributions for the copepod, euphausiid and doliolid fields (Fig. 26, Fig. 27 and Fig. 28, respectively) were calculated from a zooplankton biomass to dynamic height relationship obtained from observations for the CTZ (Mackas et al., 1991). The initial nitrate (Fig. 29) and silicate (Fig. 30) fields were obtained using the initial temperature field with the nutrient to temperature relationships obtained for the CTZ (Huyer et al., 1991). The initial ammonia and detritus fields were set to a constant value of zero.

Figure 24. Horizontal distribution of the initial large phytoplankton (color, mg N m^{-3}) and density (line contours; σ_t) at the surface derived from simulated circulation fields obtained for the CTZ by Haidvogel et al. (1991*a*) and relationships obtained from the CTZ by Chavez et al. (1991). Line contours for density range from 22.75 to 25 by intervals of 0.25. Color indicates the concentration of the large phytoplankton and ranges from 0 mg N m^{-3} (dark blue) to 88 mg N m^{-3} (dark red).

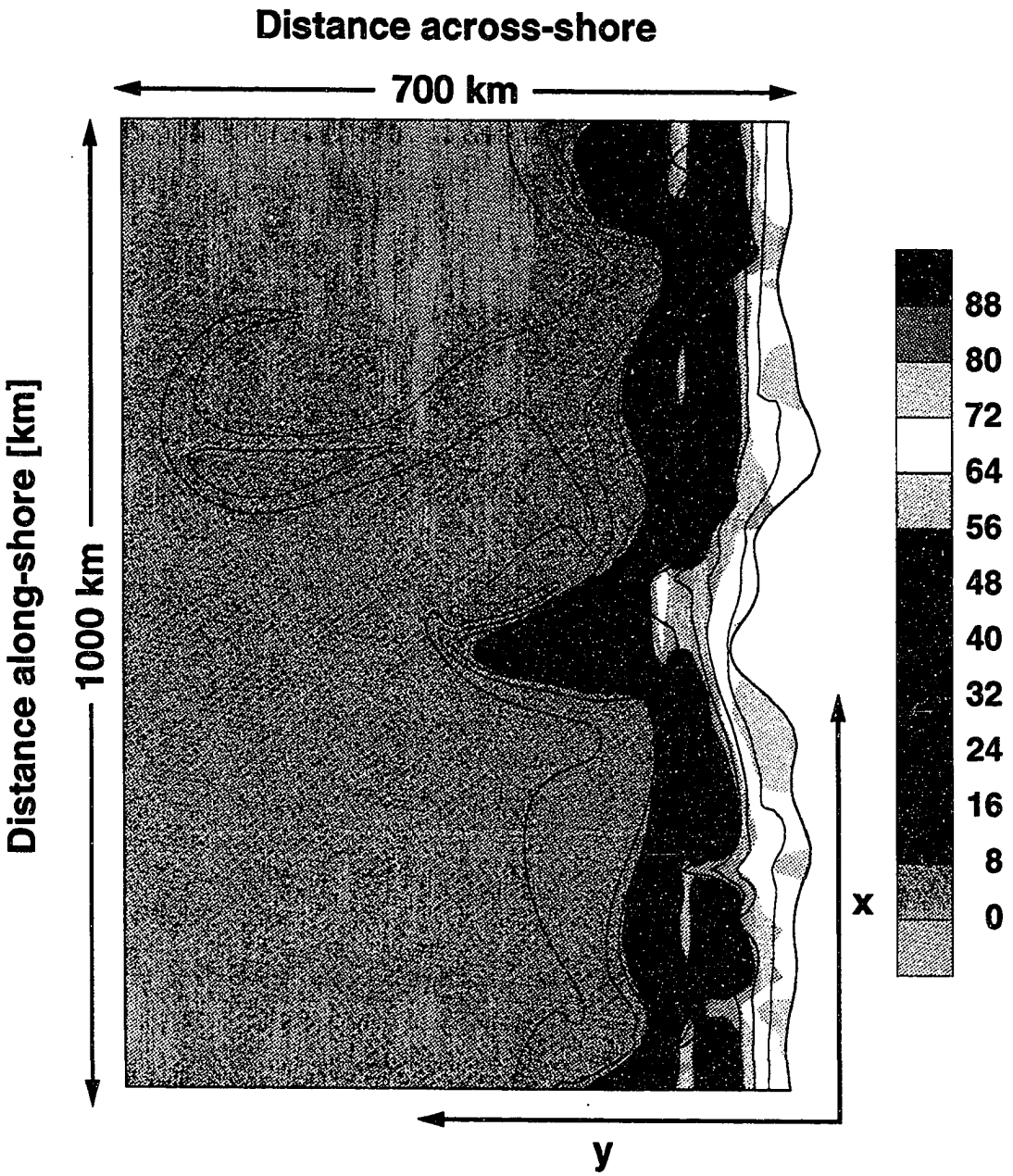

Figure 25. Horizontal distribution of the initial small phytoplankton concentration (color, mg N m^{-3}) and density (line contours; σ_t) at the surface derived from simulated circulation fields obtained for the CTZ by Haidvogel et al. (1991*a*) and relationships obtained from the CTZ by Chavez et al. (1991). Line contours for density range from 22.75 to 25 by intervals of 0.25. Color indicates the concentration of the small phytoplankton and ranges from 0 mg N m^{-3} (dark blue) to 88 mg N m^{-3} (dark red).

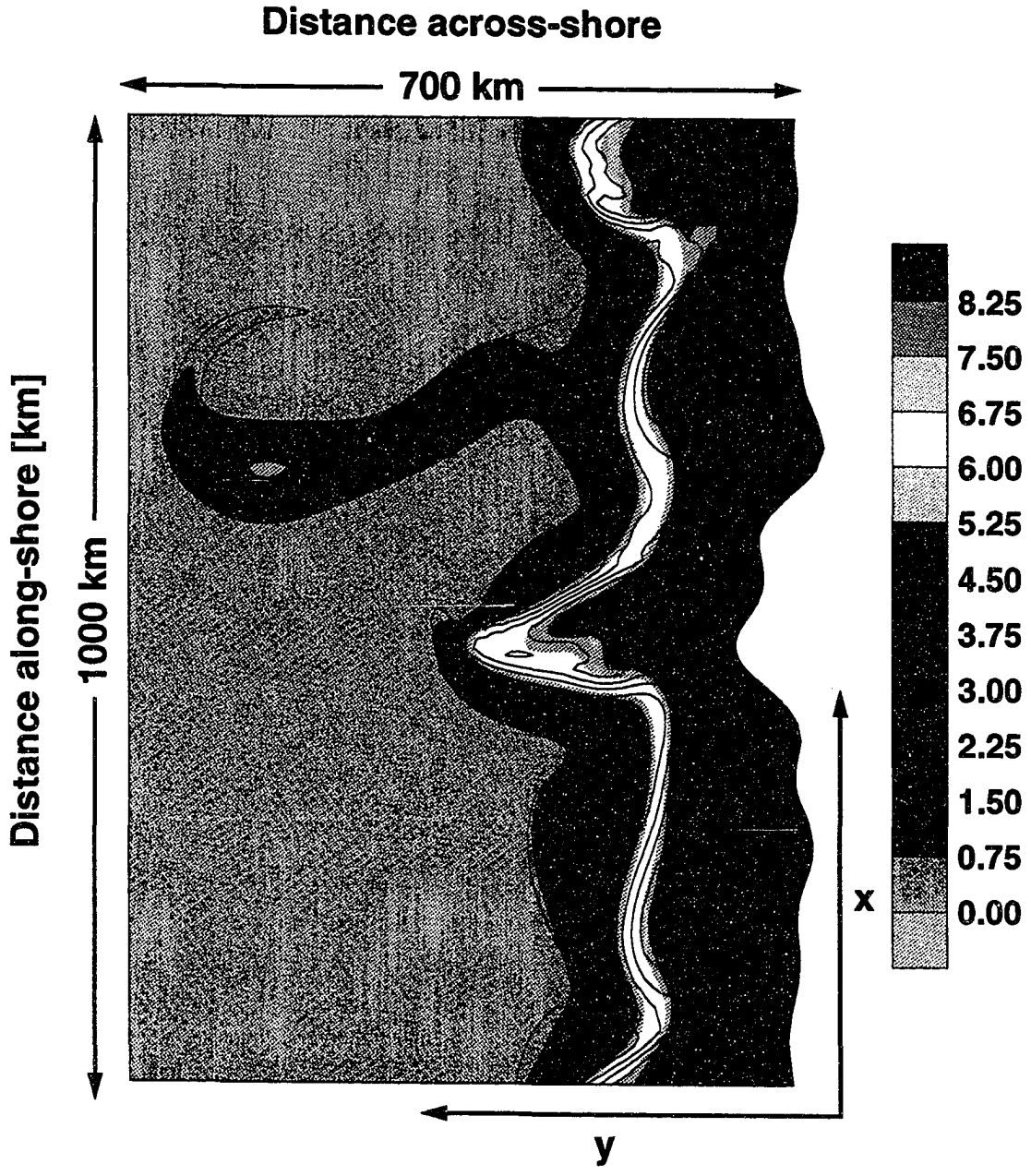

Figure 26. Horizontal distribution of the initial copepod concentration (color, mg N m^{-3}) and density (line contours; σ_t) at the surface derived from simulated circulation fields obtained for the CTZ by Haidvogel et al. (1991*a*) and relationships obtained from the CTZ by Mackas et al. (1991). Line contours for density range from 22.75 to 25 by intervals of 0.25. Color indicates the concentration of the copepods and ranges from 0 mg N m^{-3} (grey) to 2.2 mg N m^{-3} (dark red).

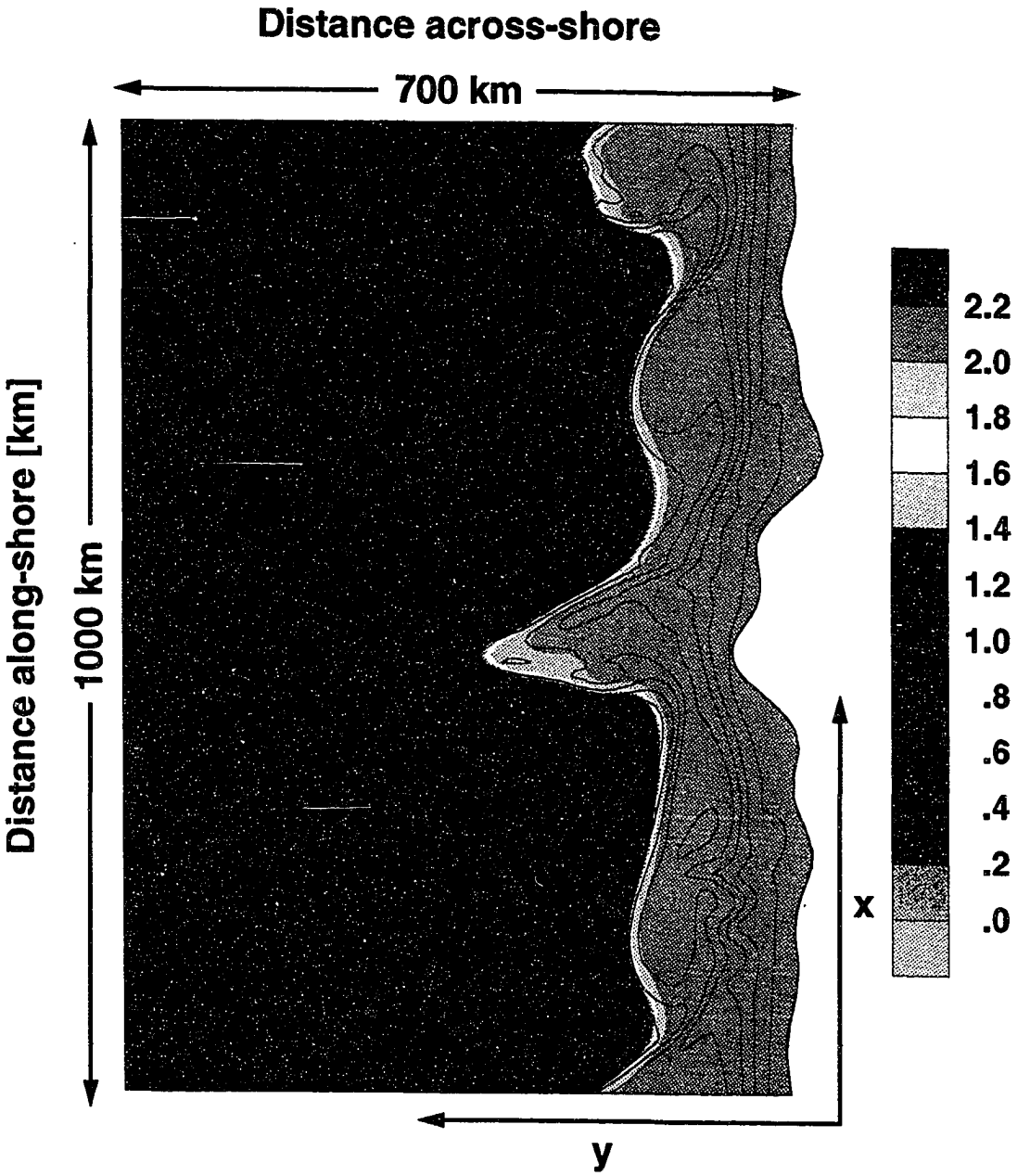

Figure 27. Horizontal distribution of the initial euphausiid concentration (color, mg N m^{-3}) and density (line contours; σ_t) at the surface derived from simulated circulation fields obtained for the CTZ by Haidvogel et al. (1991*a*) and relationships obtained from the CTZ by Mackas et al. (1991). Line contours for density range from 22.75 to 25 by intervals of 0.25. Color indicates the concentration of the euphausiids and ranges from 0 mg N m^{-3} (grey) to 2.2 mg N m^{-3} (dark red).

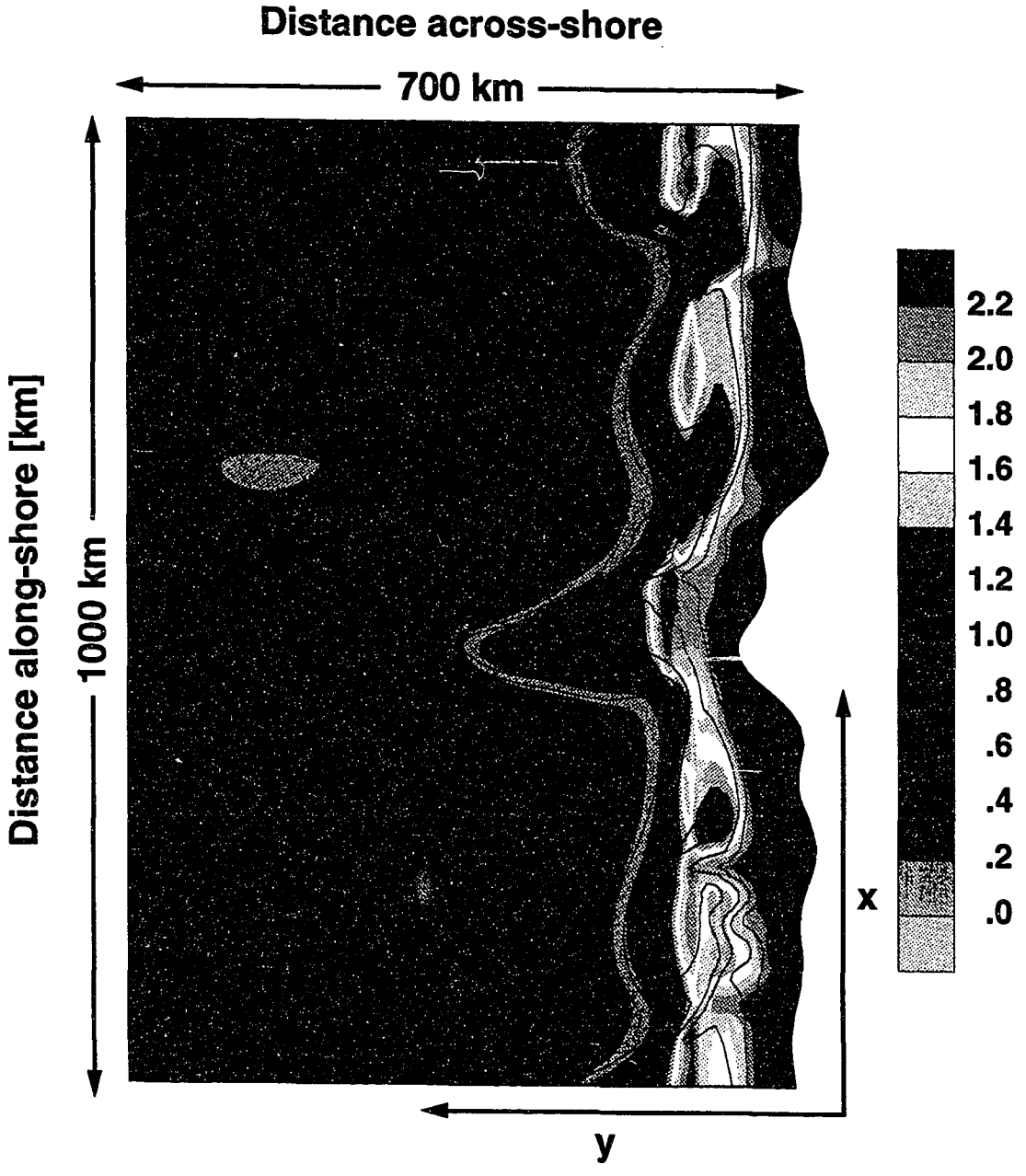

Figure 28. Horizontal distribution of the initial doliolid concentration (color, mg N m^{-3}) and density (line contours; σ_t) at the surface derived from simulated circulation fields obtained for the CTZ by Haidvogel et al. (1991*a*) and relationships obtained from the CTZ by Mackas et al. (1991). Line contours for density range from 22.75 to 25 by intervals of 0.25. Color indicates the concentration of the doliolids and ranges from 0 mg N m^{-3} (grey) to 2.2 mg N m^{-3} (dark red).

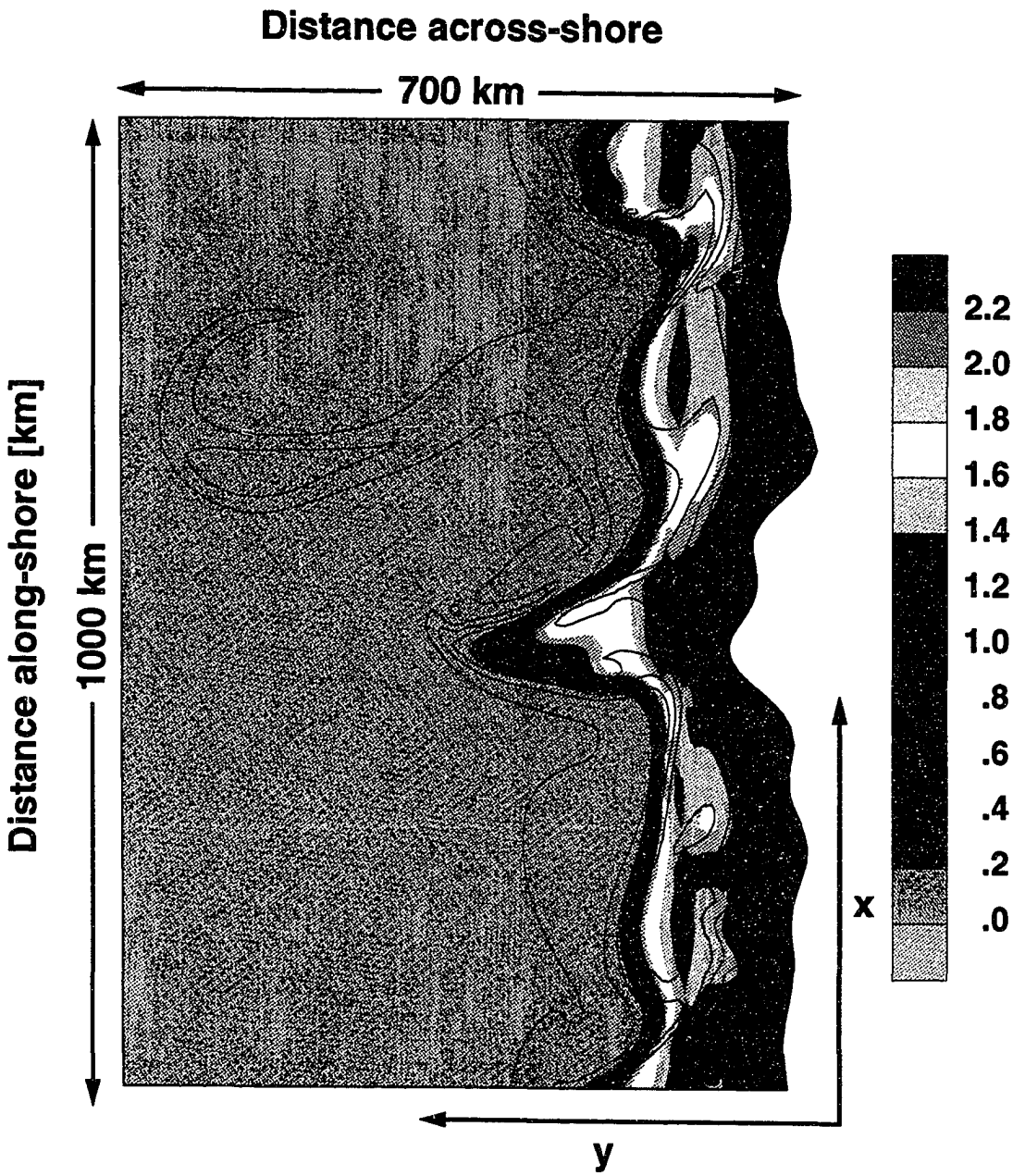

Figure 29. Horizontal distribution of the initial silicate concentration (color, mg SiO_4^- m^{-3}) and density (line contours; σ_t) at the surface derived from simulated circulation fields obtained for the CTZ by Haidvogel et al. (1991*a*) and relationships obtained from the available CTZ nutrient data. Line contours for density range from 22.75 to 25 by intervals of 0.25. Color indicates the silicate concentration and ranges from 0 mg SiO_4^- m^{-3} (grey) to 11 mg SiO_4^- m^{-3} (dark red).

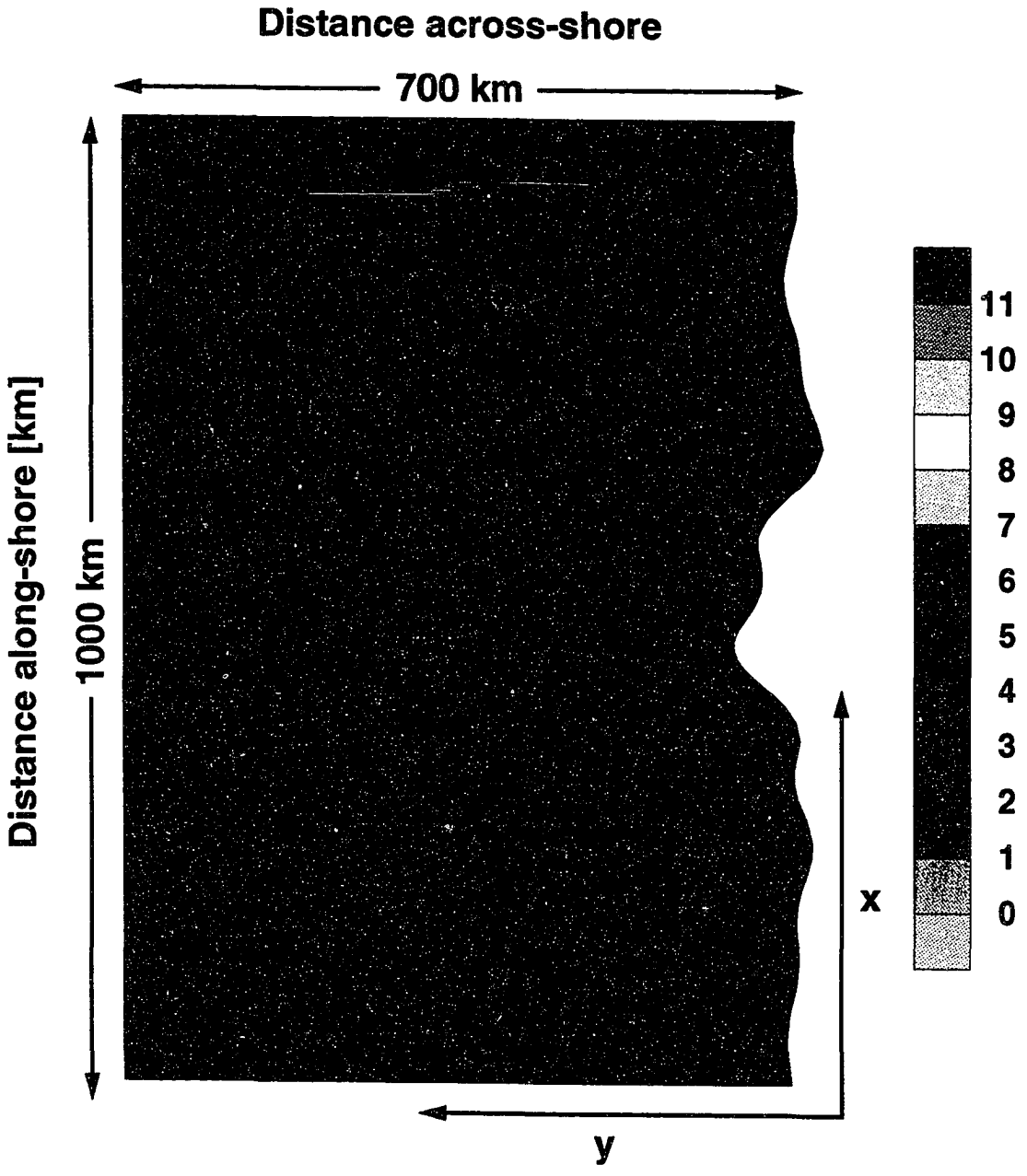

Figure 30. Horizontal distribution of the initial nitrate concentration (color, mg NO_3^- m^{-3}) and density (line contours; σ_t) at the surface derived from simulated circulation fields obtained for the CTZ by Haidvogel et al. (1991*a*) and relationships obtained from the available CTZ nutrient data. Line contours for density range from 22.75 to 25 by intervals of 0.25. Color indicates the nitrate concentration and ranges from 0 mg NO_3^- m^{-3} (grey) to 11 mg NO_3^- m^{-3} (dark red).

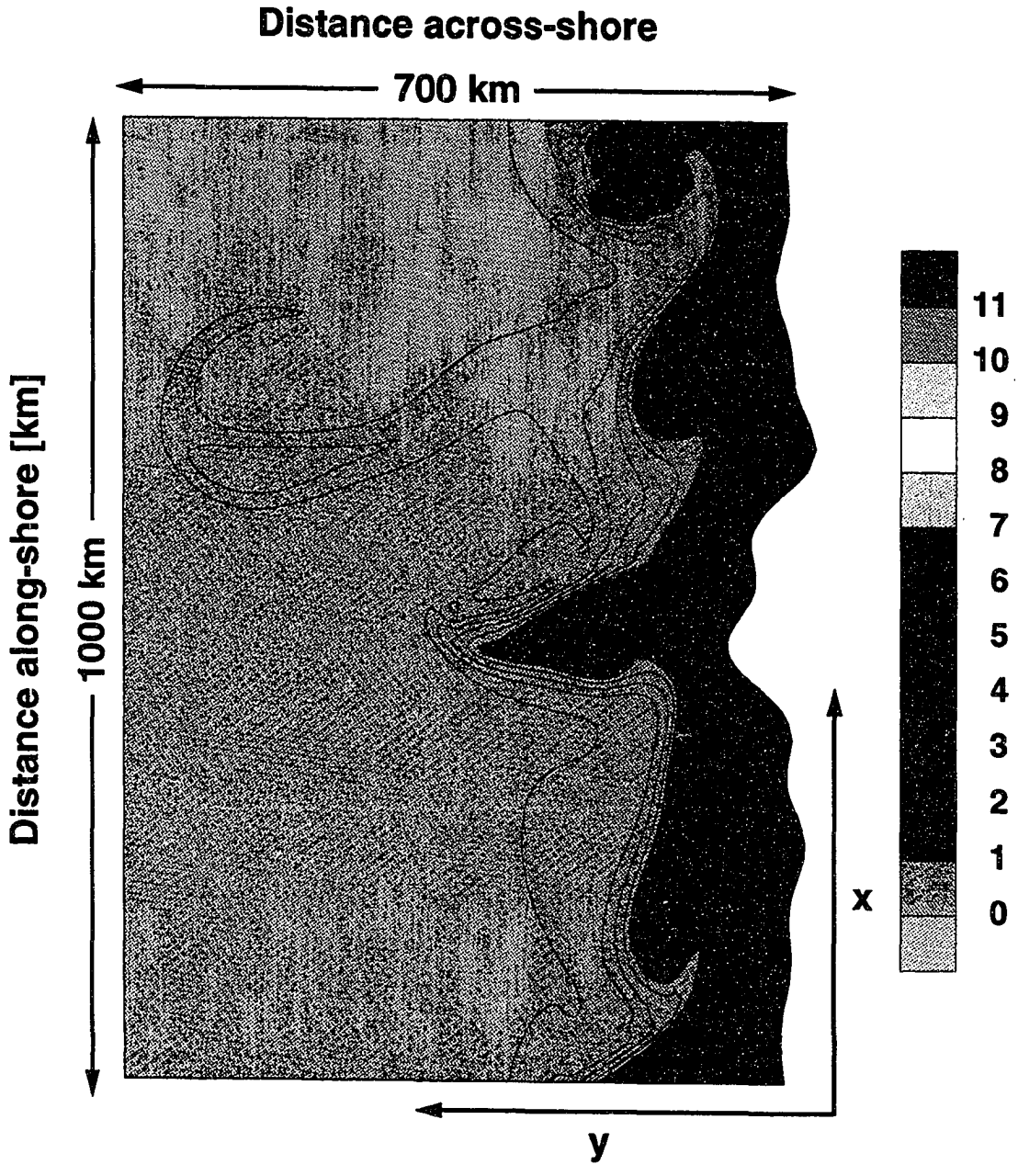

3.3 Lagrangian Tracer Experiments

Simulated Lagrangian floats, which serve as passive tracers, were released in the three-dimensional time-varying fields. The trajectories followed by these drifters were then calculated. The numerical technique used for determining the location of the Lagrangian floats at a given time is discussed in detail by Hedström (1990) and Hofmann et al. (1991). Briefly, the distance traveled by a simulated drifter in a time interval is calculated using a fourth-order Runge-Kutta scheme:

$$\vec{k}_1 = \Delta t \times \vec{v}(t, \vec{x}_n) \tag{75}$$

$$\vec{k}_2 = \Delta t \times \vec{v}(t + \frac{\Delta t}{2}, \vec{x}_n + \frac{\vec{k}_1}{2}) \tag{76}$$

$$\vec{k}_3 = \Delta t \times \vec{v}(t + \frac{\Delta t}{2}, \vec{x}_n + \frac{\vec{k}_2}{2}) \tag{77}$$

$$\vec{k}_4 = \Delta t \times \vec{v}(t + \Delta t, \vec{x}_n + \vec{k}_3) \tag{78}$$

$$\vec{x}_{n+1} = \vec{x}_n + \frac{\vec{k}_1}{6} + \frac{\vec{k}_2}{3} + \frac{\vec{k}_3}{3} + \frac{\vec{k}_4}{6} \tag{79}$$

where $\vec{x}_{n+1}$ represents the new location of a particle that is advected from its previous position $\vec{x}_n$ by the velocity $\vec{v}$ in a time interval Δt, and $\vec{k}_i$ represents the Runge-Kutta coefficients.

These tracers are capable of moving within the grid boxes, and so, the fluid velocities, $\vec{v}$, at points not represented by grid points are required for use in the Runga-Kutta scheme. The model obtains these velocities by using a horizontal, bicubic interpolation algorithm of the form:

$$\vec{v}(x_f, y_f) = \sum_{i=1,4} \sum_{j=1,4} \vec{v}(x_i, y_j) \frac{\prod_{k=1,4}^{k \neq i} (x_f - x_k) \prod_{l=1,4}^{l \neq j} (y_f - y_l)}{\prod_{k=1,4}^{k \neq i} (x_i - x_k) \prod_{l=1,4}^{l \neq j} (y_j - y_l)}, \tag{80}$$

where (x_f, y_f) is the position of the Lagrangian drifter and (x_i, y_i) are the positions of the 16 neighboring grid points.

Chapter 4

Results

The interactions and effects of physical and biological processes in the CTZ were investigated with three modeling studies. The first of these studies considered the time development of biological distributions in the vertical dimension only. The primary objective of this modeling study was to investigate interactions between the food web components and the underwater light field. The second study extends the one-dimensional model to three dimensions and includes more realistic representations of the circulation field that characterizes the CTZ. The simulated biological distributions obtained from this model provide the time evolution of the biological communities associated with the filaments in the CTZ and allow quantification of the flux of carbon and nitrogen from the CTZ. The final study provides simulations of the biological distributions that were encountered along trajectories followed by Lagrangian drifters that were released in the CTZ simulated circulation fields. The simulated distributions are compared to similar distributions obtained while following a drifter released in an offshore flowing filament during the 1988 CTZ field studies.

The simulations from the one-dimensional model are described in detail in the next section. This model is used to describe the sensitivity of the food web and

bio-optical model to parameter variations and to illustrate food web interactions. These same parameter sensitivities and interactions occur in the three-dimensional and Lagrangian drifter simulations, which are presented in sections 4.2 and 4.3, respectively.

4.1 One-Dimensional Physical-Bio-Optical Model

4.1.1 Characteristics of the Bio-Optical Model

The bio-optical model described in section 3.1 was implemented using parameter values that are characteristic of the CTZ. Coupling between the food web and underwater light field is strong. Hence, it is appropriate to describe how well the bio-optical model simulated the incident and underwater light fields of the CTZ.

Incident PAR values over 24 hours were measured at about 10 m above the sea surface during the 1988 CTZ field surveys (Curtiss O. Davis, personal communication). These values (Fig. 31) show sunrise and sunset at about 0600 and 2100 Pacific Standard Time (PST), respectively. The diurnal maximum occurred at about 1300 PST. Variations in the magnitude of the measured PAR values over the day were primarily due to cloud cover. The simulated PAR values just below the sea surface obtained from the bio-optical model match the measured PAR values in terms of the timing of the sunrise and sunset and time of the diurnal maximum. The simulated values fall within the range of the measured values. However, the simulated below-surface PAR values are lower than those measured above the sea surface because of the reflection (albedo) of both direct and diffuse

light at the air-sea interface. The simulated incident PAR field shown in Fig. 31 was used in all the simulations.

The depth-dependent PAR distributions were also measured during the 1988 CTZ field studies (Curtiss O. Davis, personal communication). These distributions and the corresponding vertical chlorophyll distributions were obtained for coastal, filament and oceanic environments. The pigment distributions from the coastal station (Fig. 32A) are characterized by low surface values (1.2 mg-chl *a* m^{-3}) which increased to a maximum of 9.4 mg-chl *a* m^{-3}at 15 m. The high chlorophyll concentrations result in a strong attenuation of PAR with depth (Fig. 32D). The estimated mean light attenuation coefficient at this location was 0.177 m^{-1}, which is within the range of values reported for coastal regions (Jerlov, 1976). The chlorophyll concentrations at the filament and offshore locations (Figs. 32B and C) are much lower and show slight increases in concentration below 20 m. As a result, the vertical light attenuation at these locations is reduced as evidenced by the lower mean attenuation coefficients of 0.113 m^{-1} and 0.0814 m^{-1} for the filament and offshore regions, respectively.

The coastal, filament and oceanic chlorophyll distributions were used with the bio-optical model to obtain a simulated depth-dependent PAR field. Overall, the simulated PAR fields (Figs. 32D, E and F) compare well with the observed vertical PAR distributions. At the coastal station, the simulated and observed PAR fields are nearly identical. Differences in the two become greater at the filament and offshore locations. These differences arise primarily from sensor noise (e.g. ship motion), because realistic PAR values do not increase with depth. The largest discrepancy occurs at the surface which is the result of the effect of clouds on

Figure 31. Comparison of the diurnal variation in the simulated below surface photosynthetically available radiation (PAR) (solid curve) with the measured (dots) PAR values which were collected 10 m above the sea surface during the 1988 CTZ field survey. The PAR measurements were provided courtesy of Dr. Curtiss O. Davis.

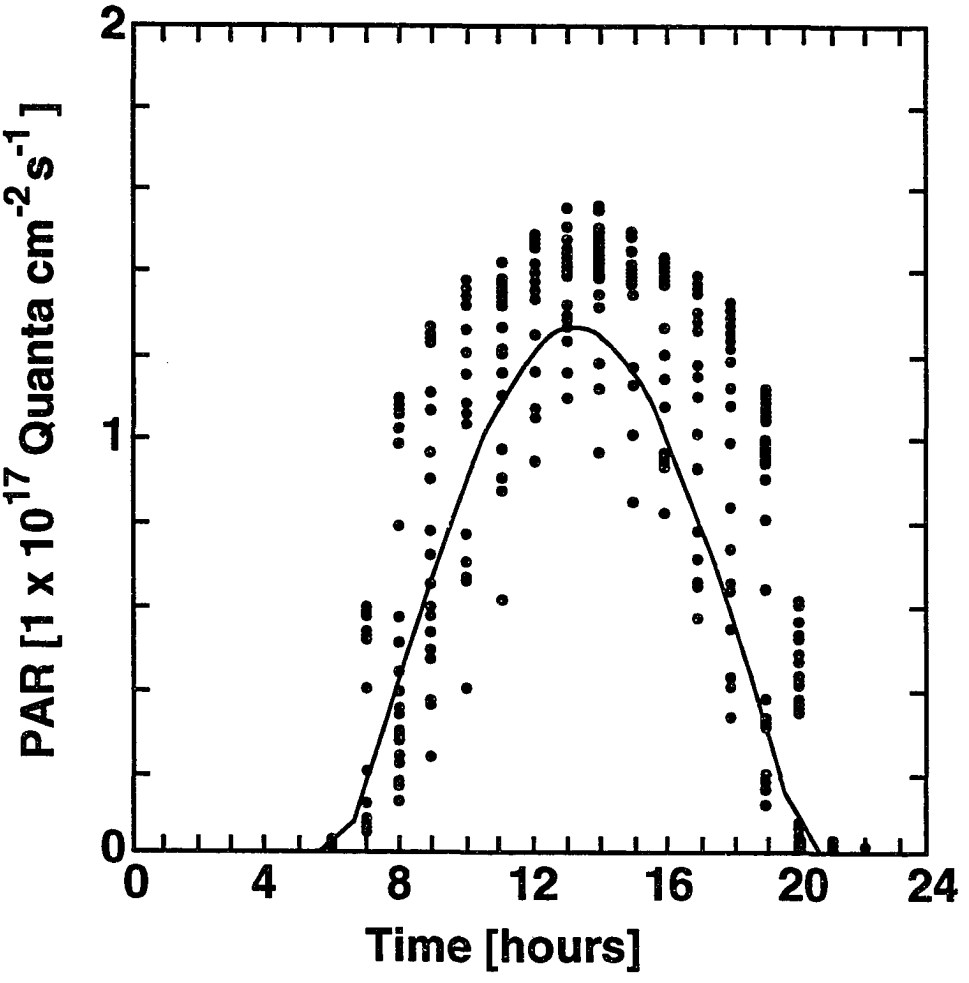

Figure 32. Vertical distribution of chlorophyll *a* measured during the 1988 CTZ field studies at **A**) coastal, **B**) filament, and **C**) offshore locations. The locations of the stations from which the measurements were obtained are shown in Fig. 19. The vertical distribution of PAR (solid line) corresponding to each chlorophyll distribution is shown in **D**, **E** and **F**, respectively. The simulated vertical PAR distributions (dashed line) obtained using the three chlorophyll profiles is also shown. The measured chlorophyll and PAR distributions are provided courtesy of Dr. Curtiss O. Davis.

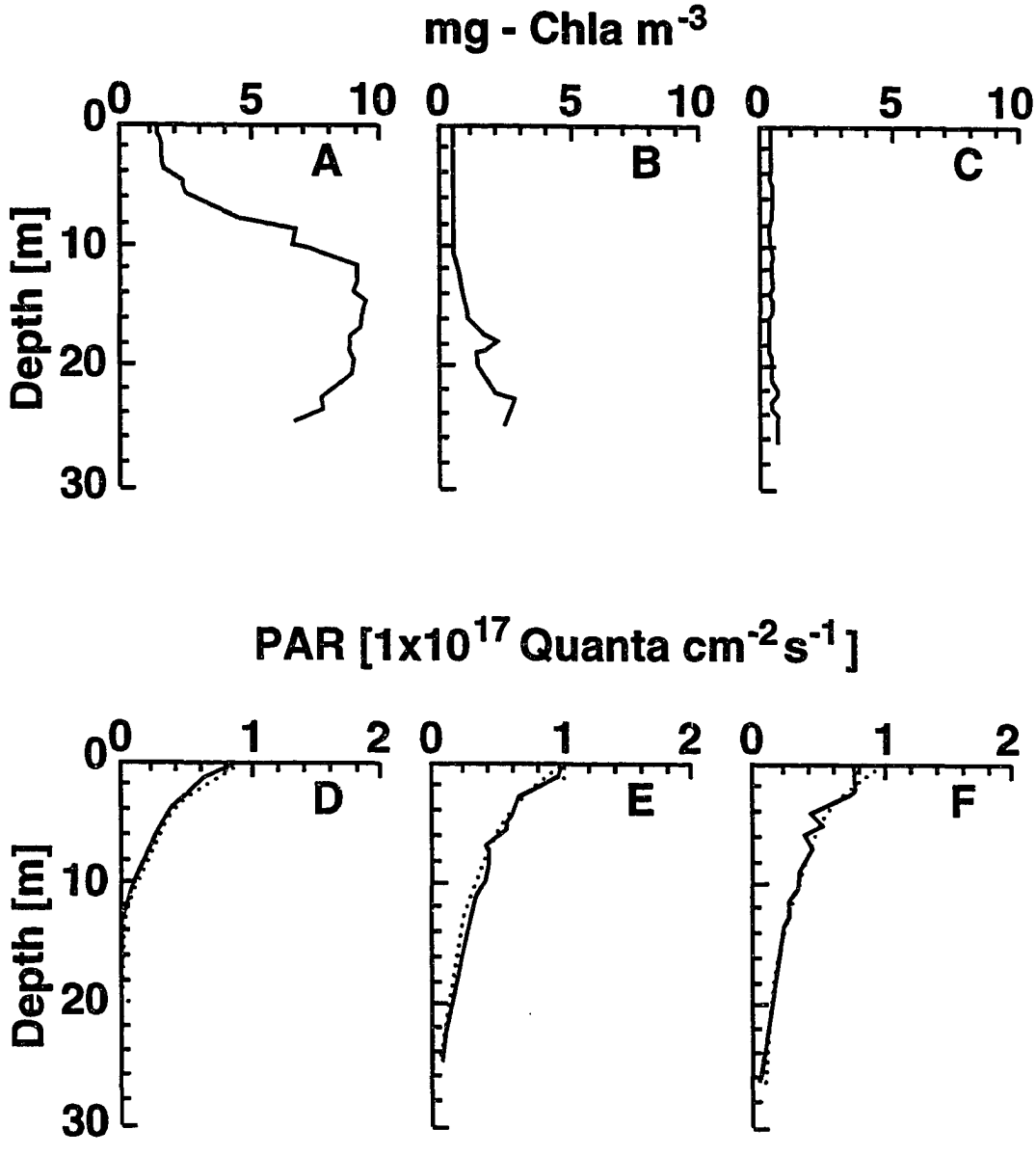

the incident light. On the basis of these comparisons, it was assumed that the bio-optical model adequately reproduced the surface and vertical PAR fields.

4.1.2 Sensitivity Analysis Model sensitivity is explored in order to determine the extent to which changes in the parameters/processes modify the model results. The non-linear interactions in the one-dimensional model demonstrated some interesting results, even though the number of links in the food web, defined as the number of nonzero elements in the interaction matrix (Table 14), was low.

The processes included in the food web and bio-optical models described in section 3 are based on formulations that contain approximately 150 parameters. Values for the majority of these parameters were specified using laboratory or field measurements, many of which were from CTZ studies. However, some of these processes, such as zooplankton mortality, are based upon formulations that include unknown, poorly known or poorly constrained parameters. Often these processes are those that control the input or removal of material at the lower and upper end of the food web. Therefore, the sensitivity analysis of the food web and bio-optical models was focused on those processes that control the rate of flow of nitrogen through the food web: the rate of vertical advection which controls nutrient input; the amount of incident radiation which controls the rate of primary production; the rate of zooplankton grazing which controls the phytoplankton standing stock; and, the rate of nutrient regeneration which determines the fraction of old versus new primary production. Model sensitivity to each of these was obtained after 20 days of simulation and was quantified by comparing the depth of the euphotic zone (1% PAR) and the total integrated old and new primary production for both phytoplankton size fractions.

Table 14. Food Web Linkage Matrix

	To								
	SiO_4^+	NO_3^-	NH_4^+	DET*	LPP*	SPP*	COP*	DOL*	EUP*
From									
SiO_4^+					-X-	-X-			
NO_3^-					-X-	-X-			
NH_4^+					-X-	-X-			
DET*	-X-		-X-					-X-	
LPP*				-X-			-X-	-X-	-X-
SPP*				-X-				-X-	
COP*			-X-	-X-					-X-
DOL*			-X-	-X-					
EUP*			-X-	-X-					

-X- denotes a linkage between the food web components
* DET = Detritus, LPP = Large Phytoplankton,
SPP = Small Phytoplankton, COP = Copepods, DOL = Doliolids
and EUP = Euphausiids

4.1.2.1 Vertical Advection

The rate of vertical advection controls the rate at which nitrate and silicate are made available to the phytoplankton. Within the CTZ, vertical advection can reach maximum upwelling or downwelling velocities of 5 m day^{-1} or more (Kadko et al., 1991). Therefore, the effect of vertical advective velocities over this range on the simulated biological distributions was tested.

As vertical velocities change from downwelling to upwelling, the rate of nutrient supply to the euphotic zone increases. As a result, phytoplankton concentrations increase, which in turn reduces the depth to which light penetrates (Fig. 33A). Downwelling velocities result in euphotic zones that are deeper than 40 m; whereas, upwelling velocities result in a euphotic zone that shallows to about 26 m for a vertical velocity of 5 m day^{-1}. The rate of change of euphotic zone depth is similar for equal changes in upwelling or downwelling velocities.

The depth-integrated primary production for the small (Fig. 33B) and large (Fig. 33C) phytoplankton size fractions shows considerable variation as the vertical velocities change from downwelling to upwelling. The small phytoplankton size fraction has highest old and new primary production rates for downwelling velocities. The large phytoplankton size fraction, by contrast, shows the highest new production rates for upwelling velocities. The old primary production rates for this size fraction are relatively constant over all vertical velocities. These differences in old and new primary production rates are the result of inter-species competition for nutrients. The small phytoplankton size fraction, which is a non-silicate-dependent oligotrophic species, outcompetes the large phytoplankton size fraction when low nutrient conditions prevail, as would occur during downwelling.

Figure 33. The effect of variable vertical velocity rates (m day^{-1}) on **A**) euphotic zone depth (1% PAR) and the depth-integrated old (solid line) and new (dashed line) primary production rates for the **B**) small and **C**) large phytoplankton size fractions. Negative vertical velocities are downwelling; positive vertical velocities are upwelling.

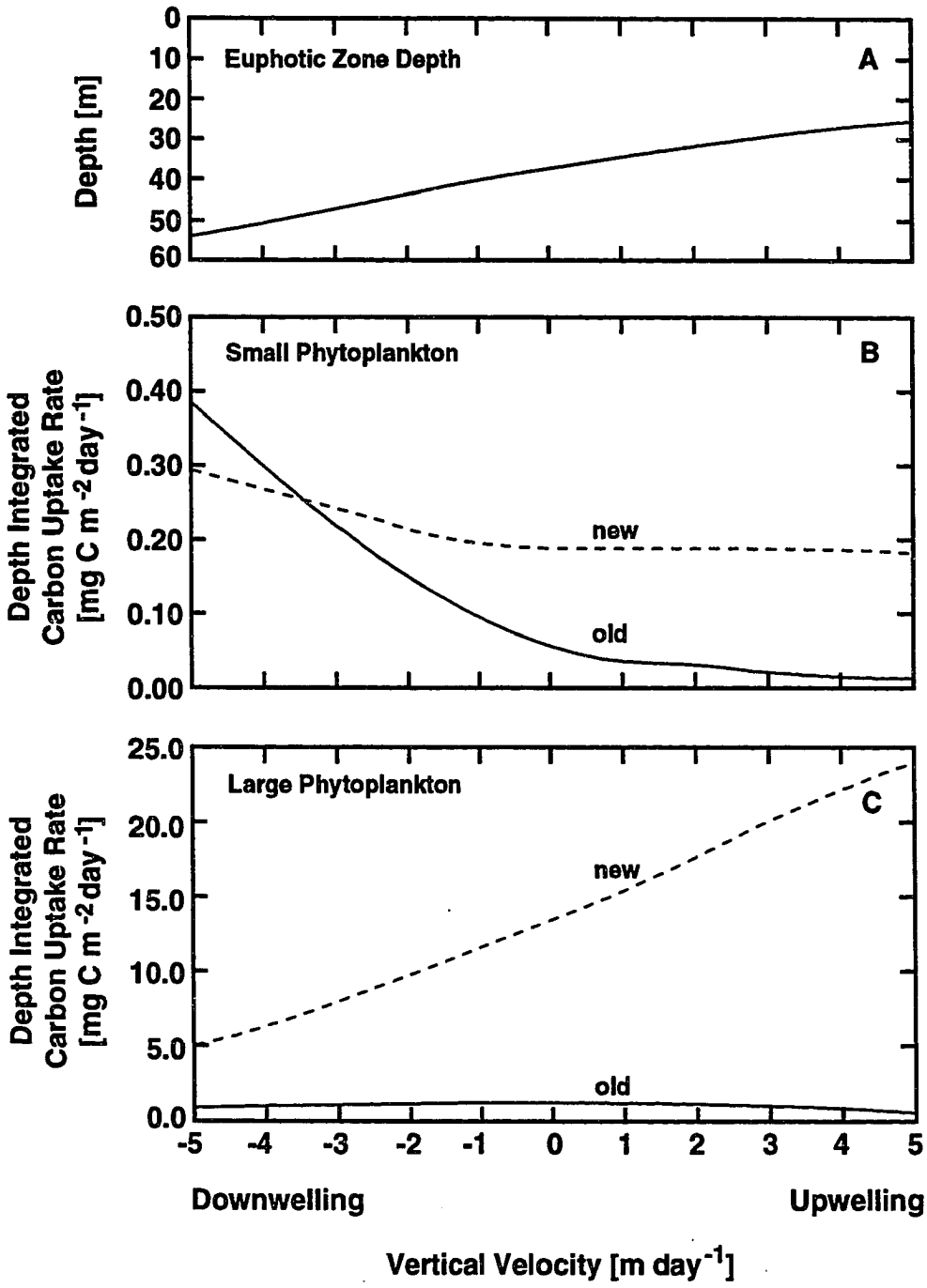

The large phytoplankton size fraction is a silicate- and nitrate-dependent neritic species and can outcompete the smaller size fraction during upwelling when high nutrient concentrations prevail. Therefore, it is the large phytoplankton size fraction that accounts for the shallowing of the euphotic zone during upwelling conditions.

The increase in the old primary production rate for the smaller phytoplankton during downwelling results from the nutrient uptake characteristics and grazing pressure experienced by the size fraction. The small phytoplankton are not silicate limited during periods of high ammonium concentration. These cells are also not grazed by the copepods or euphausiids. The net result is that the small phytoplankton are able to use the ammonium regenerated by the zooplankton and outcompete the larger phytoplankton size fraction.

4.1.2.2 Incident PAR

The second variable that controls the rate of primary production is the fraction of the incident PAR that penetrates the water column. Varying the percent of incident PAR from 0% to 200% of the mean values characteristic of the CTZ results in a euphotic zone depth that initially shallows rapidly to about 40 m, after which it slowly increases to about 50 m (Fig. 34A). The initial shallowing of the euphotic zone coincides with increased rates of depth-integrated primary production for the small and large phytoplankton size fractions (Fig. 34B and C). Overall, the change in euphotic zone depth produced by an increment change in the light level is less than that produced by an incremental change in vertical velocity.

Figure 34. The effect of variable incident radiation on **A**) euphotic zone depth (1% PAR) and the depth-integrated old (solid line) and new (dashed line) primary production rates for the **B**) small and **C**) large phytoplankton size fractions. The incident PAR values range from 0% to 200% of those calculated for the CTZ.

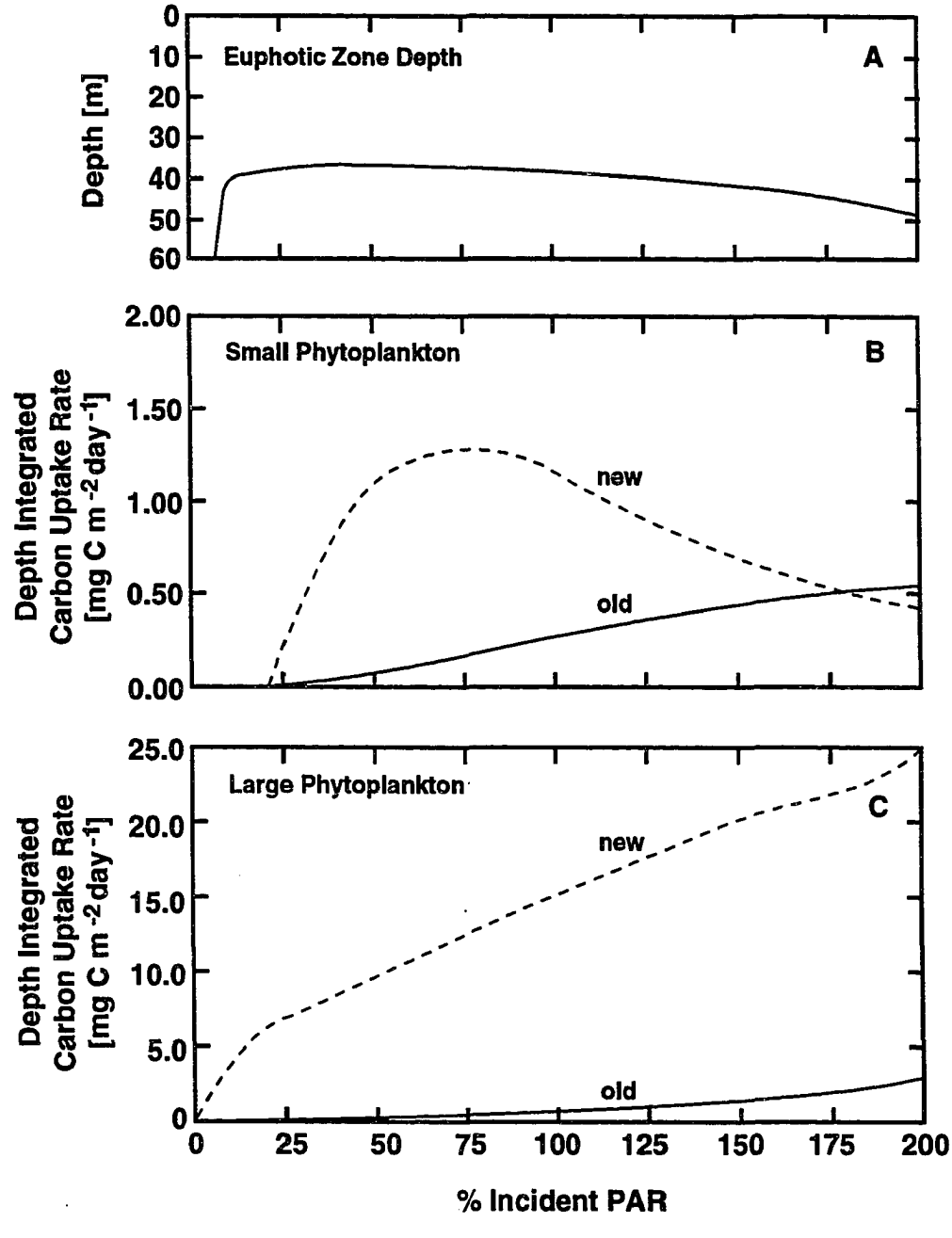

The small phytoplankton size fraction shows maximum rates of new production at about 75% incident PAR. Decreased rates of new primary production for this size fraction at higher light levels results from depleted nutrients, increased grazing pressure and photoinhibition. The large phytoplankton size fraction by contrast shows increased rates of new primary production for all light levels. Increased PAR levels results in light penetration to depths where silicate limitation on this size fraction is lowest. As a result, the rate of growth of the large phytoplankton increases with increasing incident PAR. Both size fractions show increased rates of depth-integrated old production with increasing light level. This results from ammonium regeneration that is produced by zooplankton grazing.

4.1.2.3 Zooplankton Grazing

The rate of grazing controls the transfer of nitrogen and carbon from the phytoplankton compartments to the three zooplankton compartments (cf. Fig. 7). The sensitivity of the biological distributions to different levels of grazing pressure was determined by varying the rate of grazing determined from equations 14, 23, 24, 32, 33 and 34 from 0% to 100%. Thus, the grazing pressure on the two phytoplankton size fractions was incrementally increased to its maximum values simultaneously.

Variations in zooplankton grazing rate had three obvious effects in the simulated biological distributions. First, the euphotic zone depth increased from 28 m with no grazing to about 38 m with the grazing rate determined for each zooplankton species (Fig. 35A). The deepening of the euphotic zone is due primarily to removal of light-attenuating phytoplankton. Second, the depth-integrated old

primary production rates for both phytoplankton size fractions increase with increasing grazing pressure (Figs. 35B and C). Increased grazing results in increased ammonium production which supports increased levels of old primary production. Third, the depth-integrated new and total primary production increased with increasing grazing pressure. Removal of the slowly growing nutrient-limited phytoplankton from the upper water column by grazing allows light to penetrate to the deeper nutrient-rich waters which then stimulates primary production. These results illustrate the nonlinear feedbacks that can occur in marine food webs.

These nonlinear interactions are further illustrated by two sets of simulations that used different vertical velocities and zooplankton grazing rates. In the first set of simulations no zooplankton grazing was allowed and the vertical advective velocity was specified at 1 m day^{-1} upwards, 0 m day^{-1} and 1 m day^{-1} downwards. The simulated depth of the 10% PAR level (Fig. 36) resulting from these conditions shows little variation over twenty days. However, when grazing is allowed the 10% PAR level deepens during the twenty day simulation, even for conditions of no vertical advection or upwelling.

4.1.2.4 Nutrient Regeneration

The recycling of nitrogen from the detrital compartment to the ammonium compartment provides a nutrient source for the phytoplankton. The rate at which this occurs is poorly known and can vary at seasonal and daily time scales (Wada and Hattori, 1991). Thus, the sensitivity of the simulated distributions to detrital remineralization rates that varied from 0 to 100% of the total detrital pool per day was tested.

Figure 35. The effect of variable grazing pressure on **A**) euphotic zone depth (1% PAR) and the depth-integrated old (solid line) and new (dashed line) primary production rates for the **B**) small and **C**) large phytoplankton size fractions. Grazing pressure rates varied from 0% to 100% of those obtained for the three zooplankton species included in the model from equations 14, 23, 24, 32 , 33 and 34.

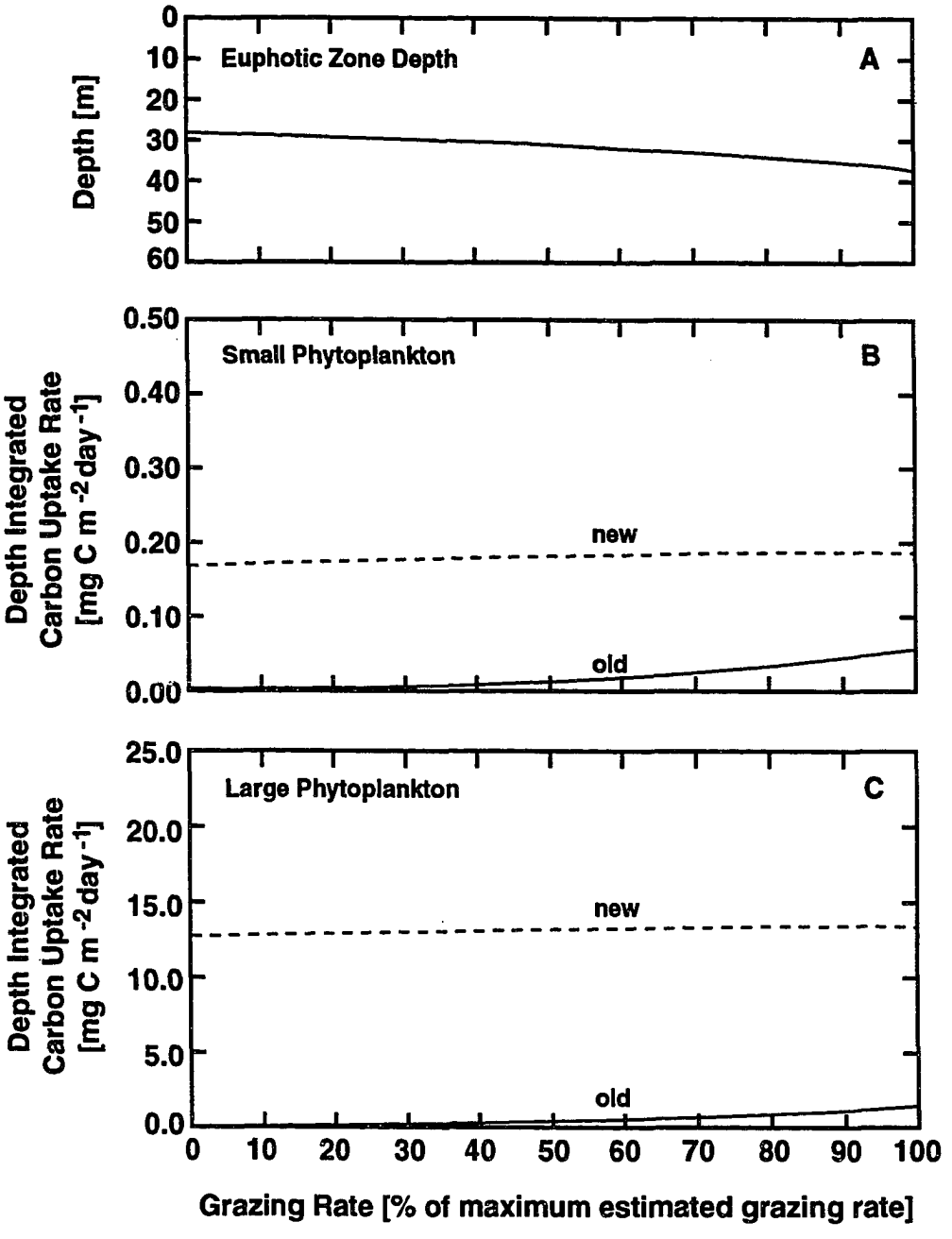

Figure 36. Simulated time evolution of the depth of the 10% PAR obtained using variable vertical velocities and grazing rates. The upper set of three curves represents the depth of the 10% PAR level for conditions of no grazing and vertical velocity rates of 1 m day^{-1} (upper dashed line; an upwelling simulation), 0 m day^{-1} (central solid line) and -1 m day^{-1} (lower dashed line; a downwelling simulation). The lower set of three curves represent the depth of the 10% PAR level when grazing is allowed with vertical advection rates of 1 m day^{-1} (upper dashed line; an upwelling simulation), 0 m day^{-1} (central solid line) and -1 m day^{-1} (lower dashed line; a downwelling simulation).

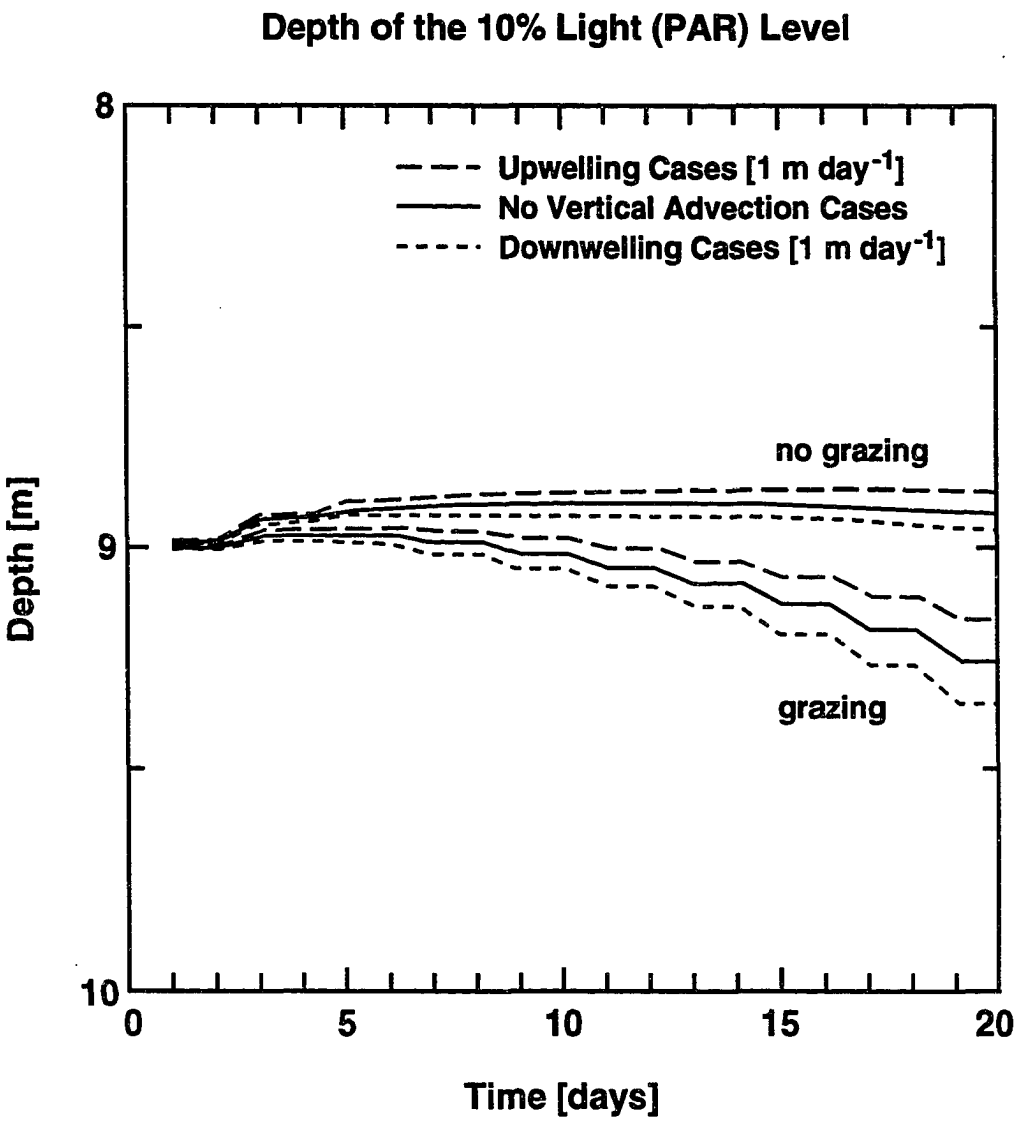

Changes in the depth of the euphotic zone in response to changes in detrital remineralization rates was most sensitive from 0 to 20% remineralization per day (Fig. 37). The deepest euphotic zone of about 48 m occurred for 10% remineralization. As the remineralization rate increased, the euphotic zone shallowed, reaching a minimum depth of about 28 m at 50% remineralization per day; and, as the remineralization rate decreased, the euphotic zone shallowed rapidly to a depth of 30 m at 0% remineralization per day. The euphotic zone depth remained essentially constant at 28 m for all other remineralization rates greater than 50%.

Variations in remineralization rate had the largest effect on the depth-integrated primary production rates for the large and small phytoplankton size fractions (Fig. 37B and C). Old primary production rates for the small phytoplankton size fraction increased rapidly with increasing remineralization rates; whereas, those for the large phytoplankton size fraction increased less rapidly. This pattern arises because detrital remineralization does not include dissolution of silicate from fecal pellets, dead phytoplankton cells and dead zooplankton. As a result, the large phytoplankton become silicate-limited over the twenty-day simulation which allows the smaller nonsilicate-limited phytoplankton to use the recycled nitrogen.

The rate of detrital remineralization had less of an effect on the depth-integrated new production. The depth-integrated new production rates for the small phytoplankton size fraction showed little change with changing remineralization rates. However, the depth-integrated new production rates for the large phytoplankton size fraction decreased rapidly from its highest value of > 10 mg N m^{-2} day^{-1} at 0% to < 1 mg N m^{-2} day^{-1} at 10% remineralization per day. This trend was expected, because the smaller phytoplankton size fraction was able to

Figure 37. The effect of variable detrital remineralization rates on **A**) euphotic zone depth (1% PAR) and the depth-integrated old (solid line) and new (dashed line) primary production rates for the **B**) small and **C**) large phytoplankton size fractions. Detrital remineralization rates ranges from 0 to 100% of the total detrital compartment per day.

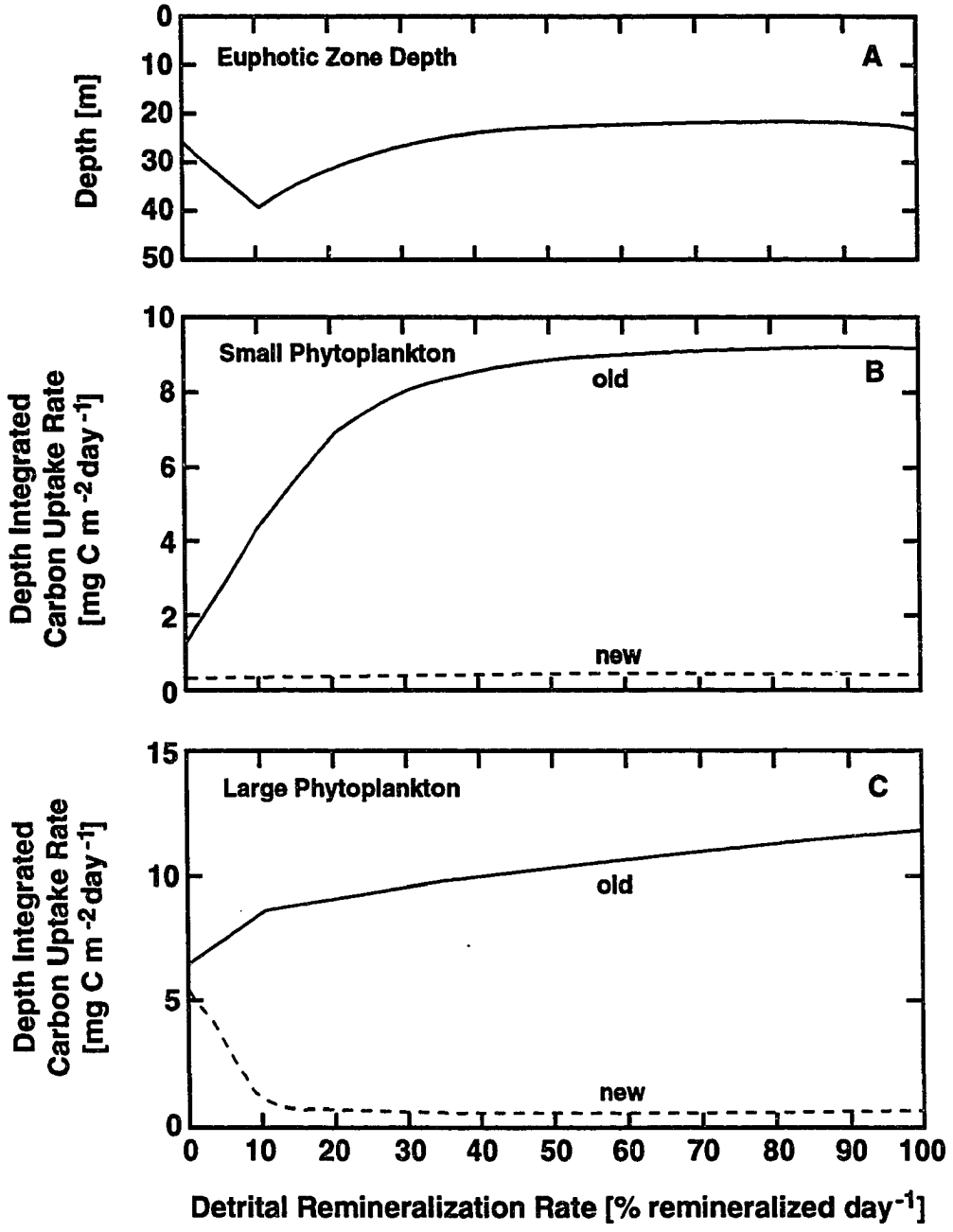

outcompete for all sources of nitrogen, e.g. nitrate and ammonium, in regions where the large phytoplankton are silicate-limited. Increased remineralization rates increases the likelihood that the large phytoplankton will be silicate-limited (cf. Fig. 12).

4.1.3 CTZ Simulations

The simulations presented in the previous sections illustrated the response of the bio-optical and food web models to variations in parameters and to variations in environmental conditions. The next application of the one-dimensional model used observed conditions from the CTZ. Specifically, the model was initialized using nutrient and phytoplankton vertical distributions that were measured in coastal, oceanic and filament waters in the CTZ (cf. Fig. 19). These regions are distinguished by water mass characteristics as described by Strub et al. (1991). For these simulations, the vertical advective velocity was assumed to be zero. This allows investigation of the interactions among biological and optical properties independent of circulation effects. This provides a basis for interpreting the patterns observed in the three-dimensional simulations that are described later. Thus, the focus of the simulations in each region is on biological processes and food web interactions.

4.1.3.1 Coastal Region Simulation

The coastal region of the CTZ is characterized by nutrient-rich, high phytoplankton concentration water. The initial depth-dependent temperature and concentrations of nitrate, ammonium, silicate and chlorophyll were obtained from data collected within the coastal region of the CTZ (Fig. 19). As a result, the coastal simulation was initialized as a cold (< 10.3 °C), nutrient-rich (> 12 μM NO_3^-; > 20 μM SiO_4^-) and high chlorophyll concentration (> 10 mg-chl a m^{-3}) water column. Partitioning of the chlorophyll between the large and small phytoplankton size fractions was accomplished using the size fraction to chlorophyll relationship of Chavez et al. (1991). Because no information was available on the

specific concentration of zooplankton in the each region, the initial concentration of copepods, euphausiids and doliolids was set to 10% of that of their prey items. These initial distributions were then allowed to evolve in the upper 100 m of the water column for twenty days.

The simulated nitrate field (Fig. 38A) indicates rapid removal of this nutrient from the upper water column and the development of a sharp nutricline at about 20 m which slowly deepens to about 30 m. The silicate distribution (not shown) showed a similar trend. The large (Fig. 38B) and small (Fig. 38C) phytoplankton size fractions maintained a distinct chlorophyll maximum throughout the 20 days of simulation. The concentration of the large phytoplankton subsurface maximum decreased from 160 mg-N m^{-3}($\approx$20 mg-chl *a* m^{-3}) to about 20 mg-N m^{-3}($\approx$2.5 mg-chl *a* m^{-3}) over twenty days. The depth of the maximum concentration increased from 15 to 30 m over this time, which gives a downward displacement of about 0.75 m day^{-1}. A comparison of the depth and chlorophyll concentration of the simulated deep chlorophyll maximum (DCM) for coastal conditions with that observed in the CTZ coastal waters is given in Table 15.

The subsurface maximum associated with the small phytoplankton size fraction, by contrast, did not persist over the twenty day simulation. Rather it was grazed by the zooplankton within the first 6 to 8 days of the simulation. Concentrations of this size phytoplankton increased in the upper 20 m of the water column during the latter part of the simulation. These cells are able to outcompete the larger phytoplankton for the regenerated nitrogen in the shallower waters, thereby increasing their concentration.

Table 15. Comparison Between Simulated and Observed Depth and Chlorophyll *a* Concentrations of the Deep Chlorophyll Maximum (DCM) for Different Regions in the CTZ.

Region	Simulated Depth (m)	Simulated Chl *a* (mg-chl *a* m^{-3})	Observed Range Depth (m)	Observed Range Chl *a* (mg-chl *a* m^{-3})	Reference
Coastal	15-30	20-2.5	≈10	> 5	Washburn et al., 1991
					Chavez et al., 1991
Filament	30-45	3.3-1.8	25-75	5-0.5	Washburn et al., 1991
					Chavez et al., 1991
Oceanic	≈70	≈0.5	> 65	< 1	Washburn et al., 1991
					Chavez et al., 1991

Figure 38. Simulated 20-day time and depth evolution of the **A**) nitrate, **B**) large and **C**) small phytoplankton size fractions, **D**) copepod, **E**) doliolid and **F**) euphausiid fields obtained for coastal waters. Contour levels are 50 mg-N m^{-3}, 5 mg-N m^{-3}, 0.5 mg-N m^{-3}, 0.5 mg-N m^{-3}, 1 mg-N m^{-3} and 1 mg-N m^{-3}, respectively.

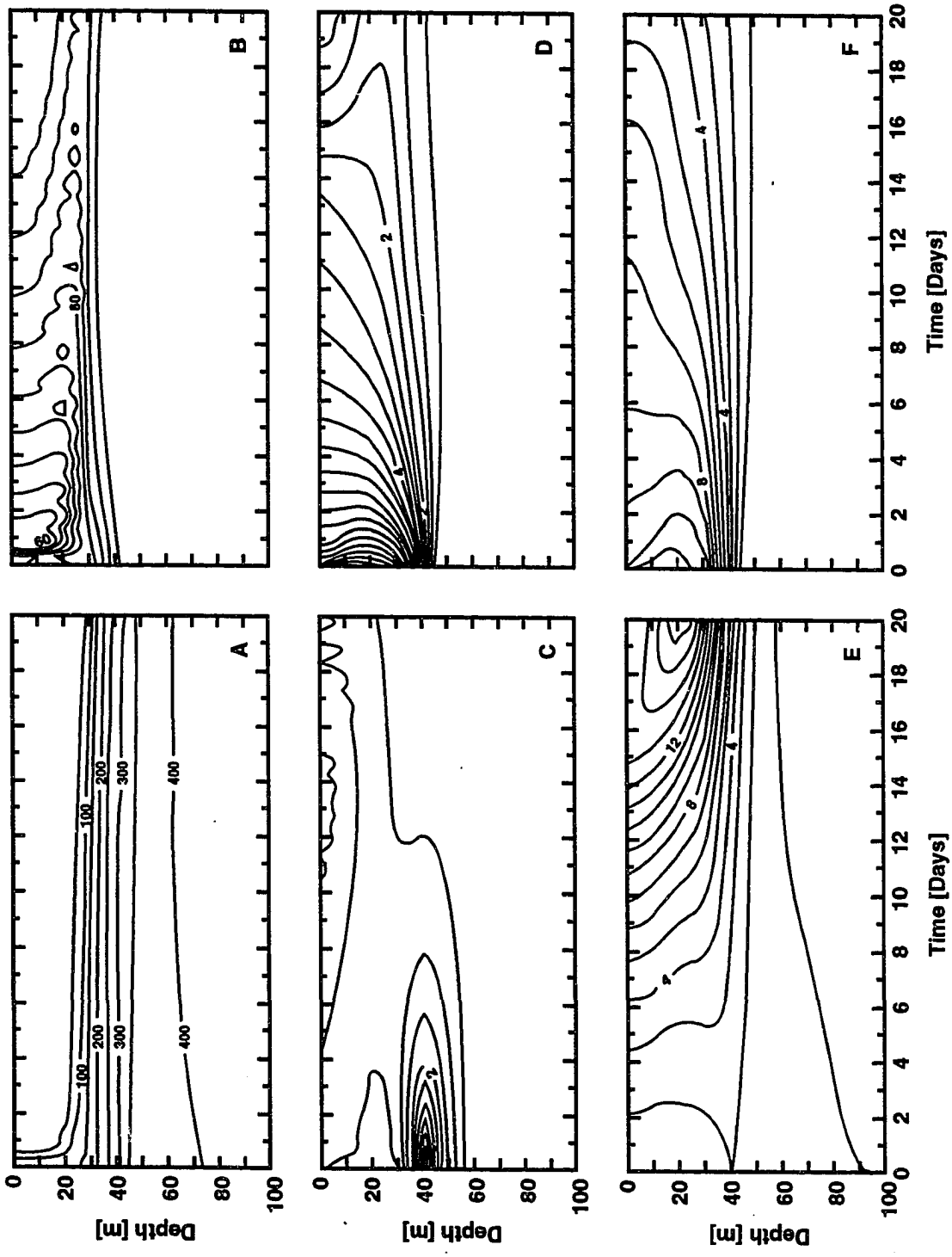

The simulated vertical distributions of the three zooplankton components (Fig. 38D, E and F) show that these animals are confined to the upper 50 m of the water column, which is consistent with the distribution of the available food. Copepod and euphausiid concentrations were highest during the first 5 to 6 days of the simulation, after which they declined. This is consistent with the decrease in the large phytoplankton concentrations, which is the primary food source for these animals. Doliolid biomass, however, was lowest (2 mg-N m^{-3}) at the beginning of the simulation and increased to a maximum of 16 mg-N m^{-3}after twenty days. The increase in doliolid concentration is in response to the increase of small phytoplankton cells in the upper 20 m at the end of the simulation.

The changes in relative abundance of the phytoplankton and zooplankton over the twenty day simulation are illustrated by the depth-integrated biomass (Fig. 39) of each component. The large phytoplankton biomass decreased by 8% (300 to 275 mg-N m^{-3}) over the simulation; whereas, the small phytoplankton biomass increased by almost a factor of three (1 to 2.7 mg-N m^{-3}). Copepod and euphausiid concentrations decreased over the simulation. The pattern and rate of this decrease are consistent with that observed for the large phytoplankton size fraction, which is their primary food source. Doliolid concentrations increase in response to the increase in the small phytoplankton. Total zooplankton biomass initially declines, but increases at the end of the simulation as the doliolids increase.

The chlorophyll maximum, defined as the depth at which the sum of both phytoplankton size fraction concentrations is maximum, was located in the simulated distributions near the nutricline and was composed primarily of large cells. The

Figure 39. The 20-day time evolution of the simulated depth integrated (0 to 100 m) simulated concentrations of the **A**) large and **B**) small phytoplankton size fractions and **C**) zooplankton for the coastal case. The zooplankton are denoted as, doliolids (small dashes), copepods (medium dashes), euphausiids (large dashes) and total zooplankton biomass (solid line).

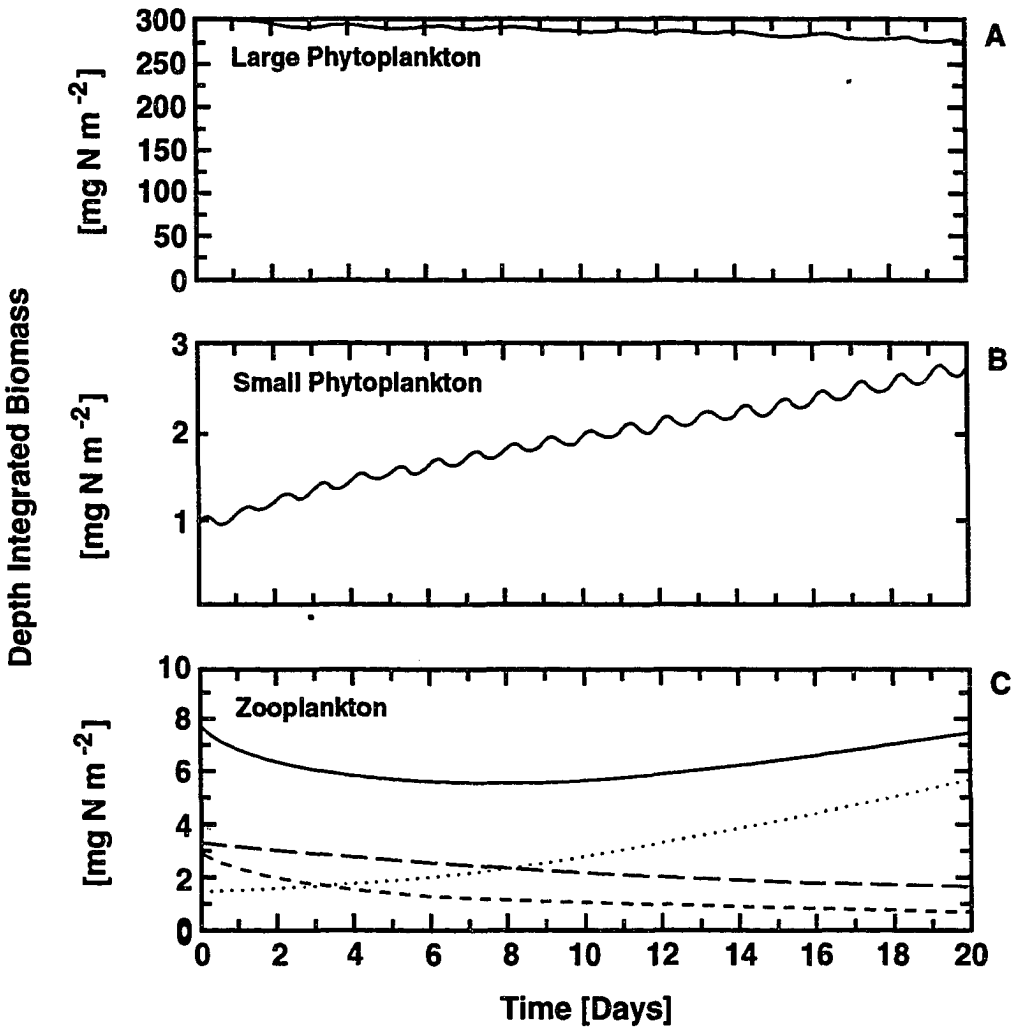

formation and maintenance of the chlorophyll maximum was controlled by various processes. The vertical distribution of these contributing processes (Fig. 40) shows that processes such as grazing play a role in the initial formation of the subsurface chlorophyll maximum. However, the chlorophyll maximum in the coastal region of the CTZ is maintained through *in situ* primary production. Indeed, the chlorophyll maximum is likely the result of the inverse relationship that exists between nutrient and light limitation effects. Maximal net growth occurred when the product of these two processes was minimal.

4.1.3.2 Oceanic Region Simulation

The oceanic regions of the CTZ are characterized by low concentrations of nutrients and phytoplankton. The oceanic simulation was initialized as a warm (> 14.3 °C), nutrient-poor (< 0.1 μM NO_3^-; < 0.2 μM SiO_4^-) and low chlorophyll concentration (< 0.02 mg-chl *a* m^{-3}) water column. The remaining components of the simulations were initialized as was done for the coastal simulation. These initial distributions were then allowed to evolve in the uppers 100 m of the water column for twenty days.

The simulated vertical nitrate distributions shows little change below 70 m over twenty days (Fig. 41A; cf. Table 14). Concentrations in the upper water column are rapidly depleted. There is a slight upward movement of the nitrate isopleths between 70 and 60 m over the simulation. Similar trends are seen in the silicate distributions (not shown). An initial maximum in the large phytoplankton concentration occurs at about 70 m. Unlike the coastal simulation, the concentrations increase from 3 to 5 mg-N m^{-3} (0.38 to 0.625 mg-chl *a* m^{-3}) as it deepens slightly over the twenty day simulation (cf. Table 14). A subsurface

Figure 40. The vertical profile of individual terms in the one-dimensional governing equations integrated over one day after (**A**) day 5 and (**B**) day 20 of the coastal simulation.

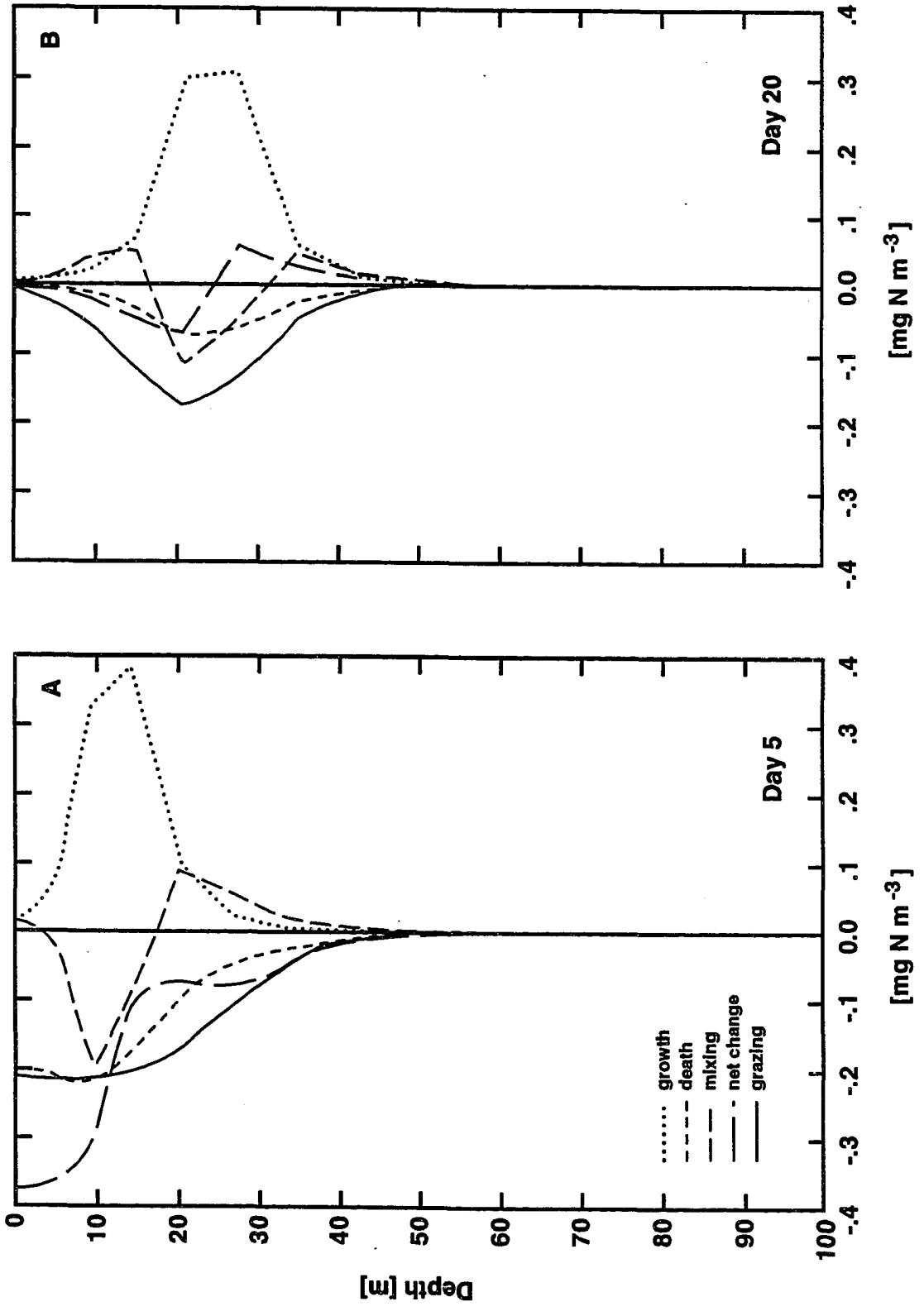

maximum is also observed in the small phytoplankton concentration. However, the maximum does not persist, but rather is grazed by the doliolids. As was found in the coastal simulation, the small cells bloom in the upper waters toward the end of the simulation in response to increased ammonium concentrations due to recycling by zooplankton.

The simulated copepod and euphausiid concentrations show variations in time and space. Both populations show initial maxima at about 70 m which was in response to the increased food supply at this depth. These deep populations decrease over about ten days. At the same time, a second bloom in copepods and euphausiids occurrs in the upper 30 m of the water column, which persists for the remainder of the simulation. The second bloom is supported by the bloom in the phytoplankton cells. Doliolids concentrations show similar trends, but with a weaker response.

The depth-integrated biomass distributions (Fig. 42) suggest that the oceanic regions of the CTZ are biologically less dynamic than the coastal regions. Concentrations of both phytoplankton size fractions increased slightly over the simulation. The depth-integrated copepod and euphausiid concentrations remained constant at low concentrations. Doliolid concentrations decreased about 60% (1.6 to 0.7 mg-N m^{-3}) over the twenty day simulation.

The vertical distribution of the processes included in the model which are responsible for the creation and maintenance of the chlorophyll maximum (Fig. 43) again indicates that *in situ* primary production maintains the subsurface chlorophyll maximum. However, there are times (day 5) when the sum of all the processes is negative, which indicates that the chlorophyll maximum is being eroded. As

Figure 41. Simulated 20-day time and depth evolution of the **A**) nitrate, **B**) large and **C**) small phytoplankton size fractions, **D**) copepod, **E**) doliolid and **F**) euphausiid fields obtained for the oceanic waters. Contour levels are 5 mg-N m^{-3}, 0.5 mg-N m^{-3}, 0.5 mg-N m^{-3}, 0.05 mg-N m^{-3}, 0.5 mg-N m^{-3} and 0.05 mg-N m^{-3}, respectively.

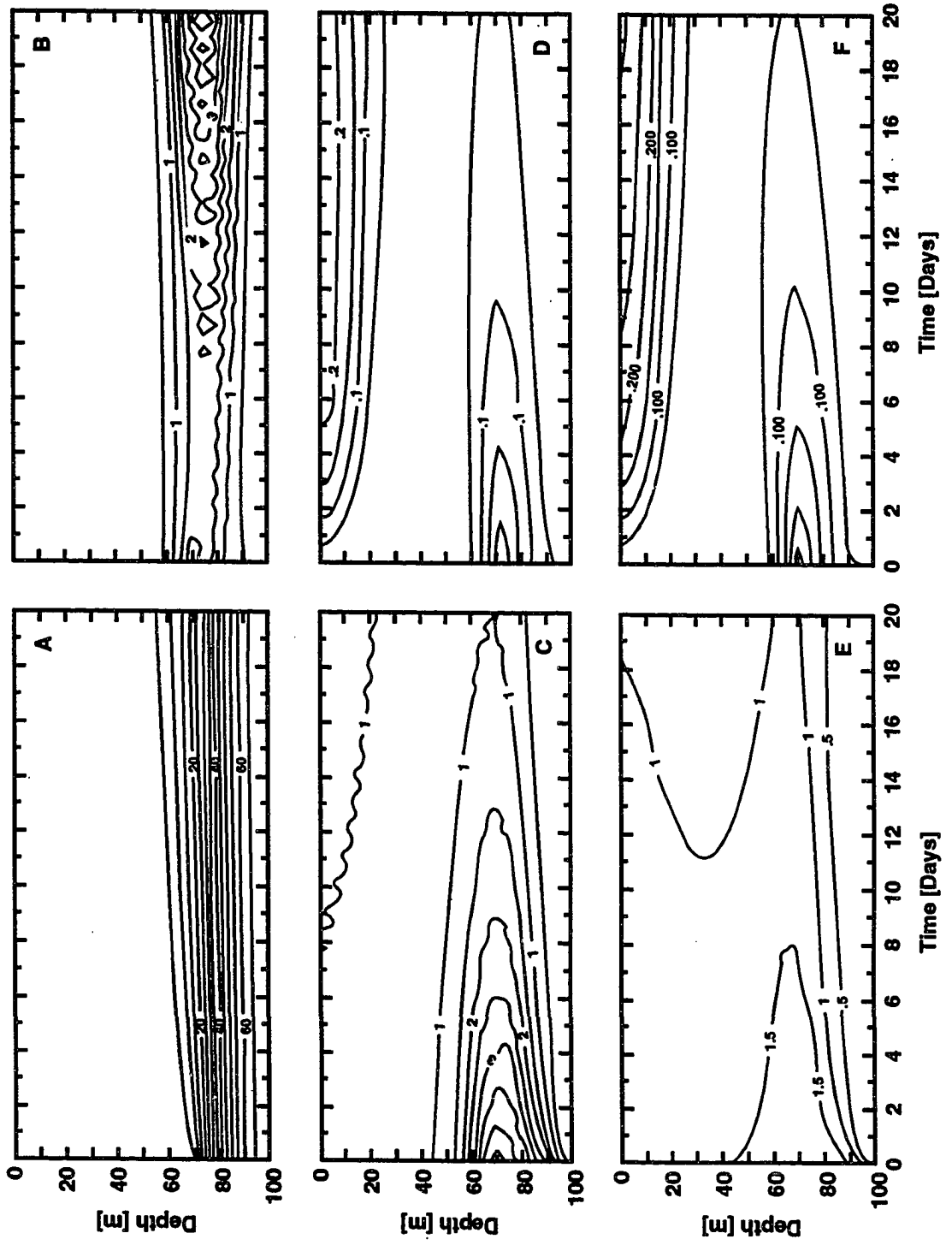

Figure 42. The 20-day time evolution of the simulated depth integrated (0 to 100 m) simulated concentrations of the **A**) large and **B**) small phytoplankton size fractions and **C**) zooplankton for the oceanic case. The zooplankton are denoted as, doliolids (small dashes), copepods (medium dashes), euphausiids (large dashes) and total zooplankton biomass (solid line).

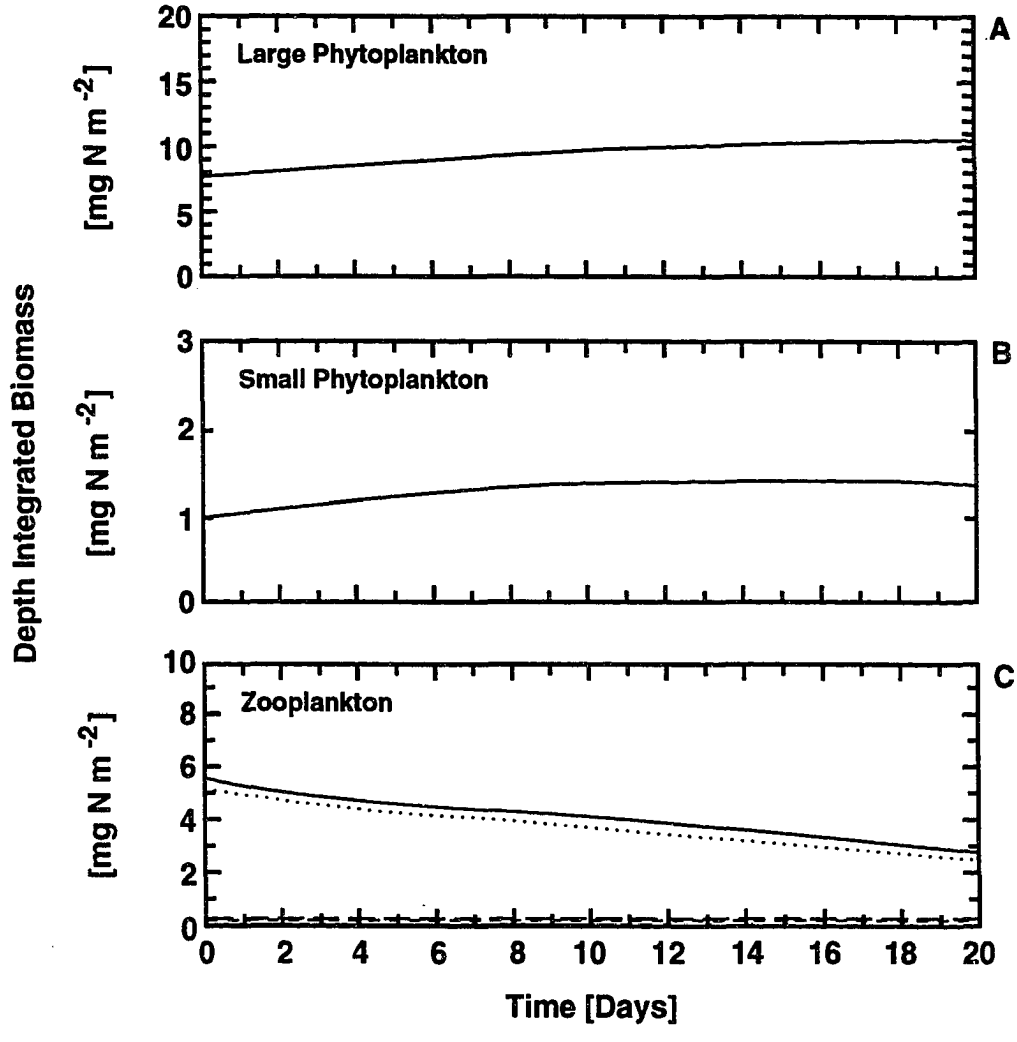

was found for the coastal simulation, it is the combination of grazing and nutrient processes that produce the simulated phytoplankton distributions.

4.1.3.3 Filament Region Simulation

The offshore extending filaments that characterize the CTZ are initially low in nutrients and intermediate between the coastal and oceanic regions in terms of phytoplankton concentrations. The filament simulation was initialized as a warm (> 12.5 °C), nutrient-poor (< 0.1 μM NO_3^-; < 0.2 μM SiO_4^-) and medium chlorophyll concentration (< 1.5 mg-chl a m^{-3}) water column. The remaining components of the food web were initialized as done for the coastal simulation. These initial distributions were then allowed to evolve in the upper 100 m of the water column for twenty days.

The simulated nitrate field (Fig. 44A) is characterized by a nutricline at about 40 m which remains essentially at this depth throughout the 20-day simulation. Unlike the coastal and oceanic simulations, this nutricline is not sharp and does not deepen over time.

The depth of the subsurface maximum in large phytoplankton increases from 30 to 45 m in over twenty days and at the same time decreases in concentration by about a factor of 2 (cf. Table 14). As found in the coastal and oceanic simulations, the small phytoplankton size fraction is grazed by the doliolids. The highest copepod and euphausiid concentrations occurred during the initial part of the simulation and were confined around 35 m. Doliolid concentrations were maximal at the end of the simulation and were found deeper ($\approx$45 m) in the water

Figure 43. The vertical profile of individual terms in the one-dimensional model governing equations integrated over 1 day after (**A**) day 5 and (**B**) day 20 of the oceanic simulation.

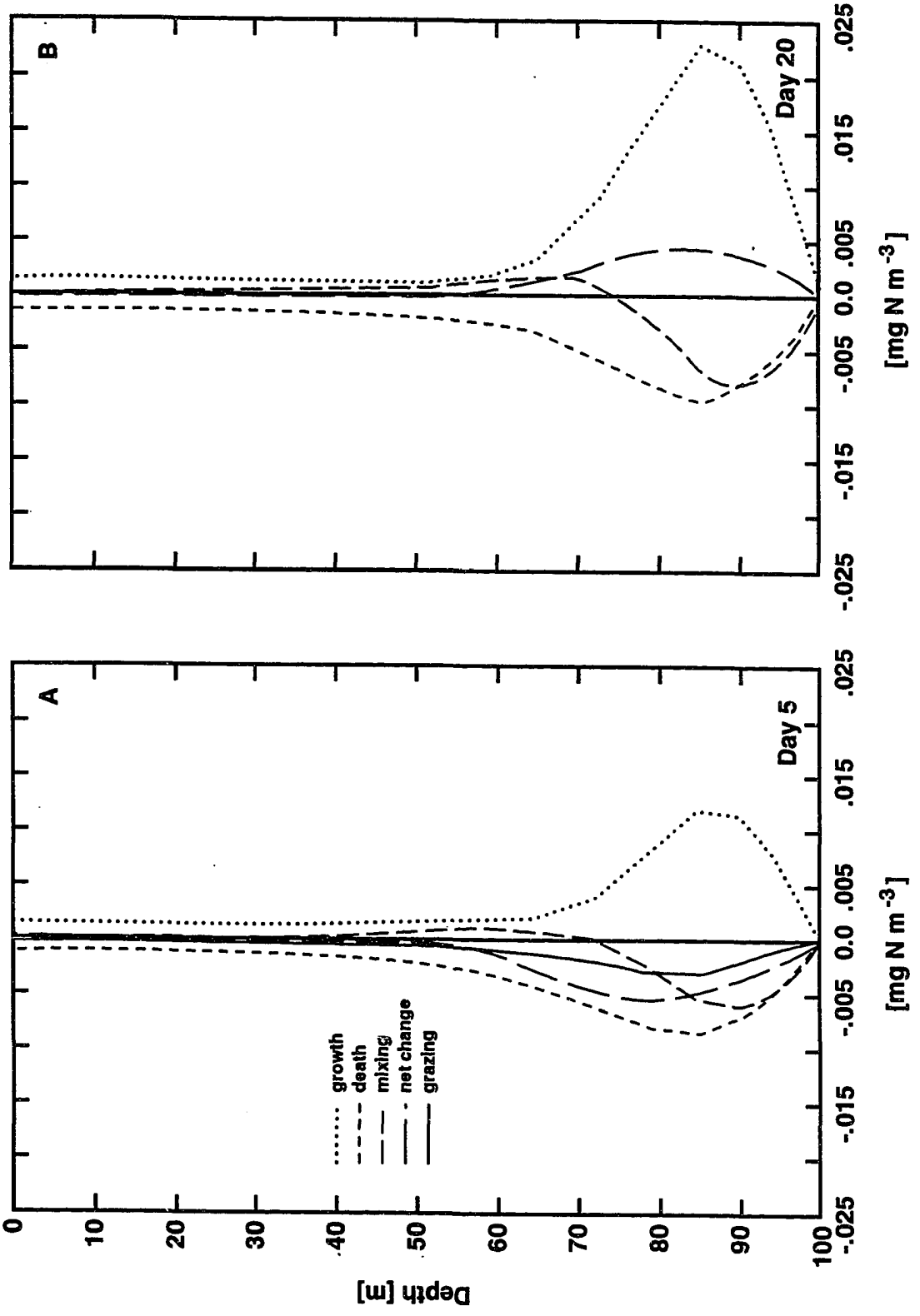

Figure 44. Simulated 20-day time and depth evolution of the **A**) nitrate, **B**) large and **C**) small phytoplankton size fractions, **D**) copepod, **E**) doliolid and **F**) euphausiid fields obtained for the filament waters. Contour levels are 50 mg-N m^{-3}, 2.5 mg-N m^{-3}, 0.5 mg-N m^{-3}, 0.5 mg-N m^{-3}, 1 mg-N m^{-3} and 1 mg-N m^{-3}, respectively.

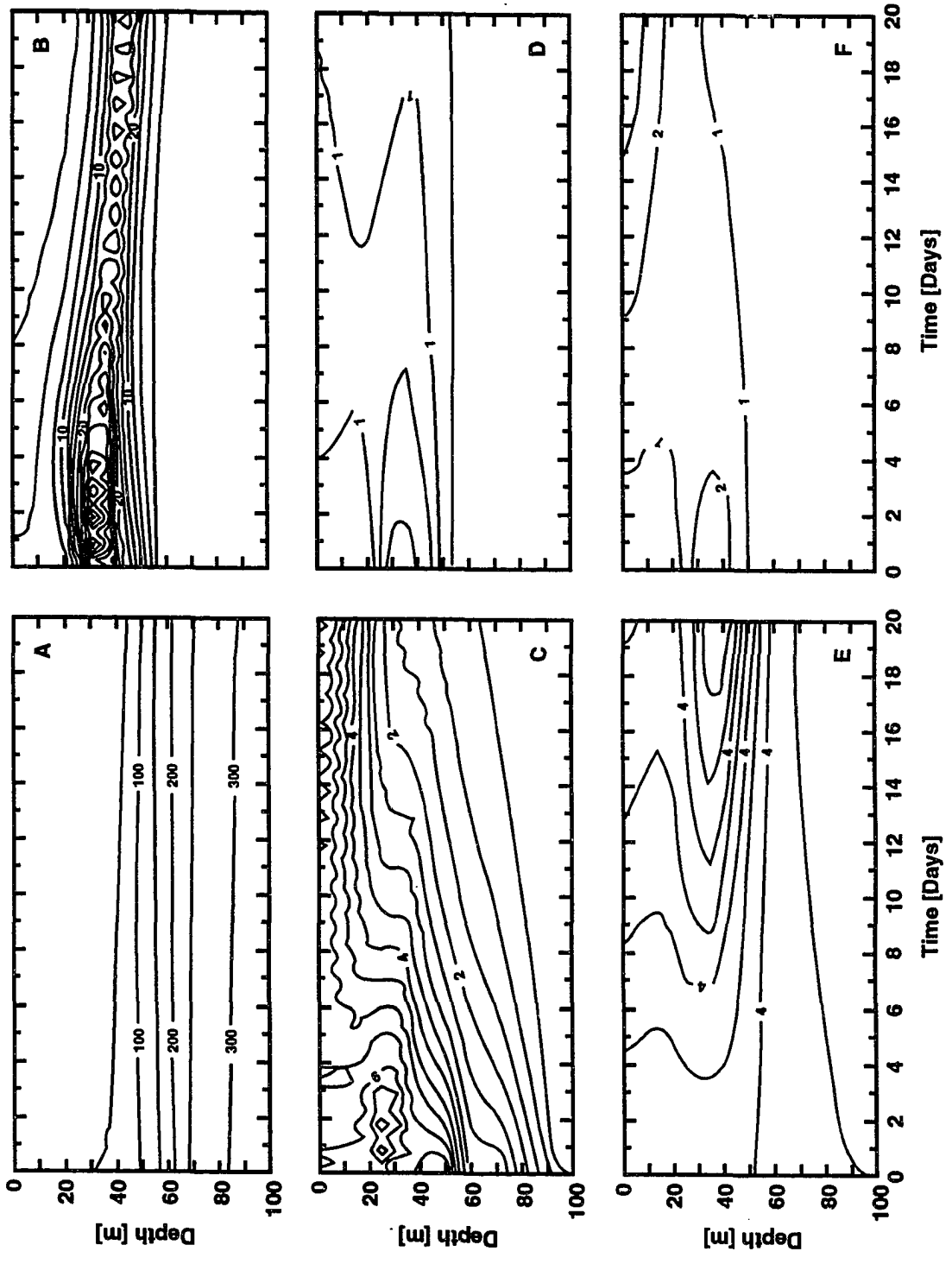

column. This trend in the simulated zooplankton distributions reflects the vertical distribution of their food supply and is similar to the patterns observed at the coastal and oceanic locations.

The depth-integrated concentrations of the large and small phytoplankton fractions (Fig. 45A and B) show a decrease and an increase, respectively, over the twenty day simulation. Copepod and euphausiid concentrations (Fig. 45C) decrease over time; whereas, doliolid concentrations increase. These patterns are similar to those obtained for the coastal location; however, the rate at which the patterns evolve is slower. As was found for the coastal and oceanic locations, the chlorophyll maximum was located near the nutricline, was composed primarily of large phytoplankton cells, and was formed as a result of *in situ* primary production (Fig. 46).

4.1.4 Lagrangian Drifter Simulation

The final set of simulations with the one-dimensional model were designed to simulate the biological distributions that would be encountered along the trajectory followed by a Lagrangian drifter released in the CTZ. The simulated distributions thus obtained can be compared to actual observations of nitrate, chlorophyll and zooplankton concentrations made while following a drifter for six days that had been released as part of the 1988 CTZ field studies. As a comparison, simulated distributions were obtained for conditions of no vertical advection and for the vertical advective field experienced by a drifter released in the simulated circulation fields (cf. Fig. 21). For the latter case, a drifter trajectory that closely followed the actual drifter trajectory was selected from the simulated drifter distributions described in Hofmann et al. (1991). The approach assumes that the

Figure 45. The 20-day time evolution of the simulated depth integrated (0 to 100 m) simulated concentrations of the **A**) large and **B**) small phytoplankton size fractions and **C**) zooplankton for the filament case. The zooplankton are denoted as, doliolids (small dashes), copepods (medium dashes), euphausiids (large dashes) and total zooplankton biomass (solid line).

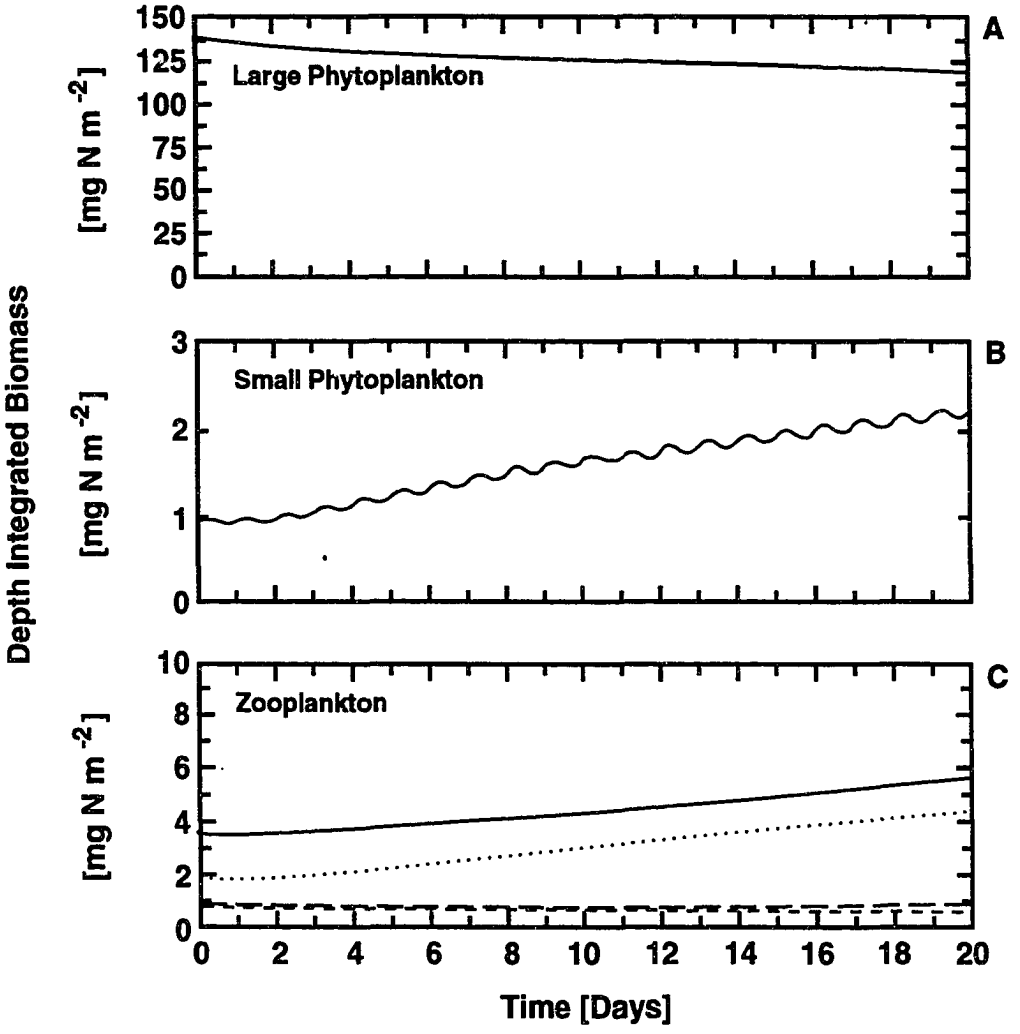

Figure 46. The vertical profile of individual terms in the one-dimensional model governing equations integrated over 1 day after (**A**) day 5 and (**B**) day 20 of the filament simulation.

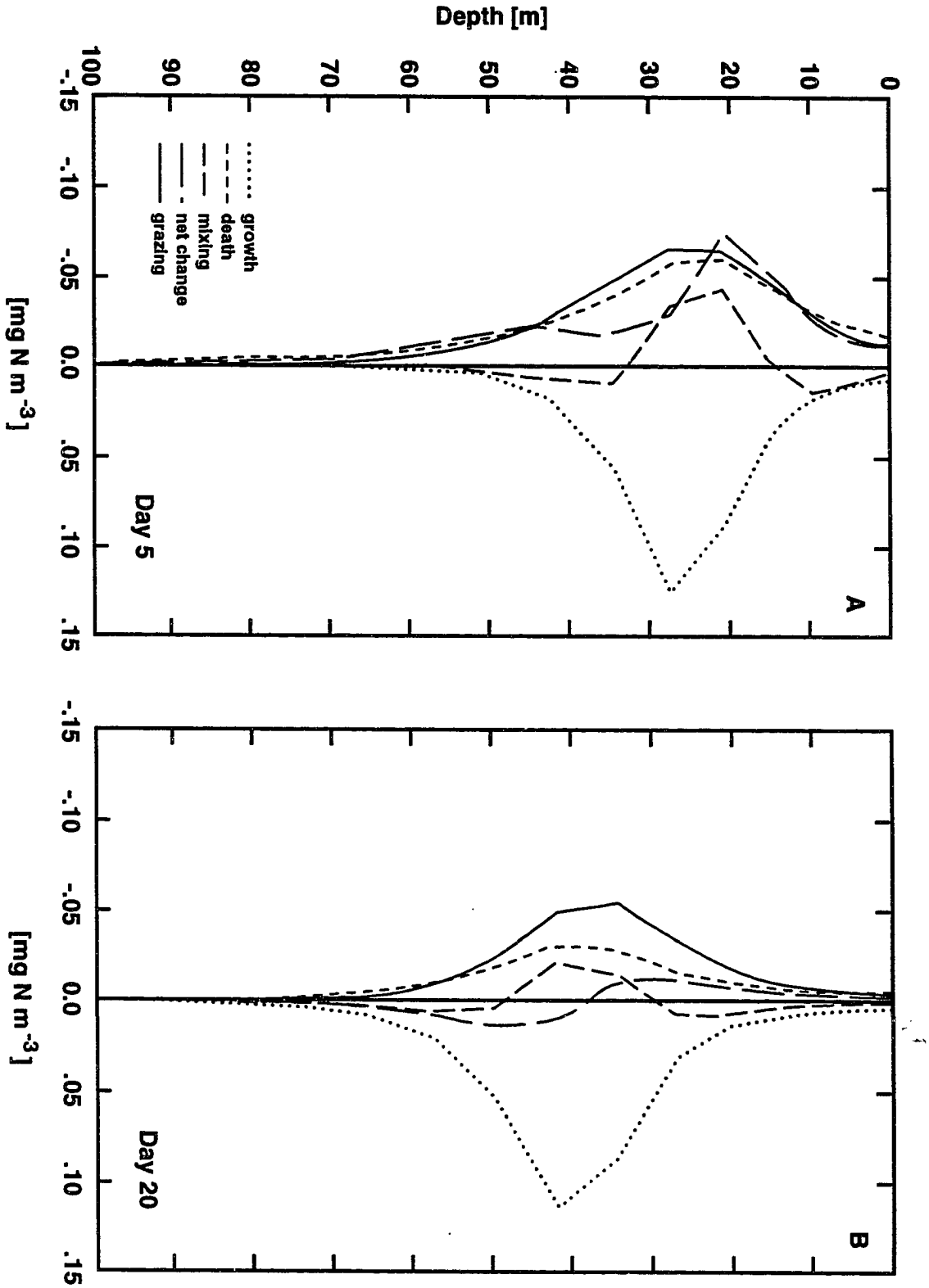

nutrient and biological distributions along the drifter trajectory result from *in situ* processes and vertical advection. Horizontal advective processes are assumed to be negligible. The temperature, nutrient and biological distributions were initialized with observations taken at the initial release point of the actual Lagrangian drifter. The orientation of the simulated drifters move from the nearshore coastal regions to offshore waters within a filament. The simulations were extended for twenty days. However, measurements made during the 1988 field study cover a period of only six days. Therefore, comparisons between the two can only be made for a short period of time.

The depth of the nutricline, defined as the depth of the 10 mg-N m^{-3}isopleth, deepens for both the no vertical advection and vertical advection conditions (Fig. 47). However, the final depth found for the former is shallower than for the latter, 45 versus 67 m. The observed depth of the nutricline (Fig. 47C) deepened from 34 to 70 m during the six days covered by the field study. This rate of decrease is much faster than that observed for either simulated distributions. Overall, the pattern in the observed nitrate field is closer to that obtained for the vertical advection case than for the no advection case.

The simulated chlorophyll fields obtained without (Fig. 48A) and with (Fig. 48B) vertical advection show the development of a subsurface chlorophyll maximum that deepens over the twenty day simulation. The rate of deepening is greater for the advective case, 1.5 m day^{-1} versus 0.75 m day^{-1}. A chlorophyll maximum was observed during the field study (Fig. 48C) and deepened from about

Figure 47. Time evolution of the simulated vertical nitrate distributions for conditions of **A**) no vertical advection and **B**) vertical advective field obtained from a circulation simulation for the CTZ. These simulated fields are compared to the **C**) observed nitrate fields measured while following a drifter released during the 1988 CTZ field studies. Triangles at the top of the lower panel indicate the times at which measurements were made. Values were obtained at intervening times by linear interpolation. Contour levels are 2.5 mg-N m^{-3} for all panels. Note scale change in the time axis between the upper two panels and the lower panel.

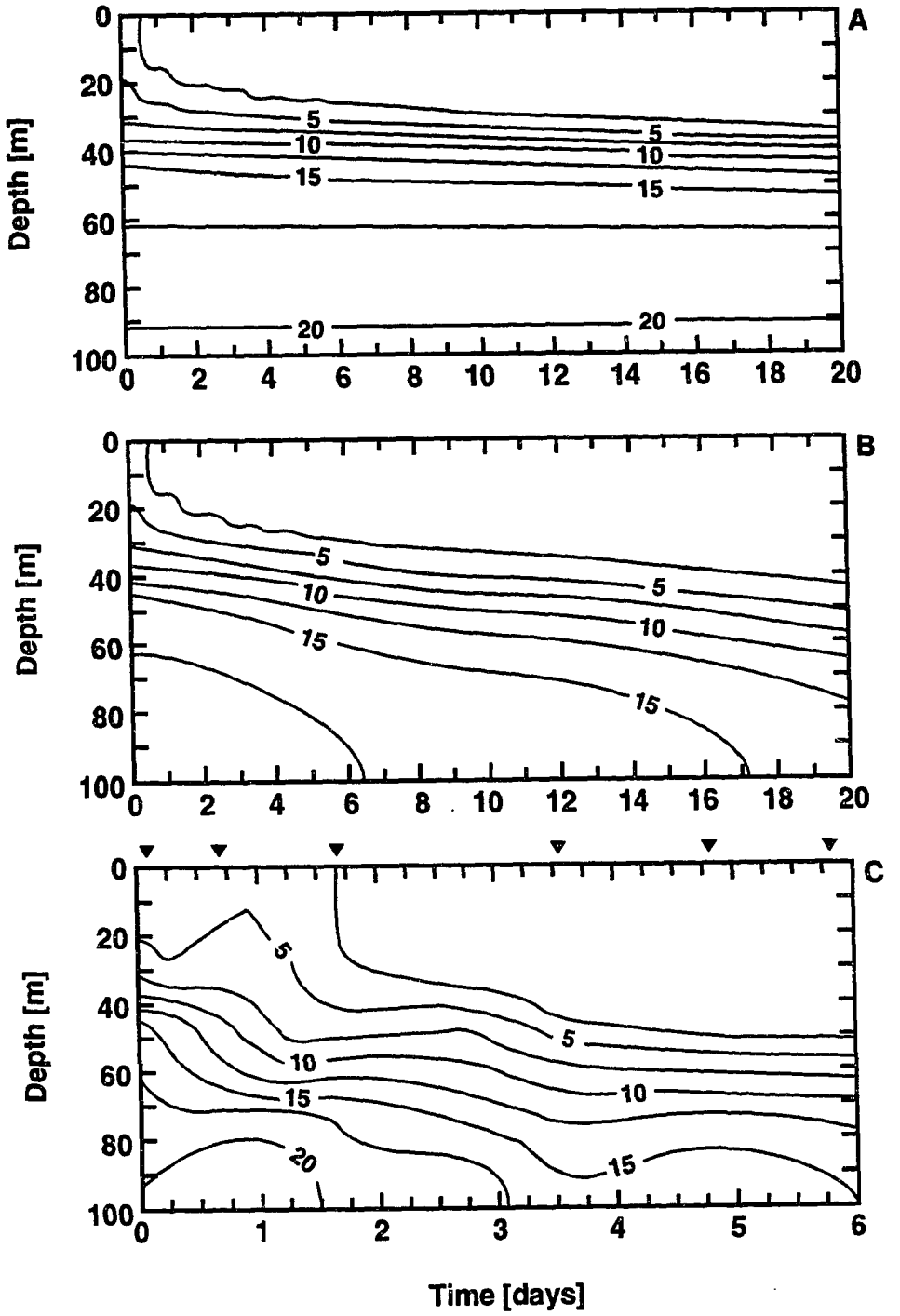

15 to 45 m during the six days encompassed by the observations. The vertical distributions and rate of deepening of the observed chlorophyll distribution is similar to that obtained for the vertical advection case.

The rapid deepening of the nutricline and chlorophyll maximum in the distributions of the CTZ field studies has been attributed to downwelling vertical velocity rates of 20 to 30 m d^{-1} (Kadko et al., 1991; Washburn et al., 1991). The maximum vertical velocities within the filament obtained from the CTZ circulation simulations are about 7 m d^{-1}. Hence, the simulated distributions will not deepen as rapidly as was observed. However, the overall patterns are similar and the simulations with and without vertical advection clearly demonstrate the importance of this process in regulating the vertical distribution of biological quantities.

As a final comparison, the simulated reproductive effort for the three zooplankton species was obtained along the drifter track from the simulation that included vertical advection (Fig. 49). The reproductive effort is defined as the amount of assimilated food remaining after growth, respiration and molting that is available for use in reproduction. The simulated reproductive effort for the copepod (*E. californicus*) and the euphausiid (*E. pacificus*) are highest during the initial six to seven days of the simulation when the simulated drifter was in the nearshore region of the filament. In contrast, the doliolid (*D. gegenbauri*) showed the highest reproductive effort at the end of the simulation when the drifter was located offshore. These simulated results are in qualitative agreement with the observations of zooplankton reproductive effort from the CTZ. Highest biomass and egg production rates for *E. californicus* and *E. pacificus* were found in the nearshore region of the filament (Smith and Lane, 1991; Mackas et al., 1991). The

Figure 48. Time evolution of the simulated vertical chlorophyll distributions for conditions of **A**) no vertical advection and **B**) vertical advective field obtained from a circulation simulation for the CTZ. These simulated fields are compared to the **C**) observed chlorophyll fields measured while following a drifter released during the 1988 CTZ field studies. Triangles at the top of the lower panel indicate the times at which measurements were made. Values were obtained at intervening times by linear interpolation. Contour levels are 0.25 mg-chl *a* m^{-3}, 0.25 mg-chl *a* m^{-3} and 0.5 mg-chl *a* m^{-3}, respectively. Note scale change in the time axis between the upper two panels and the lower panel.

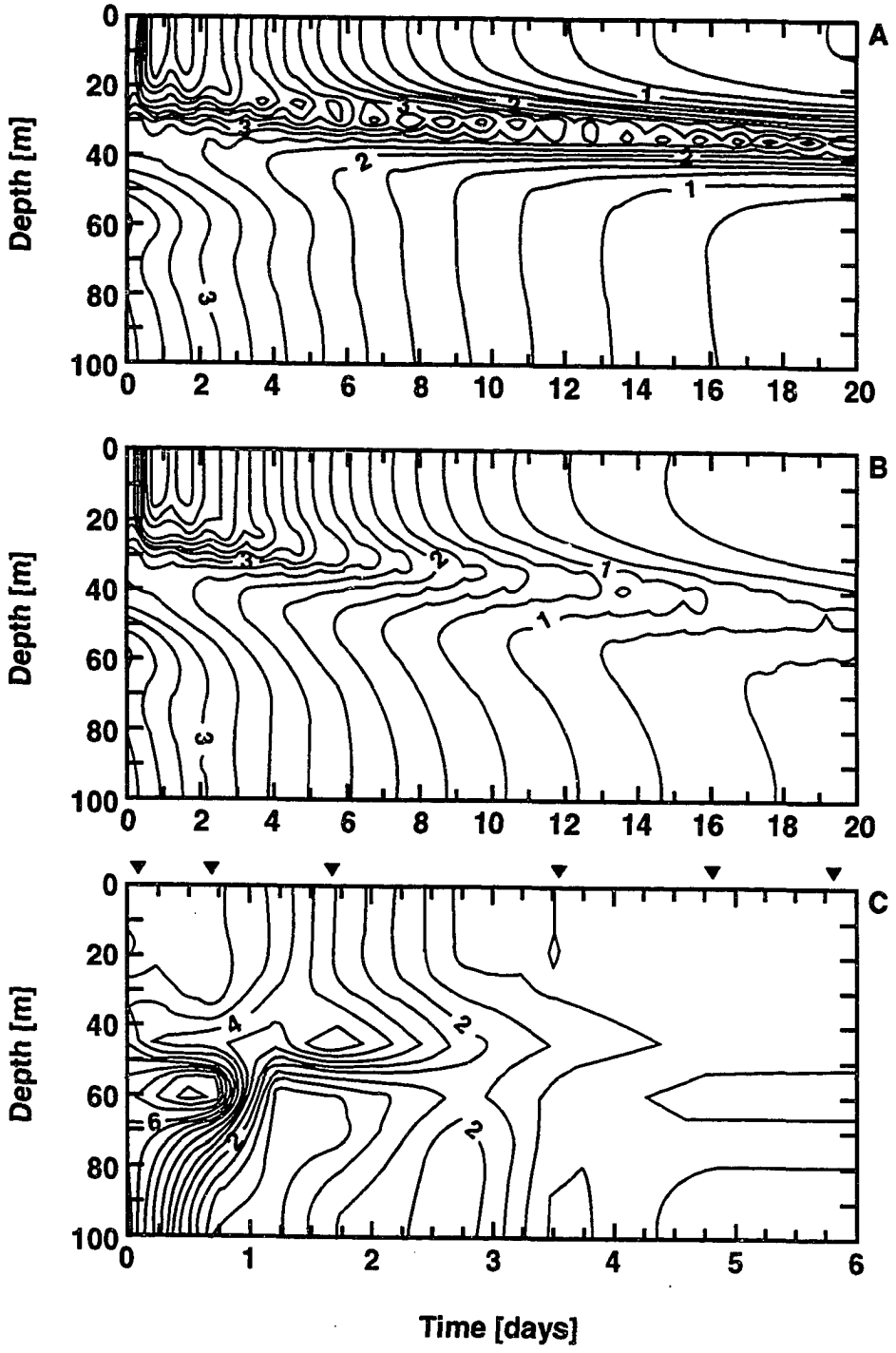

highest biomas of *D. gegenbauri* was found in the offshore regions (Mackas et al. 1991). Reproductive rates were not measured for this animal.

Figure 49. The 20-day time evolution of the simulated zooplankton reproductive effort (μg N m^{-3} day^{-1}) with depth for the vertical velocity case. High reproductive rates are observed early in the simulation for the **A**) Euphausiid and **B**) Copepod fractions, when the drifter was within region of filament formation. Conversely, the simulated reproductive rates for the Doliolid **C**) fraction was highest at the end of the simulation, when the drifter was furthest from shore. Contour levels are 100 μg N m^{-3} day^{-1}, 10 μg N m^{-3} day^{-1} and 10μg N m^{-3} day^{-1}, respectively.

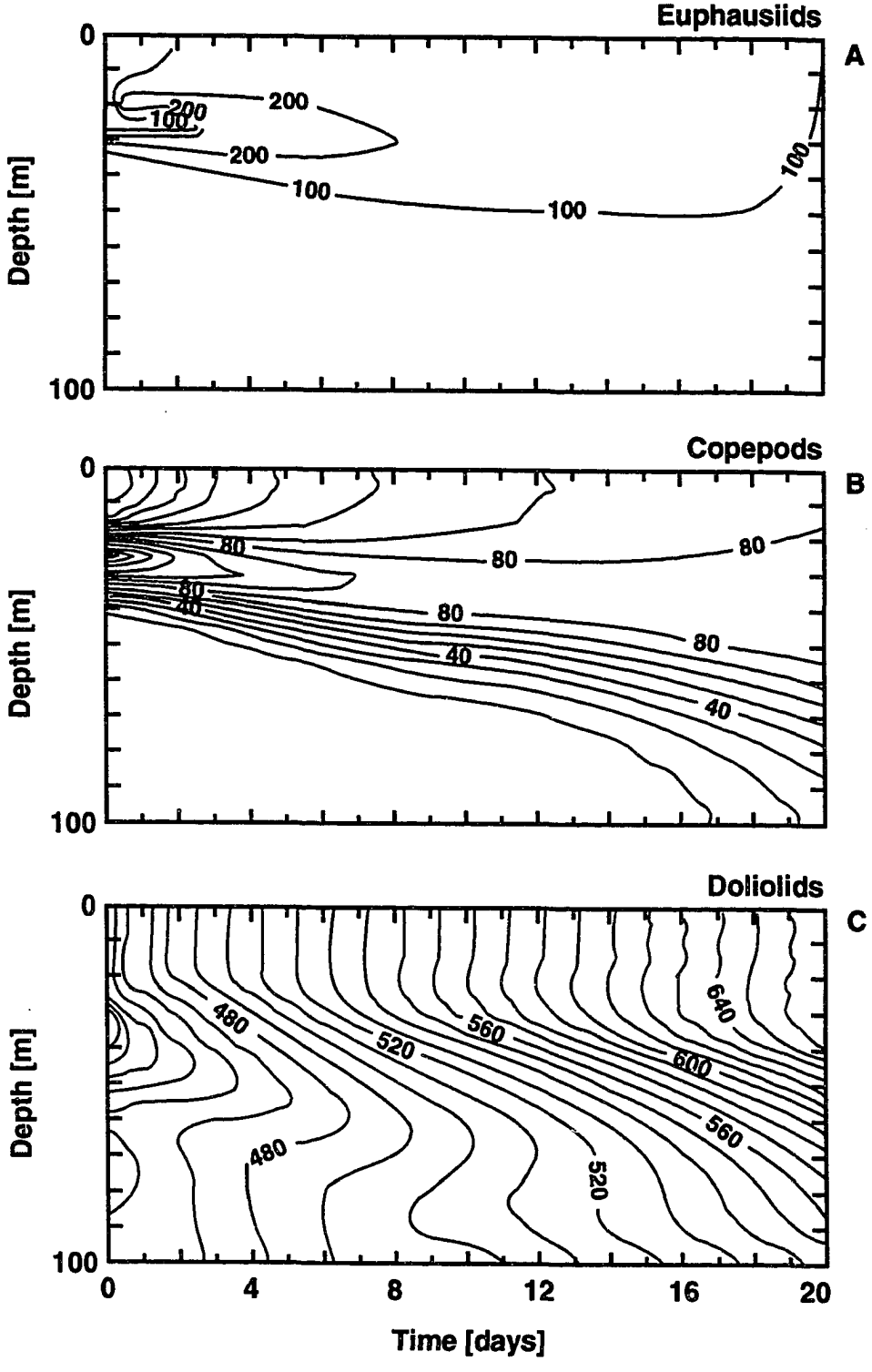

4.2 Three-Dimensional Physical-Bio-Optical Model

The results from the one-dimensional model presented in the previous section have focused on the interactions among the food web components, interactions with the underwater light field and the effect of vertical velocities. These simulations show clearly the importance of the many biological and optical processes in structuring the vertical and biological distributions. However, biological distributions in the CTZ are also affected by horizontal advective processes. Inclusion of the horizontal dimension requires that the food web and optical models be combined with a three-dimensional circulation model. For this study, the three-dimensional circulation fields obtained for the CTZ using the circulation model described in section 3.2 were used. This allows investigation of the processes that result in the three-dimensional time-dependent evolution of biological distributions in the CTZ. The following sections describe the circulation fields used to advect and diffuse the biological distributions. This is followed by a description of the simulated three-dimensional optical and biological fields.

4.2.1 Simulated Circulation Fields

The three-dimensional model simulations used twenty days of simulated circulation fields that were obtained after 140 days of integration. This time corresponds to a point in the circulation simulation when a filament was observed to form and develop offshore (Haidvogel et al. 1991*a*). The large-scale horizontal structure of the simulated flow field from day 140 (Fig. 50A), which is the initial field for the biological simulations, shows primarily southward flow along the coastal boundary that is associated with the California Current. Average southward velocities are in the order of 45 cm s^{-1}. Near the center of the model region, an offshore-extending

filament has formed in the vicinity of a coastal bump. Flow is offshore on the northern side of the filament and onshore on the southern side of the filament, with velocities on both sides of about 50 cm s^{-1}. The narrow feature located north and offshore of the filament is the remnant of a previously formed filament.

The vertical flow patterns show small-scale regions of upwelling and downwelling along the coastal shelf region and somewhat larger regions of upwelling and downwelling along the coast and near the shelf break, about 50-100 km offshore. These features have been attributed to small scale frontal instabilities and possibly coastal trapped waves (Haidvogel et al. 1991*a*). Vertical velocities in the offshore extending filament indicate downwelling and upwelling in the north and south sides of the feature, respectively. Maximum upwelling velocities are on the order of 10-20 m day^{-1}.

Ten days later (Fig. 50B), the filament has elongated and extends offshore about 430 km. The across-filament width has decreased to about 100 km and a cyclonic eddy appears to be forming at the outer end of the feature. Strong offshore and inshore velocities are found on the northern and southern sides of the filament, respectively and maximum velocities within the filament reach 73 cm s^{-1}. The filament has also moved southward by about 70 km relative to its position on day 140.

By day 160 (Fig. 50C) the filament extends offshore about 590 km and a cyclonic eddy is forming at its outer extent. A weaker anticyclonic eddy is forming to the north of the feature. Maximum velocities in the filament are about 90 cm s^{-1}.

Figure 50. Horizontal distribution of vertical velocity (color; m s^{-1}) and density (line contours; σ_t) at 100 m depth from day (**A**) 140, (**B**) 150 and (**C**) 160 of the circulation simulation. Line contours for density range from 23.6 to 25.4 by intervals of 0.2. Upwelling and downwelling velocities with magnitudes greater than 11 x 10^{-5} m s^{-1} are shown in dark red and dark blue, respectively. Details of the CTZ circulation model are given in Haidvogel et al. (1991b).

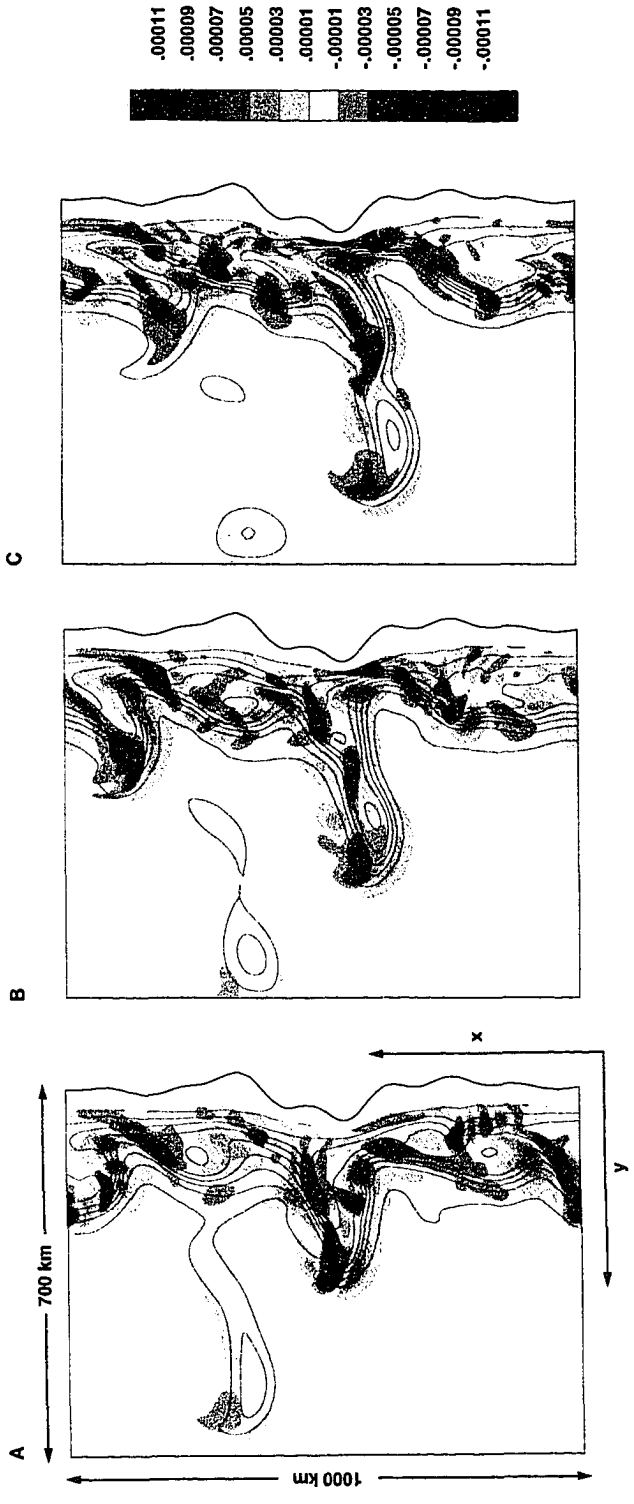

4.2.2 Simulated Biological and Optical Distributions

The distribution of the phytoplankton, integrated over the depth of the euphotic zone (1% PAR), on day 140 (Fig. 51A) show the highest concentrations ($\approx$44 mg-N m^{-3}) along the coast and within the filament. The sharp gradient in the integrated phytoplankton field at the coast coincides with the density gradient at this location (cf. Fig. 50A). The euphotic zone depth is shallowest ($\approx$30 m) along the coastal regions and within the filament, which coincide with the regions of highest chlorophyll concentration. The euphotic zone deepens to about 180 m offshore of the shelf region and outside of the filament. Sharp gradients in the depth of the euphotic zone occur in the coastal region and along the northern and southern sides of the filament.

Over the next ten days (Fig. 51B) the horizontal structure of the phytoplankton evolves similar to that for the circulation field. Phytoplankton concentrations of 25 mg-N m^{-3}now extend about 440 km offshore in the filament. However, the overall phytoplankton concentration in the filament has decreased relative to that at day 140 (Fig. 51A). The decrease arises through loss of biomass from the filament by across-filament shear (Hofmann et al. 1991) and by zooplankton grazing. The highest phytoplankton concentrations in the filament occur along the axis where the velocities are lowest. On the northern and southern sides of the filament, where velocities are the highest, a sharp gradient in phytoplankton concentration exists. This gradient is stronger on the southern side of the filament.

The large-scale patterns in euphotic zone depth are similar to those observed on day 140. The primary difference is the sharpening of the gradient in the euphotic zone at the edges of the filament. In these regions, the euphotic zone depth

Figure 51. Horizontal distributions of the phytoplankton ($LPP + SPP$) field integrated over the depth of the euphotic zone (color; mg N m^{-3}) and euphotic zone depth, (line contours; m) for day (**A**) 140, (**B**) 150 and (**C**) 160 from the three-dimensional physical-bio-optical model. Line contours for euphotic zone depth range from 30 to 180 m, 40 to 180 m and 60 to 180 m, respectively, by intervals of 10. The euphotic zone depth is defined as the depth at which PAR values are 1% of that calculated at the surface.

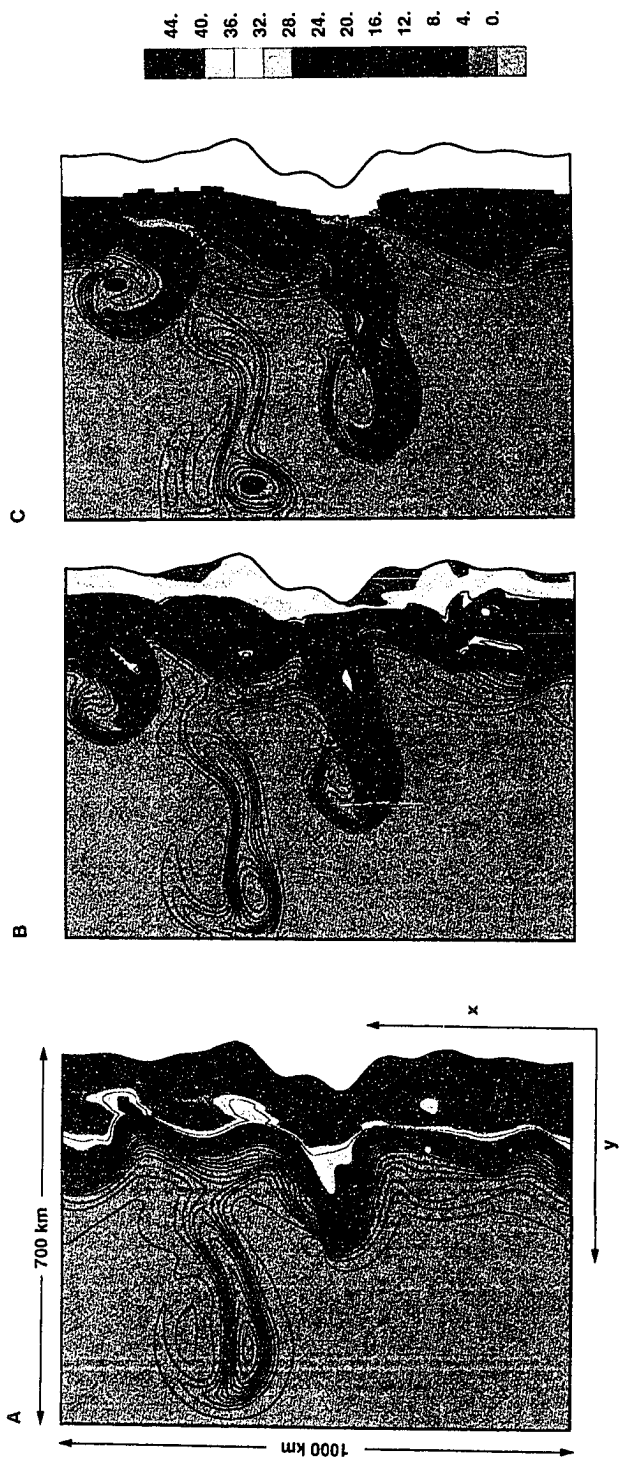

shallows from 180 m outside the filament to 40 m inside the filament in a distance of 35 km. Similar to the phytoplankton fields, the gradient in the euphotic zone depth is asymmetric, being stronger on the southern side of the feature.

After another ten days (Fig. 51C), the large scale structure in the distribution of the phytoplankton still follows that of the circulation field. However, the magnitude of the phytoplankton concentration is reduced by about 50% relative to the initial concentrations. Zooplankton grazing is the primary process responsible for this decrease in biomass. The primary change by day 160 is that the asymmetry in euphotic zone decreases and the filament has become more pronounced. On the northern side of the filament the euphotic zone depth shallows from 180 m to 60 m in a distance of 80 km, while on the southern side it shallows from 180 m to 60 m in 30 km.

The vertical distribution of the subsurface PAR field at these along-shore locations (Fig. 52) shows that the penetration of a given isolume is quite variable moving onshore to offshore in the filament. Decreased light penetration and hence, a shallower euphotic zone occurs on both edges of the filament due to the enhanced chlorophyll concentrations that develop in response to the nutrients upwelled along the edges of the filament. The magnitude of the upwelling is greater on the southern side of the filament (cf. Fig. 50); hence, the stronger gradient in euphotic zone depth.

4.2.3 Across-Shore Carbon Distribution and Flux

It has been suggested that the offshore-extending filaments in the CTZ provide a mechanism for transporting carbon and nitrogen from coastal regions to the oligotrophic offshore waters (Strub et al., 1991; Jones et al., 1991). To test this

Figure 52. Simulated vertical distributions of the upper PAR field in the upper 100 m from model day 156 from along-shelf sections located (**A**) 77 km, (**B**) 280 km and (**C**) 511 km offshore. Contours are in Einsteins m^{-2} s^{-1} x 10^{-4} with a contour interval of 1. The actual positions of these sections are shown in Figure 22.

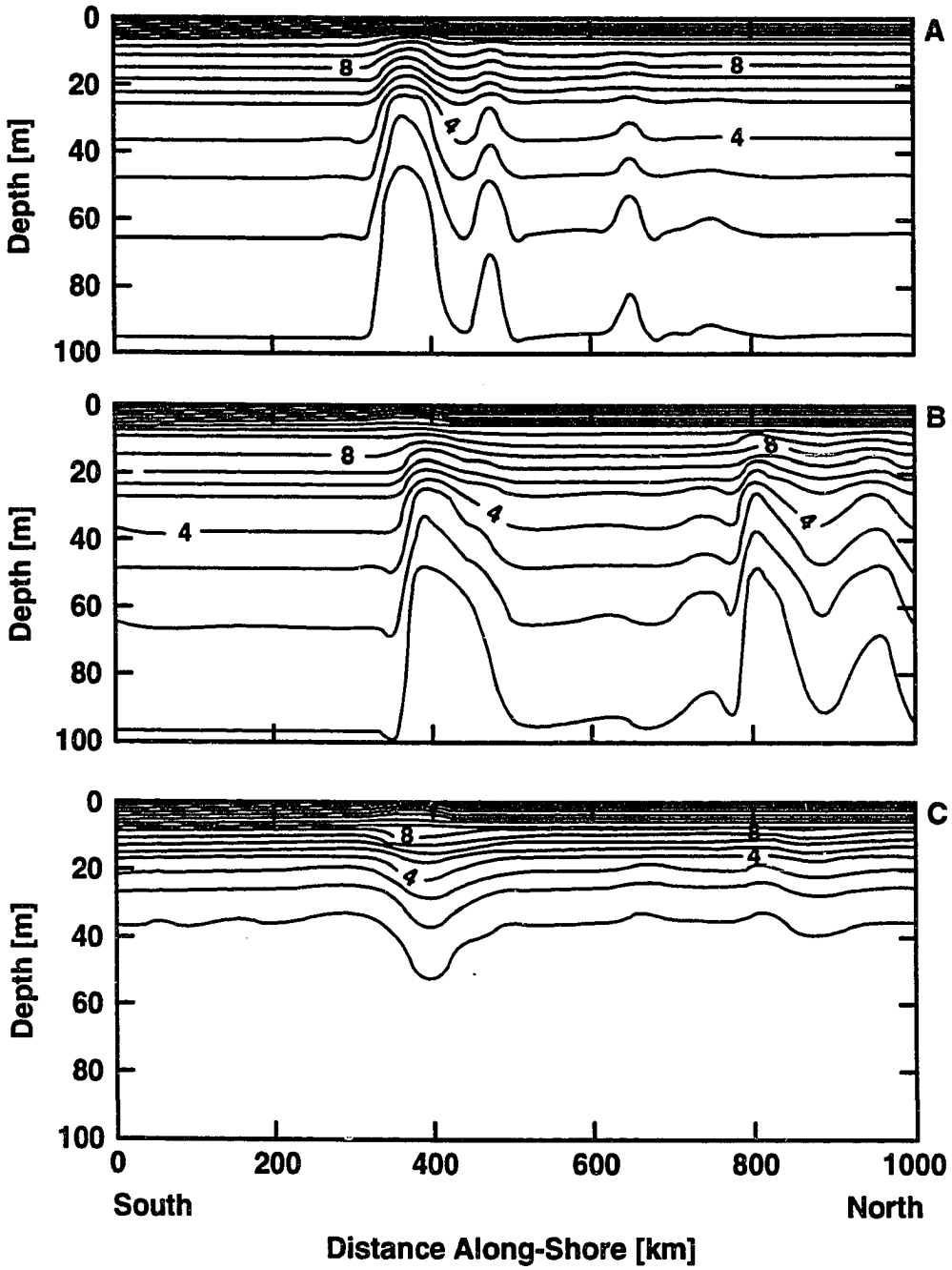

hypothesis, the simulated biological distributions were converted from nitrogen to carbon using a C:N ratio of 6 and summed. These values, when multiplied by the across-shore velocity component, provide an estimate of the total carbon flux. It should be noted that regions of high carbon flux can coincide with regions of high across-shore velocities and are not necessarily indicative of regions of high carbon concentrations. The resultant surface carbon flux distributions obtained in this manner are shown in Figs. 53 and 54.

Initially, a region of offshore surface carbon flux that reaches values of greater than 21 C $m^{-2}s^{-1}$, occurs along the northern edge of the filament (Fig. 53A). A smaller region of onshore flux occurs along the southern edge of the feature. Smaller regions of offshore and onshore surface carbon flux are distributed along the coastal and shelf break regions. These smaller scale features seen in the circulation fields.

By model day 150 (Fig. 53B), the regions of offshore and onshore carbon flux associated with the filament extend offshore to about 450 km. The offshore and onshore surface carbon fluxes are essentially equal with maximum values of about 21 mg C $^{-2}s^{-1}$. By day 160 (Fig. 53C), the across-shore surface carbon flux is reduced because of the overall reduction in phytoplankton and zooplankton concentrations. The largest offshore and onshore fluxes are still associated with the high across-shore velocities associated with the filament (Fig. 54) and are still somewhat symmetric. This pattern would then imply there is a little to no net transport of surface carbon associated with the filament.

To further investigate carbon transport in the CTZ the depth-integrated (to 1% PAR) carbon flux was calculated (Fig. 55). When presented in this fashion,

Figure 53. Horizontal distributions of the surface phytoplankton ($LPP + SPP$) carbon flux field (color; mg C m^{-2} s^{-1}) and surface phytoplankton ($LPP + SPP$) carbon field (line contours; mg C m^{-3}) for day (**A**) 140, (**B**) 150 and (**C**) 160 from the three-dimensional physical-bio-optical model. Line contours for surface phytoplankton carbon range from 25 to 400 mg C m^{-3} by intervals of 25, 25 to 175 mg C m^{-3} by intervals of 25 and 10 to 70 mg C m^{-3} by intervals of 10, respectively. Red colors indicate regions of offshore carbon flux. Dark blue colors indicate regions of onshore carbon flux.

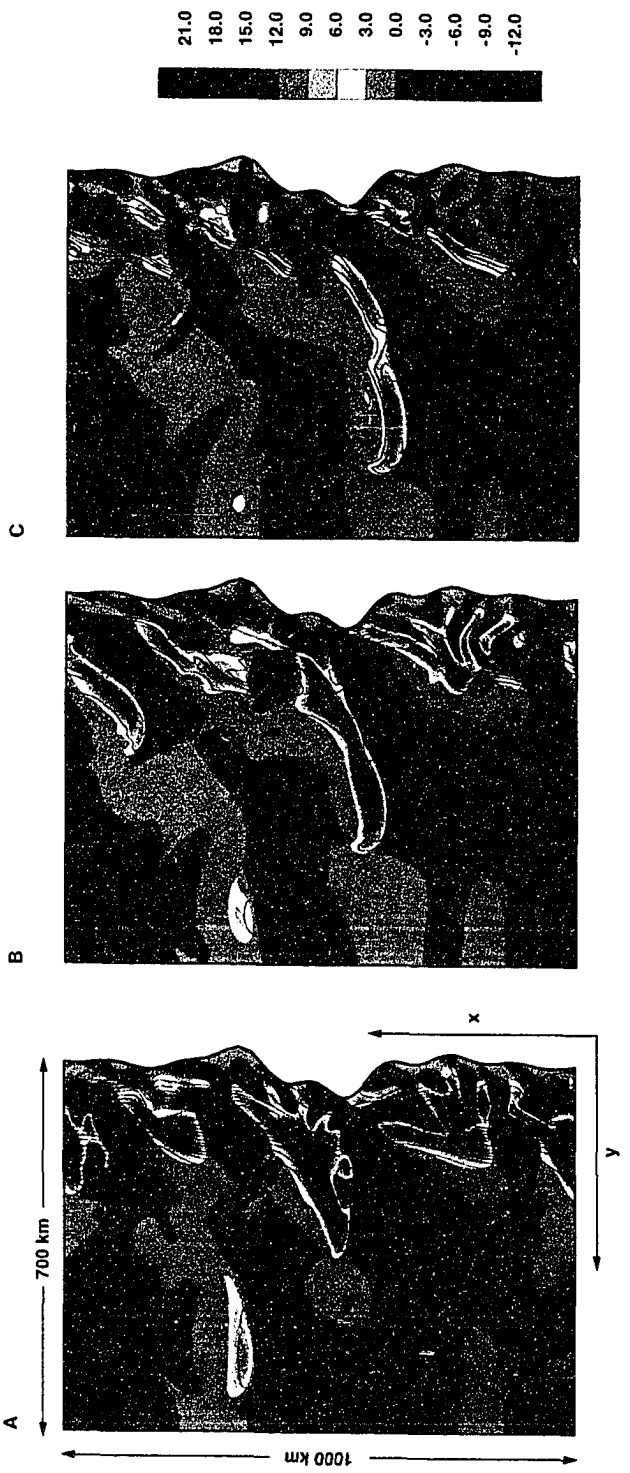

Figure 54. Horizontal distributions of the surface phytoplankton ($LPP + SPP$) carbon flux field (color; mg C m^{-2} s^{-1}) and surface across-shore velocity field (line contours; m s^{-1}) for day (**A**) 140, (**B**) 150 and (**C**) 160 from the three-dimensional physical-bio-optical model. Line contours for surface across-shore velocity field range from -0.8 to 0.9 m s^{-1}, -0.7 to 0.9 m s^{-1} and -0.6 to 1 m s^{-1}, respectively, by intervals of 0.1. Red colors indicate regions of offshore carbon flux. Dark blue colors indicate regions of onshore carbon flux.

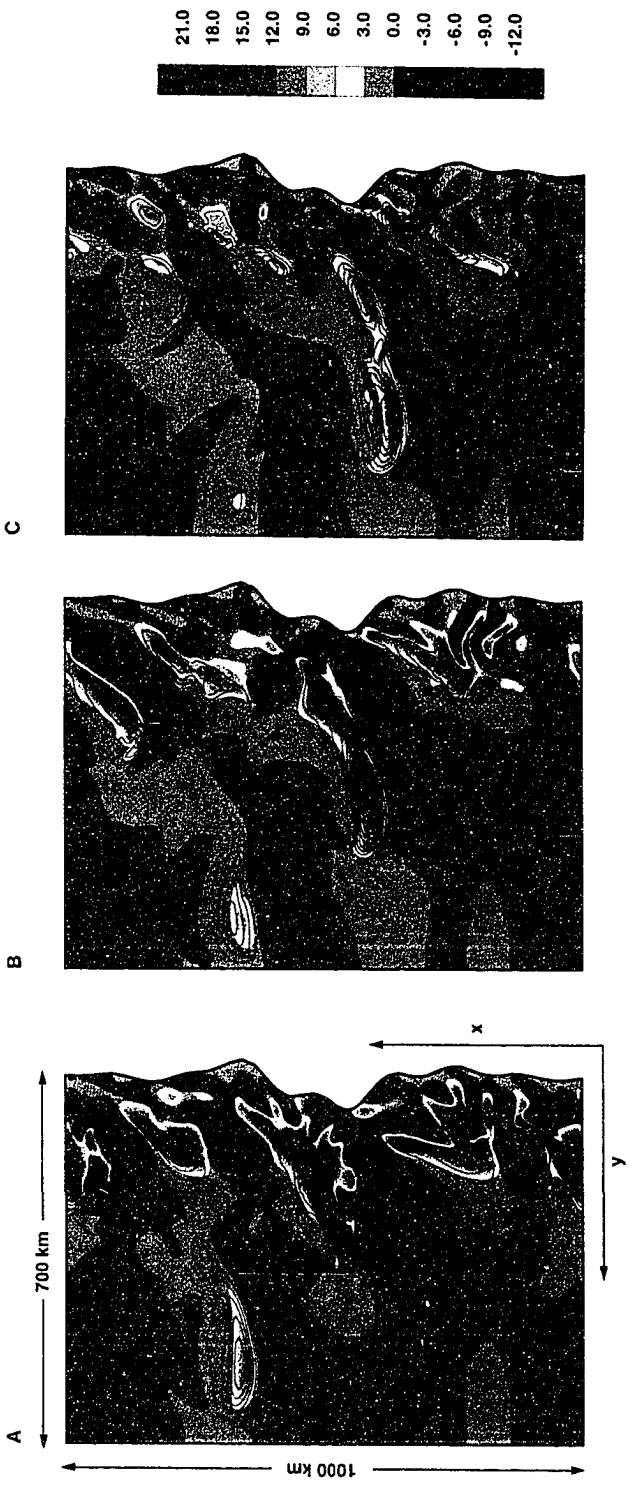

pronounced regions of asymmetry appear in the onshore and offshore carbon flux. In particular, the offshore carbon flux on the northern side of the filament is much greater than the onshore carbon flux to the south. As the simulated fields evolve over the next twenty days, this asymmetry in offshore and onshore carbon flux in the filament persists. However, the magnitude of the flux diminishes over this time.

The depth-integrated carbon flux estimates shown in Fig. 55 indicate that there may be preferred regions in the model domain for on and offshore carbon flux. To consider this, the carbon flux as a function of distance across shelf was obtained by integrating the simulated carbon distributions vertically and along shore as

$$flux(y) = \int_0^{-h} \int_0^{1000\ km} (vC)dA, \tag{81}$$

where $flux(y)$ is the across-shore carbon flux, v is the across-shore advective velocity and C is the sum of the carbon concentrations for all the biological constituents, including detritus. The resulting across-shore carbon transports calculated from the simulated distributions at days 140, 150 and 160 are shown in Fig. 56.

On day 140, the maximum offshore and onshore carbon flux (Fig. 56A) were 5600 and 4000 kg C s^{-1}, respectively. The maxima in both was located about 150 km offshore, with the onshore maximum being slightly inshore of the offshore maximum. The net across-shore carbon flux (Fig. 56B) was 2200 kg C s^{-1} offshore and was centered about 200 km offshore. Over the next twenty days of integration the magnitude of the onshore and offshore carbon fluxes diminished and the peak of the maximum flux shifts offshore. The net transport continues to be offshore

Figure 55. Horizontal distributions of the depth-integrated total carbon (*phytoplankton* + *zooplankton* + *detritus*) flux field (color; g C m^{-1} s^{-1}) and depth integrated carbon field (line contours; mg C m^{-2}) for day (**A**) 140, (**B**) 150 and (**C**) 160 from the three-dimensional physical-bio-optical model. Line contours for depth integrated carbon fields range from 25 to 425 mg C m^{-2}, 25 to 250 mg C m^{-2} and 25 to 100 mg C m^{-2}, respectively, by intervals of 25. Red colors indicate regions of offshore carbon flux. Dark blue colors indicate regions of onshore carbon flux.

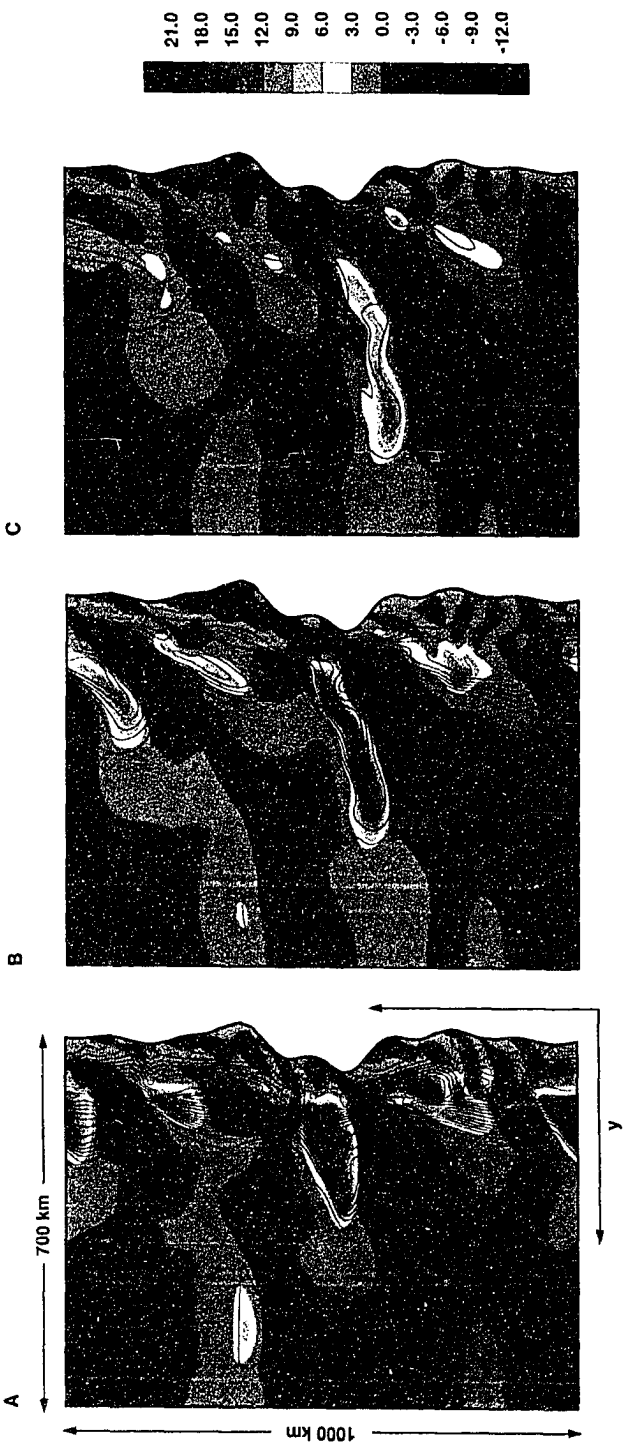

Figure 56. **A**) Area-integrated across-shelf carbon flux calculated from the simulated biological distributions on day 140, 150 and 160. **B**) Net across-shelf carbon flux for model day 140, 150 and 160. Positive values indicate offshore carbon flux; negative values are onshore flux.

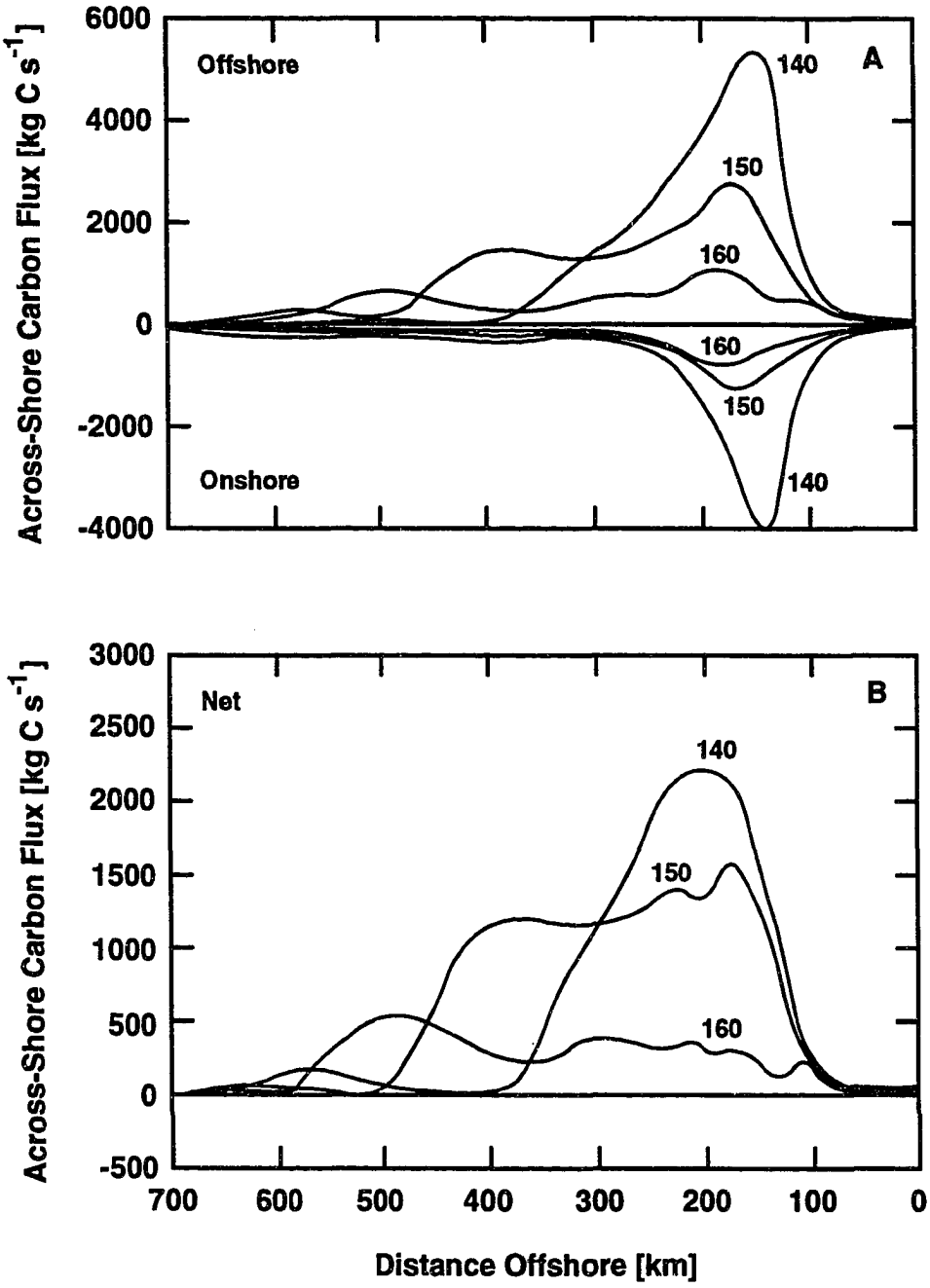

at the end of the simulation (day 160) the maximum offshore transport is 500 kg C s^{-1} and is located about 500 km from the coast.

The net across-shore carbon flux values can be further integrated over the time of the simulation to obtain a total across-shore carbon flux,

$$tflux(y) = \int_0^{20\ days} flux(y)dt, \tag{82}$$

where $tflux(y)$ is the total across-shore carbon flux. The results of this calculation (Fig. 57) show that no onshore transport of carbon occurred during the twenty day simulation. Offshore carbon transport occurred at several locations across the shelf, with the largest peak (35 x 10^9 g C) being about 500 km offshore. Smaller offshore transports occur at 100 and 300 km offshore.

4.3 Lagrangian Drifter Experiments

Simulated Lagrangian drifter experiments were carried out between model day 140 and 160. A total of 880 drifters were released in the model domain at points which surrounded the location at which a filament was observed to form (cf. Fig. 19). Three sets drifters were released at each location at depths of 30, 60 and 90 m and were followed for 20 days. The position of these drifters varied over time as a result of the vertical and horizontal velocities that they experienced. A fourth drifter set was released at each location; however this drifter set was constrained to remain at 30 m. The position of this drifter set varied over time only as a result of horizontal velocities.

The resulting simulated passive Lagrangian paths allows for tracing of the temporal evolution of the biological fields within a Lagrangian water parcel, and

Figure 57. Total across-shore carbon transport after 20 days of simulation. Positive values indicate offshore across shelf transport.

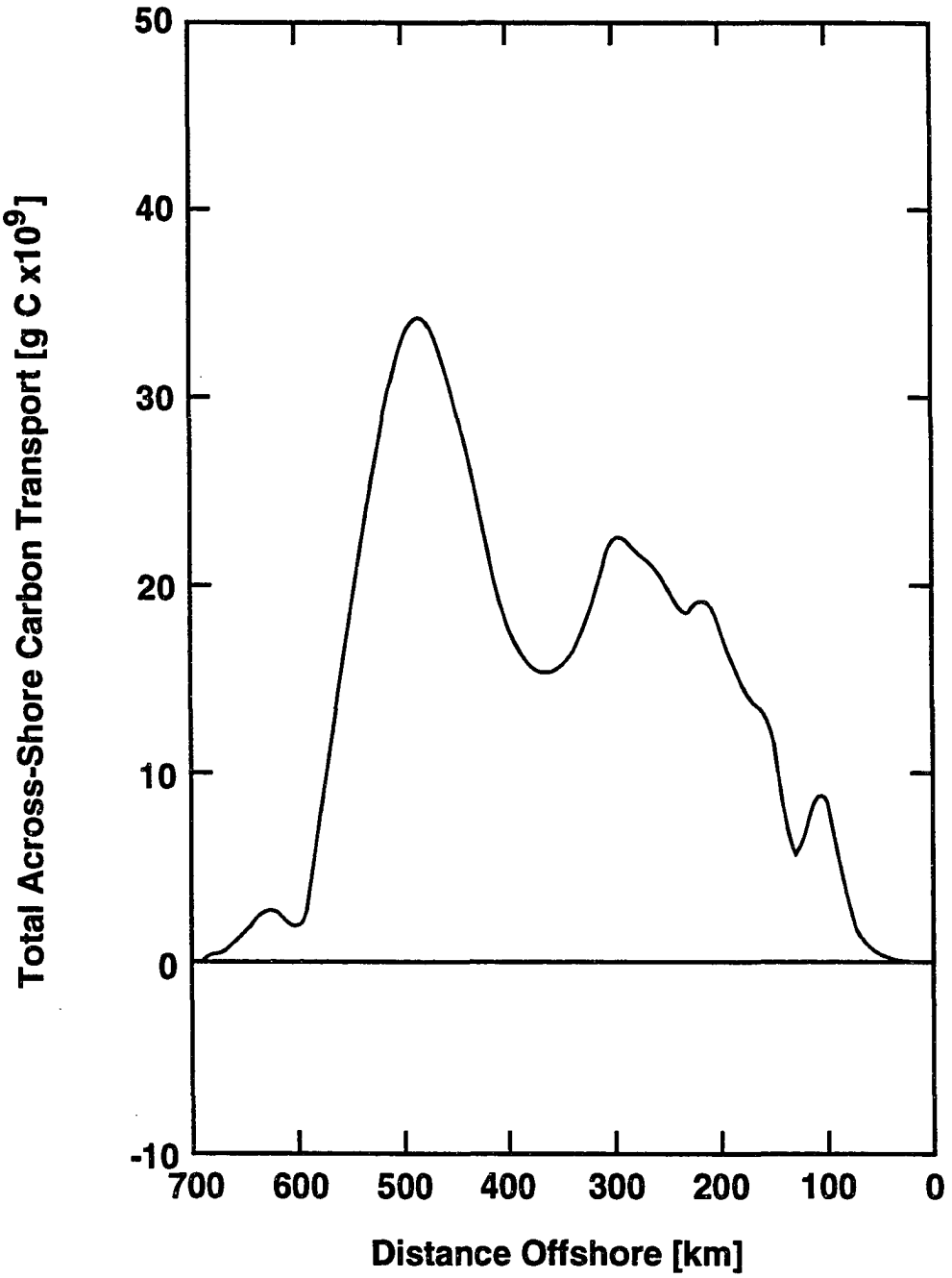

provides an estimate of the time scales of the associated CTZ plankton populations. These simulated fluid parcel paths are compared to actual drifter data obtained during the CTZ field experiments. The resulting paths taken by the drifters allows for vertical sampling of the three-dimensional fields as the drifter was advected through the model domain. This form of numerical data sampling is similar to the actual sampling scheme used by Abbott et al. (1990) and Mackas et al. (1991) and thus the results from these were compared.

The final set of results obtained from the three-dimensional physical-bio-optical model consisted of extracting the biological distributions along trajectories followed by drifters released in the simulated circulation fields. Such an approach allows quantification of the changes in relative abundance of the phytoplankton and zooplankton populations that occur moving from the nearshore neritic environment to offshore waters.

4.3.1 Composite Drifter Trajectories and Velocities

The drifter array was initially positioned upstream of a filament that formed in the model region (cf. Fig. 20). This allowed drifters to be entrained in the filament as it developed and extended offshore. A detailed analysis of the general transport patterns and residence times derived from an analysis of these drifters is given in Hofmann et al. (1991). However, a brief description is given here as a basis for the biological distributions given in the following section.

The general drifter patterns are shown in Fig. 58. Most of the drifters released within 150 km of the coast were transported to the south with the southward flow of the California Current. Those drifters released further offshore were transported offshore in the filament. Many of the drifters that were located along the southern

side of the filament were returned to the coastal regions by the cyclonic flow that occurs there. These drifters that reached the outer extent of the filament became entrained in either the cyclonic or anticyclonic eddies that formed at the offshore extent of this feature.

The vertical velocities experienced by the drifters released at 90 m (Fig. 58B) show that those drifters that were entrained in the filament were downwelled as they were transported offshore. Downwelling velocities ranged from 47 to 55 meters per day. The minimum and maximum depths experienced by these depths were 15.8 and 207.7 m respectively. Upwelling velocities were experienced by drifters on the southern side of the filament and by those transported southward along the coast.

4.3.2 Biological Distributions

The phytoplankton concentrations (small and large) along the drifter trajectories (Fig. 59) show highest concentrations, about 392.5 mg N m $^{-3}$ at the onshore end of the trajectories. As the drifters moved offshore in the filament, phytoplankton concentrations decreased. A similar decrease in concentration with time occurs along the trajectories of drifters not entrained in the filament.

The phytoplankton populations at the onshore base of the filament initially consisted of primarily large cells (Fig. 60). As the drifters moved offshore in the filament the relative abundance of the phytoplankton population shifted to dominance by the smaller size fraction. This change in dominance increased with increasing distance offshore. At the offshore extent of the filament, the phytoplankton populations to the south of the feature had a higher percentage of

Figure 58. Composite of the simulated drifter trajectories. (**A**) Vertical displacement in meters along the trajectories of the variable depth drifters released at 90-meters. Color along the trajectory indicates the depth in meters of the drifter, and ranges from 207.7 m (dark blue) to 15.8 m (dark red). Any drifter depth deeper than 150.0 m is shown in dark blue and any drifter depth shallower than 50.0 m is shown in dark red. (**B**) Vertical velocity in meters per second experienced by the variable depth 90-m drifters along their trajectories. Color along the trajectory indicates the magnitude of the vertical velocity (m s^{-1}) and the colors are chosen to show details of the vertical velocity, which ranges from -47 m day^{-1} (dark blue) to 55 m day^{-1} (dark red). Any vertical velocity larger than 10 m day^{-1} is shown in dark blue and smaller than -10 m day^{-1} is shown in dark red.

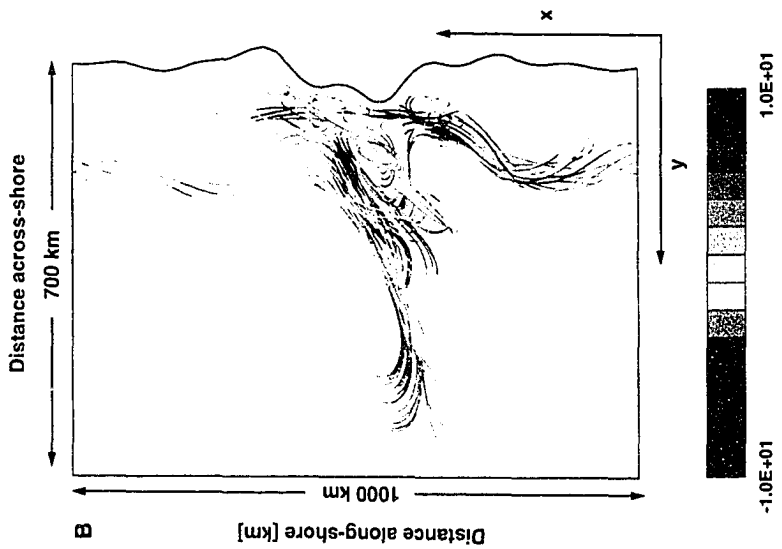

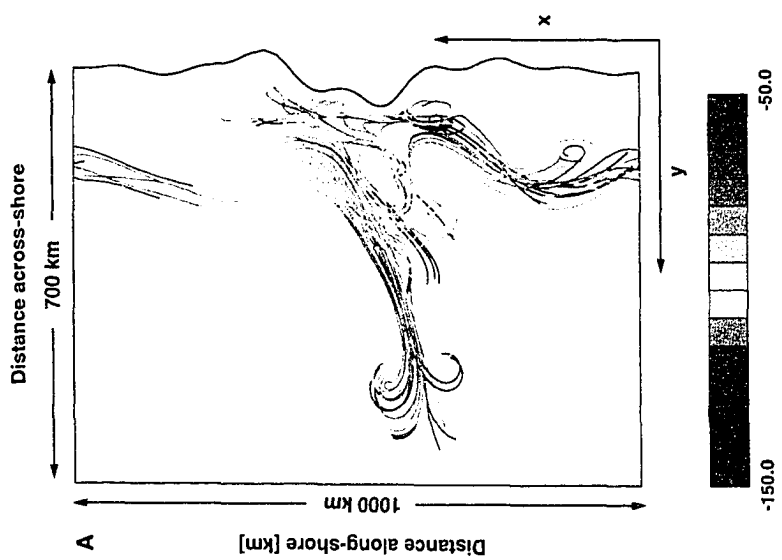

Figure 59. Composite of the simulated drifter trajectories released at 90 m showing phytoplankton concentrations along the drifter track. Color along the trajectory indicates the concentration of the large and small phytoplankton and ranges from 0 mg N m^{-3} (dark blue) to 392.45 mg N m^{-3} (dark red).

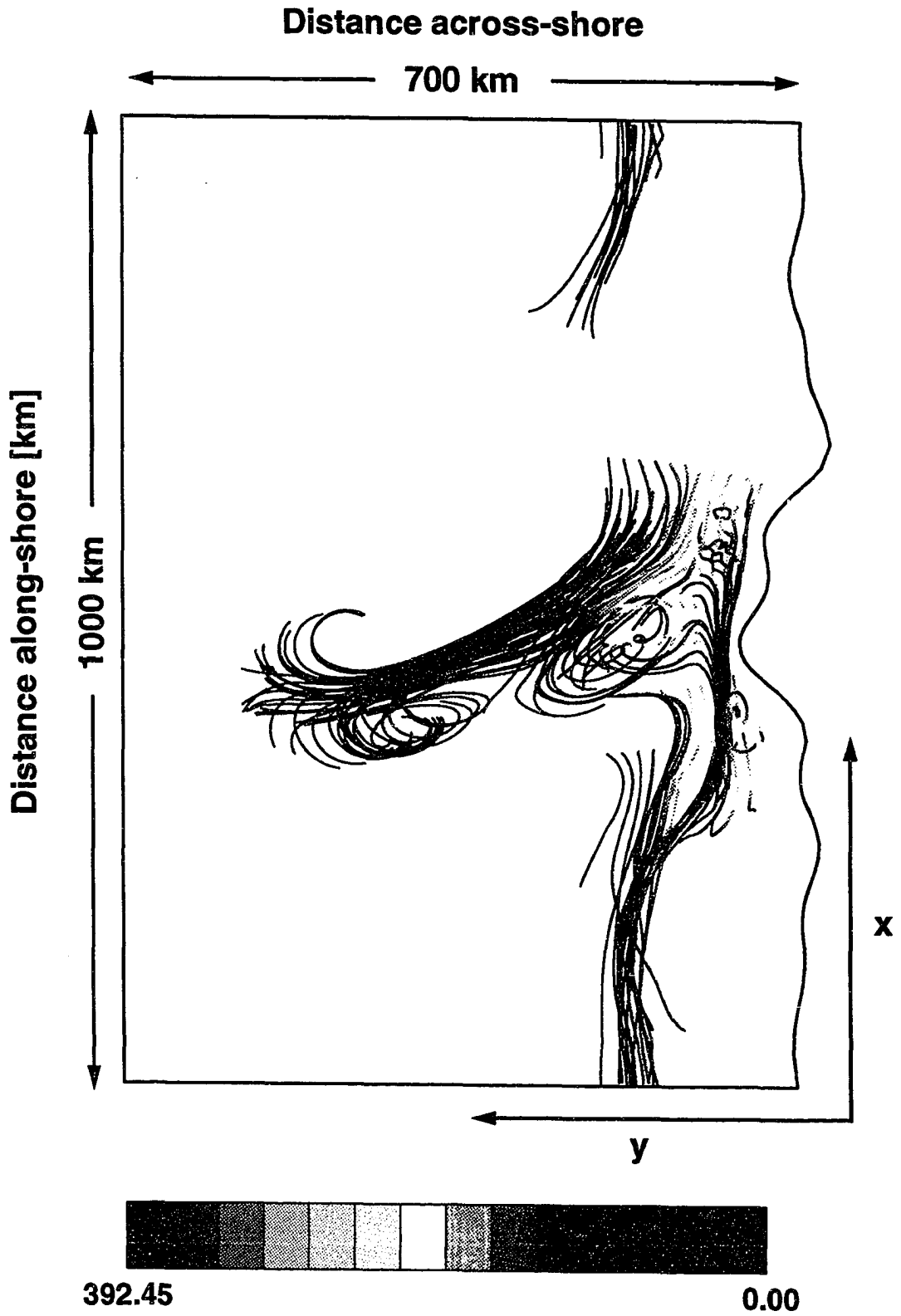

large phytoplankton cells than those to the north. This reflects the differing nutrient environments that are produced by cyclonic and anticyclonic circulations. The anticyclonic circulation on the northern side of the filament is formed form nutrient-poor, low phytoplankton biomass water, while the cyclonic circulation on the southern side of the filament is formed from the nutrient-rich, high phytoplankton biomass water from the core of the filament.

In general, the patterns in zooplankton concentrations along the drifter trajectories (Fig. 61) are similar to those obtained for the phytoplankton concentrations. Highest concentrations were inshore and decreased concentrations were found along the filament and in offshore waters. The zooplankton populations inshore of the filament were composed of about 40% euphausiids, 40% copepods and 20% doliolids. Within the filament, copepods were more dominant, with about 43% copepods, 19% euphausiids and 37% doliolids. Within the offshore portion of the filament, the copepods continued to remain dominant, with about 55% copepods, 33% euphausiids and 11% doliolids.

The vertical structure of the phytoplankton and zooplankton distributions in the upper 1000 m of the water column along the trajectory of a drifter that was transported offshore in the filament is shown in Figs. 62 and 63. Initially the phytoplankton population is dominated by large cells (Fig. 62A). However, grazing and nutrient depletion reduce the concentration of this size fraction over time and distance offshore. At the offshore end of the trajectory at day 20, the small phytoplankton fraction dominates at depth. The large cells still account for the majority of the phytoplankton biomass above 100 m. The subsurface chlorophyll maximum associated with the large phytoplankton size fraction deepens along the

Figure 60. Composite of the simulated drifter trajectories released at 90 m showing the abundance of large phytoplankton as a percent of total phytoplankton concentration. Color along the trajectory indicates the percent of large phytoplankton to total phytoplankton concentration and ranges from 0 (dark blue) to 98.57 (dark red).

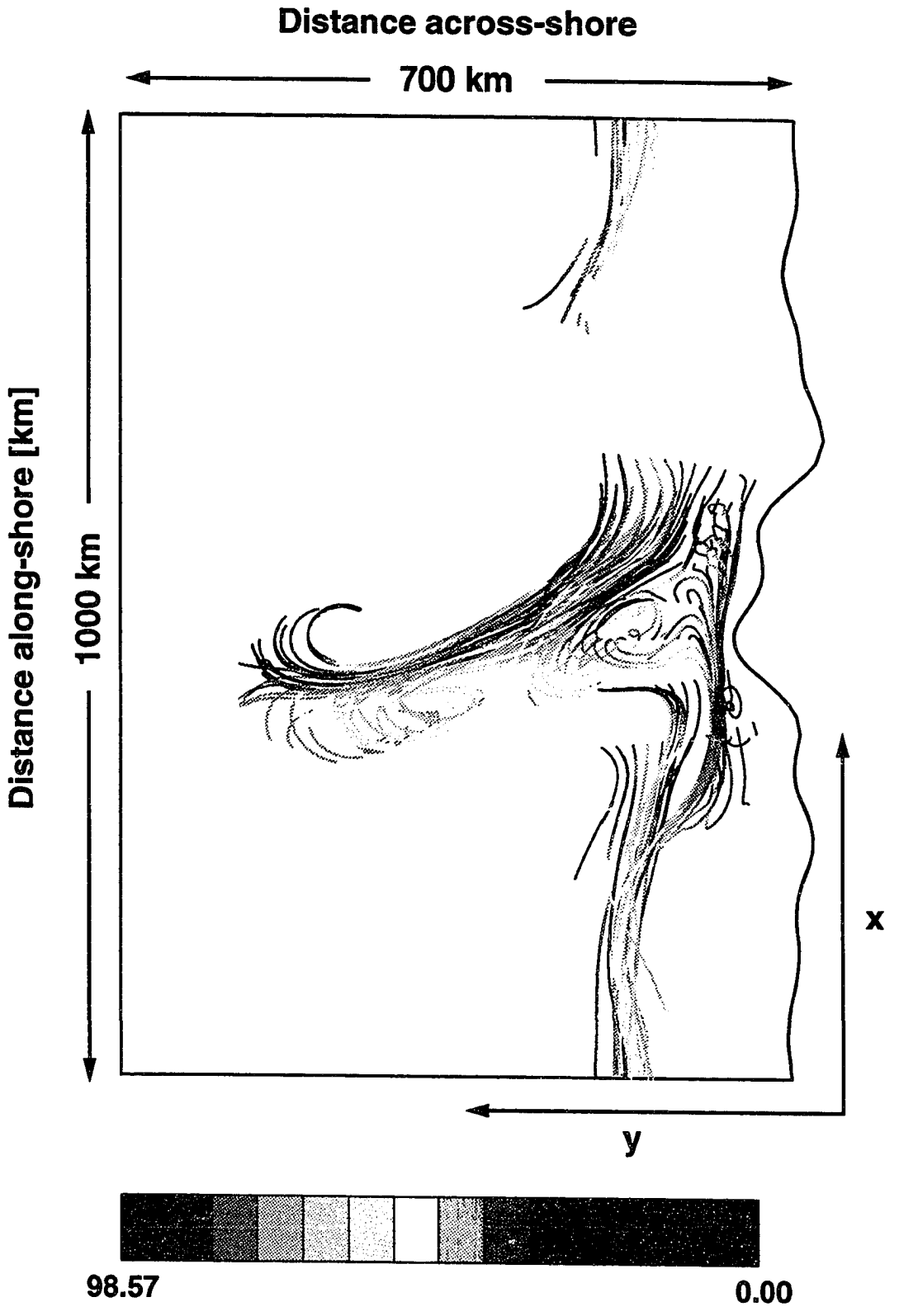

Figure 61. Composite of the simulated drifter trajectories released at 90 m showing zooplankton concentrations along the drifter track. Color along the trajectory indicates the concentration of the sum of the copepod, euphausiid and doliolid populations and ranges from 0.42 mg N m^{-3} (dark blue) to 23.75 mg N m^{-3} (dark red).

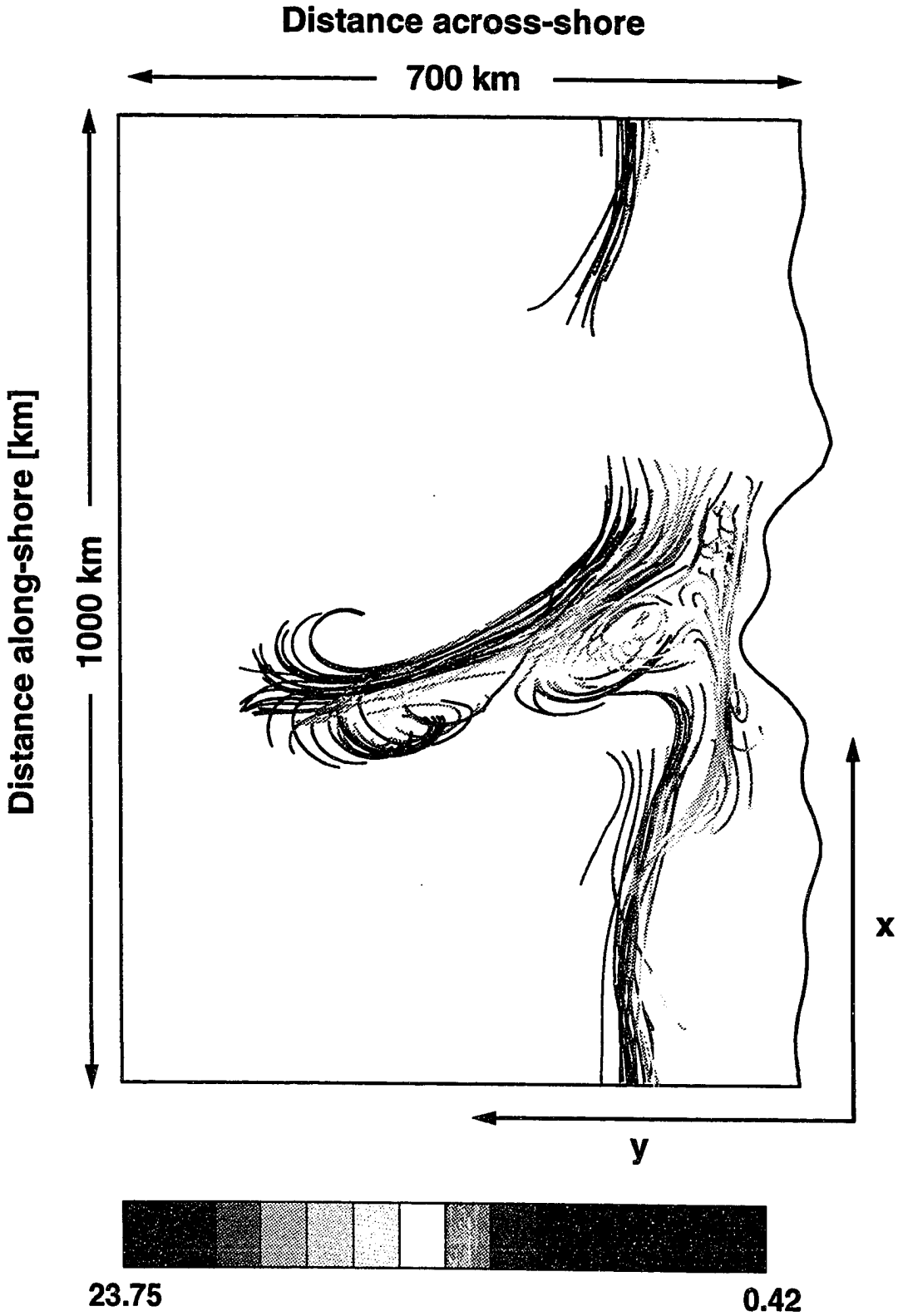

drifter trajectory. This may contribute to the apparent decrease in chlorophyll biomass at the offshore extent of the drifter trajectory.

The zooplankton distributions along the drifter trajectory show increased copepod (Fig. 63A) and euphausiid (Fig. 63B) concentrations at the offshore end of the filament between 200 and 400 m. Doliolid (Fig. 63C) populations are confined primarily to the more onshore portions of the trajectory.

Figure 62. The depth-dependent fields of the (**A**) percent of large to total phytoplankton concentration and the concentrations (mg N m^{-3}) of (**B**) large and (**C**) small phytoplankton size fractions sampled above and below a Lagrangian drifter as it was advected offshore within the filament. The solid line located initially at 90 m indicates the depth to which the drifter moved over time. This particular drifter was released at 90 m and allowed to vary in depth in response to the vertical velocities it experienced. Contour levels are 5%, 5 mg-N m^{-3} and 0.5mg-N m^{-3}, respectively.

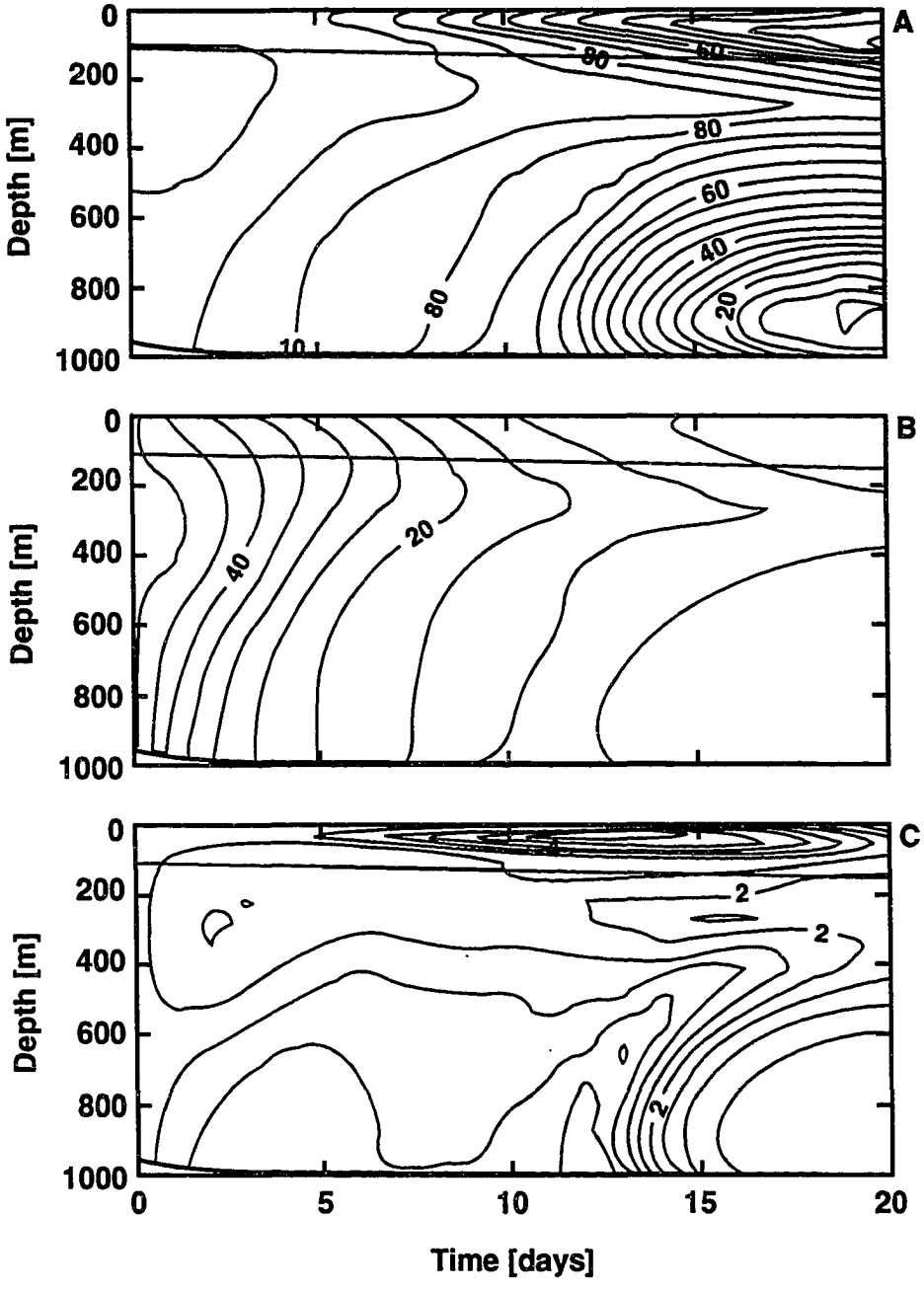

Figure 63. The depth-dependent fields of the (**A**) copepod, (**B**) doliolid and (**C**) euphausiid concentrations (mg N m^{-3}) sampled above and below a Lagrangian drifter as it was advected offshore within the filament. The solid line initially located at 90 m indicates the depth to which the drifter moved over time. This particular drifter was released at 90 m and allowed to vary in depth in response to the vertical velocities it experienced. Contour levels are 1 mg-N m^{-3}, 0.25 mg-N m^{-3} and 0.25 mg-N m^{-3}, respectively.

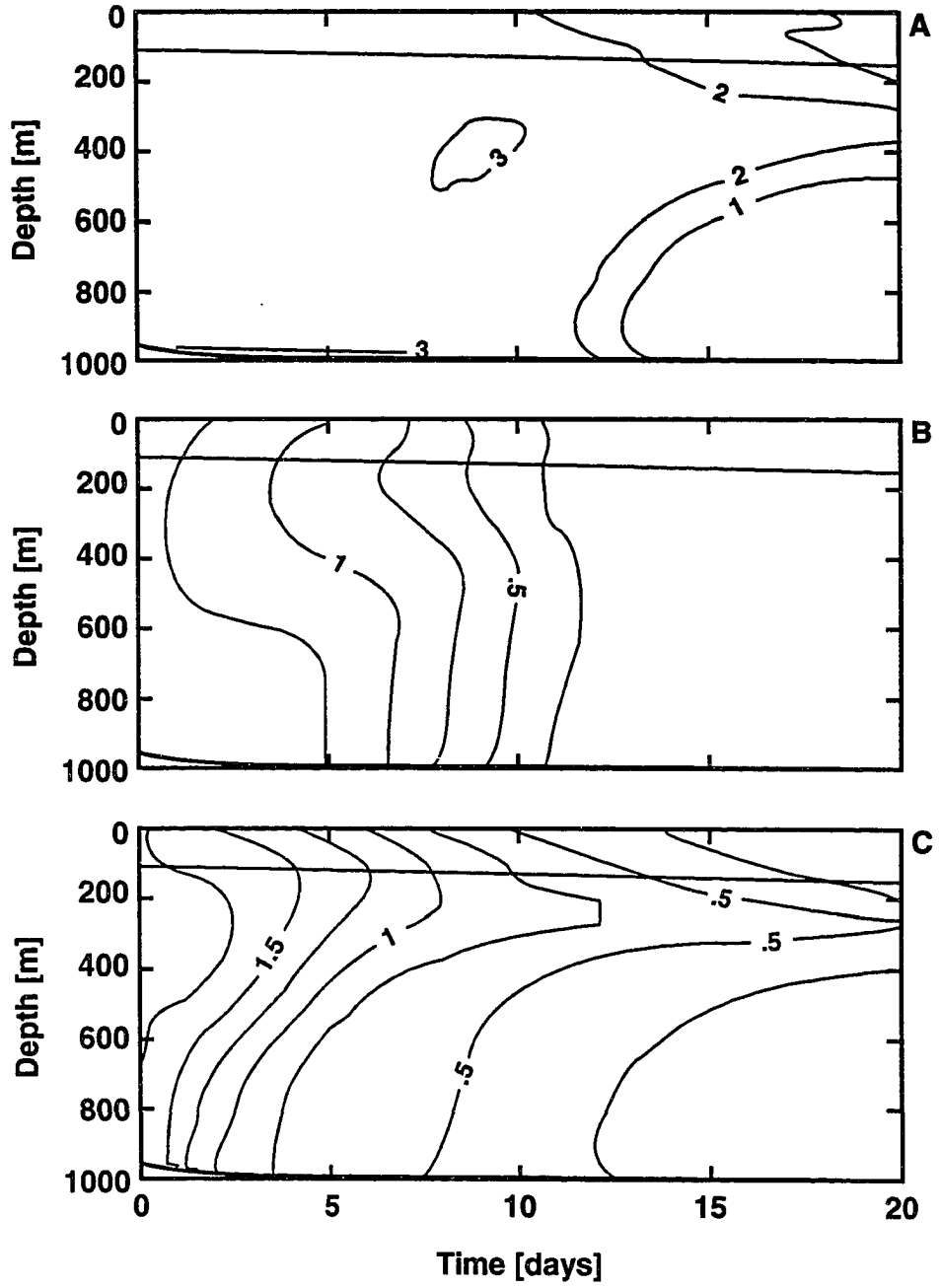

Chapter 5

Discussion

The previous chapters presented the formulation, implementation and results obtained from one- and three-dimensional physical-bio-optical models that were developed for the CTZ. The first of these models considered the time evolution of depth-dependent biological distributions that occur in response to initial nutrient and plankton profiles that are characteristic of coastal, oceanic and filament regions in the CTZ. The second model simulated the time development of the three-dimensional structure of the nutrient, plankton and underwater light field in the CTZ.

The following sections provide discussions of the results of these models in relation to observations from the CTZ and from other regions. The discussion of the one-dimensional results focuses on processes that contribute to the development and maintenance of the subsurface chlorophyll maximum. The three-dimensional model results are discussed within the context of the development and fate of the nutrient and plankton fields. Particular attention is given to the role of filaments in the CTZ to offshore carbon transport.

5.1 One-Dimensional Physical-Bio-Optical Model

5.1.1 Regional Characteristics Within the CTZ

The CTZ can be divided into inshore neritic and an offshore oligotrophic regions which differ from each other in temperature, nutrients and plankton community structure. The neritic regions of the CTZ are characterized by cold (< 9 °C), nutrient-rich (> 10 μM NO_3^- and > 8 μM SiO_4^-) waters which are supplied by local upwelling events (Huyer, 1983). The elevated nutrient concentrations serve to support a high phytoplankton biomass, which is typically dominated by silicate-dependent large centric diatoms (Hood et al., 1990 and 1991; Jones et al. 1990; Chavez et al. 1991; cf. Table 15). These phytoplankton are grazed upon by copepods and euphausiids. The combination of upwelling processes and high phytoplankton biomass in neritic regions supports the development of a shallow nutricline at about 25 m, a subsurface chlorophyll maximum in the upper 10 m, and a euphotic zone (defined as the depth of the 1% PAR isolume) depth of about 30 m (Chavez et al. 1991). The offshore oligotrophic waters lack a consistent nutrient supply mechanism, such as an upwelling season. Consequently, waters in this region are warmer and contain lower nutrient and phytoplankton concentrations. Unlike the neritic regions, the nutricline (> 80 m), subsurface chlorophyll maximum (> 50 m) and euphotic zone (> 100 m) develop deeper in the water column (Simpson et al., 1986; Hood, 1990; Hood et al., 1990 and 1991; Jones et al., 1990; Chavez, et al., 1991; cf. Table 15). Phytoplankton populations in this region tend to be dominated by smaller, < 5 μm, single-celled nitrate-dependent species such as *Synechococcus* sp. and prochlorophytes (Chavez et al., 1991).

The region separating the neritic and offshore areas is largely influenced by offshore advecting filaments (Hood et al., 1990 and 1991). The environment within the filament is dynamic because as the water is advected offshore, *in situ* processes change the nutrient levels from a eutrophic to an oligotrophic environment (Abbott et al., 1990). Initially, upwelled water is nutrient-rich, cold and contains low plankton biomass. As water is advected offshore, silicate-dependent diatoms grow rapidly and deplete the water column of nutrients after which diatom growth decreases due to silicate limitation. Eventually nitrogen is remineralized and allows the nitrogen-dependent oceanic phytoplankton to outcompete the neritic diatoms for the available nitrate. This competition for remineralized nitrogen was shown in the sensitivity analysis, where increased remineralization rates allowed the small, oceanic phytoplankton to outcompete the large, coastal phytoplankton. This change from silicate- to nitrogen-limited phytoplankton was also suggested by the nonlinear relationship observed in the NO_3^- versus SiO_4^- property plots from the CTZ survey data (cf. Fig. 11). High silicate to nitrate ratios occur in high nutrient water, e.g. nutrient-rich coastal and filament regions, where silicate uptake is high as a result of the presense of high concentrations of silicate-dependent phytoplankton. Conversely, low silicate to nitrate ratios occur in the low nutrient water, e.g. nutrient-poor oceanic water, where non-silicate dependent phytoplankton populations are dominant. As the silicate concentrations are depleted, the silicate to nitrate ratio decreases because the phytoplankton population changes to a non-silicate dependent population and the demand for silicate decreases (Chester, 1990). Finally, nutrient remineralization of ammonium, which may account for as much as 54% and 82% of the coastal and open ocean production, respectively,

would only serve to diminish this effect by helping to maintain higher silicate to nitrate ratios in the nutrient-poor oceanic waters, where remineralization of ammonium is higher (Eppley and Peterson, 1979).

The competition for nutrients along with grazing pressure causes the composition of the phytoplankton assemblage to change from a neritic diatom dominated population to an oceanic dominated population. A prominent feature of the CTZ is that phytoplankton populations approach maximum concentrations at subsubsurface levels (Hood et al., 1990 and 1991; Chavez et al., 1991; Jones et al., 1990). These chlorophyll maximums have been observed in several different environments including polar (El-Sayed and Jitts, 1973) and equatorial regions (Venrick et al., 1973; Gould, 1987).

5.1.2 Comparison With Observations

The results of the one-dimensional simulations showed that the chlorophyll maximum deepened with increasing distance from shore, ≈20 m onshore to ≈75 m offshore (Figs. 41B, 42B and 43B). This trend is in agreement with the 1988 CTZ field survey observations, where the chlorophyll maximum was found at ≈10 m onshore and ≈70 m offshore (Chavez et al., 1991, Washburn et al., 1991; cf. Table 15). However, it should be noted that much spatial variation in the depth of the chlorophyll maximum was observed due to the presence of the filaments within the CTZ field survey domain.

While the major processes that contribute to the development and maintenance of the chlorophyll maximum are known (Anderson, 1969; Roman et al., 1977; Cullen and Eppley, 1981; Cullen et al., 1982 and 1983; Venrick, 1984), little is known about their relative contribution. A disadvantage of field studies is that

sampling occurs only on small spatial scales and populations are difficult to track in space and time. The model developed by Jamart et al. (1977) to investigate vertical chlorophyll distributions off the coast of Oregon showed clearly that the relative contribution of physical and biological processes changes during the development and maintenance of the subsurface chlorophyll maximum. Their model showed that the development and subsequent sinking of the subsurface chlorophyll maximum was caused by both cell sinking associated with nutrient depletion and *in situ* primary production. Grazing played a role in the rate at which the subsurface chlorophyll maximum developed. However, *in situ* primary production was primarily responsible for its maintenance (Jamart et al., 1977).

The analysis of the processes included in the one-dimensional model show that *in situ* growth is primarily responsible for the creation and maintenance of the chlorophyll maximum layer in all regions of the CTZ. Maximum *in situ* growth occurs at depths where the effect of light limitation and nutrient limitation were least. It was the effect of nutrient limitation and light inhibition at the surface and light limitation at depth which was responsible for creating a maximum growth rate at depth, resulting in a chlorophyll maximum. The chlorophyll maximum developed deeper in the offshore region because both the nutricline (cf. Fig. 41) and the euphotic zone depth were deeper offshore. Similar results were also obtained in a physical-biological model developed by Varela et al. (1992). Their model showed that the depth and magnitude of the chlorophyll maximum was mainly determined by the vertical eddy diffusion and light attenuation, suggesting a balance between the amount of available light energy and upward flux of nutrients.

Several studies have postulated that grazing may be an important process in the development of chlorophyll maximums (Lorenzen, 1967; Venrick et al., 1973; Fairbanks and Wiebe, 1980; Longhurst and Herman, 1981; Roman et al., 1986; Gould, 1987). Roman et al. (1986) hypothesized that grazing serves to remove phytoplankton biomass in the upper water column and shifts absolute production to depth. This effect was also observed in the one-dimensional model results. In the simulations, the depth at which grazing pressure was strongest had the most effect in the chlorophyll maximum. Most often, the highest grazing pressure occurred at a depth just above the maximum *in situ* growth rate. In these cases, grazing enhanced the rate of development of the chlorophyll maximum by removing the slower growing phytoplankton population at the surface and allowing more light to penetrate deeper into the water column. Any grazing which occurred between the region of maximal growth and the final depth at which the chlorophyll maximum developed slowed the development of the chlorophyll maximum by reducing the rate at which the phytoplankton could grow and assimilate nutrients. A similar trend was observed with natural phytoplankton mortality rates. However, after the chlorophyll maximum layer had developed, neither of these processes contributed to its maintenance.

Vertical diffusion also had an effect on the development and maintenance of the chlorophyll maximum. The vertical diffusion of phytoplankton in conjunction with grazing pressure served to move the location of the chlorophyll maximum downward into the water column. The upward diffusion of nutrients decreased the level of nutrient-limitation and maintained the chlorophyll maximum at a shallower depth. This downward movement of the chlorophyll maximum ceased when the

upward diffusion of nutrients within the chlorophyll maximum was balanced by the uptake of nutrients from *in situ* growth.

Water mass subduction has been shown to be an important process associated with the offshore flowing portion of the filament (Washburn et al., 1991). To simulate the effects of subduction on the chlorophyll maximum, vertical velocities experienced by a simulated Lagrangian drifter (cf. Fig. 20), as it was advected offshore while entrained within the filament, were used to specify the vertical velocities in the one-dimensional model. The time evolution of the biological distributions obtained from following the simulated Lagrangian drifter were compared with similar distributions obtained following an actual drifter in the CTZ. Simulated nutrient and phytoplankton distributions from the downwelling simulation (cf. Fig. 47B) compared well with the actual "semi-Lagrangian" data (cf. Fig. 48C) that was transported offshore in a filament. The simulated distributions obtained with no vertical advection (cf. Figs. 47A and 48A) did not compare well with observations.

Downwelling along the northern offshore-flowing side of the filament was observed to be as high as 20-40 m day^{-1} (Kadko et al., 1991; Dewey et al., 1991). The rapid subduction of water has a considerable effect on the plankton dynamics. Results from the model simulations show that downwelling vertical velocities cause the nutricline and chlorophyll maximum to develop at greater depths (cf. Figs. 47 and 48). Washburn et al. (1991) suggested that the phytoplankton in the water column within the filament may have been downwelled over 100 m as they were advected offshore while entrained within the filament. Also, Abbott et al. (1990) favored the explanation that downwelling was in part responsible for the optical

and biological properties measured by a fixed-depth drifter as it was advected offshore while entrained within a filament. The downwelling of water in the model also caused the euphotic zone to deepen and the f-ratio to decrease as the supply of new nutrients decreased. For upwelling simulations, the effect was reversed. The implication and effect that this has on the across-shore transport of new and old production will be discussed in the next section.

High reproductive efforts in the copepod *E. californicus* have previously been observed off the California coast (Smith et al., 1986*a*; 1991) and within the filament (Smith, 1991). Copepod and euphausiid populations in the model had higher reproductive effort in regions of high large phytoplankton biomass where the silicate concentrations were less limiting. Conversely, the doliolids were more able to reproduce in the offshore water where the smaller phytoplankton and detrital concentrations were highest.

5.2 Three-Dimensional Physical-Bio-Optical Model

Circulation patterns within the CTZ are dynamic and have been observed to contain a variety of circulation features such as mesoscale eddies, squirts, meandering jets and upwelling zones (Flament et al., 1985; Hayward and Mantla, 1990; Strub et al., 1991; Brink and Cowles, 1991; Huyer et al., 1991). These features vary on time scales of days to weeks and their production varies seasonally (Brink and Cowles, 1991; Strub et al., 1991). The contribution that the circulation fields play in determining the time evolution of the nutrient, biological and optical fields is difficult to examine through field studies alone. A three-dimensional model provides a mechanism that can be used to understand the effects of circulation on the distribution and transport of nutrients and plankton populations. Also, because filaments advect water and, thus, carbon onshore and offshore, the simulated distributions can be used to quantify across-shore fluxes of carbon.

5.2.1 Three-Dimensional Circulation Fields

The simulated circulation patterns used for the 20-day integration of the biological quantities include the development of a distinct offshore propagating filament (cf. Fig. 50). The processes and dynamical balances underlying the formation of this filament have been previously discussed in Haidvogel et al. (1991a). However, it is appropriate to mention the aspects of the simulated circulation fields that are relevant to the development of the patterns observed in the simulated biological fields.

The circulation fields show several distinct features that occur at a variety of length and time scales. By model day 140, a meander developed near the coastal

bump and over the course of the 20-day simulation this meander propagated offshore to form a filament. By model day 160, an eddy dipole had formed at the offshore tip of the filament, which is consistent with observed circulation features in the CTZ. The characteristic length scales and velocities for the simulated filament are fairly representative of those observed within the CTZ. The filament was advected offshore ≈500 km and the width of the filament was about 75 km (Haidvogel et al., 1991a), which compare well to the the CTZ field data. The filaments observed within the CTZ typically extend offshore more than 300 km (Flament et al., 1985), and have widths of ≈75 km (Strub et al., 1991). Maximum horizontal velocities within the simulated filament (0.8 to 1 m s^{-1}) were similar to those observed in the CTZ field data, 0.8 m s^{-1}, (Kosro and Huyer, 1986; Brink and Cowles, 1991; Strub et al., 1991). The offshore flowing regions associated with the filament observed in the CTZ have been associated with large downwelling velocities of up to 10-40 m day^{-1} (Kadko et al., 1991; Dewey et al., 1991). Maximum downwelling velocities of ≈12 m day^{-1} were observed in the simulated circulation field. As in the field observations, these downwelling regions were also located in the northern offshore flowing region of the simulated filament.

Other circulation patterns were observed within the simulated circulation pattern which play a role in the development of the resulting biological and optical distributions. Mesoscale meanders propagate along the shelf, deforming the developing density field as they propagated south. Along these density fronts, frontal instabilities developed (Haidvogel et al., 1991a) which moved south along the density front. Onshore of this density front, a series of wave-like downwelling/upwelling regions propagated to the north which was evidence for coastally-trapped waves

(Dr. Dale Haidvogel, personal communication). While the filament was the dominant circulation feature affecting the development of the biological fields, these smaller scale circulation patterns also played a role. The effect of these smaller-scale features on the across-shore flux and transport of carbon will be discussed in section 5.2.3.

Finally, the physical model was able to reproduce qualitatively other features within the CTZ such as the California Current and the California Countercurrent (Haidvogel et al., 1991a). However, except for the filament region, most of the variability of the simulated biological fields was in vertical and across the shore directions. The along-shore circulation had less of a role in structuring these distributions. Therefore, the discussion of the resulting bio-optical fields, which follows in the next section, is focused on across-shore and within-filament variations.

5.2.2 Three-Dimensional Bio-Optical Fields

The simulated nutrient and phytoplankton fields show that as the filament began to form, nutrient-rich water was upwelled into the upper water column where it was removed by phytoplankton. This is consistent with the CTZ field observations, where over the initial 3-5 days of filament formation, the diatom community underwent a period of rapid growth in the core of a filament (Hood et al., 1990 and 1991; Chavez et al., 1991). As the simulated filament matured, nutrients were depleted and the phytoplankton population diminished as a result of nutrient limitation and increased grazing pressure. Thus, the simulated filaments also served as a stimulus for secondary production by providing conditions favorable for zooplankton growth and reproduction as these populations are advected

offshore. These results are in agreement with observations of elevated zooplankton concentrations in the offshore regions of the CCS (Chelton et al., 1982).

The general across-shore, model-derived phytoplankton distributions are similar to those observed within the CTZ. Phytoplankton concentrations are highest onshore (e.g. > 1 mg-chl a m^{-3}) and decreased rapidly (e.g. < 0.1 mg-chl a m^{-3}) across the density front (Hood et al., 1990 and 1991; Chavez, et al., 1991). However, the decrease in the mean concentration of the phytoplankton over the course of the model simulation suggests that the model does not adequately simulate either the nutrient flux or remineralization processes, or that zooplankton grazing rates were too high. Both increased remineralization rates and decreased zooplankton grazing rates would have helped to maintain a constant mean phytoplankton concentration over the 20-day simulation.

The simulated phytoplankton concentrations were highest in the core of the filament (e.g. > 2.5 mg-chl a m^{-3}) and decreased across the filament's density front (e.g. < 0.5 mg-chl a m^{-3}) on the outer edges of the filament. The distance over which this change took place was shorter (30 km) in the southern onshore-flowing southern flank of the filament where upwelling velocities were high. In the northern offshore-flowing flank of the filament, high downwelling velocities and substantial across-jet exchange (Hofmann et al., 1991) caused this change to occur over a longer distance (80 km).

Due to the paucity of data on the spatial distribution of the subsurface light field within in the CTZ, comparison of the simulated light fields with observations is very limited. The general across-shelf variations in the depth of the simulated euphotic zone depth ranged between $\approx$30 m onshore to $\approx$180 m offshore, with

the largest change in euphotic zone depths occurring in the region of the density fronts. The available 1% PAR measurements from the CTZ (cf. Fig. 32) show a similar trend, with the shallowest 1% PAR level being about ($\approx$20 m) onshore and deepening to a maximum (> 130 m) 1% offshore. Shallow 1% PAR levels ($\approx$30 m) were also observed within the filaments (Washburn et al., 1991).

As in the simulated phytoplankton fields, the across-filament variation in the depth of the euphotic zone is asymmetric. The euphotic zone shallows more rapidly on the southern, onshore flowing portion of the simulated filament and mesoscale meanders and eddies. The available light measurements from the CTZ do not have sufficient spatial resolution to provide a detailed comparison to the simulated feature. However, because such asymmetry is observed in the across-filament CTZ phytoplankton fields (Jones et al., 1991), such a feature should exist due to attenuation of light by the phytoplankton populations.

The euphotic zone depth is the result of the interaction of several biological processes. Grazing removed the nutrient-limited, slow growing phytoplankton from the upper regions in the water column which then let light penetrate further into the water column. This increase in light penetration allowed enhanced phytoplankton growth at depth. Thus, the net effect of zooplankton grazing was to increase the total integrated primary production within the water column. The interplay of these processes in affecting euphotic zone depth is discussed in the sensitivity analysis of the one-dimensional model.

5.2.3 Across-Shore Carbon Flux and Transport

The across-shelf flux of carbon, which occurs in productive coastal regions (Yoder and Ishimaru, 1989) may be an important carbon pathway in the ocean

biogeochemical carbon cycle (Jahnke, 1990). However, little is known about the relative contribution of carbon export from coastal regions to the open ocean to the overall global carbon cycle. The magnitude of carbon flow through this pathway needs to be known to better understand the fate and ultimate effect of natural and anthropogenic carbon inputs on the ocean.

As the filament developed in the simulated circulation fields, it moved offshore about 300 km in 20 days. The circulation fields associated with such features are composed of a translation and swirl/rotational velocity field (Kirwan et al. 1984a and b). Because of this, the across-shore flux and transport of carbon should be discussed in terms of their translational and swirl components. By doing so, the across-shore flux and transport patterns become analogous to those expected from an eddy being advected offshore. The discussion which follows will expand upon this analogy.

The simulated surface carbon flux fields (cf. Figs. 53 and 54) suggest that there are specific regions within the filament which are responsible for the majority of the across-shore flux of carbon. The highest offshore surface carbon flux (e.g. $>$ 21 mg C m^{-2} s^{-1}) occurred along the northern flank of the filament, coincident with the region of highest offshore velocities, such as would be expected from an eddy analogy. Likewise, the highest onshore surface carbon flux (e.g. $>$ 12 mg C m^{-2} s^{-1}) occurred along the southern flank of the filament in the region of highest onshore velocities. The velocities were larger in the offshore flowing portion of the filament than in the onshore flowing portion due to the effect of the offshore translational velocity component. Along the core of the filament, where phytoplankton concentrations are highest, the across-shore flux of carbon is lowest because of the

low across-shore velocities coincident with the high carbon concentrations. The net effect of the translational velocity component is to increase (decrease) the areal extent of the offshore (onshore) surface carbon flux field regions.

The patterns in transport of new and old production in the filament can be related to the vertical and horizontal velocity distributions along and across the feature. The offshore-directed flow transports waters from the inshore region into the ocean interior. The fraction of the total phytoplankton production attributed to new production decreases rapidly away from the core of the filament. Along the northern flank of the filament, downwelling velocities associated with the offshore-flowing portion of the filament enhanced the decrease in the new production rates. Conversely, along the southern flank, upwelling velocities associated with the onshore-flowing portion of the filament retarded the decrease in new production rates. In summary, the translational velocities within the filament core advected new production offshore. The swirl/rotational velocities along the flanks of the filament advected older production offshore in the north and newer production onshore in the south.

Estimates of surface across-shore flux of carbon have not been made from measurements from the CTZ. However, the simulated surface horizontal velocity and phytoplankton fields, which were used to calculate the surface across-shore carbon flux fields, resemble those measured within the CTZ (Flament et al., 1985; Hayward and Mantyla, 1990; Hood et al., 1990 and 1991; Huyer et al., 1991; Washburn et al., 1991; Jones et al., 1991; Strub et al., 1991). The near-surface chlorophyll and nitrate concentrations and temperature fields obtained in July 1986, for a region offshore Pt. Arena during a filament event, can be used to verify

the model-derived distributions. Water temperatures were lower than 12°C, along the coast and within the core of the filament which was observed to extend seaward near Pt. Arena. High chlorophyll ($\geq$ 5 mg m^{-3}) and nitrate ($\geq$ 10 mg m^{-3}) concentrations were coincident with these regions of colder temperatures (Jones et al., 1991). Satellite-derived estimates of sea surface temperature and pigment concentrations (cf. Fig. 2; Brink and Cowles, 1991) show similar patterns. Other field studies which measured the pigment concentrations within the CTZ region (Hood et al., 1990 and 1991; Chavez, et al., 1991) also found high chlorophyll coincident with cold temperatures.

All CTZ field surveys measured a strong seaward flow north of the observed temperature minimum in the filament with maximum velocities of about 0.8 m s^{-1} (Huyer et al., 1991). Velocities were minimal within the pigment core of the filament and a slower onshore velocities were observed on the southern flank (Reinecker and Mooers, 1989; Huyer et al., 1991, Chavez et al., 1991; Jones et al., 1991). Again, these results suggest a developing circulation feature composed of both a translational and swirl/rotational components. The resulting lower onshore velocities on the southern flank of the observed filaments suggest the offshore translation of the observed circulation pattern.

From the circulation patterns observed in the CTZ field surveys and the observed surface nutrient concentrations, Chavez et al. (1991) concluded that, "the strong baroclinic jets commonly found in the coastal transition zone are not responsible for significant transport of coastally upwelled, high-nutrient water into the interior." Their conclusion was based on the observation that the regions of highest nutrients and phytoplankton biomass were not associated with the observed

high offshore velocites. This was also observed in the model results. However, the values of the across-shore flux of carbon and nutrients are obtained by the product of the concentration of carbon or nutrients and the across-shore velocities. Therefore, regions of high across-shore velocities can also be regions of high across-shore flux of carbon and nutrients, such is observed in the simulated carbon flux distributions.

In addition to filament-related features, several other circulation features present in the simulated fields warrant discussion because of their role in the across-shore flux and transport of carbon. The mesoscale meanders and eddies were characterized by high phytoplankton concentrations, especially along the axis of the meanders. Also, high across-shore velocities were observed to be associated with the density fronts of the meanders and eddies. The resulting patterns in the across-shore surface carbon flux of these meanders/eddies resembles that observed in the filament. The highest offshore surface carbon flux occurred within the northern flank of the meanders/eddies, coincident with the region of highest offshore velocities. Likewise, the highest onshore surface carbon flux occurred within the southern flank of the meanders/eddies in the region of highest onshore velocities. Again, these results are primarily due to the swirl velocity components associated with the meander.

The presence of the frontal instabilities (Haidvogel et al., 1991a) and phenomenon resembling coastally trapped waves introduced even smaller scale variability in the simulated circulation and biological fields. Such wavelike features were observed in the AVHRR (Reinecker and Moores, 1989) and CZCS (Paláez and

McGowan, 1986) imagery of the filaments in the CTZ. The effect of these small-scale features on the across-shore flux of carbon may be important. Because the frontal instabilities are superimposed upon the mesoscale meanders/eddies, their contribution to the across-shore carbon flux is difficult to quantify in the simulated across-shelf carbon flux fields. However, because the phenomenon resembling coastally trapped waves was located onshore of the density front, its contribution to the surface across-shore flux of carbon is clearly observable. Small-scale wavelike regions off onshore and offshore velocities create a similar small-scale wavelike patterns in the surface across-shore carbon flux.

The depth-integrated total across-shore carbon flux fields calculated from the simulated fields (cf. Fig. 55) show a different pattern than that observed in the surface across-shore flux fields (cf. Fig. 54). The depth-integrated across-shore carbon flux is primarily offshore because the net volume flux is offshore due to the offshore velocities in the feature. The net offshore volume flux allows the filament to elongate as a result of the translation velocity component. Such an net offshore volume flux within the filament was observed in the CTZ by Jones et al. (1991). In their study they observed a 0.80 Sv volume flux in the offshore direction and 0.72 Sv flux in the onshore direction within the top 100 m of a filament. This resulted in a net offshore volume flux of 0.08 Sv. However, it is difficult to directly compare these field results with the model results given the temporal and spatial dependence of these simulated and observed fields.

The time series of the simulated area-integrated across-shore carbon flux demonstrates how variable the carbon flux estimates are in time and distance from shore (cf. Fig. 56). The difference between the offshore and onshore flux

estimates (cf. Fig. 56A) gives the net across-shore flux at any distance offshore (cf. Fig. 61B). The area-integrated values of the net across-shore carbon flux essentially removes the effect of the swirl/rotational velocity components from the across-shore carbon flux estimates by canceling the onshore (-) and offshore (+) carbon flux due to the swirl velocities. On model day 140, there is a maximum in the net across-shore carbon flux at about 200 km from the coast. By model day 150, the elongation of the filament had modified the form of the net across-shore carbon flux. While a maximum is still observed at ≈200 km offshore, across-shore flux values are higher than 1000 kg C s^{-1} between ≈150 and 450 km offshore. The effect of the eddy dipoles which were observed to form at the offshore end of the filament are responsible for the offshore maximum in the across-shore flux at ≈500 km on model day 160.

The resulting time-integrated total across-shore carbon transport for the 20 days over which the model was integrated is everywhere offshore (cf. Fig. 57). The highest across-shore transport of carbon is ≈35 g C x 10^9 and occurs ≈500 km from shore. Most of this transport is composed of phytoplankton biomass. If a constant carbon to chlorophyll ratio of 40 (mg C :: mg chl *a*) is assumed, the maximum carbon transport coverts to a chlorophyll transport of ≈506 g chl s^{-1}. Jones et al. (1991) obtained transport values of 280 g chl s^{-1} by integrating a 110 km wide filament cross-section from 0 to 100 m. A higher estimate of 347 g chl s^{-1} was obtained by Strub et al. (1991) by integrating a 200 km wide filament cross-section from 0 to 100 m. Keeping in mind the highly variable nature of the filaments in time and space, the model-derived estimate of the across-shore transport agrees reasonably with that obtained from the CTZ field data.

An estimate of the total annual transport of carbon can be obtained from the above transport estimates. Filaments are generated within the CTZ from May to October for a total of about 3-6 months (Strub et al., 1991) and have a lifetime of about one month. Also, as many as 1-6 filaments have been observed in various stages of development along the western coast of the United States (Strub et al., 1991). Using these estimates, the filaments along the California coast can transport between 158 and 1890 g C m^{-2} yr^{-1} as much as 500 km offshore. This large offshore transport of carbon may supply the high zooplankton biomass observed to exist $\approx$200 km offshore in the southern region of the CTZ (Chelton et al., 1982).

Numerous estimates of across-shelf flux of carbon have been made for different regions (Table 16). The large differences that exist between these environments make comparisons difficult. However, even with these differences, the CTZ is potentially an important site for across-shelf carbon transport.

Table 16. Estimates of Across-Shelf Carbon Transport Obtained for a Variety of Environments.

Region	Estimated Across-Shelf Flux	Reference
Texas–Louisiana Shelf	56 g C m^{-2} yr^{-1}*	Walsh, 1988
Southeastern Bering Sea	79 g C m^{-2} yr^{-1}	Walsh, 1988
New York Shelf	180 g C m^{-2} yr^{-1}*	Walsh, 1988
Anadyr Water, Bering Sea	118 g C m^{-2} yr^{-1}*	Walsh, 1988
Georges Bank	240 g C m^{-2} yr^{-1}	Walsh, 1988
Peru (≈1966-1969)†	82 g C m^{-2} yr^{-1}*	Walsh, 1988
Peru (≈1976-1979)‡	591 g C m^{-2} yr^{-1}*	Walsh, 1988
CTZ	158-1890 g C m^{-2} yr^{-1}	This Study

* Includes burial

† Before overfishing of anchovy population

‡ After overfishing of anchovy population

Chapter 6

Conclusions

This study used one and three-dimensional physical-bio-optical models to investigate the processes that regulate nutrient and plankton distributions in the CTZ. The model results provide a basis for several general conclusions about how circulation, biological and optical processes interact to produce the horizontal and vertical biological distributions observed in the CTZ. First, the subsurface chlorophyll maximum in the CTZ is primarily the result of *in situ* growth by phytoplankton populations. This result was obtained for coastal, oceanic and filament conditions. The depth and magnitude of chlorophyll *a* concentration varied between environments in response to vertical nutrient and light gradients and zooplankton grazing. The one-dimensional model was limited in its ability to accurately simulate the characteristics of the subsurface chlorophyll maximum in the coastal regions. This discrepancy may be attributed to a mismatch in where data were obtained to use in the model and where observations were obtained for comparison. However, it may also indicate limitations in the physical-bio-optical dynamics included in the model. Second, the rate at which detritus is remineralized had a pronounced effect on the relative amounts of old and new primary production. This points to the importance of including realistic formulations for nutrient remineralization processes in marine ecosystem models, e.g. inclusion of the microbial loop. Third, nonlinear interactions in marine food webs can have a large effect on euphotic

zone depth and biological production. For example, removal of phytoplankton in the upper water column by zooplankton grazing allows deeper light penetration which can stimulate primary production. Hence, the species assemblage at a particular time or location can alter the characteristics of the underwater light field. Fourth, the offshore-extending filaments in the CTZ account for the majority of offshore nutrient and carbon transport. The total amount of carbon that can be potentially exported from the CTZ, as estimated from the simulated biological distributions, is between 158 to 1890 g C m^{-2} yr^{-1}. This may represent a significant carbon source to offshore oceanic waters and as such may play a role in structuring distributional patterns of high trophic level organisms such as zooplankton and fish.

This study provides the first implementation of a regional physical-bio-optical model. However, coupling between the circulation, biology and optics in these models was one way, i.e. no feedbacks occurred between biological and circulation processes. In reality there should be linkages between the biological and optical models and the circulation model through modification of thermal structure of the upper water column. Inclusion of these linkages requires coupling through a mixed-layer model. Hence, continued development of circulation-bio-optical models must also include development of mixed layer models. Such models are necessary if questions of climate change effects on marine production are to be addressed.

References

Abbott, M. R., and B. Barksdale, Phytoplankton pigment patterns and wind forcing off central California, *J. Geophys. Res.*, *96*, 14,649-14,667, 1991.

Abbott, M. R., and P. M. Zion, Satellite observations of phytoplankton variability during an upwelling event, *Cont. Shelf. Res.*, *4*, 661-680, 1985.

Abbott, M. R., and P. M. Zion, Spatial and temporal variability of phytoplankton pigment off northern California during Coastal Ocean Dynamics Experiment I, *J. Geophys. Res.*, *92*, 1745-1756, 1987.

Abbott, M. R., K. H. Brink, C. R. Booth, D. Blasco, L. A. Codispoti, P. P. Niiler, and S. R. Ramp, Observations of phytoplankton and nutrients from a Lagrangian drifter off northern California, *J. Geophys. Res.*, *95*, 9393-9409, 1990.

Allen, J. S., L. J. Walstad, and P. A. Newberger, Dynamics of the coastal transition zone jet, 2, Nonlinear finite amplitude behavior, *J. Geophys. Res.*, *96*, 14,995-15,016, 1991.

Anderson, G. G., Subsurface chlorophyll maximum in the northeast Pacific Ocean, *Limnol. Oceanogr.*, *14*, 386-391, 1969.

Atkinson, L. P., K. H. Brink, R. E. Davis, B. H. Jones, T. Paluszkiewicz, and D. W. Stuart, Mesoscale variability in the vicinity of points Conception and Arguello during April-May 1983: The OPUS 1983 Experiment, *J. Geophys. Res.*, *91*, 12,899-12,918, 1986.

Barth, J. A., and K. H. Brink, Shipboard acoustic Doppler profiler velocity observations near Point Conception: Spring 1983, *J. Geophys. Res.*, *92*, 3925-3943, 1987.

Batteen, M. L., R. L. Haney, T. A. Tielking, and P. G. Renaud, A numerical study of wind forcing of eddies and jets in the California Current system, *J. Mar. Res.*, *47*, 493-523, 1989.

Batteen, M. L., R. W. Edson, and C. S. Nelson, Effects of spatially varying winds on central California Current System, *Eos Trans. AGU*, 71, 148, 1990.

Beardsley, R. C., C. E. Dorman, C. A. Frieche, L. K. Rosenfeld, and C. D. Winant, Local atmospheric forcing during the Coastal Ocean Dynamics Experiment, 1, A description of the marine boundary layer and atmospheric conditions over a northern California upwelling region, *J. Geophys. Res.*, *92*, 1467-1487, 1987.

Bernstein, R. L., L. Breaker, and R. Whritner, California Current eddy formation: Ship, air, and satellite results, *Science*, *195*, 353-359, 1977.

Bidigare, R. R., R. C. Smith, K. S. Baker, and J. Marra, Oceanic primary production estimates from measurements of spectral irradiance and pigment concentrations, *Global Biogeochemical Cycles*, *1*, 171-186, 1987.

Bidigare, R. R., M. E. Ondrusek, J. H. Morrow, and D. A. Kiefer, *In vivo* absorption properties of algal pigments, *SPIE*, *1302*, *Ocean Optics X*, 290-302, 1990*a*.

Bienfang, P., and J. Szyper, Effects of temperature and salinity on sinking rates of the centric diatom *Ditylum brightwelli*, *Biol. Oceanogr.*, *1*, 211-223, 1982.

Bienfang, P., J. Szyper, and E. Laws, Sinking rate and pigment responses to light-limitation of a marine diatom: Implications to dynamics of chlorophyll maximum layers, *Oceanol. Acta*, *6*, 55-62, 1982.

Bird, R. E., A simple, solar spectral model for direct-normal and diffuse horizontal irradiance, *Solar Energy*, *32*, 461-471, 1984.

Bird, R. E., and C. Riordan, Simple solar spectral model for direct and diffuse irradiance on horizontal and tilted planes at the Earth's surface for cloudless atmospheres, *J. Climate and Applied Meteorology*, *25*, 87-97, 1986.

Breaker, L. C., and R. P. Gilliland, A satellite sequence on upwelling along the California coast, in *Coastal Upwelling, Coastal Estuarine Sci.*, vol. 1, edited by F. A. Richards, pp. 87-94, AGU, Washington, D. C., 1981.

Bricaud, A., A. Morel, and L. Prieur, Absorption by dissolved organic matter of the sea (yellow substance) in the UV and visible domains, *Limnol. Oceanogr.*, *26*, 43-53, 1981.

Brink, K. H., The near-surface dynamics of coastal upwelling, *Prog. Oceanogr.*, *12*, 223-257, 1983.

Brink, K. H., D. Halpern, A. Huyer, and R. L. Smith, The physical environment of the Peruvian upwelling system, *Prog. Oceanogr.*, *12*, 285-305, 1983.

Brink, K. H. and T. J. Cowles, The Coastal Transition Zone program, *J. Geophys. Res.*, *96*, 14,637-14,647, 1991.

Brink, K. H., R. C. Beardsley, P. P. Niiler, M. Abbott, A. Huyer, S. Ramp, T. Stanton, and D. Stuart, Statistical properties of near-surface flow in the California coastal transition zone, *J. Geophys. Res.*, *96*, 14,693-14,706, 1991.

Bucklin, A.,M. M. Rienecker and C. N. K. Mooers, Genetic tracers of zooplankton transport in coastal filaments off northern California, *J. Geophys. Res.*, *94*, 8277-8288, 1989.

Bucklin, A., Population genetic responses of the planktonic copepod, *Metridia pacifica*, to a coastal eddy in the California current, *J. Geophys. Res.*, *96*, 14,799-14,808, 1991.

Carder, K. L., R. G. Steward, G. R. Harvey, and P. B. Ortner, Marine humic and fulvic acids: Their effects on remote sensing of ocean chlorophyll, *Limnol. Oceanogr.*, *34*, 68-81, 1989.

Chavez, F., R. T. Barber, A. Huyer, P. M. Kosro, S. Ramp, T. Stanton and Blanca Rojas de Mendiola, Horizontal transport of nutrients in the Coastal Transition Zone off northern California: effects on primary production, phytoplankton biomass, and species composition, *J. Geophys. Res.*, *96*, 14,809-14,831, 1991.

Chelton, D. B., Seasonal variability of alongshore geostrophic velocity off central California, *J. Geophys. Res.*, *89*, 3473-3486, 1984.

Chelton, D. B., P. A. Bernal, and J. A. McGowan, Large-scale interannual physical and biological interaction in the California Current *J. Mar. Res.*, *40*, 1095-1125, 1982.

Chelton, D. B., A. W. Bratkovich, R. L. Bernstein, and P. M. Kosro, Poleward flow off central California during the spring and summer of 1981 and 1984, *J. Geophys. Res.*, *93*, 10,604-10,620, 1988.

Chester, R., *Marine Chemistry*, Unwin Hyman Ltd., London, England, pp. 698, 1990.

Chia, F., R. W. Griffiths, and P. F. Linden, Laboratory experiments on fronts, II, The formation of cyclonic eddies at upwelling fronts, *Geophys. Astrophys. Fluid Dyn.*, *19*, 189-206, 1982.

Coastal Transition Zone Group, The Coastal Transition Zone Program, *Eos Trans. AGU*, *69(27)*, 698-699, 1988.

Cullen, J. J., The deep chlorophyll maximum: Comparing vertical profiles of chlorophyll *a*, *Can. J. Fish. Aquat. Sci.*, *39*, 791-803, 1982.

Cullen, J. J., and R. W. Eppley, Chlorophyll maximum layers of the southern California Bight and possible mechanisms of their formation and maintenance, *Oceanol. Acta*, *4*, 23-32, 1981.

Cullen, J. J., F. M. H., Reid, and E. Stewart, Phytoplankton in the surface and the chlorophyll maximum off southern California in August, 1978, *J. Plankton. Res.*, *4*, 665-694, 1982.

Cullen, J. J., E. Stewart, E. Renger, R. W. Eppley, and C. D. Winant, Vertical motion in the thermocline, nitracline, and chlorophyll maximum layers in relation to currents on the southern California shelf, *J. Mar. Res.*, *41*, 239-262, 1983.

Dagg, M. J., J. Vidal, T. E. Whitledge, R. L. Iverson, and J. J. Goering, The feeding, respiration and excretion of zooplankton in the Bering Sea during a spring bloom, *Deep-Sea Res.*, *29*, 45-63, 1982.

Davis, C. O., N. F. Brientner, and P. J. Harrison, Continuous culture of marine diatoms under silicon limitation. 3. A model of Si-limited growth, *Limnol. Oceanogr.*, *23*, 41-52, 1978.

De Groot, W. T., Modelling the multiple nutrient limitation of algal growth, *Ecological Modelling*, *18*, 99-119, 1983.

Deibel, D., Laboratory determined mortality, fecundity and growth rates of *Thalia democratica* Forskal and *Dolioletta gegenbauri* Uljanin (Tunicata, Thaliacea), *J. Plankton Res.*, *4*, 143-153, 1982*a*.

Deibel, D., Laboratory-measured grazing and ingestion reates of the salp, *Thalia democratica* Forskal, and the doliolid, *Dolioletta gegenbauri* Uljanin (Tunicata, Thaliacea), *J. Plankton Res.*, *4*, 189-201, 1982*b*.

Deibel, D., Clearance rates of the salp *Thalia democratica* fed naturally occurring particles, *Mar. Biol.*, *86*, 47-54, 1985.

Dewey, R. K., and J. N. Moum, Enhancement of fronts by vertical mixing, *J. Geophys. Res.*, *95*, 9433-9445, 1990.

Dewey, R. K., J. N. Moum, C. A. Paulson, D. R. Caldwell, and S. D. Pierce, Structure and dynamics of a coastal filament, *J. Geophys. Res.*, *96*, 14,885-14,907, 1991.

Downing, J. A., and F. h. Rigler, *A Manual on Methods for the Assessment of Secondary Productivity in Fresh Waters.*, Blackwell Scientific Publications, pp. 501, Great Yarmouth, Norfolk, England, 1984.

Dugdale, R. C., and J. J. Goering, Uptake of new and generated forms of nitrogen in primary productivity, *Limnol. Oceanogr.*, *12*, 196-219, 1967.

Dugdale, R. C., B. H. Jones, J. J. MacIsaac, and J. J. Goering, Adaptation of nutrient assimilation, In *Physiological Bases of Phytoplankton Ecology, Can. Bull. Fish. Aq. Sci.*, edited by T. Platt, pp. 234-250, 1981.

Dugdale, R. C., and F. P. Wilkerson, New production in the upwelling center at Point Conception, California: temporal and spatial patterns, *Deep-Sea Res.*, *36*, 985-1007, 1989.

El-Sayed, S. Z. and H. R. Jitts, Phytoplankton production in the southeastern Indean Ocean, In *Ecological Studies, Analysis and Synthesis, Vol. 3*, edited by B. Zeitzschel, pp. 131-142, Springer-Verlag, Berlin, 1973.

Eppley, R. W., and B. J. Peterson, Particulate organic flux and planktonic new production in the deep ocean, *Nature*, *282*, 677-680, 1979.

Eppley, R. W., J. N. Rogers, and J. J. McCarthy, Half-saturation constants for uptake of nitrate and ammonium by various phytoplankton, *Limnol. Oceanogr.*, *14*, 912-920, 1969.

Eppley, R. W., E. H. Renger, and W. G. Harrison, Nitrate and phytoplankton production in southern California coastal waters, *Limnol. Oceanogr.*, *24*, 483-494, 1979*a*.

Eppley, R. W., E. H. Renger, W. G. Harrison, and J. J. Cullen, Ammonium distribution in southern California coastal waters and its role in the growth of phytoplankton, *Limnol. Oceanogr.*, *24*, 495-509, 1979*b*.

Fairbanks, R. G. and P. H. Weibe, Foraminifera and chlorophyll maximum: vertical distribution, seasonal succession, and paleooceanographic significance, *Science*, *209*, 1524-1529, 1980.

Flament, P., L. Armi and L. Washburn, The evolving structure of an upwelling filament, *J. Geophys. Res.*, *90*, 11,765-11,778, 1985.

Frost, B. W., Effects of size and concentration of food particles on the feeding behavior of the marine planktonic copepod *Calanus pacificus*, *Limnol. Oceanogr.*, *6*, 805-915, 1972.

Frost, B. W., A threshold feeding behavior in *C. pacificus*, *Limnol. Oceanogr.*, *20*, 263-266, 1975.

Frost, B. W., The inadequacy of body size as an indicator of niches in the zooplankton, in *Evolution and Ecology of Zooplankton Communities*, edited by W. C. Kerfoot, pp. 742-753, The University Press of New England, 1980.

Frost, B. W., Food limitation of the planktonic marine copepods *Calanus pacificus* and *Pseudocalanus* sp. in a temperate fjord, *Arch. Hydrobiol. Beih. Ergebn. Limnol.*, *21*, 1-13, 1985.

Frost, B. W., Variability and possible adaptive significance of diel vertical migration in *Calanus pacificus*, A plankton marine copepod, *Bull. Mar. Sci.*, *43*, 675-694, 1988.

Gould, R. W., The deep chlorophyll maximum in the world ocean: A review, *The Biologist*, *66*, 4-13, 1987.

Griffiths, R. W., and P. F. Linden, Laboratory experiments on fronts, I, Density–driven boundary currents, *Geophys. Astrophys. Fluid Dyn.*, *19*, 159-187, 1982.

Haidvogel, D. B., A. Beckmann and K. S. Hedström, Dynamical simulations of filament formation and evolution in the Coastal Transition Zone, *J. Geophys. Res.*, *96*, 15,017-15,040, 1991a.

Haidvogel, D. B., J. Wilkin and R. E. Young, A semi-spectral primitive equation ocean circulation model using vertical sigma and orthogonal curvilinear coordinates, *J. Comp. Phys.*, *94*, 151-185, 1991b.

Harding, L. W., Jr., B. W. Meeseon, B. B. Prezlin, and B. M. Sweeny, Diel periodicity of photosynthesis in marine phytoplankton, *Mar. Biol.*, *61*, 95-105, 1981.

Harding, L. W., Jr., B. B. Prézlin, B. M.Sweeney, and J. L. Cox, Diel oscillations of the photosynthesis irradiance (P-I) relationship in natural assemblages of phytoplankton, *Mar. Biol.*, *67*, 167-178, 1982*a*.

Harding, L, W., Jr., B. B. Prézlin, B. M. Sweeny, and J. L. Cox, Primary production as influenced by diel periodicity of phytoplankton photosynthesis, *Mar. Biol.*, *67*, 179-186, 1982*b*.

Harding, L. W., Jr., and J. F. Heinbokel, Periodicities of photosynthesis and cell division: behavior of phase-lagged replicate cultures of *Ditylum brightwellii* in a diurnally varying photic regime, *Mar. Ecol. Prog. Ser.*, *15*, 225-232, 1984.

Harrison, W. G., T. Platt, and M. L. Lewis, *f*-Ratio and its relationship to ambient nitrate concentration in coastal waters, *J. Plankton. Res.*, *9*, 235-248, 1987.

Haynes, R., and E. D. Barton, A poleward flow along the Atlantic coast of the Iberian Peninsula, *J. Geophys. Res.*, *95*, 11,425-11,141, 1990.

Hayes, R., and E. D. Barton, Lagrangian observations in the Iberian coastal transition zone, *J. Geophys. Res.*, *96*, 14,731-14,741, 1991.

Hayward, T. L., and A. Mantyla, Physical, chemical and biological structure of a coastal eddy near Cape Mendocino, *J. Mar. Res.*, *48*, 825-850, 1990.

Hedström, K. S., User's manual for a semi-spectral primitive equation regional ocean-circulation model. Version 3. 0, *Institute of Naval Oceanography Technical Note FY90-2*, pp. 82, 1991.

Heron, A. C., Population ecology of a colonizing species: The pelagic tunicate *Thalia democratica*. I. Population growth rate, *Oecologia*, *10*, 294-312, 1972*a*.

Heron, A. C., Population ecology of a colonizing species: The pelagic tunicate *Thalia democratica*. II. Individual growth rate and generation time, *Oecologia*, *10*, 269-293, 1972*b*.

Heron, A. C., and E. E. Benham, Individual growth rates of salps in three populations, *J. Plankton Res.*, *6*, 811-828, 1984.

Hickey, B. M., The California Current system – Hypotheses and facts, *Prog. Oceanogr.*, *8*, 191-279, 1979.

Hoepffner, N., and S. Sathyendranath, Effect of pigment composition on the absorption properties of phytoplankton, *Mar. Ecol. Prog. Ser.*, In Press, 1991.

Hofmann, E. E., K. S. Hedström, J. R. Moisan, D. B. Haidvogel and D. L. Mackas, The use of simulated drifter tracks to investigate general transport patterns and residence times in the Coastal Transition Zone, *J. Geophys. Res.*, *96*, 15,041-15,052, 1991.

Hofmann, E. E. and J. W. Ambler, Plankton dynamics on the outer southeastern U. S. continental shelf. Part II: A time-dependent biological model, *J. Mar. Res.*, *46*, 883-917, 1988.

Hood, R. R., Phytoplankton biomass, photosynthetic light response, and physical structure in a northern California upwelling system, Ph. D. thesis, 141 pp., Scripps Inst. of Oceanogr., La Jolla, California, 1990.

Hood, R. R., M. R. Abbott, A. Huyer, and P. M. Kosro, Surface patterns in temperature, flow, phytoplankton biomass, and species composition in the coastal transition zone off northern California *J. Geophys. Res.*, *95*, 18,081-18,094, 1990.

Hood, R. R., M. R. Abbott, and A. Huyer, Phytoplankton and photosynthetic light response in the coastal transition zone off northern California in June 1987, *J. Geophys. Res.*, *96*, 14,769-14,780, 1991.

Huyer, A. E., Coastal upwelling in the California Current system, *Prog. Oceanogr.*, *12*, 259-284, 1983.

Huyer, A., Hydrographic observations along the CODE central line off northern California, 1981, *J. Phys. Oceanogr.*, *14*, 1647-1658, 1984.

Huyer, A., and R. L. Smith, Observations of a poleward undercurrent over the continental shelf off Oregon, May–June 1975, *Eos Trans. AGU*, *57*, 263 pp. , 1975.

Huyer, A., and P. M. Kosro, Mesoscale surveys over the shelf and slope in the upwelling region near Point Arena, California, *J. Geophys. Res.*, *92*, 1655-1682, 1987.

Huyer, A., P. M. Kosro, S. Lentz, and R. C. Beardsley, Poleward flow in the California Current system, in *Poleward Flows Along Eastern Ocean Boundaries, Coastal Estuar. Studies*, vol. 34, edited by S. Neshyba, C. N. K. Mooers, R. L. Smith, and R. T. Barber, pp. 142-156, Springer-Verlag, New York, 1989.

Huyer, A. J., P. M. Kosro, J. Fleischbein, S.,R. Ramp, T. Stanton, L. Washburn, F. P. Chavez, T. J. Cowles, S. D. Pierce, and R. L. Smith, Currents and water masses of the coastal transition zone off northern California, June to August 1988 *J. Geophys. Res.*, *96*, 14,809-14,831, 1991.

Ikeda, M., and W. J. Emery, Satellite observations and modeling of meanders in the California Current system off Oregon and northern California, *J. Phys. Oceanogr.*, *14*, 1434-1450, 1984.

Ishizaka, J. , Coupling of Coastal Zone Color Scanner data to a physical-biological model of the southeastern U. S. continental shelf ecosystem, 3. Nutrient and phytoplankton fluxes and CZCS data assimilation, *J. Geophys. Res.*, *95*, 20,201-20,212, 1990.

Jahnke, R. A., Ocean flux studies: a status report, *Reviews of Geophysics*, *28*, 381-398, 1990.

Jamart, B. M., D. F. Winter, K. Banse, G. C. Anderson and R. K. Lam, A theoretical study of phytoplankton growth and nutrient distribution in the Pacific Ocean off the northwestern U. S. coast, *Deep-Sea Res.*, *24*, 753-773, 1977.

Jeffries, C., Stability of ecosystems with complex food webs, *Theor. Pop. Biol.*, *7*, 149-155, 1975.

Jeffrey, S. W., Algal pigment systems, In *Primary Productivity in the Sea*, edited by P. Falkowski, Plenum, New York, pp. 33-58, 1980.

Jerlov, N. G., *Marine Optics*, *Elsevier Oceanographic Series 5*, Elsevier, New York, 1976.

Jones, B. H., C. N. K. Mooers, M. M. Rienecker, T. Stanton, and L. Washburn, Chemical and biological structure and transport of a cool filament associated with a jet-eddy system off northern California in July 1986 (OPTOMA21), *J. Geophys. Res.*, *96*, 22,207-22,225, 1991.

Kadko, D. C., L. Washburn, and B. Jones, Evidence of subduction within cold filaments of the northern California coastal transition zone, *J. Geophys. Res.*, *96*, 14,909-14,926, 1991.

Kirwan, A. D., W. J. Merrell, Jr., J. K. Lewis, and R. E. Whitaker, Lagrangian observations of an anticyclonic ring in the Western Gulf of Mexico, *J. Geophys. Res.*, *89*, 3417-3424, 1984.

Kirwan, A. D., W. J. Merrell, Jr., J. K. Lewis, R. E. Whitaker, and R. Legeckis, A model for the analysis of drifter data with an application to a warm core ring in the Gulf of Mexico, *J. Geophys. Res.*, *89*, 3425-3438, 1984.

Kosro, P. M., and A. Huyer, CTD and velocity surveys of seaward jets off northern California, July 1981 and 1982, *J. Geophys. Res.*, *91*, 7680-7690, 1986.

Kosro, P. M., Structure of the coastal current field off northern California during the Coastal Dynamics Experiment, *J. Geophys. Res.*, *92*, 1655-1681, 1987.

Kosro, P. M., A. Huyer, S. R. Ramp, R. L. Smith, F. P. Chavez, T. J. Cowles, M. R. Abbott, P. T. Strub, R. T. Barber, P. Jessen, and L. F. Small, The structure of the transition zone between coastal waters and the open ocean off northern California, winter and spring 1987, *J. Geophys. Res.*, *96*, 14,707-14,730, 1991.

Landry, M. R., R. P. Hassett, V. Fagerness, J. Downs and C. J. Lorenzen, Effect of food acclimation on assimilation efficiency of *Calanus pacificus*, *Limnol. Oceanogr.*, *29*, 361-364, 1984.

Lasker, R., Feeding, growth, respiration, and carbon utilization of a euphausiid crustacean, *J. Fish. Res. Bd. Canada*, *23*, 1291-1317, 1966.

Lentz, S. J., A description of the 1981 and 1982 spring transitions over the northern California shelf, *J. Geophys. Res.*, *92*, 1545-1567, 1987

Longhurst, A. R., and A. W. Herman, Do oceanic zooplankton aggregate at, or near, the deap chlorophyll maximum?, *J. Mar. Res.*, *39*, 353-356, 1981.

Lorenzen, C. J., Vertical distribution of chlorophyll and pheao-pigments: Baja California, *Deep-Sea Res.*, *14*, 735-745, 1967.

Lutjeharms, J. R. E., and P. L. Stockton, Kinematics of the upwelling front off southern Africa, *So. Afr. J. Mar. Sci.*, *5*, 35-50, 1987.

Lynn, R. J., and J. J. Simpson, The California Current system: The seasonal variability of its physical characteristics, *J. Geophys. Res.*, *92*, 12,947-12,966, 1987.

Lynn, R. J., and J. J. Simpson, The flow of the undercurrent over the continental borderland off southern California, *J. Geophys. Res.*, *95*, 12,995-13,008, 1990.

MacCaull, W. A., and T. Platt, Diel variations in the photosynthetic parameters of coastal marine phytoplankton, *Limnol. Oceanogr.*, *22*, 723-731, 1977.

MacIsaac, J. J., and R. C. Dugdale, The kinetics of nitrate and ammonia uptake by natural populations of marine phytoplankton, *Deep-Sea Res.*, *16*, 45-57, 1969.

MacIsaac, J. J., and R. C. Dugdale, Interactions of light and inorganic nitrogen in controlling nitrogen uptake in the sea, *Deep-Sea Res.*, *19*, 209-232, 1972.

Mackas, D. L., L. Washburn and S. Smith, Zooplankton community pattern associated with a California Current cold filament, *J. Geophys. Res.*, *96*, 14,781-14,797, 1991.

Madin, L. P., Field observations on the feeding behavior of salps *Tunicata: Thaliacea*, *Mar. Biol.*, *25*, 143-147, 1974.

Magnell, B. A., N. A. Bray, C. D. Winant, C. L. Greengrove, J. Largier, J. F. Borchardt, R. L. Bernstein, and C. E. Dorman, Convergent shelf flow at Cape Mendocino, *Oceanography*, *3*, 4-11, 1990.

McCarthy, J. J., The kinetics of nutrient utilization, In *Physiological Bases of Phytoplankton Ecology, Can. Bull. Fish. Aq. Sci.*, edited by T. Platt, pp. 211-233, 1981.

McCreary, J. P., Y. Fukamachi, and P. K. Kundu, A numerical investigation of jets and eddies near an eastern ocean boundary, *J. Geophys. Res.*, *96*, 2515-2534, 1991.

Michaelsen, J., X. Zhang, and R. C. Smith, Variability of pigment biomass in the California Current system, *J. Geophys. Res.*, *93*, 10,883-10,896, 1988.

Mooers, C. N. K. and A. R. Robinson, Turbulent jets and eddies in the California Current and inferred cross-shore transports, *Science*, *223*, 51-53, 1984.

Narimousa, S., and T. Maxworthy, Two-layer model of shear-driven coastal upwelling in the presence of bottom topography, *J. Fluid. Mech.*, *159*, 503-531, 1985.

Narimousa, S., and T. Maxworthy, Laboratory modeling of coastal upwelling, *Eos Trans. AGU*, 67, 2-3, 1986.

Narimousa, S., and T. Maxworthy, On the effects of coastline perturbations on coastal currents and fronts, *J. Phys. Oceanogr.*, *17*, 1296-1303, 1987.

Narimousa, S., and T. Maxworthy, Application of a laboratory model to the interpretation of satellite and field observations of coastal upwelling, *Dyn. Atmos. Oceans*, *13*, 1-46, 1989.

Ohman, M. D., Sources of variability in measurements of copepod lipids and gut fluorescence in the California Current coastal zone, *Mar. Ecol. Prog. Ser.*, *42*, 143-153, 1988.

Omori, M., and T. Ikeda *Methods in Marine Zooplankton Ecology.*, John Wiley & Sons, Inc., New York, New York, 1984.

Paasche, E., Silicon and the ecology of marine plankton diatoms. I. *Thalassiosira pseudonana* (*Cyclotella nana*) grown in a chemostat with silicate as limiting nutrient, *Mar. Biol.*, *19*, 117-126, 1973.

Paasche, E., Silicon and the ecology of marine plankton diatoms. II. Silicate-uptake kinetics in five diatom species, *Mar. Biol.*, *19*, 262-269, 1973.

Paduan, J. D. and P. P. Niiler, A Lagrangian description of motion in northern California coastal transition filaments, *J. Geophys. Res.*, *95*, 18,095-18,109, 1990.

Paffenhöfer, G. -A., and T. N. Lee, Development and persistence of patches of Thaliacea, In *The Benguela and Comparable Ecosystems*, Edited by A. I. L. Payne, J. A. Gulland, and K. H. Brink, *S. Afr. J. Mar. Sci.*, 5, 305-318, 1987.

Pavlova, Y. V., Seasonal variations in the California Current, *Oceanology*, *6*, 806-814, 1969.

Peacock, T.G., K. L. Carder, R. G. Steward, and C. O. Davis, Components of spectral attenuation for an offshore jet in the California Current coastal transition zone, *Eos Trans. AGU*, *69*, 1125, 1988.

Pelaéz, J. and J. A. McGowan, Phytoplankton pigment patterns in the California Current as determined by satellite, *Limnol. Oceanogr.*, *31*, 927-950, 1986.

Pierce, S. D., J. S. Allen, and L. J. Walstad, Dynamics of the coastal transition zone jet, 1, Linear stability analysis, *J. Geophys. Res.*, *96*, 14,979-14,993, 1991.

Platt, T., C. L. Gallegos, and W. G. Harrison, Photoinhibition of photosynthesis in natural assemblages of marine phytoplankton, *J. Mar. Res.*, *38*, 687-701, 1980.

Prézelin, B. B., M. Putt, and H. E. Glover, Diurnal patterns in photosynthetic capacity and depth-dependent photosynthesis-irradiance relationships in *Synechococcus* spp. and larger phytoplankton in three water masses in the northwest Atlantic Ocean, *Mar. Biol.*, *91*, 205-217, 1986*a*.

Prézelin, B. B., R. R. Bidigare, H. A. Matlick, M. Putt, and B. Ver Hoven, Diurnal patterns of size-fractioned primary productivity across a coastal front, *Mar. Biol.*, *96*, 563-574, 1987.

Price, H. J., G. -A. Paffenhöfer, Modes of cell capture in calanoid copepods, *Limnol. Oceanogr.*, *28*, 116-123, 1983.

Price, H. J., G. -A. Paffenhöfer, Effects of feeding experience on the copepod *Eucalanus pileatus*: a cinematographic study, *Mar. Biol.*, *84*, 35-40, 1984.

Price, H. J., K. R. Boyd, and C. M. Boyd, Omnivorous feeding behavior of the Antarctic krill *Euphausia superba*, *Mar. Biol.*, *97*, 67-77, 1988.

Prieur, L., and S. Sathyendranath, An optical classification of coastal and oceanic waters based on the specific spectral absorption curves of phytoplankton pigments, dissolved organic matter, and other particulate materials, *Limnol Oceanogr.*, *26*, 671-689, 1981.

Putt, M., R. B. Rivkin, and B. B. Prèzelin, Effects of altered photic regimes on diel patterns of species-specific photosynthesis, *Mar. Biol.*, *97*, 435-443, 1988.

Putt, M., and B. B. Prézelin, Diel periodicity of photosynthesis and cell division compared in *Thalassiosira weissflogii* (Bacillariophyceae), *J. Phycol.*, *24*, 315-324, 1988.

Ramp, S. R., P. F. Jessen, K. H. Brink, P. P. Niiler, F. L. Daggett, and J. S. Best, The physical structure of cold filaments near Point Arena, California, during June 1987, *J. Geophys. Res.*, *96*, 14,859-14,883, 1991*a*.

Ramp, S. R., R. W. Garwood, C. O. Davis, and R. L. Snow, Surface heating and patchiness in the coastal ocean off central California during a wind relaxation event, *J. Geophys. Res.*, *96*, 14,947-14,957, 1991*b*.

Reinecker, M. M., C. N. K. Mooers, D. E. Hagan, and A. R. Robinson, A cool anomaly off northern California: An investigation using IR imagery and in situ data, *J. Geophys. Res.*, *90*, 4807-4818, 1985.

Reinecker, M. M., C. N. K. Mooers, and A. R. Robinson, Dynamical interpolation and forecast of the evolution of mesoscale features off northern California, *J. Phys. Oceanog.*, *17*, 1189-1213, 1987.

Reinecker, M. M. and C. N. K. Mooers, Mesoscale eddies, jets, and fronts off Point Arena, California, July 1986, *J. Geophys. Res.*, *94*, 12,555-12,569, 1989*a*.

Rienecker, M. M., and C. N. K. Mooers, A summary of the OPTOMA program's mesoscale ocean prediction studies in the California Current System, in *Mesoscale/Synoptic Coherent Structures in Geophysical Turbulence*, edited by J. C. J. Nihoul and B. M. Jamart, pp. 519-548, Elsevier, Amsterdam, 1989*b*.

Roman, M. R., C. S. Yentch, A. L. Gauzens and D. A. Phinney, Grazer control of the fine-scale distribution of phytoplankton in warm-core Gulf Stream rings, *J. Mar. Res.*, *44*, 795-813, 1986.

Ross, R. M., Laboratory culture and development of *Euphausia pacifica*, *Limnol. Oceanogr.*, *26*, 235-246, 1981.

Ross, R. M., Reproductive cycle and fecundity of *Euphausia pacifica* in Puget Sound, Washington, *Limnol. Oceanogr.*, *27*, 304-314, 1982*a*.

Ross, R. M., Energetics of *Euphausia pacifica*. I. Effects of body carbon and nitrogen and temperature on measured and predicted production, *Mar. Biol.*, *68*, 1-13, 1982*b*.

Ross, R. M., Energetics of *Euphausia pacifica*. II. Complete carbon and nitrogen budgets at 8°and 12°C throughout the life span, *Mar. Biol.*, *68*, 15-23, 1982*c*.

Runge, J. A., Relationship of egg production of *Calanus pacificus* to seasonal changes in phytoplankton availability in Puget Sound, Washington, *Limnol. Oceanogr.*, *30*, 382-396, 1985.

Ryther, J. H., Photosynthesis and Fish Production in the Sea, *Science*, *166*, 72-76, 1969.

Sathyendranath, S., L. Lazzara, and L. Prieur, Variations in the spectral values of specific absorption of phytoplankton, *Limnol. Oceanogr.*, *32*, 403-415, 1987.

Sathyendranath, S., and T. Platt, The spectral irradiance field at the surface and in the interior of the ocean: A model for applications in oceanography and remote sensing, *J. Geophys. Res.*, *95*, 9270-9280, 1988.

Sathyendranath, S., and T. Platt, Remote sensing of ocean chlorophyll: Consequence of nonuniform pigment profile, *Appl. Opt.*, *28*, 490-495, 1989.

Sathyendranath, S., and T. Platt, Angular distribution of the submarine light field: Modification by multiple scattering, *Proc. Roy. Soc. Lond. Ser. A.*, In Press, 1991.

Shannon, L. V., P. Schlittenhardt, and S. A. Mostert, The NIMBUS 7 CZCS experiment in the Benguela current off southern Africa, February 1980, 2. Interpretation of imagery and oceanographic implications, *J. Geophys. Res.*, *89*, 4968-4976, 1984.

Simpson, J. J., C. J. Koblinsky, L. R. Haury, and T. D. Dickey, An offshore eddy in the California Current System, *Prog. Oceanogr.*, *13*, 1-111, 1984.

Simpson, J. J., C. J. Koblinsky, J. Pelaèz, L. R. Haury, and D. Wiesenhaln, Temperature-plant pigment-optical relations in a recurrent offshore mesoscale eddy near Point Conception, California, *J. Geophys. Res.*, *91*, 12,919-12,936, 1986.

Simpson, J. J., and R. J. Lynn, A mesoscale eddy dipole in the offshore California current, *J. Geophys. Res.*, *95*, 13,009-13,122, 1990.

Smayda, T. J., The suspension and sinking of phytoplankton in the sea, *Oceanogr. Mar. Biol.*, *8*, 353-414, 1970.

Smetacek, V. S., Role of sinking in diatom life history cycles: ecological, evolutionary and geological significance, *Mar. Biol.*, *84*, 234-251, 1985.

Smith, R. C., X. Zhang, and J. Michaelsen, Variability of pigment biomass in the California Current system as determined by satellite imagery, 1, Spatial variability, *J. Geophys. Res.*, *93*, 10,863-10,882, 1988.

Smith, R. C., B. B. Prézelin, R. R. Bidigare, K. S. Baker, Bio-optical modeling of photosynthetic production in coastal waters, *Limnol. Oceanogr.*, *34*, 1524-1544, 1989.

Smith, S. L., B. H. Jones, L. P. Atkinson, and K. H. Brink, Zooplankton in the upwelling fronts off Point Conception, California, in *Marine Interfaces Ecohydrodynamics, Elsevier Oceanogr. Ser.*, vol. 42, edited by J. C. J. Nihoul, pp. 195-213, Elsevier, New York, 1986*a*.

Smith, S. L., and V. P. Lane, Grazing of the spring diatom bloom in the New York Bight by the calanoid copepods *Calanus finmarchicus*, *Metridia lucens* and *Centropages typicus*, *Cont. Shelf Res.*, *8*, 485-509, 1988.

Smith, S. L. and P. V. Z. Lane, The jet off Point Arena, California: Its role in secondary production of the copepod *Eucalanus californicus* Johnson, *J. Geophys. Res.*, *96*, 14,849-14,858, 1991.

Stauber, J. L., and S. W. Jeffrey, Photosynthetic pigments in fifty-one species of marine diatoms, *J. Phycol.*, *24*, 158-172, 1988.

Stramma, L., P. Cornillon, R. A. Weller, J. F. Price, and M. G. Briscoe, Large diurnal sea surface temperature variability: Satellite and in situ measurements, *J. Phys. Oceanogr.*, *16*, 827-837, 1986.

Strub, P. T., J. S. Allen, A. Huyer, and R. L. Smith, Seasonal cycles of currents, temperatures, winds, and sea level over the northeast Pacific continental shelf: 35°N to 48°N, *J. Geophys. Res.*, *92*, 1507-1526, 1987*a*.

Strub, P. T., J. S. Allen, A. Huyer, and R. L. Smith, Large-scale structure of the spring transition in the coastal ocean off western North America, *J. Geophys. Res.*, *92*, 1527-1544, 1987*b*.

Strub, P. T., C. James, A. C. Thomas, and M. R. Abbott, Seasonal and nonseasonal variability of satellite-derived surface pigment concentrations in the California Current, *J. Geophys. Res.*, *95*, 11,501-11,530, 1990.

Strub, P. T., Kosro, P. M., Huyer, A. and the CTZ Collaborators, The nature of the cold filaments in the California Current system, *J. Geophys. Res.*, *96*, 14,743-14,768, 1991.

Sverdrup, H. U., and R. H. Fleming, The waters off the coast of southern California, March to July 1967, *Scripps Ints. Oce. Bull.*, *4*, 261-387, 1941.

Tchernia, P., *Descriptive Regional Oceanography*, 253 pp., Pergamon Press, New York, 1978.

Thomas, A. C., and P. T. Strub, Interannual variability in phytoplankton pigment distributions during the spring transition along the west coast of North America, *J. Geophys. Res.*, *94*, 18,095-18,117, 1989.

Thomas, A. C., and P. T. Strub, Seasonal and interannual variability of pigment concentrations across a California Current frontal zone, *J. Geophys. Res.*, *95*, 13,023-13,042, 1990.

Thomson, R. E., and J. E. Papadakis, Upwelling filaments and motion of a satellite-tracked drifter along the west coast of North America, *J. Geophys. Res.*, *92*, 6445-6461, 1987.

Traganza, E. D., D. A. Nestor, and A. K. McDonald, Satellite observations of a nutrient upwelling off the coast of California, *J. Geophys. Res.*, *85*, 4104-4106, 1980.

Traganza, E. D., J. C. Conrad, and L. C. Breaker, Satellite observations of a cyclonic upwelling system and a giant plume in the California current, in *Coastal Upwelling, Coastal Estuarine Sci.*, vol. 1, edited by F. A. Richards, pp. 228-241, AGU, Washington, D. C., 1981.

Tsuchiya, M., Subsurface countercurrents in the Pacific Ocean, *J. Mar. Res.*, *33*, (suppl.) 145-175, 1975.

Varela, R. A. , A. Cruzado, J. Tintore, and E. G. Ladona, Modelling the deep-chlorophyll maximum: A coupled physical-biological approach, *J. Mar. Res.*, *50*, 441-463, 1992.

Venrick, E. L, Winter mixing and the vertical stratification of phytoplankton — another look, *Limnol. Oceanogr.*, *29*, 636-640, 1984.

Venrick, E. L, J. A. McGowan, and A. W. Mantyla, Deep maxima of photosynthetic chlorophyll in the Pacific Ocean, *Fish. Bull.*, *71*, 41-52, 1973.

Vidal, J., Physioecology of zooplankton. I. Effects of phytoplankton concentration, temperature, and body size on the growth rate of *Calanus pacificus* and *Pseudocalanus* sp., *Mar. Biol.*, *56*, 111-134, 1980*a*.

Vidal, J., Physioecology of zooplankton. II. Effects of phytoplankton concentration, temperature, and the development and molting rates of *Calanus pacificus* and *Pseudocalanus* sp., *Mar. Biol.*, *56*, 135-146, 1980*b*.

Vidal, J., Physioecology of zooplankton. I. Effects of phytoplankton concentration, temperature, and body size on the metabolic rate of *Calanus pacificus*, *Mar. Biol.*, *56*, 195-202, 1980*c*.

Vidal, J., Physioecology of zooplankton. I. Effects of phytoplankton concentration, temperature, and body size on the net production efficiency of *Calanus pacificus*, *Mar. Biol.*, *56*, 203-211, 1980*d*.

Vidal, J., and T. E. Whitledge, Rates of metabolism of planktonic crustaceans as related to body weight and temperature, *J. Plankton Res.*, *4*, 77-84, 1982.

Vidal, J. P., and S. L. Smith, Biomass, growth, and development of populations of herbivorous zooplankton in the southeastern Bering Sea during spring, Brookhaven National Laboratory Technical Report *51941*, pp. 69, 1985.

Wada, E., and A. Hattori, *Nitrogen in the Sea: Forms, Abundances, and Rate Processes*, *CRC Press*, 208 pp., 1991.

Walsh, J. J., *On the Nature of Continental Shelves.*, Academic Press, New York, New York, 1988.

Walstad, L. J., J. S. Allen, P. M. Kosro, and A. Huyer, Dynamics of the coastal transition zone in 1987 through data assimilation studies *J. Geophys. Res.*, *96*, 14,959-14,977, 1991.

Washburn, L., D. C. Kadko, B. H. Jones, T. Hayward, P. M. Kosro, T. P. Stanton, S. Ramp, and T. Cowles, Water mass subduction and the transport of phytoplankton in a coastal upwelling system, *J. Geophys. Res.*, *96*, 14,927-14,945, 1991.

White, W. B., C. -K. Tai, and J. DiMento, Annual Rossby waves characteristics in the California Current region from Geosat exact repeat mission, *J. Phys. Oceanogr.*, *20*, 1297-1310, 1990.

Wooster, W. S., and J. L. Reid., Jr., Eastern boundary currents, in *The Sea*, vol. 6(11), pp. 253-260, M. N. Hill, New York, N. Y., 1963.

Wroblewski, J. S., The role of modeling in biological oceanography, *Ocean Science and Engineering*, *8*, 245-285, 1983.

Autobiographical Statement

John Roland Moisan

Personal Data

I was born on October 10, 1961, in Biddeford, Maine, U.S.A. My parents are Conrad and Joan Moisan. I am the third child in a family of eleven children and second generation Franco-American. I married Tiffany Kay Ashworth on August 18, 1990.

Formal Education

B.S. Marine Biology, May 1983, University of New England, U.S.A.

Publications

Stephens, Carol F., Michael F. Ondrusek, Robert R. Bidigare, Sayed Z. El-Sayed, John R. Moisan and James M. Brooks, 1990: The Influence of UV radiation on Carbon Fixation Rates and Pigment Composition of Antarctic Phytoplankton, *Deep Sea Research*, Submitted.

Hofmann, Eileen E., Katherine S. Hedström, John R. Moisan, Dale B. Haidvogel and David L. Mackas, 1991: The Use of Simulated Drifter Tracks to Investigate General Transport Patterns and Residence Times in the Coastal Transition Zone, *Journal of Geophysical Research*, **96(C8)** 15,041-15,052.

Other Publications and Abstracts

Moisan, John R., 1988: Response of Antarctic Marine Phytoplankton Primary Production Rates to Changes in Solar UV-B Radiation, *EOS*, **69(44)**, 1082.

Moisan, John R., 1990: A Model of Nutrient and Plankton Processes in the Coastal Transition Zone, *EOS*, **71(2)**, 145.

Hofmann, Eileen E., Katherine S. Hedström, John R. Moisan, Dale B. Haidvogel and David L. Mackas, 1990: The Use of Simulated Drifter Tracks to Investigate General Transport Patterns and Residence Times in the Coastal Transition Zone, *EOS*, **71(43)**, 1360.

Moisan, John R., 1990: A Three-Dimensional Time-Dependent Physical-Biological Model of Nutrient and Plankton Processes in the Coastal Transition Zone, *EOS*, **71(43)**, 1361.

Moisan, John R. and Eileen E. Hofmann, 1991: Circulation and Bio-optical Models: An Example From the Coastal Transition Zone, *EOS*, **72(44)**, 252.

Haidvogel, Dale B., Moisan, John R. and Eileen E. Hofmann, 1991: Simulated Lagrangian Drifter Experiments in the California Coastal Transition Zone Using a 3-D Coupled Physical Bio-Optical Model , *EOS*, **72(51)**, 46-47.

Moisan, John R., 1991: Using a 3-D Physical Bio-Optical Model to Investigate New Production and Cross-Shelf Carbon Transport in the California Coastal Transition Zone , *EOS*, **72(51)**, 61.

Moisan, John R. and Eileen E. Hofmann, 1992: A Coupled 1-D Mixed-Layer Bio-Optical Model , *ASLO Aquatic Sciences Meeting, Sante Fe, New Mexico.*

Moisan, John R., 1992: A Vertical, Time-Dependent Bio-Optical Model. "Primary Productivity and Biogeochemical Cycles in the Sea," edited by P. G. Falkowski and A. D. Woodhead, Plenum Press, New York, 522-523.

Books Reviewed

Hofmann, Eileen E. and John R. Moisan, 1991: "Network Analysis in Marine Ecology - Methods and Applications," edited by F. Wulff, J. G. Field, and K. H. Mann, *The Quarterly Review of Biology*, **66(1)**, 97.

Appointments, Positions

Teaching Assistant, University of New England; Sept. 1979 to May 1983.
Research Assistant, University of New England; Sept. 1981 to Sept. 1983.
Research Assistant, Bigelow Laboratory for Ocean Sciences; May 1987 to Aug. 1987.
Graduate Research Assistant, Department of Oceanography, Texas A&M University; Sept. 1987 to Aug. 1989.
Graduate Research Assistant, Department of Oceanography, Old Dominion University; Sept. 1989 to Present.
Student, NASA Summer School for High Performance Computational Sciences, NASA Goddard Space Flight Center; Aug. 1991.

Awards

U.S. Antarctic Service Medal, U.S. Dept. of the Navy and The National Science Foundation; 1988.

Memberships

American Society of Limnology and Oceanography
American Geophysical Union
The Oceanography Society